



DOCTORAL PROGRAM IN FLUID THERMODYNAMICS ENGINEERING

PHD THESIS:

Thermophysical Properties of Aqueous Amines Solutions for CO₂ Capture Applications

Submitted by Yisel Pérez Milian

in fulfilment of the requirements for PhD Degree from the University of Valladolid

Supervised by:

Dr. David Vega Maza

Dr. Alejandro Moreau Ortega





PROGRAMA DE DOCTORADO EN INGENIERÍA TERMODINÁMICA DE FLUIDOS

TESIS DOCTORAL:

Propiedades Termofísicas de Soluciones Acuosas de Aminas para Aplicaciones de Captura de CO₂

Presentada por **Yisel Pérez Milian**para optar al grado de

Doctora por la Universidad de Valladolid

Dirigida por:

Dr. David Vega Maza

Dr. Alejandro Moreau Ortega

A mi familia

Financiación

Yisel Pérez Milian ha sido financiada con cargo a la convocatoria de contratos predoctorales UVa 2021, cofinanciada por el Banco Santander.

Funding

Yisel Pérez Milian has been funded by the for predoctoral contracts call UVa 2021, co-funded by Banco Santander.

RESUMEN

La crisis climática actual es un desafío sin precedentes para la humanidad. Esta crisis viene dada por el exponencial desarrollo de las actividades antropogénicas, las cuales han llevado a un aumento acelerado de las emisiones de gases de efecto invernadero (GEI), como el dióxido de carbono (CO₂) y el metano (CH₄). El gradual aumento de la presencia de estos gases en la atmósfera ha llevado al incremento sustancial de la temperatura de la superficie global, produciendo el llamado cambio climático. Una de las principales fuentes antropogénicas de emisiones de CO₂ es la quema de combustibles fósiles proveniente de industrias como la de generación de energía, la cementera y la metalúrgica. Varias acciones han sido propuestas con la finalidad de impulsar la sostenibilidad ambiental de estos procesos o directamente reemplazar el uso de combustibles fósiles. Entre estas alternativas están el uso de energías renovables, la eficiencia energética y la captura, almacenamiento y uso del CO₂ (CCUS por sus siglas en inglés).

La absorción química de CO₂ usando aminas constituye la tecnología más madura en el mercado entre las tecnologías de captura de CO2 que actualmente están disponibles. Sin embargo, entre los aspectos a mejorar se incluyen la baja eficiencia de captura (80 - 90 %) en comparación con otras tecnologías, la alta demanda de energía en la etapa de regeneración y la baja estabilidad del solvente a altas temperaturas. En este sentido, el foco de la investigación para la optimización de este proceso recae en la búsqueda de soluciones acuosas de una amina o la mezcla de varias que permitan alcanzar una alta separación del CO₂ y, a su vez, que la regeneración del solvente se pueda realizar a temperaturas altas, garantizando la estabilidad del mismo para su reutilización. La amina primaria monoetanolamina (MEA) es sin dudas el solvente más usado en el proceso de absorción química por su rápida reactividad con el CO2. No obstante, otros tipos de amina como las terciarias, cíclicas y las que presentan impedimento estérico han demostrado que pueden alcanzar mayores porcentajes de remoción de CO₂, menores requerimientos energéticos en la etapa de regeneración y una buena estabilidad frente a la posible degradación térmica y oxidativa a la que está expuesto el solvente. A pesar de estas ventajas, la reacción con CO2 de las aminas terciarias y las que presentan impedimento estérico suele ser lenta, encareciendo el proceso de captura, y aunque las aminas cíclicas reaccionan rápidamente con el CO₂, su baja solubilidad en agua y alta viscosidad dificultan su comportamiento.

Como solución a esta problemática, investigadores del ámbito han puesto sus esfuerzos en combinar diferentes tipos de aminas, aprovechando las bondades que ofrece cada una para optimizar la captura. Aunque estos trabajos de investigación van ganando presencia en publicaciones científicas, todavía es necesaria la completa caracterización de las mezclas fluidas involucradas en la captura de CO₂ usando soluciones acuosas de aminas. Esta caracterización viene dada por la precisa medida de propiedades termofísicas como la densidad, la viscosidad y la capacidad calorífica, entre otras. En el presente trabajo

se ofrece una detallada descripción de la influencia de estas propiedades en el mejoramiento del proceso de captura. Se han estudiado diferentes sistemas líquidos binarios (amina + H₂O), ternarios (amina + H₂O + CO₂) y cuaternarios (amina + amina + H₂O + CO₂). Como solventes objeto de estudio se han escogido diferentes tipos de aminas, como monoetanolamina (MEA), dietanolamina (DEA), 2-(etilamino)etanol (EAE), metildietanolamina (MDEA), 2-(dimetilamino)etanol (DMEA), 2-dietilaminoetanol (DEAE), 2-amino-2-metil-1-propanol (AMP), 3-(methylamino)propylamine (MAPA), 1-metilpiperazina (1-MPZ) y piperazina (PZ). Las condiciones de medida (temperatura, presión y concentraciones) fueron establecidas como resultado de la rigurosa revisión bibliográfica realizada con la finalidad de encontrar los rangos más comunes de medida y carencia de datos experimentales reportados.

En este sentido y con el objetivo principal de cubrir gran parte de la laguna existente en la bibliografía, el presente estudio contribuye al campo de la captura de CO₂ mediante la generación de un amplio conjunto de datos experimentales precisos sobre las propiedades volumétricas, energéticas y de transporte de mezclas binarias, ternarias y cuaternarias en las que intervienen soluciones de aminas, ofreciendo explicaciones teóricas de los comportamientos identificados. Además, se propusieron rigurosos modelos de correlación optimizados usando los datos experimentales obtenidos como fruto de este trabajo. Para el cumplimiento de este objetivo general, se plantearon varios objetivos específicos a los cuales se les dio cumplimiento a lo largo de la tesis doctoral. A continuación, se presenta un resumen con los principales resultados obtenidos en este trabajo, los cuales están explicados en detalle en los capítulos que componen esta tesis doctoral.

En el **Capítulo 3**, se agrupa todo lo concerniente al manejo y preparación de las mezclas a estudiar. Primeramente, se realizó un profundo estudio de las hojas de datos de seguridad de cada sustancia (MSDS por sus siglas en inglés) que se utilizó, identificando los principales riesgos a los que se está expuesto. Mediante la elaboración del documento "Control de Sustancias Peligrosas para la Salud" (COSHH por sus siglas en inglés) se identificaron a las aminas como las de mayor precaución en su manejo, siendo necesario el uso siempre de equipamiento de protección personal como batas de laboratorio, guantes y gafas de seguridad, además de resultar imprescindible su manejo exclusivamente debajo de la campana de seguridad por los efectos negativos que causan en el ser humano. Posteriormente, se brindó una descripción detallada del método de preparación de las mezclas usadas en el presente estudio. Las composiciones de las muestras binarias se determinaron mediante pesada usando una precisa balanza analítica de la marca Radwag PS750/C/2 con 1 mg de resolución. La carga de CO₂ en las soluciones acuosas de aminas se realizó usando dos celdas de equilibrio, técnica que posibilitó alcanzar una incertidumbre relativa expandida máxima de 0.4 % (para un nivel de confianza del 95.5 %) en la carga. Las muestras fueron conservadas en frascos limpios de cristal sellados con su tapa y film, y posteriormente almacenados dentro de armarios, evitando el contacto con la luz. La

estabilidad de las muestras se logró mantener hasta un mes después de su preparación; esto fue validado con la monitorización de la densidad y del *pH* de las muestras.

En el Capítulo 4, se llevó a cabo una detallada descripción del densímetro de tubo vibrante (VTD por sus siglas en inglés) usado para las medidas experimentales de la densidad, además de la explicación teórica de la técnica de oscilación mecánica en la que se basa su funcionamiento. Esta técnica, comúnmente usada, permitió obtener densidades en un amplio rango de temperaturas y presiones. El principal componente del VTD es un tubo hueco con forma de "U", el cual es excitado electromagnéticamente. En las medidas, el interior del tubo se llenó con el fluido a estudiar. El principio de operación de este equipo permitió relacionar el periodo de resonancia con la densidad del fluido. Otros aspectos fundamentales que integran el sistema del VTD fueron explicados en detalle, como el sistema termostático, el de control de la presión y el sistema de vacío usado en la limpieza. Se presentó en este capítulo una detallada descripción del procedimiento de medida empleado y del método de limpieza del equipo. En este capítulo se presentó un análisis detallado de los factores de riesgo al operar con este equipo, los cuales vienen dados fundamentalmente por las altas condiciones de temperatura y presión que se alcanzan en las medidas. A partir de ello se decidió instalar válvulas de alivio y discos de ruptura como elementos de seguridad. Una vez tomadas todas las medidas de seguridad pertinentes, se procedió a la calibración del VTD usando vacío y agua siguiendo el método de Lagourette, el cual se explica en detalle en este capítulo. Se realizó también un exhaustivo análisis de la incertidumbre en la medida de la densidad, obteniendo una incertidumbre relativa expandida máxima del 0.2 % para un nivel de confianza del 95.5 %. Por último, para comprobar la correcta calibración del equipo, se llevó a cabo la medida de la densidad del tolueno, ya que este fluido está muy bien caracterizado en la literatura, facilitando la validación de la densidad medida en nuestro equipo.

En el Capítulo 5, se presentó una completa descripción del calorímetro de flujo empleado para las determinaciones experimentales de las capacidades caloríficas isobáricas de los fluidos objeto de estudio. Las principales partes de este equipo fueron descritas en detalle, como el sistema termostático, el de control de la presión, la bomba isocrática que permite el flujo constante y la celda calorimétrica como elemento fundamental del calorímetro de flujo. Este equipo basa su funcionamiento en la medida de la potencia neta de un fluido que circula a flujo constante por dentro de una celda calorimétrica. A medida que la muestra fluye por dentro de la celda, un proceso simultáneo de calentamiento y enfriamiento es llevado a cabo con el objetivo de mantener una diferencia fija de 0.5 K entre la temperatura de salida y la de entrada. Se determinó la contribución de la disipación viscosa en el término de la potencia neta debido a la pérdida de presión causada por la fricción a lo largo del tubo. Además, se detalló en este capítulo el procedimiento experimental seguido para la medida de la capacidad calorífica isobárica. Se realizó una completa revisión de la seguridad del equipo, identificando los principales riesgos asociados a la actividad experimental y resultando sin cambios en la configuración

que ya está establecida previamente. La calibración del calorímetro de flujo fue realizada acorde al procedimiento descrito en los anteriores trabajos de investigación desarrollados en este equipo, usando agua como sustancia para la calibración. Un detallado análisis de incertidumbre en la medida arrojó un resultado de incertidumbre relativa expandida del 1 % para un nivel de confianza del 95.5 %, viniendo las principales contribuciones de la no linealidad de la potencia neta y la repetibilidad de la capacidad calorífica isobárica. La verificación de este procedimiento se realizó usando tolueno como fluido objeto de estudio, ya que, al igual que con la densidad, la capacidad calorífica de esta sustancia está ampliamente reportada en la literatura.

En el Capítulo 6, se realizó una profunda descripción del viscosímetro capilar Ubbelohde que fue usado para las determinaciones de la viscosidad cinemática de las soluciones acuosas de amina (con y sin carga de CO₂) estudiadas como parte de la estancia de investigación realizada en el laboratorio de termofísica del Imperial College London en Reino Unido. Se llevó a cabo una descripción de las partes que integran este equipo, como son el capilar de vidrio, el sistema termostático y el cronómetro electrónico. Este último dispositivo fue recientemente incorporado al equipo en sustitución del cronómetro manual, permitiendo mejorar la incertidumbre en la medida de la viscosidad, disminuyéndola hasta una incertidumbre expandida relativa del 1 % para un nivel de confianza del 95.5 %. El exhaustivo análisis de la incertidumbre asociada a la medida reveló que son medidas más precisas que lo que se suele reportar en la literatura usando otros tipos de viscosímetros. El riesgo asociado a la operación del viscosímetro capilar fue identificado como bajo al trabajar solo a presión atmosférica y temperaturas moderadas (hasta 353.15 K). El procedimiento experimental fue explicado, destacando que este método no está automatizado, por lo que no se considera que la adquisición de datos sea rápida. Este equipo fue calibrado usando agua desgasificada y desionizada y aceites certificados por Paragon Scientific Ltd. para su uso como estándares de calibración de viscosímetros. Determinaciones experimentales de densidad fueron también realizadas usando un viscosímetro cinemático automático Anton Paar SVM 3001. Estos valores de densidad experimentales se usaron para calcular la viscosidad dinámica de las muestras estudiadas.

En el Capítulo 7, se presentaron los resultados experimentales de las medidas de densidad de cinco sistemas binarios (amina + H₂O), cuatro ternarios (amina + H₂O + CO₂) y uno cuaternario (amina + amina + H₂O + CO₂). Se proporcionaron datos de densidades experimentales en un amplio rango de temperatura, presión y concentraciones. Se midieron seis isotermas de temperatura con valores desde 293.15 K hasta 393.15 K y presiones hasta 100 MPa. Para los sistemas binarios fueron estudiadas fracciones másicas de amina de 0.1, 0.2, 0.3 y 0.4. La máxima carga de CO₂ en los sistemas ternarios varió en función de la mezcla estudiada, alcanzando valores de 0.6 mol-CO₂/mol-amina en las soluciones de MEA, 0.9 mol-CO₂/mol-amina en las soluciones de MDEA, 0.5 mol-CO₂/mol-amina en las soluciones de DEA. Para la mezcla cuaternaria

DMEA + MAPA+ H₂O + CO₂, la mayor carga de CO₂ que se alcanzó fue de 0.8 mol-CO₂/mol-aminas. La fracción másica de amina en términos de solución acuosa de amina sin CO₂ para los sistemas ternarios fue de 0.3, mientras que para el sistema cuaternario se estableció una fracción másica de amina de 0.4. Los resultados experimentales arrojaron que la densidad de la mayoría de los sistemas binarios estudiados disminuye con el aumento de la fracción másica de amina, excepto para las soluciones acuosas de 1-MPZ en las que la tendencia de la densidad con la fracción másica de amina depende de las condiciones de temperatura de la medida, como fue explicado en este capítulo. Con respecto a las mezclas ternarias y la cuaternaria, las cuales incluyen al CO₂ como componente, el aumento de la carga de CO₂ trajo consigo un aumento en la densidad. La comparación de los datos experimentales obtenidos en este estudio con los pocos datos disponibles en la literatura arrojó desviaciones relativas acordes con la incertidumbre experimental reportada. Se demostró que una versión modificada de la ecuación de Tammann-Tait, que incluye la dependencia de la molalidad, es adecuada para correlacionar los datos experimentales de densidad en función de la presión, la temperatura y la molalidad, alcanzándose buenas desviaciones relativas absolutas promedio (AAD \leq 0.03 %). Este modelo fue validado con datos experimentales de densidad reportados en la literatura para condiciones de temperatura y fracción másica de amina o carga de CO₂ diferentes a las de medida, obteniendo buenos resultados.

En el Capítulo 8, se mostraron los resultados experimentales de la medida de la capacidad calorífica isobárica de cinco sistemas binarios (amina + H₂O) y tres ternarios (amina + H₂O + CO₂). Las mediciones abarcaron un intervalo de presiones de hasta 25 MPa para las soluciones binarias y de 20 MPa para las ternarias, con cuatro puntos de temperatura entre 293.15 K y 353.15 K. En las soluciones acuosas de aminas sin CO₂ estudiadas se cubrió un rango de fracción másica de amina de 0.1 hasta 0.4, excepto para AMP, que solo fue medida a fracción másica de amina de 0.3. En las mezclas ternarias, el rango de carga de CO2 dependió de las características del sistema estudiado, identificando en la mayoría de los casos la presencia del efecto de Le Chatelier a altas cargas de CO2 cuando se aumentaban las condiciones de temperatura por encima de 333.15 K. Como resultado fundamental de las tendencias en las medidas experimentales, se encontró que la capacidad calorífica isobárica disminuye con el aumento de la fracción másica de amina en las mezclas binarias y también con la carga de CO2 en las mezclas ternarias. Las capacidades caloríficas experimentales obtenidas en este capítulo demostraron una buena concordancia con las limitadas referencias que se encuentran en la bibliografía, teniendo en cuenta las incertidumbres asociadas. Una ecuación empírica fue utilizada para correlacionar la capacidad calorífica isobárica de los sistemas binarios en función de la temperatura y la fracción másica de amina. Se empleó un programa de regresión simbólica TuringBot para encontrar el modelo que mejor describiera el comportamiento de la capacidad calorífica isobárica de los sistemas cargados con CO2 en función de la temperatura y la carga de CO₂. Como resultado de la aplicación de ambos modelos, los parámetros estadísticos obtenidos estuvieron en correspondencia con la incertidumbre experimental. Estos modelos fueron validados con los escasos datos experimentales de capacidad calorífica isobárica

reportados en la literatura para condiciones de temperatura y fracción másica de amina o carga de CO₂ diferentes a las de medida, obteniendo buenos resultados.

En el Capítulo 9, se presentaron los resultados obtenidos como fruto de la estancia de investigación realizada por la doctoranda en el laboratorio de termofísica del Imperial College London en Reino Unido. Fueron llevadas a cabo medidas experimentales de viscosidad de los sistemas 30 %wt. MDEA + H₂O + CO₂, 30 %wt. AMP + H₂O + CO₂, 35 %wt. MDEA + 5 %wt. PZ + H₂O + CO₂, 35 %wt. MDEA + 5 %wt. AMP + H₂O + CO₂, y 20 %wt. MDEA + 10 %wt. PZ + H₂O + CO₂. También se midieron densidades de los sistemas 35 %wt. MDEA + 5 %wt. PZ + H₂O + CO₂, 35 %wt. MDEA + 5 %wt. AMP + H₂O + CO₂, y 20 %wt. MDEA + 10 %wt. PZ + H₂O + CO₂. Estos datos experimentales fueron obtenidos a presión atmosférica, en un rango de temperaturas desde 293.15 K hasta 353.15 K y a varias cargas de CO2. Se detectó que a altas temperaturas y cargas de CO2 aparecían burbujas dentro del viscosímetro capilar de vidrio y también dentro del tubo vibrante del densímetro. Esto conllevó una pérdida del CO2 disuelto en la solución, por lo que fue imposible medir a estas condiciones. La viscosidad resultó ser muy sensible al cambio de la temperatura; al aumentar la temperatura, la viscosidad disminuyó drásticamente. Por otro lado, un aumento en la carga de CO2 llevó consigo un aumento de la viscosidad. Solo se encontraron datos de viscosidad experimentales disponibles en la literatura para los sistemas 30 %wt. MDEA + H₂O + CO₂ y 30 %wt. AMP + H₂O + CO₂. Como resultado de esta comparación se encontraron desviaciones relativas con valores hasta el 9 %, evidenciando la dificultad de la medida de la viscosidad y las altas incertidumbres experimentales usualmente reportadas en estos trabajos. Se generaron adecuados modelos basados en la ecuación de Vogel-Fulcher-Tammann (VFT) usando un programa de regresión simbólica TuringBot para describir el comportamiento de la viscosidad dinámica en función de la temperatura y la carga de CO₂. La densidad también fue correlacionada como función de la temperatura y la carga de CO2 usando una ecuación empírica, alcanzando resultados adecuados.

Esta investigación proporciona valiosos datos experimentales y correlaciones sólidas para las propiedades termodinámicas de los absorbentes de CO₂ usando aminas, lo que contribuye al avance de tecnologías de captura de CO₂ más eficientes y sostenibles.

ABSTRACT

The current climate crisis is an unprecedented challenge for humanity. This crisis is caused by the exponential development of anthropogenic activities, which have led to a rapid increase in greenhouse gas (GHG) emissions, such as carbon dioxide (CO₂) and methane (CH₄). The gradual increase in the presence of these gases in the atmosphere has led to a substantial rise in global surface temperature, producing what is known as climate change. One of the main anthropogenic sources of CO₂ emissions is the burning of fossil fuels from industries such as energy generation, cement, and metallurgy. Several actions have been proposed to promote the environmental sustainability of these processes or directly replace fossil fuels. Among these alternatives are renewable energies, energy efficiency, and carbon capture, utilisation and storage (CCUS).

Chemical absorption of CO₂ using amines is the most mature technology among the CO₂ capture technologies currently available. However, the aspects to be improved are the low capture efficiency (80 – 90 %) compared to other technologies, the high energy demand in the regeneration stage, and the low stability of the solvent at high temperatures. In this sense, the focus of the research for the optimisation of this process lies in searching aqueous solutions of a single amine or the mixture of several that allow for high CO₂ separation and, at the same time, enable the solvent regeneration to be carried out at high temperatures, ensuring its stability for reuse. The primary amine monoethanolamine (MEA) is undoubtedly the most used solvent in chemical absorption due to its rapid reactivity with CO₂. However, other types of amines such as tertiary, cyclic, and those with steric hindrance have shown that higher percentages of CO₂ removal can be achieved, lower energy requirements in the regeneration stage, and good stability against solvent thermal and oxidative degradation. Despite these advantages, the reaction of tertiary amines and those with steric hindrance with CO₂ is usually slow, increasing the cost of the capture process, and although cyclic amines react quickly with CO₂, their low solubility in water and high viscosity restrict their performance.

Researchers in the field have focused on combining different types of amines, taking advantage of the benefits each one offers to optimise capture. Although these research works are gaining presence in scientific publications, a complete characterisation of the fluid mixtures involved in CO_2 capture using aqueous amine solutions is still necessary. This characterisation is provided by the precise measurement of thermophysical properties such as density, viscosity, and isobaric heat capacity, among others. In the present work, a detailed description is provided of why measuring these properties influences the improvement of the capture process. Various binary liquid systems (amine $+ H_2O$), ternary systems (amine $+ H_2O + CO_2$) and quaternary systems (amine $+ amine + H_2O + CO_2$) have been studied. Different types of amines have been chosen as solvents under study, such as monoethanolamine (MEA), diethanolamine (DEA), 2-(ethylamino)ethanol (EAE), methyldiethanolamine (MDEA), 2-

(dimethylamino)ethanol (DMEA), 2-diethylaminoethanol (DEAE), 2-amino-2-methyl-1-propanol (AMP), 3-(methylamino)propylamine (MAPA), 1-methylpiperazine (1-MPZ), and piperazine (PZ). The measurement conditions (temperature, pressure, and concentrations) were established as a result of a rigorous literature review conducted to find the most common measurement ranges and the lack of reported experimental data.

To cover a significant gap in the existing literature, the present study contributes to the field of CO₂ capture by generating a comprehensive set of precise experimental data on the volumetric, energetic, and transport properties of binary, ternary, and quaternary mixtures involving amine solutions, offering theoretical explanations for the identified behaviours. Additionally, rigorous correlation models were proposed and optimised using the experimental data obtained as a result of this work. To achieve this general objective, several specific objectives were proposed, which were fulfilled throughout the doctoral thesis. A summary of the main results obtained in this work is shown below, which are explained in detail in the chapters that make up this doctoral thesis.

In Chapter 3, the aspects related to the handling and mixture preparation to be studied are explained. First, a thorough study of the material safety data sheets (MSDS) for each substance handled was conducted, identifying the main risks to which one is exposed. Through the preparation of the "Control of Substances Hazardous to Health" (COSHH) report, amines were identified as the most hazardous to handle, making the use of personal protective equipment such as lab coats, gloves, and safety goggles always necessary. Additionally, it is essential to handle them exclusively under the safety hood due to the negative effects they cause on humans. Subsequently, a detailed description of the method for preparing the mixtures used in the present study was provided. The compositions of the binary samples were determined by weighing using a precise analytical balance from the brand Radwag PS750/C/2 with a resolution of 1 mg. The loading of CO₂ in the aqueous amine solutions was carried out using two equilibrium cells. This technique made it possible to achieve a maximum expanded relative uncertainty of 0.4 % (for a 95.5 % confidence level) in the CO₂ loading. The samples were stored in clean glass bottles sealed with their lids and film and successively stored inside cabinets, avoiding contact with light. The stability of the samples was maintained for up to a month after their preparation; this was validated by monitoring the density and pH of the samples.

In **Chapter 4**, a detailed description of the vibrating tube densimeter (VTD) used for experimental density measurements was provided, along with the theoretical explanation of the mechanical oscillation technique on which its operation is based. This commonly used technique allowed for density measurements over a wide range of temperatures and pressures. The main component of the VTD is a hollow tube in the shape of a "U", which is excited electromagnetically. In the measurements, the interior of the tube was filled with the fluid to be studied. The operating principle of this equipment

allowed the relationship between the resonance period and the fluid density to be established. Other fundamental aspects that integrate the VTD system were explained in detail, such as the thermostatic system, the pressure control system, and the vacuum system used in the cleaning process. A detailed description of the measurement procedure used, and the equipment cleaning method was presented. In this chapter, a detailed analysis of the risk factors when operating this equipment was presented, which are fundamentally given by the high temperature and pressure conditions reached during the measurements. From this, it was decided to install relief valves and rupture discs as safety elements. Once all the pertinent safety measures were taken, the VTD was calibrated using vacuum and water following the Lagourette method, which is explained in detail in this chapter. A thorough analysis of the uncertainty in the density measurement was also conducted, obtaining a maximum expanded relative uncertainty of 0.2 % for a 95.5 % confidence level. Finally, to verify the correct calibration of the equipment, the density of toluene was measured, as this fluid is well characterised in the literature, facilitating the validation of the density measured with our equipment.

In Chapter 5, a complete description of the flow calorimeter used for the isobaric heat capacity experimental determinations of the fluids under study was presented. This equipment operates based on the measurement of the net power of a fluid that circulates at a constant flow rate through a calorimetric cell. As the sample flows through the cell, a simultaneous process of heating and cooling is carried out to maintain a fixed difference of 0.5 K between the outlet and inlet temperatures. The contribution of viscous dissipation to the net power term due to the pressure drop caused by friction along the tube was determined. The main parts of this equipment were described in detail, such as the thermostatic system, the pressure control system, the isocratic pump that allows for constant flow, and the calorimetric cell as the fundamental element of the flow calorimeter. Additionally, this chapter details the experimental procedure followed for measuring the isobaric heat capacity. A complete review of the equipment's safety was conducted, identifying the main risks associated with the experimental activity and resulting in no changes to the previously established configuration. The calibration of the flow calorimeter was carried out according to the procedure described in previous research works developed with this equipment, using water as the calibration chemical. A detailed uncertainty analysis of the measurement yielded an expanded relative uncertainty result of 1 % for a 95.5 % confidence level, with the main contributions coming from the non-linearity of the net power and the repeatability of the isobaric heat capacity. The verification of this procedure was carried out using toluene as the fluid under study since, like with density, the isobaric heat capacity of this chemical is widely reported in the literature.

In **Chapter 6**, a detailed description of the Ubbelohde capillary viscometer was provided, which was used for the determinations of the kinematic viscosity of aqueous amine solutions (with and without CO₂ loading) studied as part of the research stay conducted in the Thermophysics laboratory at Imperial College London in the United Kingdom. A description of the components that make up this equipment

was carried out, such as the glass capillary, the thermostatic system, and the electronic stopwatch. This last device was recently incorporated into the equipment in place of the manual stopwatch, allowing for improved uncertainty in the viscosity measurement, reducing it to an expanded relative uncertainty of 1 % for a confidence level of 95.5 %. The exhaustive analysis of the uncertainty associated with the measurement revealed that they are more precise measurements than what is usually reported in the literature using other types of viscometers. The risk associated with the operation of the capillary viscometer was identified as low when working only at atmospheric pressure and moderate temperatures (up to 353.15 K). The experimental procedure was explained, highlighting that this method is not automated, so the data acquisition is not considered fast. This equipment was calibrated using degassed and deionised water and oils certified by Paragon Scientific Ltd. for use as viscometer calibration standards. Experimental determinations of density were also carried out using an automatic kinematic viscometer Anton Paar SVM 3001. These experimental density values were used to calculate the dynamic viscosity of the studied samples.

In Chapter 7, the experimental results of the density measurements were presented for five binary systems (amine + H₂O), four ternary systems (amine + H₂O + CO₂) and one quaternary system (amine + amine + H₂O + CO₂). Experimental density data were provided over a wide range of temperature, pressure, and concentrations. Six temperature isotherms were measured with values ranging from 293.15 K to 393.15 K and pressures up to 100 MPa. For the binary systems, amine mass fractions of 0.1, 0.2, 0.3, and 0.4 were studied. The maximum CO₂ loading in the ternary systems varied depending on the mixture studied, reaching values of 0.6 mol-CO₂/mol-amine in MEA solutions, 0.9 mol-CO₂/mol-amine in MDEA solutions, 0.5 mol-CO₂/mol-amine in AMP solutions, and 0.6 mol-CO₂/molamine in DEA solutions. For the quaternary mixture DMEA + MAPA + H₂O + CO₂, the highest CO₂ loading achieved was 0.8 mol-CO₂/mol-amines. The mass fraction of amine in terms of aqueous amine solution without CO₂ for the ternary systems was 0.3, while for the quaternary system, a mass fraction of amine of 0.4 was established. The experimental results showed that the density of most of the binary systems studied decreases with the increase in the mass fraction of amine, except for the aqueous solutions of 1-MPZ where the trend of the density with the mass fraction of amine depends on the temperature conditions of the measurement as explained in this chapter. Regarding the ternary and quaternary mixtures that include CO2 as a component, the increase in CO2 load brought about an increase in density. The comparison of the experimental data obtained in this study with the few data available in the literature showed relative deviations in line with the reported uncertainty for these measurements. It was demonstrated that a modified version of the Tammann-Tait equation, which includes molality dependence, is suitable for correlating experimental density data as a function of pressure, temperature, and molality, achieving good average absolute relative deviations (AAD ≤ 0.03 %). This model was validated using experimental density data reported in the literature for temperature

and amine mass fraction or CO₂ loading conditions different from those measured, obtaining good results.

In Chapter 8, the experimental results of the isobaric heat capacity measurement of five binary systems (amine $+ H_2O$) and three ternary systems (amine $+ H_2O + CO_2$) were presented. The measurements covered a pressure range of up to 25 MPa for the binary solutions and 20 MPa for ternary ones, with four temperature points between 293.15 K and 353.15 K. In the CO₂-unloaded aqueous amine solutions studied, a mass fraction range of amine from 0.1 to 0.4 was covered, except for AMP, which was only measured at a mass fraction of amine of 0.3. In ternary mixtures, the range of CO₂ loading depended on the characteristics of the studied system, identifying in most cases the presence of the Le Chatelier effect at high CO₂ loadings when the temperature conditions were increased above 333.15 K. As a fundamental result of the trends in the experimental measurements, it was found that the isobaric heat capacity decreases with the increase in the amine mass fraction in binary mixtures and the CO₂ loading in ternary mixtures. The experimental isobaric heat capacities obtained in this chapter showed good agreement with the limited references found in the literature, considering the associated uncertainties. An empirical equation was used to correlate the isobaric heat capacity of the binary systems as a function of temperature and amine mass fraction. A symbolic regression program TuringBot was used to find the model that best described the behaviour of the isobaric heat capacity of the CO2-loaded systems as a function of temperature and CO₂ loading. As a result of the application of both models, the obtained statistical parameters were under experimental uncertainty. These models were validated with the limited experimental data of isobaric heat capacity reported in the literature for temperature and mass fraction of amine or CO₂ loading conditions different from those measured, obtaining good results.

In Chapter 9, the results obtained as a result of the PhD student's research visit at the Thermophysics laboratory of Imperial College London in the United Kingdom were presented. Experimental viscosity measurements were carried out for the systems 30 %wt. MDEA + H₂O + CO₂, 30 %wt. AMP + H₂O + CO₂, 35 %wt. MDEA + 5 %wt. PZ + H₂O + CO₂, 35 %wt. MDEA + 5 %wt. AMP + H₂O + CO₂, and 20 %wt. MDEA + 10 %wt. PZ + H₂O + CO₂. Densities of the systems 35 %wt. MDEA + 5 %wt. PZ + H₂O + CO₂, 35 %wt. MDEA + 5 %wt. AMP + H₂O + CO₂, and 20 %wt. MDEA + 10 %wt. PZ + H₂O + CO₂ were also measured. These experimental data were obtained at atmospheric pressure, in a temperature range from 293.15 K to 353.15 K, and at various CO₂ loads. It was detected that at high temperatures and high CO₂ loads, bubbles appeared inside the glass capillary viscometer and the vibrating tube of the densimeter. This led to a loss of dissolved CO₂ in the solution, making it impossible to measure under these conditions. The viscosity turned out to be very sensitive to temperature changes; as the temperature increased, the viscosity decreased drastically. On the other hand, an increase in the CO₂ loading led to an increase in viscosity. Only experimental viscosity data were found in the literature for the systems MDEA + H₂O and AMP + H₂O. As a result of this comparison, relative deviations of

up to 9 % were found, highlighting the difficulty of measuring viscosity and the high experimental uncertainty usually reported in these studies. Adequate models based on the Vogel-Fulcher-Tammann (VFT) equation were generated using a TuringBot symbolic regression program to describe the dynamic viscosity behaviour as a function of temperature and CO₂ loading. Density was also correlated as a function of temperature and CO₂ loading using an empirical equation, achieving adequate results.

This research provides valuable experimental data and robust correlations for the thermodynamic properties of amine-based CO₂ absorbents, contributing to the advancement of more efficient and sustainable CO₂ capture technologies.

LIST OF SYMBOLS

- ρ Density
- κ_T Isothermal compressibility coefficient
- β Isobaric expansion coefficient
- v Kinematic viscosity
- η Dynamic viscosity
- α CO₂ loading in terms of mol CO₂ per mol of amine
- au Vibrating period of the tube in the vibrating tube densimeter
- σ Standard deviation

TABLE OF CONTENTS

l. Int	troduction and Objectives	8
1.1.	Climate Change and Carbon Dioxide Emissions	8
1.1	.1. Carbon Dioxide Capture Technologies	10
1.1	.2. Amine Scrubbing for CO ₂ Capture	12
1.2.	Role of Thermophysical Properties in Carbon Capture and Storage (CCS)	16
1.3.	Literature Review: Selected Properties and Solutions	17
1.4.	Research Objectives	18
1.5.	Structure of the thesis	18
2. Th	eory	38
2.1.	Densimetry Basics	38
2.2.	Calorimetry Basics	39
2.3.	Viscometry Basics	42
3. Pro	eparation of the Mixtures	46
3.1.	Sample Handling Safety	46
3.2.	Mixtures Samples Preparation	50
3.2	2.1. CO ₂ Loading into Aqueous Amine Solution	51
4. Vil	brating Tube Densimeterbrating Tube	56
4.1.	Introduction	56
4.2.	Principle of Measurement	56
4.3.	Apparatus Description and Experimental Procedure	58
4.3	3.1. HPM DMA Unit	59
4.3	3.2. Temperature Control System	60
4.3	3.3. Pressure Control System	61
4.3	3.4. Pre-measurement Setup and Measurement Experimental Procedures	61
4.4.	Design Considerations for Safety	62
4.5.	Calibration Procedure	64
4.6.	Uncertainty Budget	66
47	Exparimental Validation	70

<i>5</i> .	Flo	w Calorimeter	76
	5.1.	Introduction	76
	5.2.	Principle of Measurement	76
	5.3.	The Viscous Dissipation	78
	5.4.	Apparatus Description and Experimental Procedure	78
	5.4.		
	5.4.	2. Temperature Control System	80
	5.4.	3. Pressure Control System	81
	5.4.	4. Isocratic Pump	81
	5.4.	5. Pre-measurement Setup and Measurement Experimental Procedures	82
	5.5.	Design Considerations for Safety	83
	5.6.	Calibration Procedure	84
	5.7.	Uncertainty Budget	85
	5.8.	Experimental Validation	87
6.	Cap	oillary Viscometer	92
	6.1.	Introduction	92
	6.2.	Apparatus Description	92
	6.3.	Viscosity Uncertainty Budget	94
	6.4.	Experimental Validation	96
	6.5.	Automatic Kinematic Viscometer Anton Paar SVM 3001	97
<i>7</i> .	Exp	perimental Density	102
	7.1.	Introduction	102
	7.2.	Binary Mixtures. CO ₂ -Unloaded Aqueous Amine Solutions	103
	7.2.	1. DEAE + H ₂ O	103
	7	.2.1.1. Experimental Density	103
	7	.2.1.2. Comparison with Literature	108
	7.2.	2. $EAE + H_2O$	109
	7	.2.2.1. Experimental Density	109
	7	.2.2.2. Comparison with Literature	114
	7.2.		
	7	.2.3.1. Experimental Density	115

-	7.2.3.2.	Comparison with Literature	119
7.2	2.4.	1-MPZ + H ₂ O	120
7	7.2.4.1.	Experimental Density	120
7	7.2.4.2.	Comparison with Literature	125
7.2	2.5.	AMP + H ₂ O	126
7	7.2.5.1.	Experimental Density	126
-	7.2.5.2.	Comparison with Literature	131
7.2	2.6.	Discussion	133
7.2	2.7.	Experimental Density Data Fitting	134
-	7.2.7.1.	Comparison of Calculated Density with Experimental Literature Data	141
7.3.	Tern	ary Mixtures. CO2-Loaded Aqueous Amine Solutions	144
7.3	.1.	MEA + H ₂ O + CO ₂	144
-	7.3.1.1.	Experimental Density	144
	7.3.1.2.	Comparison with Literature	148
7.3	5.2.	MDEA + H ₂ O + CO ₂	150
,	7.3.2.1.	Experimental Density	150
,	7.3.2.2.	Comparison with Literature	154
7.3	.3.	$AMP + H_2O + CO_2$	156
,	7.3.3.1.	Experimental Density	156
-	7.3.3.2.	Comparison with Literature	159
7.3	5.4.	DEA + H ₂ O + CO ₂	161
7	7.3.4.1.	Experimental Density	161
	7.3.4.2.	Comparison with Literature	164
7.3	5.5.	Discussion	166
7.3	.6.	Experimental Density Data Fitting	167
,	7.3.6.1.	Comparison of Calculated Density with Experimental Literature Data	172
7.4.	Quat	ernary Mixtures. Aqueous Solution of Two Amines Loaded with CO2	175
7.4	.1.	DMEA + MAPA + H ₂ O + CO ₂	175
-	7.4.1.1.	Experimental Density	175
8. Ex	perime	ntal Isobaric Heat Capacity	182
8.1.	Intro	duction	182
8.2.		ry Mixtures. CO2-Unloaded Aqueous Amine Solutions DEAE + H2O	
8.2	8.2.1.1.	Experimental Isobaric Heat Capacity	
	8.2.1.1. 8.2.1.2.		
(v.∠.ı.∠.	Companson with Literature	100

	8.2.2.	$EAE + H_2O$	187
	8.2.2.1	1. Experimental Isobaric Heat Capacity	187
	8.2.2.2	2. Comparison with Literature	189
	8.2.3.	$MAPA + H_2O$	189
	8.2.3.1	1. Experimental Isobaric Heat Capacity	190
	8.2.4.	$1-MPZ + H_2O$	192
	8.2.4.1	1. Experimental Isobaric Heat Capacity	192
	8.2.4.2	2. Comparison with Literature	194
	8.2.5.	$AMP + H_2O$	195
	8.2.5.1	1. Experimental Isobaric Heat Capacity	195
	8.2.6.	Discussion	195
	8.2.7.	Experimental Isobaric Heat Capacity Data Fitting	196
	8.2.7.1	1. Comparison of Calculated Isobaric Heat Capacity with Experim	nental Literature
	Data	198	
8	3.3. Ter	nary Mixtures. CO2-Loaded Aqueous Amine Solutions	199
	8.3.1.	MEA + H ₂ O + CO ₂	
	8.3.1.1	1. Experimental Isobaric Heat Capacity	199
	8.3.2.	MDEA + $H_2O + CO_2$	
	8.3.2.1	1. Experimental Isobaric Heat Capacity	201
	8.3.3.	$AMP + H_2O + CO_2$	204
	8.3.3.1	1. Experimental Isobaric Heat Capacity	204
	8.3.4.	Discussion	205
	8.3.5.	Experimental Isobaric Heat Capacity Data Fitting	206
	8.3.5.1	1. Comparison of Calculated Isobaric Heat Capacity with Experim	nental Literature
	Data	208	
9.	Eynerim	nental Density and Viscosity	212
	•	·	
9	.1. Inti	roduction	212
9	.2. Ter	nary Mixtures	213
	9.2.1.	MDEA + H2O + CO2	213
	9.2.1.1	1. Experimental Viscosity	213
	9.2.1.2	2. Comparison with Literature	214
	9.2.2.	AMP + H2O + CO2	215
	9.2.2.1	1. Experimental Viscosity	215
	9.2.2.2	2. Comparison with Literature	217
	9.2.3.	Discussion	218

9.3.	Quater	nary Mixtures	219
9.3.1.	. M	DEA + PZ + H_2O + CO_2 (w_{amines} = 0.4000 CO_2 -free basis)	219
9.3	3.1.1.	Experimental Density	219
9.3	3.1.2.	Experimental Viscosity	220
9.3.2.	. M	DEA + AMP + H ₂ O + CO ₂	222
9.3	3.2.1.	Experimental Density	222
9.3	3.2.2.	Experimental Viscosity	223
9.3.3.	. M	DEA + PZ + H_2O + CO_2 (w_{amines} = 0.3021 CO_2 -free basis)	225
9.3	3.3.1.	Experimental Density	225
9.3	3.3.2.	Experimental Viscosity	226
9.3	3.3.3.	Experimental Viscosity Comparison with Literature	227
9.3.4.	. Di	scussion	228
9.4.]	Experi	mental Density Data Fitting	230
9.5.]	Experi	mental Viscosity Data Fitting	231
9.5.1.	. Co	omparison of Calculated Dynamic Viscosity with Experimental Literature Data	235
CONCLU	SIONS	<u></u>	240
FUTURE	WORI	Υ	242
REFERE	NCES -		246
ABOUT T	THE AU	UTHOR	264



1. Introduction and Objectives

1.1. Climate Change and Carbon Dioxide Emissions

Climate change, caused by both natural and anthropogenic processes and agents, is the result of disparities in the Earth's energy balance. Particularly, anthropogenic or human activities like transport, agriculture, power and heat generation, and industrial processes have led to a substantial increase in greenhouse gases (GHGs) emissions over the last 200 years (**Figure 1.1**), resulting in a constant increase in the world's surface temperature at a rate not seen in the previous 2000 years (**Figure 1.2**) [1,2].

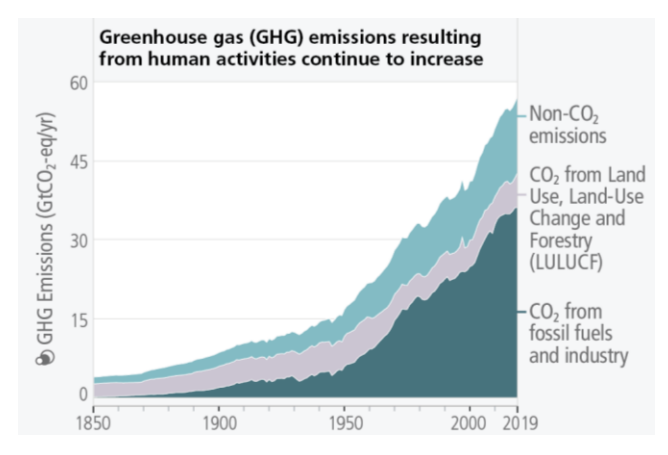


Figure 1.1. Greenhouse gas emissions from 1850 to 2019 (Source: IPCC [2]).

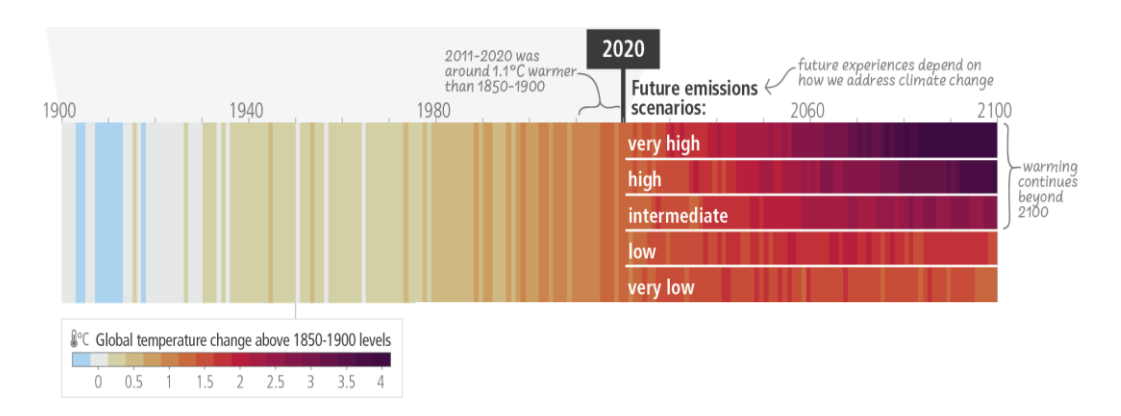


Figure 1.2. Changes in global surface temperature observed from 1900 to 2020 and future projected (2021–2100) relative to 1850 – 1900 (Source: IPCC [2]).

The concentrations of the primary GHGs in the atmosphere have increased over the last ten years, reaching record highs in 2024. The average annual concentrations of carbon dioxide (CO₂), methane (CH₄), and nitrous oxide (N₂O) are 422 parts per million (ppm), 1936 parts per billion (ppb), and 338 ppb, respectively [3,4]. Even though the CH₄ is the GHG with the highest global warming potential (GWP) is less abundant than CO₂. In this sense, it is a matter of concern that the atmospheric CO₂ is 50 % higher than 1750 levels with an increase of more than 2 ppm per year since 2014 according to NOAA's monitoring records [3,4], as shown in **Figure 1.3**.

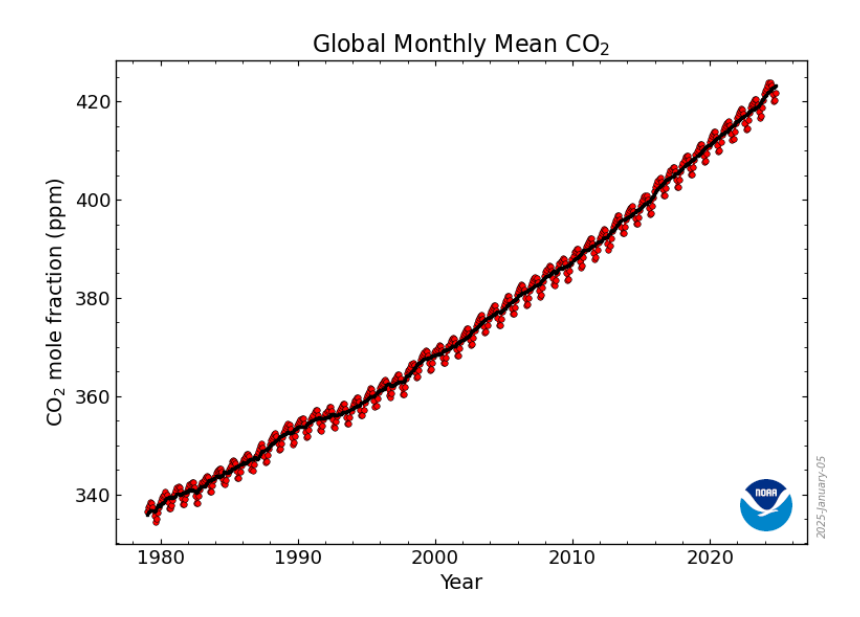


Figure 1.3. Global monthly means of CO₂ concentration in ppm from 1980 to 2024 (Source: Lan et al. [3]).

To tackle climate change, the Paris Agreement was approved by the 195 members of the United Nations Framework Convention on Climate Change (UNFCCC) on December 12th 2015 [5]. It guarantees the continuation of the efforts made with the Kyoto Protocol beyond 2020. Furthermore, the Paris Agreement establishes a global goal to keep average surface temperatures above pre-industrial levels to "well below 2 °C" and net zero emissions over the coming decades [5]. To achieve this agreement, the European Union aims to reduce GHG emissions by at least 55 % in 2030, compared to 1990 levels [6] by means of mitigation strategies and climate action.

Consequently, last IPCC scenarios [2] include Carbon Capture, Utilisation and Storage (CCUS) from industry (e.g.: power plants, natural gas sweetening, steel mills, cement plants, and refineries) and negative emissions technologies like Direct Air Capture (DAC) and Bioenergy with Carbon Capture and Storage (BECCS) [7–10] as mitigation strategies (see **Figure 1.4**) required to achieve Net Zero targets. DAC process allows for the capture of CO₂ directly from the atmosphere, while BECCS is based on the capture and geological storage of CO₂ emissions from the burning of biomass for power plants; this biomass previously absorbed CO₂ from the atmosphere [11]. On the other hand, CCUS is also a technology to reduce the emissions of CO₂ before they enter the atmosphere in hard-to- abate industrial sectors like iron, steel, cement and chemicals [9,12,13]. In this Chapter, a review of the principles and challenges of the CO₂ capture processes will be delivered, specifically the chemical absorption using amines.

CCUS & Net Zero Carbon Capture, Utilisation and Storage (CCUS) enables the production of low-carbon power, decarbonised heating and industry, and carbon dioxide removal (CDR) technologies, to prevent/remove CO2 from the atmosphere and transport it to safe and secure storage sites, ensuring a smooth transition to Net Zero by 2050. Power Heating Industry CDR Transport Storage Concentrated clusters Enabling the uptake of more renewables and the use of curtailed energy. to taraet heavy industry and power Commercial Cluster Helping to decarbonise electricity, businesss, Capture (DAC Low-carbon production of Sustainable Aviation Fuel, chemicals, transport and heating ransportatio hydrogen, etc. Low-carbon heated homes General Various transportation options: road, rail, shipping, and pipeline. Carbon Capture Low-carbon large-scale CO, can be utilised to produce useful products. power production such as BECCS and Gas-CCS. CDR technologies, such as Bioenergy with Carbon Capture and Storage (BECCS) and DAC to remove CO₂ from Long term storage options in deep geological formations, permenantly storing the CO₂ safely underground. the atmosphere.

Figure 1.4. Carbon Capture, Utilisation and Storage (CCUS) explanation (Credit: Dr. Mathew Dennis Wilkes in [14]).

Credit: Dr Mathew Dennis Wilkes

1.1.1. Carbon Dioxide Capture Technologies

There are three main methods [7] for capturing CO₂ from the flue gas emitted from an industrial process:

- 1. Pre-combustion.
- 2. Oxyfuel combustion.
- 3. Post-combustion.

Pre-combustion capture, as the name implies, removes CO₂ from the fuel before combustion occurs. The fuel is reacted with oxygen, air, and/or steam to produce a synthesis gas (syngas), mainly consisting of hydrogen and CO₂. The CO₂ is subsequently separated from the syngas. Almost pure hydrogen is also generated through this process called "blue hydrogen", in contrast to "green hydrogen" which is produced in electrolysers using renewable electricity [15,16].

In contrast, in oxyfuel combustion capture, the fuel is burned with pure oxygen instead of air at very high temperatures, resulting in recycled combustion gases (mostly CO₂ and water). The water is subsequently removed from the gas by a condensation process. The resulting stream (of about 95 to 99 % CO₂) is compressed and moved to permanent geological storage [9,13,17].

In post-combustion capture processes, the CO_2 is captured after the combustion is finished in a retrofitted plant, without changes to the basic design of power plants. An excess of air is delivered in the combustion process, allowing an exhaust gas to typically contain a low concentration (4 - 20 %) of CO_2 , along with excess oxygen, nitrogen, and water. The exhaust gas next passes through a capture procedure in which the CO_2 is selectively separated from the gas and then compressed and stored or utilised. This capture method includes multiple advantages compared to pre-combustion and oxyfuel combustion, including the ability to use a variety of fuels, the low CO_2 concentration in the flue gas, and the maturity of the technology that is commercially available and suitable for existing infrastructure [18]. However, there are still challenges from low capture efficiency (80 - 90 %) and energy penalty in the solvent regeneration process. Post-combustion capture takes advantage of adequate materials selectivity for CO_2 . These materials can remove CO_2 from the mix of gases left after burning fuel. A common example is a group of chemicals called amines, which are mixed with water for this purpose [17]. This capture technology will be explained in depth in the next section.

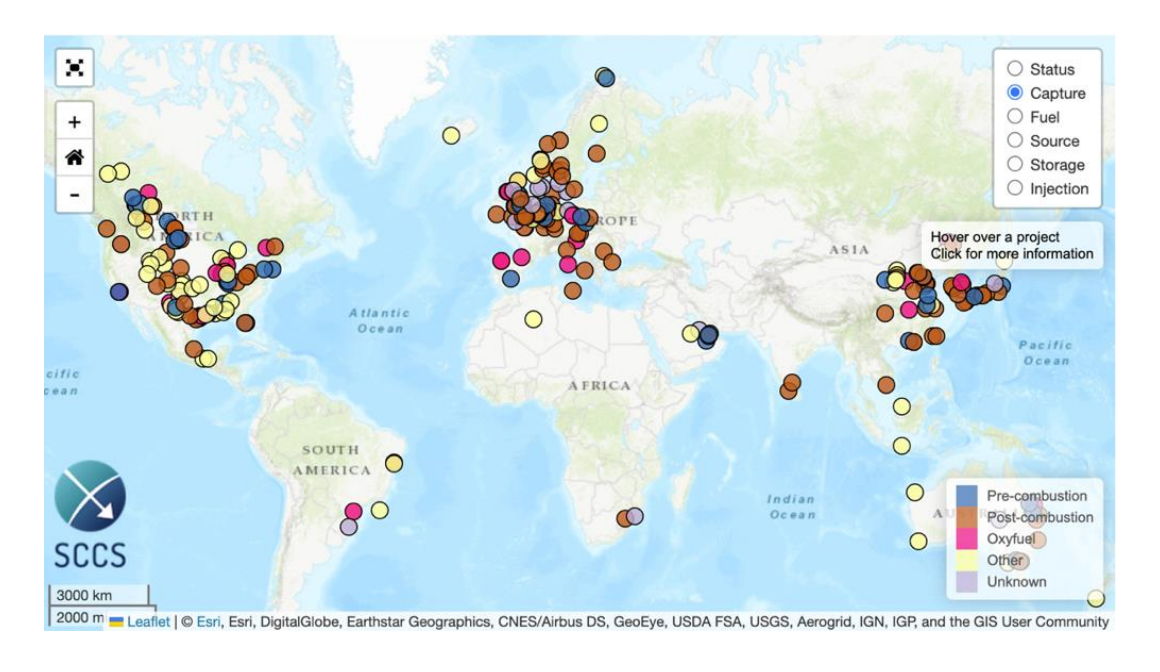


Figure 1.5. Global CCS Map in 2024 (Source: Scottish Carbon Capture & Storage [19]).

There are several post-combustion capture facilities in a variety of industries, capturing tens of millions of tonnes each year, as shown in **Figure 1.5**. According to the Global CCS Institute [20], there are, up to 2024, 628 commercial plants worldwide: 50 in operation, 44 under construction, and 534 in advanced or early development. These facilities have captured more than 400 million tonnes of CO₂, with a capture capacity of 51 million tonnes per annum.

1.1.2. Amine Scrubbing for CO₂ Capture

Patented in 1930 by Bottoms [21], amine-based CO₂ capture is a well-established and widely used gas separation technology. The knowledge has undoubtedly progressed and improved since then, but the core ideas of Bottoms have remained unchanged. While low temperature and high pressure provide the most favourable conditions for absorption [22,23], post-combustion carbon capture typically operates at atmospheric pressure [9,17]. However, amine-based gas separation technology is also employed for large-scale purification of gases like gas sweetening, where CO₂ and H₂S are removed utilising high-pressure amine absorption [7]. Notable examples include the Khurmala field in Iraqi Kurdistan, employing an absorption pressure of 7 MPa, and the Sulfa-Check project in California, operating at 4 MPa [24,25].

During the amine scrubbing process, the flue gas enters an absorption tower, where it contacts a lean amine solvent (aqueous amine solution), as illustrated in **Figure 1.6**. The top of the tower is equipped with a liquid distributor to ensure a uniform downflow of the lean absorbent. This absorption process takes place at pressure near to the atmospheric pressure, and the reaction temperatures typically range from 298.15 K to 318.15 K, with 313.15 K the most common value. The CO₂-rich liquid (rich absorbent) then exits the bottom of the tower, and the clean gas is out for the top. In the regeneration tower, the absorbed CO₂ is released by heating the rich absorbent at temperatures between 363.15 K and 403.15 K. The regenerated lean solvent is recirculated back into the absorption tower to continue absorbing CO₂. Finally, the captured CO₂ is compressed into a liquid form for transport and eventual storage or use it [26,27]. A 30 % amine mass percent is typically used as the concentration of the aqueous amine solution; a higher concentration would produce corrosion difficulties in equipment and increase the probability of amine degradation [17,22].

Amines are organic compounds derived from ammonia (NH₃) by replacing one or more hydrogen atoms with hydrocarbon groups. Their classification is based on the number of hydrogen atoms remaining connected to the central nitrogen atom. Primary amines have two active hydrogens, allowing them to easily carry out chemical reactions. Secondary amines have one active hydrogen, and tertiary amines lack them totally. Furthermore, amines can be classified as single-amine (having only one nitrogen atom) or multi-amine (containing two or more nitrogen atoms) [28]. Amines have a strong basicity due to the presence of an amino group (-NH₂) in their structure, resulting in a fast absorption rate, large absorption volume, and high selectivity for CO₂ [18,26].

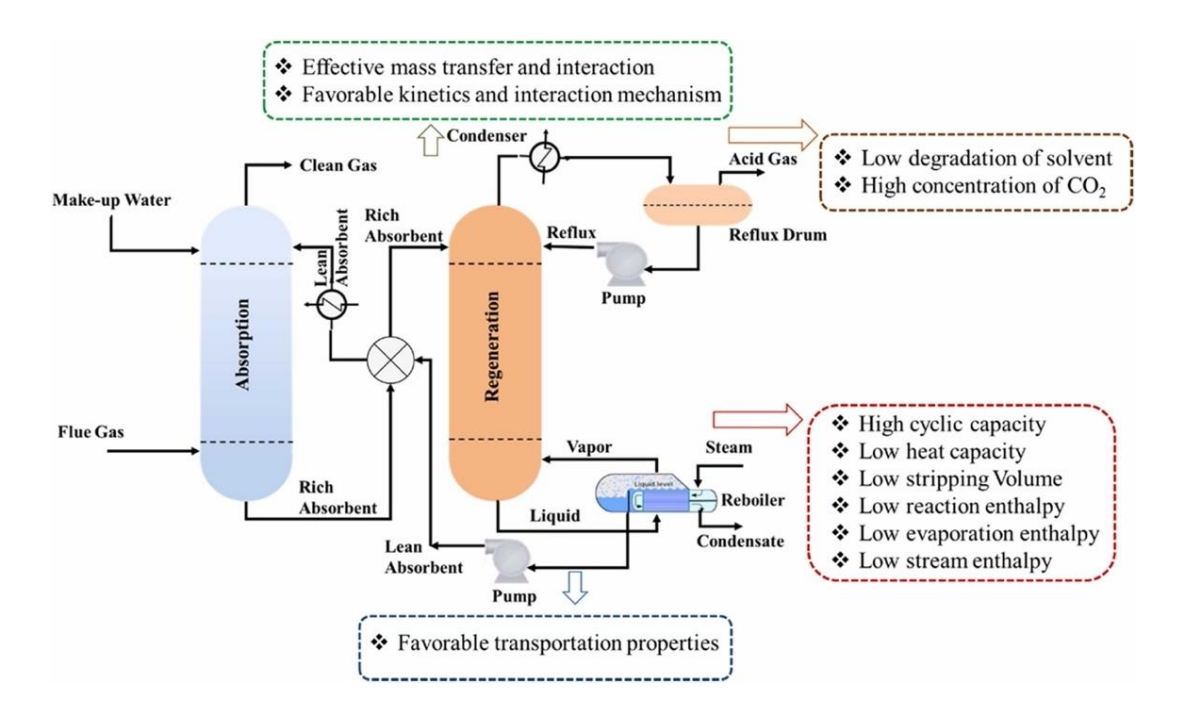


Figure 1.6. The process flow of amine-based CO₂ capture (Source: Tiwari et al. [29]).

Monoethanolamine (MEA), a primary amine, is the benchmark solvent used in this process, having good absorption capacity, high reactivity with CO₂ and proven stability [18,27]. Despite this, primary and secondary amines, e.g. MEA and diethanolamine (DEA), show some drawbacks such as higher enthalpy of absorption, lower CO₂ loading capacities, and higher susceptibility to oxidation and thermal degradation in the regeneration process [26,30].

Sterically hindered amines, e.g. 2-amino-2-methyl-1-propanol (AMP), are primary or secondary features with bulky groups near the nitrogen atom, limiting their reactivity with high enthalpy of absorption [31]. However, this type of amine shows CO₂ loading capacities like tertiary amines [32], while also offering faster reaction kinetics and better degradation resistance [33,34].

Cyclic amines, e.g. piperazine (PZ), are secondary and/or tertiary in a cyclic structure, although their properties differ from chain-based amines. This form of amine reacts very fast with CO₂, exhibits a high absorption capacity and high degradation temperature; however, it is less soluble in water with a high enthalpy of absorption [29,34]. Recently, PZ derivatives, which include 1-methylpiperazine (1-MPZ) have gained interest due to their thermal resistance, fast kinetics with CO₂, high solubility in water and low melting point [35–38].

Regarding tertiary amines, such as methyldiethanolamine (MDEA), this type of amine has high CO₂ absorption capacities and a low enthalpy of absorption but slow kinetics in their reaction with CO₂, which makes their use in gas scrubbing difficult. **Figure 1.7** summarises the most important characteristics of the main solvent used for amine-based CO₂ capture.

When looking for an ideal solvent for CO₂ absorption, certain characteristics are desirable, such as a high absorption capacity, a low enthalpy of absorption, fast reaction with CO₂, high CO₂ selectivity, high degradation resistance, and good thermophysical properties that improve their performance [39]. In this regard, a low enthalpy of absorption implies a reduction in the required load energy by the amine scrubbing separation process, lowering the energy penalty and increasing the efficiency [31]. Another critical aspect is how thermophysical parameters like density, isobaric heat capacity, and viscosity of the aqueous amine solution impact their efficacy while capturing CO₂, which will be studied in further depth in the next sections.

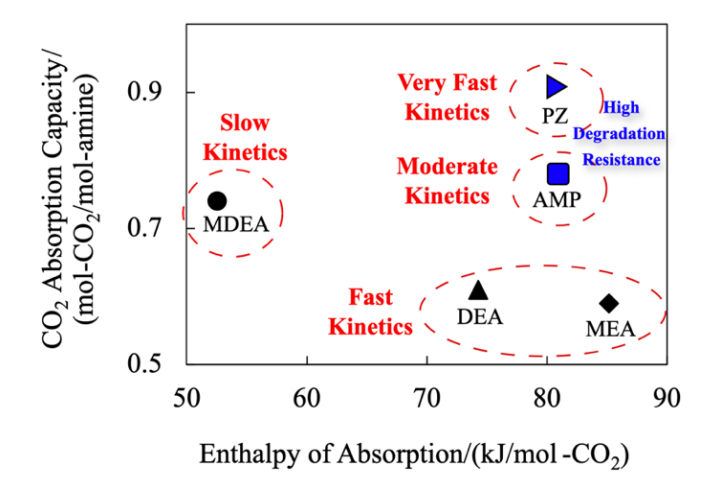


Figure 1.7. Features of the main solvents used in CO₂ capture. The enthalpy of absorption and CO₂ absorption capacity were taken from a study at 30 % amine mass percent and 313.15 K [31].

Blended amine solutions have also grown in popularity due to the combination of each amine's advantages: fast reaction from a primary, secondary or cyclic amine and high absorption capacity and low solvent regeneration cost from a tertiary, sterically hindered or cyclic amine [33]. Recently researchers have focused on promoting the reaction between tertiary amines and CO₂ using multi-amines such as PZ and 3-(methylamino)propylamine (MAPA) or sterically hindered single-amines such as AMP. These studies have examined the kinetics of CO₂ absorption, CO₂ solubility, and the performance of these mixtures in pilot plants [40–48]. Despite this, there is still a lack of data on thermophysical properties such as density, isobaric heat capacity and viscosity, particularly at high CO₂ loading. In this sense, our study provides density and viscosity experimental data for quaternary systems like DMEA + MAPA + H₂O + CO₂, MDEA + PZ + H₂O + CO₂ and MDEA + AMP + H₂O + CO₂, all are promising candidates for CO₂ capture. **Table 1.1** gives a list of the most important characteristics of the amines employed in the present study.

The capture of CO₂ by aqueous amine solutions is a complex process with reaction mechanisms that vary depending on the type of amine employed. Primary and secondary (R¹R²NH) amines react with CO₂ to form stable carbamate as the main product. This reaction follows a well-studied "zwitterionic"

mechanism [26], as illustrated in **Equations 1.1 to 1.2**. This mechanism proposes the intermediate formation of a zwitterionic ($R^1R^2NH^+COO^-$), as detailed in **Equation 1.1**. Subsequently, the zwitterionic reacts with the free amine (R^1R^2NH), resulting in the generation of the protonated amine ($R^1R^2NH_2^+$) and the carbamate ions ($R^1R^2NCOO^-$), as shown in **Equation 1.2**.

$$R^{1}R^{2}NH + CO_{2} \rightleftharpoons R^{1}R^{2}NH^{+}COO^{-}$$
 (1.1)

$$R^{1}R^{2}NH + R^{1}R^{2}NH^{+}COO^{-} \rightleftharpoons R^{1}R^{2}NH_{2}^{+} + R^{1}R^{2}NCOO^{-}$$
 (1.2)

Theoretically, this process leads to a 0.5:1 stoichiometry between CO₂ and amine (0.5 mol CO₂ per mol amine). However, at higher CO₂ loading, some of the carbamates can undergo hydrolysis reactions (see **Equation 1.3**), regenerating free amine and producing bicarbonate ions (HCO₃⁻). This hydrolysis pathway allows for a slightly higher CO₂ capture capacity for primary and secondary amines compared to the theoretical limit based just on carbamate formation.

$$R^{1}R^{2}NCOO^{-} + H_{2}O \rightleftharpoons R^{1}R^{2}NH + HCO_{3}^{-}$$
 (1.3)

Although sterically hindered amines are primary or secondary amines, these amines create unstable carbamates due to the bulky group next to the amino group. The hydrolysis of the large carbamates results in a preferred bicarbonate production process, raising the theoretical loading capacity of the sterically hindered amines up to 1 mol-CO₂/mol-amine [33].

Tertiary amines (R¹R²R³N) react with CO₂ to form an unstable carbamate. Their basicity makes them a catalyst in the CO₂ hydrolysis reaction, which produces bicarbonate ions as the main outcome (see **Equation 1.4**). As a result, it is possible to achieve CO₂ absorption capacity of 1 mol-CO₂/mol-amine [30].

$$R^{1}R^{2}R^{3}N + H_{2}O + CO_{2} \rightleftharpoons R^{1}R^{2}R^{3}NH^{+} + HCO_{3}^{-}$$
(1.4)

Figure 1.8. General reaction mechanisms between the aqueous amine solution and CO₂ (Source: Wang & Song [49]).

1.2. Role of Thermophysical Properties in Carbon Capture and Storage (CCS)

 CO_2 capture is the bottleneck of CCS process due to its high energy demand, accounting for roughly (60-70) % of the cost per tonne of CO_2 [7]. Amine scrubbing, the most mature technology for CO_2 capture and the only one commercially deployed in power plants [50], relies on understanding the thermophysical properties of the involved fluids for optimisation.

Density takes part in all material, momentum, and energy balances. Its dependence on temperature, pressure, compositions and concentrations must be well characterised prior to any engineering activities involving design, operation, and optimisation.

Isobaric heat capacity is crucial for calculating the heat required in the regeneration column. The total regeneration heat covers three components [29,31]:

- Enthalpy of desorption: the heat needed to release CO₂ from the CO₂-loaded aqueous amine solution.
- Sensible heat: the heat needed to increase the solution temperature in the regeneration step, which depends on the isobaric heat capacity of the solution.
- Latent heat: the energy required to vaporise the amine solution in the regenerator.

Minimising the enthalpy of absorption has been a primary focus; however, neglecting other properties like isobaric heat capacity and the enthalpy of vaporization of the solvent can lead to underestimating the thermal requirements of the regeneration step [50]. Based on this, accurate isobaric heat capacity experimental data for alkanolamine solutions is essential for designing efficient heat exchangers in CO₂ capture facilities [26,33,51].

Transport properties of the solvent, particularly viscosity, significantly influence process unit sizing in CO₂ capture optimisation [50]. In addition, viscosity has a significant impact on the mass transfer rate, since these properties are inversely proportional [29]. On the other hand, understanding solution density and viscosity is essential to operating pumps, heat exchangers, and designing gas-liquid contactors [33]. These two properties are also useful in determining liquid diffusivity and reaction rate constants, especially in kinetic studies involving wetted-wall columns. Furthermore, density and viscosity play a key role in mass transfer rate modelling for absorbers and regenerators because they affect the liquid film coefficient. The effect of viscosity on cost reduction that is comparable to vapor-liquid equilibrium (VLE) data and enthalpy of absorption [33]. Therefore, their inclusion becomes essential for a detailed cost analysis.

Furthermore, density, isobaric heat capacity, and viscosity are key to completing a comprehensive thermodynamic characterisation of those mixtures and increasing our understanding of molecular

interactions, thus improving predictive models. This point is illustrated by Zarogiannis et al. [39], whose comprehensive thermodynamic study explored solvent selection criteria for CO₂ capture performance.

However, these thermophysical properties remain largely absent in the literature for CO₂-loaded or CO₂-unloaded aqueous amine solutions across a wide range of pressures, concentrations, and temperatures, hindering the optimisation of amine-based CO₂ capture process [52]. The proposed amines in this study and their blends lack thermophysical data and models that would assess their performance against currently used solvents. This work is part of our effort aimed at filling these data gaps in different properties and conditions of operation.

1.3. Literature Review: Selected Properties and Solutions

A comprehensive literature review was conducted to identify all relevant studies reporting experimental data on density, isobaric heat capacity, and viscosity for the studied amines solutions (listed in **Table 1.1**). For the binary mixtures DEAE + H₂O, EAE + H₂O, MAPA + H₂O, 1-MPZ + H₂O and AMP + H₂O, detailed in **Table 1.2**, the temperature range covered from 278.15 K to 373.15 K. Most studies focused on temperatures up to 353.15 K, with measurements conducted at atmospheric pressure. A wide range of amine mass fractions were reported across the considered systems. Notably, the AMP + H₂O system gathered significant interest in the literature, as evidenced by the extensive data availability.

For the ternary systems MEA + H₂O + CO₂, MDEA + H₂O + CO₂, AMP + H₂O + CO₂ and DEA + H₂O + CO₂, the reported temperature range extended from 293.15 K to 423.15 K, as shown in **Table 1.3**. Studies considering pressures different from 0.1 MPa were scarce. Literature has documented a wide variety of amine mass fractions (CO₂-free basis) for MEA solutions, with a particular emphasis on values between 0.3 and 0.4. Reported CO₂ loading values reached up to 0.6 mol-CO₂/mol-amine. It is important to note that the mainstream of references for ternary systems report high experimental uncertainties due to the significant contribution of the uncertainty associated with CO₂ loading.

To the best of our knowledge, no experimental data on density have been reported for the quaternary system DMEA + MAPA + H_2O + CO_2 . However, research efforts have focused on other aspects relevant to CO_2 capture performance for this mixture [53–56]. Rahimi et al. [56] investigated the solubility and enthalpy of absorption for this system at a specific amine mass (45 % total, with 40 % DMEA and 5 % MAPA). Their findings suggest a high CO_2 absorption capacity for the DMEA + MAPA + H_2O blend.

On the other hand, PZ and AMP, as tertiary amine reaction promoters, have been shown in several studies to improve stability and resistance to thermal degradation and to offer enhanced adsorption capacity [41,48]. In addition, kinetic studies have shown that adding these promoters to the solvent

CHAPTER 1: INTRODUCTION AND OBJECTIVES

solution improves the kinetic rate, making it comparable to the MEA solution [40,42]. Only a few studies on density and viscosity properties are found in the literature, as detailed in **Table 1.4**.

1.4. Research Objectives

This study aims to contribute to the field of CO₂ capture by generating a comprehensive experimental dataset on the volumetric, energetic, and transport properties of binary, ternary, and quaternary mixtures involving amine solutions and giving theoretical explanations for these behaviours. The study establishes the following specific objectives for this purpose:

- 1. Enhance experimental equipment design through safety-driven analysis.
- 2. Provide an extensive experimental dataset on density, viscosity, and isobaric heat capacity across a wide range of conditions of temperature, pressure, and concentration.
- 3. Study theoretical explanations of the influence of temperature, pressure, and component concentrations on the density, viscosity, and isobaric heat capacity of the studied systems.
- 4. Quantify measurement uncertainty.
- 5. Perform a comparison between the obtained experimental data and existing literature data.
- 6. Correlate experimental data using established and potentially novel models.

1.5. Structure of the thesis

This manuscript, comprising nine chapters and three additional sections, accomplishes the requirements for the Doctor of Philosophy (Ph.D.) degree with an International Mention. The contents of each section are detailed below.

Chapter 1: Introduction. This section introduces the context of climate change and carbon dioxide emissions, followed by a description of various carbon capture technologies, with a specific focus on the amine scrubbing process. It then explores the crucial role of thermophysical properties in Carbon Capture and Storage (CCS) and presents a literature review of relevant properties and solutions. Finally, the research objectives and overall structure of this thesis are outlined.

Chapter 2: Theory. The theoretical foundations of the densimetry, calorimetry, and viscometry techniques employed in this thesis are presented in this section. It also includes a description of Le Chatelier's principle as it relates to chemical equilibrium.

Chapter 3: Preparation of the Mixtures. This section covers laboratory safety protocols for handling samples, provides a description of mixture preparation, outlines the characteristics of the chemical species employed in this study, and describes the procedure for loading carbon dioxide into the aqueous amine solution.

CHAPTER 1: INTRODUCTION AND OBJECTIVES

Chapter 4: Vibrating Tube Densimeter. This section describes the density determination method using a vibrating tube densimeter DMA HPM, including the fundamental measurement principle, a detailed description of the apparatus and experimental procedure, safety protocols, calibration procedures, uncertainty analysis, and experimental validation.

Chapter 5: Flow Calorimeter. A comprehensive description of the isobaric heat capacity measurement method using a flow calorimeter is provided in this section. This includes the fundamental measurement principle, viscous dissipation considerations, a detailed explanation of the apparatus and experimental procedure, safety protocols, calibration procedures, uncertainty analysis, and experimental validation.

Chapter 6: Capillary Viscometer. The capillary viscometer employed in the dynamic viscosity determination is described in this section. A detailed explanation of the uncertainty calculation methodology and the experimental validation process is provided. Furthermore, the automatic kinematic viscometer, SMW 3001, is described.

Chapter 7: Experimental Density. The experimental densities of CO₂-unloaded and CO₂-loaded aqueous amine solutions, measured using a vibrating tube densimeter DMA HPM, are presented in this section. Moreover, the dependence of these densities on temperature, pressure, and concentration is investigated. Where applicable, comparisons with literature values are provided. Finally, a detailed description of the optimisation process employed to fit the experimental density data as a function of temperature, pressure, and concentration is given.

Chapter 8: Experimental Isobaric Heat Capacity. This section presents experimental isobaric heat capacity data for CO₂-unloaded and CO₂-loaded aqueous amine solutions, measured using a flow calorimeter. The influence of temperature, pressure, and concentration is investigated, and comparisons with literature values are provided where possible. Finally, the optimisation process used to fit the data as a function of temperature and concentration is detailed.

Chapter 9: Experimental Density and Viscosity. This section presents the experimental dynamic viscosities of CO₂-unloaded and CO₂-loaded aqueous amine solutions, measured using a capillary viscometer. It investigates the influence of temperature and CO₂ loading on this property and provides comparisons with literature values where available. For systems where density was not measured using the vibrating tube densimeter (Anton Paar DMA HPM) and it is not reported in Chapter 7, this property was measured with an automatic kinematic viscometer (Anton Paar SMW 3001), which is also described here. Finally, this chapter details the optimisation process used to fit the experimental density and viscosity data as functions of temperature and CO₂ loading.

Conclusions and Future Work. This section concludes the research by presenting the main findings and outlining guidelines for future work.

CHAPTER 1: INTRODUCTION AND OBJECTIVES

References. This section presents the complete references cited in this thesis.

About the author. This section includes a brief bibliography of the author, detailing principal predoctoral activities. These include scientific publications in a high-impact journal, conference contributions, relevant coursework, and a research visit to the Thermophysics Laboratory at Imperial College London in the UK.

Table 1.1. Principal features of the amines used in this study (Source: PubChem database [57,58]).

Amines	CAS Number	Molecular Formula	Structure	Molecular Weight (g·mol ⁻¹)	Type of Amine
Monoethanolamine (MEA)	141-43-5	$\mathrm{C_2H_7N}$	H N H	61.08	Primary amine
Diethanolamine (DEA)	111-42-2	C ₄ H ₁₁ NO ₂	H O H	105.14	Secondary amine
2-(Ethylamino)ethanol (EAE)	110-73-6	C ₄ H ₁₁ NO	N H	89.14	Secondary amine
Methyldiethanolamine (MDEA)	105-59-9	C ₅ H ₁₃ NO ₂	H O H	119.16	Tertiary amine
2-(Dimethylamino)ethanol (DMEA)	108-01-0	C ₄ H ₁₁ NO	O H	89.14	Tertiary amine
2-Diethylaminoethanol (DEAE)	100-37-8	C ₆ H ₁₅ NO	O H	117.19	Tertiary amine

2-Amino-2-methyl-1-propanol (AMP)	124-68-5	C ₄ H ₁₁ NO	H	89.14	Primary amine and sterically hindered amine
3-(Methylamino)propylamine (MAPA)	6291-84-5	$C_4H_{12}N_2$	T Z	88.15	Diamine (one primary and one secondary amino groups)
Piperazine (PZ)	110-85-0	$C_4H_{10}N_2$	1-Z Z-I	86.14	Diamine (cyclic amine with 1-ring)
1-Methylpiperazine (1-MPZ)	109-01-3	C ₅ H ₁₂ N ₂	H	100.16	Diamine (cyclic amine with 1-ring)

Table 1.2. Literature experimental measurements of density, viscosity and isobaric heat capacities of the binary mixtures.

Binary	Property	Amine mass	s fraction (w)	Temperat	ure (<i>T</i>)/K	Apparatus	No. of Data	$U_{ m r}^{ m a}$	Reference
System	rroperty	Low	High	Low	High	Apparatus	Points	$U_{\rm r}$	Reference
		0.1	0.60	298.15	333.15	Anton Paar DMA5000	15	0.02 %	[59]
		0.02	1.00	278.15	353.15	Anton Paar DMA 45	140	NA ^c	[60]
		0.1	1.0	303.15	353.15	Anton Paar DMA 4500	60	NA ^c	[61]
		0.3	1.0	293.15	363.15	Anton Paar DMA 4500	27	1 %	[62]
	Density	0.1	1.0	293.15	353.15	Anton Paar DMA 4500M	130	0.006 %	[63]
		0.03	1.00	298.15	318.15	Anton Paar DMA 602	78	NA ^c	[64]
		0.2	1.0	293.15	313.15	Anton Paar DMA 602	96	NA ^c	[65]
		0.4	1.0	293.15	313.15	Single-capillary	30	0.1 %	[66]
$DEAE + H_2O$		0.1	1.0	273.13	313.13	pycnometer	30	0.1 70	[00]
_		0.02	0.20	298.15	333.15	A&D sine-wave Vibro	25	6 %	[59]
		0.02	0.20	2,000	200110	viscometer (model SV-10)		0 / 0	[67]
		0.4	1.0	303.15	353.15	U-tube glass viscometer	60	NA ^c	[61]
						Ubbelohde-type			
	Viscosity	0.02	1.00	298.15	353.15	viscometers (Schott Gerate	100	0.2 %	[67]
						type 24 501)			
						Double-gap pressure cell			
		0.3	1.0	293.15	363.15	XL in Physica MCR 101	33	4 %	[68]
						rheometer			

	Isobaric Heat	0.1	0.9	298.15	313.15	Adiabatic Calorimeter	2	NA ^c	[69]
	Capacity	0.1	0.9	290.13	313.13	Adiabatic Calorinietei	2	INA	[09]
		0.1	1.0	293.15	333.15	Anton Paar DMA 4500M	55	0.02 %	[70]
		0.1	1.0	303.15	323.15	Pycnometer (MBL)	85	0.4 %	[71]
						Stabinger-type kinematic			
	Density	0.2	1.0	293.15	363.15	viscometer-densimeter	40	0.4 %	[72]
						(SVM 3001, Anton Paar)			
		0.1	0.3	293.15	333.15	Anton Paar DMA 35	54	0.3 %	[73]
		(0.5	298.15	323.15	Anton Paar DSA 5000	6	0.02 %	[74]
		0.1	1.0	293.15	333.15	Anton Paar Lovis 2000	55	2 %	[70]
						ME			
		0.2	1.0	303.15	323.15	B-type and D-type	85	0.04 %	[71]
$EAE + H_2O$						Ostwald viscometer			
		0.0	1.0		262.15	Stabinger-type kinematic	40	7 0 (5=01
	Viscosity	0.2	1.0	293.15	363.15	viscometer (SVM 3001,	40	5 %	[72]
	_					Anton Paar)			
		0.1	0.3	293.15	333.15	A&D sine-wave Vibro	54	3 %	[73]
	-					viscometer (model SV-10)			
		0.1	0.4	293.15	323.15	Lovis 2000 M/ME Anton	28	NA ^c	[75]
				200.15	323.15	Paar	-	0.02 %	[7.4]
	Isobaric Heat).5 T	298.15	323.13	Schott Capillary	6	0.02 %	[74]
		0.1	0.9	298.15	313.15	Adiabatic Calorimeter	2	NA°	[69]
	Capacity								

		0.1	0.4	293.15	343.15	Anton Paar DMA 4500	30	0.006 %	[76]
	Density	0.4	1.0	298.15	363.15	Anton Paar DMA 4500M	70	0.006 %	[63]
$MAPA + H_2O$		0.02	1.0	283.15	363.15	Anton Paar DMA 5000 M	144	0.001 %	[77]
	Viscosity	0.1	0.4	293.15	353.15	Anton Paar Rheometer Physica MCR 100	40	4 %	[76]
	Density	0.2	1.0	298.15	343.15	Anton Paar DMA 4500	72	NA°	[78]
	Density	0.1	1.0	298.15	348.15	Anton Paar DMA 4500	55	0.06 %	[38]
1 MP7 + H.O	Viscosity	0.2	1.0	298.15	343.15	U-tube Glass Cannon- Ubbelohde viscometer	72	NA°	[78]
1-WI Z + 1120	-MPZ + H ₂ O Viscosity	0.1	1.0	298.15	348.15	Cannon-Fenske type capillary tube viscometers	55	4 %	[38]
	Isobaric Heat Capacity	0.4	1.0	298.15	353.15	C80 heat flow calorimeter (SETARAM)	120	1 %	[79]
		0	.5	298.15	323.15	Anton Paar DSA 5000	6	0.02 %	[80]
		0.3	0.4	293.15	343.15	Anton Paar DMA-58	12	0.02 %	[81]
		0	.3	298	333	Gay-Lussac pycnometer	8	0.01 %	[82]
AMP + H ₂ O	Density	0	.3	293.15	333.15	Kyoto Electronics KEM DA-645	6	NA°	[83]
Alvii + 112O	Density	0.3	1.0	303.15	333.15	Anton Paar DMA 4500	56	NA°	[84]
		0.2	1.0	298.15	343.15	Anton Paar DMA 4500	66	NA°	[85]
		0.04	1.00	298.15	353.15	Anton Paar DMA 45	90	NA°	[86]
		0.1	1.0	293.15	363.85	25-mL pycnometer bottles	35	NA°	[87]
		0.1	0.3	298.15	333.15	Anton Paar DMA 5000	24	0.006 %	[88]

		0.2	0.3	303.15	353.15	Gay-Lussac pycnometer	12	NA ^c	[89]
		0	.3	298	323	Pyrex England pycnometer	6	0.8 %	[90]
		0.3	0.9	313.15	333.15	Anton Paar DMA 45	10	NA°	[91]
		0	.3	293.15	323.15	Gay-Lussac pycnometer	7	NA°	[92]
						Stabinger-type kinematic			
		0	.3	303.15	343.15	viscometer (SVM3000,	5	0.1 %	[93]
						Anton Paar)			
		0.2	0.5	313.13	362.73	Anton Paar DMA 60/512P	450	0.02 %	[94] ^b
		0.4	1.0	303.15	343.15	Anton Paar DMA 4500 M	45	NA ^c	[95]
		0.5	.5	283.15	353.15	Gay-Lussac pycnometer	4	NA ^c	[96]
		0.5		298.15	323.15	Capillary supplied by Schott	6	0.02 %	[80]
	0	0.02	0.02 0.20		323.1	Schott-Geräte AVS 350 automatic Ubbelohde viscosimeter	7	NA°	[97]
	Viscosity	0	.2	293.1	323.1	Schott-Geräte AVS 350 automatic Ubbelohde viscosimeter	7	NA°	[98]
	0.5		.5	283.15	333.15	Cannon-Fenske type capillary tube viscometers	6	NA ^c	[96]
			1.0	298.15	343.15	Cannon-Ubbelohde viscometers (0, 0B, 0C, 1, 1B, 2C-Cole Parmer)	70	1 %	[85]

		0.2	0.3	303.15	353.15	Cannon-Fenske	18	NAc	[89]
			0.3	200	222	viscometer Ostwald viscometer	0	2.0/	[O2]
				298	333		8	2 %	[82]
		0.1	0.3	298.15	333.15	Ubbelohde viscometer	24	2 %	[88]
		0.2	0.3	296.75	349.85	Cannon-Fenske	12	NA°	[87]
		0.2	0.5	250.75	317.03	viscometer	12	1471	[07]
			-1			Ostwald viscometer			
		(0.3	298	323	(Model: 11619/01,	6	2 %	[90]
						Stanhope-seta, UK)			
		0.02	0.20	29	8	Ubbelohde viscosimeter	13	NA ^c	[99]
		(0.3	293.15	333.15	Ostwald viscometer	7	NA ^c	[92]
					343.15	Stabinger-type kinematic			
		(0.3	303.15		viscometer (SVM3000,	5	0.7 %	[93]
						Anton Paar)			
		0.3	0.6	303.15	373.15	Anton-Paar Physica MCR	60	2 %	Γ100 1
		0.3	0.6	303.13	3/3.13	101 rheometer	60	2 %	[100]
		0.4	1.0	303.15	343.15	iVisc capillary viscometer	45	3 %	[0.5]
		0.4	1.0	303.13	343.13	LAUDA	43	3 %	[95]
		0.2	1.0	279.15	269.15	CSC 4100 heat-flux DSC	200	NTAC	[101]
	Isobaric Heat	0.2	1.0	278.15	368.15	calorimeter	200	NA°	[101]
	Capacity	0.6	1.0	303.15	353.15	DSC-2010 calorimeter	44	NA ^c	[102]
		0.6	1.0	303.15	353.15	DSC-2010 calorimeter	44	NA ^c	[103]
MDEA + H ₂ O	Viscosity	0.1	0.4	293.15	353.15	Falling body viscometer	140	3 %	[104]

	0.1	0.5	285.15	333.15	Cannon-Fenske routine viscometer	39	NA ^c	[105]
	0	.3	303.15	353.15	Cannon-Fenske routine viscometer	6	NA°	[89]
	0.1	0.5	333.15	353.15	Two Cannon- Fenske-type viscometers (sizes 50 and 100) and one Ubbelohde-type viscometer (size 0)	14	NA°	[106]
	0	.3	293.15	323.15	Ostwald viscometer	7	NA°	[92]
	0.3	0.6	298.15		Cannon-Fenske viscometer	4	NA ^c	[107]

^aRelative expanded uncertainty (k = 2), %.

^bPressure range from 0.5 MPa to 24 MPa.

^cNA: Not Available.

Table 1.3. Literature experimental measurements of density, viscosity and isobaric heat capacities of the ternary mixtures.

CO ₂ -loaded		Amin	e mass	CO ₂ lo	oading	Tempe	rature		No. of		
Solution	Property	fract	ion (w)	(6	a)	(<i>T</i>)	/ K	Apparatus	Data	$U_{ m r}{}^{ m a}$	Reference
Solution		Low	High	Low	High	Low	High		Points		
		0.2	0.4	0.1	0.5	298.15	353.15	Anton Paar DMA 4500	68	0.4 %	[108]
		0.3	0.6	0.1	0.56	298.15	413.15	Anton Paar DMA 4500 and DMA HPM	204	0.3 %	[109] ^b
		0.062	0.300	0.1	0.5	293.15	353.15	Anton Paar DMA 4500	68	0.002 %	[110]
		0.2	0.4	0	0.5	298	3.15	Anton Paar DMA 4500	15	0.4 %	[111]
$MEA + H_2O + CO_2$	Density	(0.3	0	0.49	298.15	353.15	Anton Paar DMA 5000M	32	0.01 %	[112]
		0.2	0.7	0	0.5	303.15	333.15	Anton Paar DMA 4500M and DMA HPM	144	0.4 %	[113] ^c
		().8	0.07	0.51	313.15	343.15	Anton Paar DMA 4500M and DMA HPM	77	0.6 %	[114]°
		0.1	0.4	0	0.5	298	3.15	Hydrometer	44	NA ^f	[107]

	0.3	0.5	0.1	0.5	293.15	353.15	Anton Paar DMA 4500	105	0.8 %	[115]
	().3	0.1	0.4	293.15	343.15	Anton Paar DMA 4500	20	0.3 %	[116]
	0.2	0.4	0.1	0.5	293.15	333.15	KEM Kyoto Electronics DA-645 densimeter	90	0.005 %	[117]
	0.1	0.2	0.1	0.8	29	98	Anton Paar DMA 512P	17	0.4 %	[118]
	(0.3	0.1	0.4	298.15	343.15	Anton Paar Lovis 2000 ME rolling-ball viscometer	20	6 %	[116]
	0.1	0.4	0	0.5	298	.15	Cannon-Fenske viscometer	24	NA ^f	[107]
	0.2	0.4	0.1	0.5	298.15	353.15	Viscometer (Z1DIN)	75	0.1 %	[108]
Viscosity	0.062	0.300	0.1	0.5	293.15	353.15	Anton Paar MCR 100 rheometer with a double gap measuring cell (DG-26.7)	100	0.1 %	[110]
	().3	0.14	0.49	298.15	353.15	U-tube capillary viscometers (PSL)	23	2 %	[119]
	0.5	0.8	0.08	0.52	298.15	373.15	Anton Paar Physica MCR 101 rheometer	320	2 %	[120] ^d

								with a double-gap pressure cell XL			
		0.1	0.5	0.1	0.5	293.15	423.15	MCR 101 Anton Paar double-gap rheometer	375	0.4 %	[121]
		0.2	0.4	0.1	0.5	298	.15	NDJ-1 rotational viscometer	15	0.1 %	[122]
		0.2	0.4	0	0.5	298	.15	Rotational viscometer (model SMART, Fungilab S.A.)	15	2 %	[111]
		0.30	0.43	0.1	0.5	313.15	333.15	Cannon-Fenske viscometer	27	NA ^f	[123]
	Isobaric Heat Capacity	0.1	0.4	0	0.5	298	.15	Stoppered and gently- stirred Dewar flask	24	NA ^f	[124]
		0.	.45	0.119	0.999	303.15	363.15	Anton Paar DMA HPM	33	0.3 %	[125]
		0.238	0.500	0.04	0.4	293.15	353.15	Anton Paar DMA 4500M	45	0.003 %	[63]
$MDEA + H_2O + CO_2$	Density	0.3	0.6	0	0.5	298	.15	Hydrometer	44	NA ^f	[107]
MDLA - 1120 - CO2	Density	0.3	0.4	0.1	0.5	298.15	423.15	Anton Paar DMA 4500 and DMA HPM	110	1 %	[126] ^e
		0.5	0.8	0	0.5	293.15	423.15	Anton Paar DMA 4500M and DMA HPM	560	0.3 %	[127] ^e

		0	.45	0.119	0.999	303.15	363.15	Falling weight viscometer (FV)	29	3 %	[125]
	Viscosity	().5	0.0452	0.1863	293.15	353.15	Anton Paar physica MCR 100 rheometer	24	NA ^f	[63]
		0.3	0.6	0	0.5	298	.15	Cannon-Fenske viscometer	44	NA ^f	[107]
	Isobaric Heat Capacity	0.3	0.6	0	0.64	298	.15	Stoppered and gently- stirred Dewar flask	40	NA ^f	[124]
$AMP + H_2O + CO_2$	Density	().3	0	0.5	293.15	333.15	KEM Kyoto Electronics DA-645 densimeter	36	NA ^f	[83]
		0.1	0.4	0	0.5	298	.15	Hydrometer	44	NA ^f	[107]
	Density	0.3	0.4	0.1	0.5	298.15	423.15	Anton Paar DMA 4500 and DMA HPM	110	1 %	[126] ^e
$DEA + H_2O + CO_2$	2 3.33.4	0.5	0.8	0	0.5	293.15	423.15	Anton Paar DMA 4500M and DMA HPM	560	0.3 %	[127] ^e
	Viscosity	0.1	0.4	0	0.5	298	.15	Cannon-Fenske viscometer	24	NA ^f	[107]
	Isobaric Heat Capacity	0.1	0.4	0	0.5	298	.15	Stoppered and gently- stirred Dewar flask	24	NA ^f	[124]

^aRelative expanded uncertainty (k = 2), %.

^bPressure range from 0.1 MPa to 0.7 MPa.

^cPressure at 0.8 MPa.

^dPressure at 0.4 MPa.

^ePressure range from 0.1 MPa to 0.8 MPa.

^fNA: Not Available.

Table 1.4. Literature experimental measurements of density and viscosity of the quaternary mixtures.

CO ₂ -loaded Solution	Property	Total amine mass fraction $(w_1 + w_2)$		CO ₂ loading (α)		Temperature (<i>T</i>)/K		Apparatus	No. of Data Points	$U_{ m r}^{ m a}$	Reference
		Low	High	Low	High	Low	High		1 Offics		
	Density	0.264	0.468	0	0.903	303.15	363.15	Anton Paar DMA HPM	70	0.4 %	[128]
	Delisity	0.	30	0		298	313	Gay-Lussac pycnometer	16	NA ^b	[45]
$MDEA + PZ + H_2O + CO_2$	Viscosity	0.25	0.50	0	0.81	303.15	373.15	Anton-Paar Physica MCR 101 rheometer with a double-gap pressure cell XL	360	3 %	[129]
		0.5		0 0.6		293.15	323.15	NDJ-1 rotational viscometer	112	2 %	[130]
				0		298	313	Ostwald viscometer	16	1 %	[45]
	Density	0.45		0	1.616	303.15	363.15	Anton Paar DMA HPM	33	0.3 %	[125]
		0.45		0 1.616		303.15	363.15	Falling weight viscometer	24	6 %	[125]
$\begin{aligned} \text{MDEA} + \text{AMP} \\ + \text{H}_2\text{O} + \text{CO}_2 \end{aligned}$	Viscosity	0.3	0.6	0	0.8	303.15	373.15	Anton-Paar Physica MCR 101 rheometer with a double-gap pressure cell XL	237	3 %	[100]

^aRelative expanded uncertainty (k = 2), %.

^bNA: Not Available.

2. Theory

2.1. Densimetry Basics

A detailed understanding of the thermodynamic properties of fluids is critical for both scientific advancement and industrial applications. Combining non-reacting liquids alters their physical characteristics, thereby influencing the associated thermodynamic quantities. This effect is particularly pronounced for density, a fundamental fluid property used in characterising the thermodynamic state and calculating derived quantities.

Density ρ defined as mass per unit volume, is crucial for developing equations of state, facilitating fluid custody transfer, and designing and implementing industrial processes. In the International System of Units (SI), the unit of density (kg·m⁻³) is derived from the unit of mass kg and the unit of length m. Accurate density measurement plays an essential role in optimising various processes. It aids in [131]:

- Theoretical Model Development: Enables the creation of models to predict and understand material behaviour.
- Pressure and Temperature Dependence: Allows for designing equipment like rectification towers based on density variations.
- Petroleum Industry Optimisation: Optimises operational conditions and product distribution within the petroleum industry.
- Solubility and Viscosity Calculations: Contributes to calculating properties like solubility and viscosity.
- Predictive Modelling: Supports the development of predictive models for various physical properties.
- Solvent Capacity Determination: Determines the solvent capacity of a fluid, a key characteristic
 in designing room-temperature ionic liquids and supercritical extraction processes.
- Determination of the isothermal compressibility and isobaric expansion coefficients.

Pressure/volume/temperature (pVT) measurements yield two crucial parameters: the isothermal compressibility coefficient κ_T and the isobaric expansion coefficient β , defined in **Equations 2.1 and 2.2**. These coefficients depend on pressure, temperature, and molecular structure and provide insights into intermolecular attractive and repulsive forces by aiding in pressure determination [132,133]. The current lack of a comprehensive theory for understanding the complex thermodynamic behaviour of fluid mixtures requires a primarily experimental approach. This needs a systematic selection of mixtures alongside experimental data to advance our understanding of fluid thermodynamics and develop quantitative prediction methods.

$$\kappa_T = -\frac{1}{V} \left(\frac{\partial V}{\partial P} \right)_T \tag{2.1}$$

$$\beta = \frac{1}{V} \left(\frac{\partial V}{\partial T} \right)_{P} \tag{2.2}$$

A substantial body of literature exists detailing various experimental methods for determining the density of liquids and gases. These methods can be mostly classified into two main categories: direct and indirect techniques.

- 1. Direct techniques: directly measure the volume occupied by a fluid sample, frequently needing to be calibrated using reference materials. Common examples include pycnometers, the hydrostatic method, and magnetic float densimeters:
 - A pycnometer is a calibrated container of known volume used to calculate the volume of a specific amount of fluid, whose density is calculated from the mass and volume.
 - The hydrostatic method utilises Archimedes' principle, where the floating force applied to an
 object submerged in a fluid equals the weight of the displaced fluid. The density of the object
 can be determined by measuring the floating force and its own volume.
 - The magnetic float densimeters employ a hollow, magnetic float that experiences a floating force within the fluid. The density and geometry of the float are known, allowing for the determination of the density of the density of the surrounding fluid [134].
- 2. Indirect techniques: rely on measuring properties related to density, often requiring calibration with standard substances. Despite this indirect approach, they can achieve high accuracy. A prominent example are the vibrating body densimeters. These instruments measure the resonant frequency of a vibrating element (e.g., a U-shaped tube or wire) influenced by the density of the surrounding fluid [134–136], allowing density measurements across a wide range of temperatures and pressures.
 - Vibrating tube densimeters, in which the resonant frequency of a U-shaped tube containing the fluid sample is measured (detailed descriptions can be found in Chapter 4).
 - Vibrating wire densimeters employ a vibrating wire sensor that detects the floating force on a submerged object. In addition, these apparatuses measure density.

2.2. Calorimetry Basics

The heat capacity of a liquid is a fundamental thermodynamic property. Knowledge of it is not only necessary for engineering, but is also a very important source of information for discerning the structure and molecular interactions of liquid solutions, which serve as a basis for the development of models used in industry [137,138]. Heat capacity c is defined as the ratio between the amount of heat Q that a

body or system gains or losses and the corresponding increase or decrease in temperature T that the body or system experiences, as detailed in **Equation 2.3** [132].

$$c = \frac{\delta Q}{dT} \tag{2.3}$$

Mathematically, isobaric heat capacity (constant-pressure heat capacity), denoted by c_p , relates to the enthalpy H and Gibbs free energy G through their derivatives, as shown in **Equation 2.4**.

$$c_{p} = \left(\frac{\partial H}{\partial T}\right)_{p, x_{i}} = -T \left(\frac{\partial^{2} G}{\partial T^{2}}\right)_{p, x_{i}} = T \left(\frac{\partial S}{\partial T}\right)_{p, x_{i}} \tag{2.4}$$

This relationship between c_p and these fundamental thermodynamic functions allows to derive expressions for changes in enthalpy ΔH , Gibbs free energy ΔG , and entropy ΔS with respect to temperature, as detailed in **Equation 2.4**. Furthermore, when combined with pVT data, extensive heat capacity measurements across a wide range of pressures and temperatures can be employed to extract other crucial thermodynamic properties. This comprehensive dataset facilitates a complete understanding of the thermodynamic behaviour of the system under investigation.

The definition of enthalpy H encompasses both molar and specific isobaric heat capacities. The type (molar or specific) depends on the units employed for H. **Equation 2.5** provides the means to calculate enthalpy.

$$\partial H = \left(\frac{\partial H}{\partial T}\right)_p dT + \left(\frac{\partial H}{\partial p}\right)_T dp \tag{2.5}$$

For a closed system undergoing a constant-pressure process, where enthalpy is independent of pressure, **Equation 2.6** can be directly substituted into **Equation 2.5**. This substitution simplifies **Equation 2.5** to **Equation 2.7**, which subsequently leads to **Equation 2.8**.

$$\left(\frac{\partial H}{\partial p}\right)_T dp = 0 \tag{2.6}$$

$$\partial H = \left(\frac{\partial H}{\partial T}\right)_p dT = c_p dT \tag{2.7}$$

$$\Delta H = \int_{T_1}^{T_2} c_p dT \tag{2.8}$$

where, T_1 is the initial temperature and T_2 is the final temperature. Applying the First Law of Thermodynamics to a mechanically reversible, constant-pressure process yields **Equation 2.9**. Since

enthalpy and heat capacity at constant pressure are all state functions, **Equation 2.9** is applicable to any process where the final pressure (p_2) equals the initial pressure (p_1) , regardless of whether the process actually occurs at constant pressure [132].

$$Q = \Delta H = \int_{T_1}^{T_2} c_p dT$$
 (2.9)

The isobaric heat capacity of liquids exhibits a relatively weak dependence on temperature across a wide range. This trend holds true until the reduced temperature T_r is between 0.7 and 0.8, which is typically close to the normal boiling point of the liquid. In this region, a shallow minimum in the isobaric heat capacity is frequently observed. However, at higher reduced temperatures, the relationship between the isobaric heat capacity and temperature becomes significantly stronger. As the system approaches its critical point, the isobaric heat capacity increases dramatically and tends towards infinity. This temperature dependence of the isobaric heat capacity can be determined using calorimetric techniques [139].

Even though there is no recognised classification of calorimetric techniques, four types of calorimeters are frequently employed for measuring isobaric heat capacity in liquids: Brönsted's calorimeter, Tian-Calvet calorimeter, differential scanning calorimeter (DSC), and flow calorimeter [140].

Von Steinwehr and Brönsted applied Brönsted's calorimeter for the first time in 1901 and 1906, respectively. This method is based on the endothermic dissolution of an amount of solution in a water-filled Dewar vessel and the gradual mixing of the content with a stirrer. An electric heater produces a regulated heat output, which keeps the solution temperature constant. Voltage and current are consistently measured with high accuracy over time. Therefore, the electrically generated compensatory heat is equal to the heat of solution. The isobaric heat capacity is then calculated from these values, as detailed in Zijlema et al. [141]. Because a resistor can only generate heat, this method is limited to measuring endothermic effects. Exothermic effects can be compensated for in principle by using electric cooling based on the Peltier effect [142].

Calvet & Prat [143] provide a detailed description of Tian's calorimeter, which the former modified. According to the Tian-Calvet heat principle, the pile of thermocouples around the calorimetric container conducts the majority of the heat produced within it to the external jacket. The heat flow rate in the thermocouple pile is proportional to the amount of calorific power delivered. The Tian-Calvet calorimeter is very sensitive and versatile, making it appropriate for a wide range of calorimetric measurements, including isobaric heat capacity determination [144]. According to the studies [79,145,146], a C80 heat flow calorimeter (SETARAM Instrumentation, France) is commonly used to measure isobaric heat capacities in liquid mixtures.

IUPAC defines differential scanning calorimeter (DSC) as any instrument capable of measuring thermal power during a temperature scan, regardless of mode of operation. DSC is a technique for measuring the temperature-dependent differential in heat flow between a sample and a reference material [140]. Specifically, the heat flux DSC apparatus is the most common type of DSC used in liquid isobaric heat capacity measurement [147–149], consisting of a furnace with a thermoelectric device to measure heat fluxes and two crucibles, one containing the sample under study and the other carrying the reference material [140].

In recent years, flow calorimetry has become a common method for measuring heat effects in mixing operations, as well as determining the isobaric heat capacity of fluids and fluid mixtures [140]. This study employed a flow calorimeter to determine isobaric heat capacity. Chapter 5 provides a full and complete overview of this technique.

2.3. Viscometry Basics

A fundamental transport property of all liquids is their viscosity. Liquids exhibit internal resistance to flow; in this regard, viscosity is a measurement of the liquid's resistance to flow with a velocity gradient. Thus, viscosity measures the internal fluid friction. This property depends on temperature and pressure and varies in different ways with the influence of these parameters. Along with density, viscosity reflects the effects of molecular motion and interaction. There are two ways to express viscosity: dynamic viscosity η and kinematic viscosity v. The dynamic viscosity is expressed in terms of tangential force per unit area divided by a velocity gradient; the unit should be (force)·(time)/(length)². In the older reported studies, viscosity was given in poises (P) or centipoises (cP); nowadays pascals per second (Pa·s) or millipascals per second (mPa·s) are the most common SI unit. Throughout this work, the dynamic viscosity unit will be mPa·s, which is the most common unit in the literature for liquid mixtures and a sub-multiple of SI unit. For clarity, the following conversion factors apply to viscosity units:

$$0.1 \text{ N} \cdot \text{s} \cdot \text{m}^{-2} = 1 \text{ g} \cdot \text{cm}^{-1} \cdot \text{s}^{-1} = 1 \text{ P} = 100 \text{ cP} = 0.1 \text{ Pa} \cdot \text{s} = 100 \text{ mPa} \cdot \text{s}$$

On the other hand, the sample's density is a necessary input for the determination of kinematic viscosity. In this sense, kinematic viscosity is defined like the relation between dynamic viscosity and density under the same conditions of temperature and pressure. The SI unit of kinematic viscosity is m²·s⁻¹, due to this unit is too big, normally kinematic viscosity is reported in mm²·s⁻¹ [139,150].

The literature describes the use of various methods for measuring liquid mixture viscosities. Viscometers can be divided into four main groups, according to [150]: capillary viscometers, vibration viscometers, rotational viscometers, and other types.

- 1. Capillary viscometers: the most frequently used viscometers for liquids, specifically in aqueous solutions, providing measurements at atmospheric pressure in a wide range of temperatures, as can be seen in Tables 1.2 and 1.3 in Chapter 1. The excellent repeatability of capillary viscometers is their most crucial feature. This technique can be divided into three groups: the modified Ostwald, suspended level, and reverse flow types [150].
 - Modified Ostwald: the Cannon Fenske Routine viscometer is employed to measure the kinematic viscosity of transparent liquids over the range of (0.5 to 20 000) mm²·s⁻¹.
 - Suspended level viscometers: Ubbelohde viscometers enable the measurement of transparent liquid kinematic viscosities up to 100 000 mm²·s⁻¹ using 16 different viscometers. Since this method was used to measure the viscosities reported in this study, Chapter 6 provides a detailed discussion of this technique along with a description of the equipment used.
 - Reverse flow viscometers: the Cannon-Fenske viscometers measure kinematic viscosity in the range of (0.4 to 20 000) mm²·s⁻¹. Because the liquid travels from the capillary to the measuring bulb, this method works for both opaque and transparent liquids.
- 2. Vibrating wire viscometer: a well-known apparatus with the ability to produce accurate results with relatively small relative uncertainty. This technique consists of a thin wire that is submerged in the fluid of interest and is made to oscillate transversely. The method works particularly well for measuring viscosity over a wide temperature range and at high pressures (up to 200 MPa). This technique is viable in electrically-insulating fluids like hydrocarbon liquids [151–153].
- 3. Falling ball/piston viscometer: consisting of a tube containing the liquid being tested, a piston or ball inside the tube, an electrical magnet, and a magnetic switch. The material used to make the ball or piston is ferromagnetic. The magnet raises it to the top of the tube first, and then gravity allows it to descend to the bottom of the tube. A magnetic switch detects when the ball or piston contacts the bottom. Viscosity is determined from the time it takes to travel the length of the tube [150,154].
- 4. Rolling ball viscometer measures the time it takes for a ball submerged in the test fluid to roll down a slope. This time is related to the viscosity of transparent and opaque liquids. It can be applied to liquids at temperatures between 5 and 100 °C with a viscosity up to 10 000 mPa·s [150,155].



3. Preparation of the Mixtures

3.1. Sample Handling Safety

This chapter details the methodologies employed in preparing mixtures of CO₂-unloaded and CO₂-loaded aqueous amine solutions. Prior to handling, a comprehensive risk assessment was conducted to ensure the safe manipulation and preservation of the involved substances, thereby minimising sample contamination.

Material Safety Data Sheets (MSDS), readily accessible from each supplier's website, were consulted for all chemicals. This information served as the basis for a "Control of Substances Hazardous to Health (COSHH) Essentials" report [156,157]. The MSDS provided crucial details such as risk phrases and Workplace Exposure Limits (WEL), typically expressed in parts per million (ppm) for vapours and milligrams per cubic meter (mg·m⁻³) for particulates. COSHH Essentials aligns with the European REACH Regulation [158] in identifying risk management measures for specific exposure scenarios. This report encompassed a detailed standard operating procedure (SOP) for the equipment utilized, encompassing all chemicals involved in cleaning and sample preparation.

Following a thorough review of the MSDS, an approach was adopted to evaluate the overall risk associated with handling each substance:

- Health Hazard Score (A): If a chemical exhibited multiple risk phrases, the highest assigned health hazard score was assigned.
- Volatility Score (B): To establish this score, the boiling points of each substance were found and assigned a corresponding value based on **Figure 3.1**.
- Quantity Score (C): This score considered both the volume in the stock bottle and the volume of aliquots used. The basis for this approach lies in the potential for a greater risk scenario if the entire stock bottle's contents were to spill during aliquot removal. In this study, most chemicals were used in medium quantities: 1 to 100 g (mL). Exceptions included carbon dioxide and cryogenic nitrogen, which were assigned a medium score.

The overall risk level was estimated by multiplying scores A, B, and C. The resulting values were categorized as follows: ≤ 8 (low), 9-12 (medium), and ≥ 13 (high). As shown in **Table 3.1**, 2 of the 13 evaluated chemicals received the "high" overall risk level classification, and 8 the "medium" classification. As a conclusion, it is always necessary to use personal protective equipment such as lab coats, gloves, and safety goggles, and it is essential to handle them exclusively under the safety hood due to the negative effects on humans.

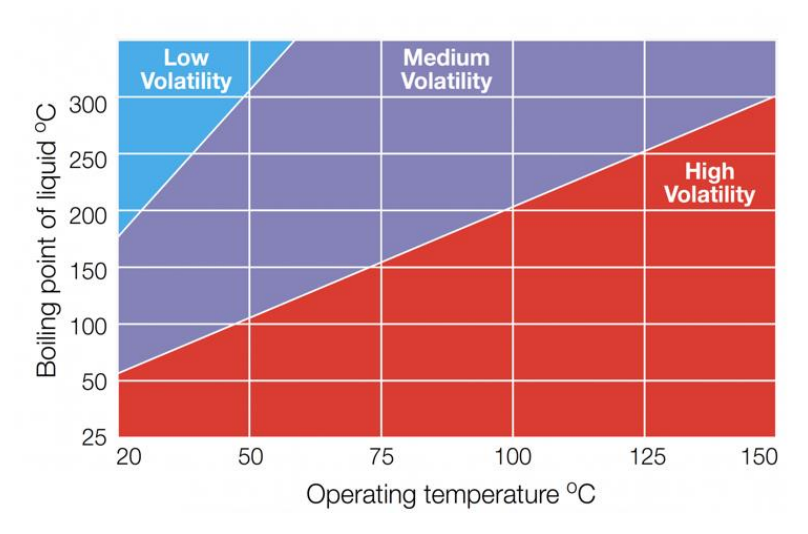


Figure 3.1. Volatility Score (Source: [159]).

Table 3.1. Hazard Evaluation and Risk Determination section in the "Control of Substances Hazardous to Health (COSHH) Essentials" report [156].

	Route of Exposure							A	В	C	A x	ВхС
Chemical	Inhalation	(Ingestion	Skin Contact	Penetration	© Eye Splash	Hazard Statement(s)	Workplace Exposure Limit (WEL)	Health Hazard Score	Volatility Score	Quantity Score		all Risk evel
Monoethanolamine (MEA)	X	X	X	X	X	H302/312/332, H314, H318, H335, H412	TWA 1 ppm	3	2	2	12	M
Diethanolamine (DEA)	X	X	X		X	H302, H315, H318, H373, H412	VLA-ED 0.2 ppm	3	1	2	6	L
1-Methylpiperazine (1-MPZ)	X		X	X	X	H226, H312, H314, H331	NS	3	2	2	12	M
2-(Diethylamino)ethanol (DEAE)	X	X	X	X	X	H226, H302, H311, H314, H331, H335	VLA-ED 2 ppm	3	2	2	12	M
2-(Ethylamino)etanol (EAE)		X	X	X	X	H302, H314, H318	NS	3	2	2	12	M
2-Amino-2-methyl-1-propanol (AMP)			X		X	H314, H318, H412	NS	3	2	2	12	M
3-(Methylamino)propylamine (MAPA)	X	X	X	X	X	H226, H302/312/332, H314, H318	NS	3	2	2	12	M
N-Methyldiethanolamine (MDEA)					X	H319	NS	2	2	2	8	L

2-Dimethylaminoethanol (DMEA)	X		X	X	X	H226, H302/312, H314, H331, H335	NS	3	2	2	12	M
Piperazine (PZ)	X		X	X	X	H228, H314, H318, H334, H317, H361fd	TWA 0.1 ppm	3	1	2	6	L
Carbon Dioxide (CO ₂)	X					H280	TWA 5000 ppm	2	3	2	12	M
Cryogenic Nitrogen	X	X	X	X		H281	Oxygen Depletion (Asphyxiant)	2	3	3	18	Н
Isopropanol (2-propanol)	X	X	X		X	H225, H319, H336	VLA-ED 200 ppm	3	3	2	18	Н

VLA-ED: Daily environmental exposure limit value.

TWA: Time Weighted Average.

NS: Contains no substances with occupational exposure limit values.

3.2. Mixtures Samples Preparation

In this work the following chemicals samples were used: monoethanolamine (MEA), diethanolamine (DEA), 2-(ethylamino)ethanol (EAE), methyldiethanolamine (MDEA), 2-(dimethylamino)ethanol (DMEA), 2-diethylaminoethanol (DEAE), 2-amino-2-methyl-1-propanol (AMP), 3-(methylamino)propylamine (MAPA), 1-methylpiperazine (1-MPZ), piperazine (PZ), water (H₂O) and carbon dioxide (CO₂). As provided by the supplier, the chemical purities of these samples are detailed in **Table 3.2** and more information about the features is provided in Chapter 1. No additional purification procedures were carried out.

Table 3.2. Description of Chemical Samples.

Chemical Name	CAS Number	Source	Mass Percent Purity ^a
MEA	141-43-5	Sigma-Aldrich	≥ 99.5 %
DEA	111-42-2	Sigma-Aldrich	≥ 99 %
EAE	110-73-6	Sigma-Aldrich	≥ 98 %
MDEA	105-59-9	Sigma-Aldrich	≥ 99 %
DMEA	108-01-0	Sigma-Aldrich	≥ 99 %
DEAE	100-37-8	Sigma-Aldrich	≥ 99.5 %
AMP^b	124-68-5	Sigma-Aldrich	≥ 97 %
AMP^{c}	124-68-5	Fisher Scientific	≥ 99 %
MAPA	6291-84-5	Sigma-Aldrich	≥ 97 %
1-MPZ	109-01-3	Sigma-Aldrich	≥ 99 %
PZ	110-85-0	Sigma-Aldrich	≥ 99 %
Water ^b	7732-18-5	Sigma-Aldrich	conductivity $\leq 2 \cdot 10^{-6} \Omega^{-1} \cdot \text{cm}^{-1}$
Water ^c	7722 10 5	Millipore Direct-Q	electrical resistivity $\geq 18\mathrm{M}\Omega$ ·cm at
water	7732-18-5	UV3 apparatus	T = 298 K
$\mathrm{CO_2}^\mathrm{b}$	124-38-9	Air Liquid	≥ 99.98 %
$\mathrm{CO_2}^\mathrm{b}$	124-38-9	Messer	≥ 99.9998 %
$\mathrm{CO_2}^\mathrm{c}$	124-38-9	BOC	≥ 99.999 %

^a As stated by the supplier by gas chromatography.

The CO₂-unloaded aqueous amine solutions were prepared using an analytical balance Radwag PS750/C/2 with 1 mg of resolution. Immediately upon preparation, mixtures were degassed using a water-filled ultrasonic bath (Branson 3210). To minimise potential CO₂ absorption from the air and

^bFor density and isobaric heat capacity measurements.

^cFor viscosity measurements.

prevent contamination and oxidative degradation, the solutions were stored in the dark in glass containers with film wrapped around the lid. Repeated density and pH measurements confirmed the stability of samples, retaining dissolved CO₂ for up to a month in the case of CO₂-loaded solutions. For pH measurements, a Mettler Toledo FiveEasy Plus pH-meter was used, and a vibrating tube densimeter Anton Paar DMA58 was employed for this density measurement.

The reaction between an aqueous amine solution (an alkaline solution) and CO₂ results in the formation of carbamates or bicarbonates, which are more acidic than the original amine. This acidification typically leads to a decrease in solution pH, often from a range around 12 to a range around 8 [160,161]. Measuring the solution's pH after the CO₂ reaction provides valuable insights into the extent of the reaction and the acidity of the resulting solution. If absorbed CO₂ is lost, the pH of the solution will increase. On the other hand, as explained in Chapter 7, the reaction between an aqueous amine solution and CO₂ leads to an increase in the density of the solution. Therefore, if the solution loses CO₂, the density will decrease.

The oxidative degradation of an aqueous amine solution leads to the formation of various products, such as organic acids, and will depend on the type of amine involved [162,163]. As a direct consequence, the density and pH of an aqueous amine solution are affected. Regarding pH, and given the acidic nature of the degradation products, as their concentration in the sample increases, pH will decrease. According to Ju et al. [111] study, as the concentration of degradation products increases, so will the density of the sample. A visual aspect that helps determine whether or not oxidative degradation has occurred is the colour change of the solution from transparent to brown.

3.2.1.CO₂ Loading into Aqueous Amine Solution

CO₂ was loaded into the aqueous amine solution using a vapor-liquid equilibrium (VLE) cell. For the mixtures discussed in Chapters 7 and 8, the VLE cell at the TermoCal Laboratory at the University of Valladolid (Spain) was utilised. CO₂ loading α was defined as a mol CO₂ per mol of amine. The relative expanded combined uncertainty for CO₂ loading was 0.3 % at a 95.5 % confidence level. The details of this apparatus will be provided in Juan D. Arroyave's PhD dissertation and in the scientific paper titled "Experimental measurements and modelling of CO₂ solubility in single aqueous amines" to be published. For the mixtures presented in Chapter 9, CO₂ loading was performed using a VLE cell located in the Thermophysics Laboratory at Imperial College London (United Kingdom). The relative expanded combined uncertainty for CO₂ loading with this cell was 0.4 % at a 95.5 % confidence level. The details of this apparatus will be provided in Hossam Qusty's PhD dissertation.

In both cases, a precise mass of CO₂ was delivered into the equilibrium cell containing a degassed mixture of amine and water, enabling the calculation of CO₂ loading. The temperature inside the cell

was maintained at 313.15 K throughout the experiment. Maximum CO₂ loading was chosen to ensure chemical solubility and to keep the equilibrium total pressure below atmospheric pressure (0.1 MPa) to prevent the loss of dissolved CO₂ in the liquid phase. Upon reaction completion, the cell was opened, and the resulting solution was used for density, isobaric heat capacity, or viscosity measurements. Partially loaded solutions were prepared gravimetrically by blending saturated and unloaded solutions using an analytical balance.

CCO₂) CHAPTER 4: VIBRATING TUBE DENSIMETER

4. Vibrating Tube Densimeter

4.1. Introduction

Fluid density measurement using vibrating tube densimeters (VTDs) offers the capability to achieve precise experimental data across a wide range of temperatures and pressures. The literature includes several VTD designs, both commercially available instruments [164,165] and custom-built apparatus [134,135]. Typically, density measurements can be achieved with a precision of ±0.01 kg·m⁻³ [136]. The VTDs are incredibly versatile with a wide range of conditions such as elevated temperatures (up to 623 K) and pressures (up to 140 MPa) [166–168]. The original work of Stabinger et al. [169] and Kratky et al. [170] put the basis for this technology.

A fundamental component of a VTD is a hollow tube, typically fixed into a U- or V-shape. During measurement, this tube is filled with the sample fluid. The U-shape facilitates the excitation and monitoring of the tube's fundamental bending mode using wire-coil electromagnets. Its principle of operation is based on the relationship between the resonant frequency of the U-shaped tube and the density of the sample fluid inside the tube. The sample becomes an integral part of the vibrating system, directly influencing its mass and, therefore, its resonant frequency. To ensure accurate measurements, VTDs require calibration using fluids with a precisely known density. The small size of VTDs allows for the cost-effective use of materials such as stainless steel and specific alloys including Hastelloy and Inconel, allowing operation under highly corrosive conditions. However, caution is recommended when employing VTDs with systems likely to solid phase formation [134].

This chapter studies the detailed principles of VTD measurement, including design considerations for safety, calibration procedure, validation technique, and a complete analysis of associated measurement uncertainties.

4.2. Principle of Measurement

A vibrating tube densimeter typically involves a thin-walled, hollow tube (metallic or glass) with a "U" or "V" shape. This tube is fixed to a heavy metal block, which itself is attached to a large mass. This system effectively isolates the tube from external vibrations. The sample fluid fills the tube, which vibrates perpendicular to its plane within an electromagnetic field. The mechanical system is excited externally until the oscillator enters resonance with its natural frequency. In this way, the amplitude of the oscillations is maximised. The frequency of the oscillator depends only on the mass of fluid plus the mass of the tube in the vibrating part of the tube. The resonant frequency of this harmonic oscillation directly correlates to the density of the fluid inside the tube [131,134].

Two electromagnetic assemblies, each consisting of a permanent magnet and a wire coil (or simply a wire), are commonly used. One assembly generates the vibration in the tube, while the other detects its frequency. The original design by Kratky et al. [170] employed wire-coil electromagnets, and this configuration remains widespread in commercial instruments from companies like Anton Paar. As an example, Anton Paar DMA HPM densimeter utilizes a U-shaped Hastelloy C-276 oscillating tube with two coupled coils for mechanical vibration, enabling density measurements at pressures up to 140 MPa and temperatures ranging from (263.15 to 473.15) K [134,171].

A vibrating tube shares fundamental similarities with a vibrating rod clamped at both ends. Therefore, the same mathematical framework can be applied to describe their oscillations. The derivation of the principal working equations relies on an expression for the vibrating period τ , of the tube when it oscillates at its fundamental harmonic mode and its resonant frequency, given as **Equations 4.1** and **4.2**.

$$\tau = 2 \cdot \pi \sqrt{\frac{m_0 + \rho \cdot V_i}{k}} \tag{4.1}$$

$$\tau^2 = 4 \cdot \pi^2 \cdot \frac{m_0}{k} + 4 \cdot \pi^2 \cdot \frac{\rho \cdot V_i}{k} \tag{4.2}$$

where m_0 and V_i are the mass and inner volume of the tube, respectively, and ρ is the density of the fluid inside the tube. The parameter k is the force constant which depends on the size and shape of the tube and is proportional to the Young's modulus of the tube material. The density of the fluid can be written as a linear function of the square of the vibrating period using **Equation 4.3**.

$$\rho = \frac{k}{4 \cdot \pi^2 \cdot V_i} \cdot \tau^2 - \frac{m_0}{V_i} \tag{4.3}$$

when m_0 and V_i are assumed to be constant for the tube.

The parameters A and B, which depend on both temperature and pressure, are defined from **Equation** 4.3 as detailed in **Equations 4.4** and 5.5, respectively.

$$A = \frac{k}{4 \cdot \pi^2 \cdot V_i} \tag{4.4}$$

$$B = \frac{m_0}{V_i} \tag{4.5}$$

Then, Equation 4.3 can be rewritten as Equation 4.6.

$$\rho(T,p) = A(T,p) \cdot \tau^2(T,p) - B(T,p) \tag{4.6}$$

Despite having physical meaning related to the oscillating tube, parameters A and B are typically determined through calibration using two fluids with well-defined densities, which will be explained in Section 4.5. Additionally, depending on the calibration procedure to be used, A may depend only on temperature or on temperature as well as pressure, while B depends on both.

The vibrating period τ is typically determined using a simple digital counter. When precise temperature and pressure control are established, short-term stability (over approximately 10^3 seconds) on the order of $\pm \tau \cdot 10^{-6}$ can be achieved. This stability can improve even additional under near-ambient conditions [134].

4.3. Apparatus Description and Experimental Procedure

The base of the system is the Anton Paar DMA HPM vibrating-tube densimeter, a commercially available instrument. However, to realize the full experimental capabilities, the setup requires the construction and integration of supplementary equipment and peripheral units. The employed method measured densities from (0 to 3000) kg·m⁻³, with a resolution of 10⁻² kg·m⁻³. The period is measured using a mPDS 2000V3 evaluation unit. Temperature in the densimeter was measured with a calibrated Pt100 probe with an expanded uncertainty of 0.02 K (95.5 % confidence level). The pressure system employs a Druck DPI 104 transducer with a range up to 140 MPa and an expanded uncertainty of 0.02 MPa. Excluding the filling and cleaning process, the apparatus works in a fully automated fashion, controlled by code implemented in Agilent VEE Pro software [166]. **Figure 4.1** shows a schematic description of the equipment used.

A detailed description of all the components of the vibrating tube densimeter will be provided below.

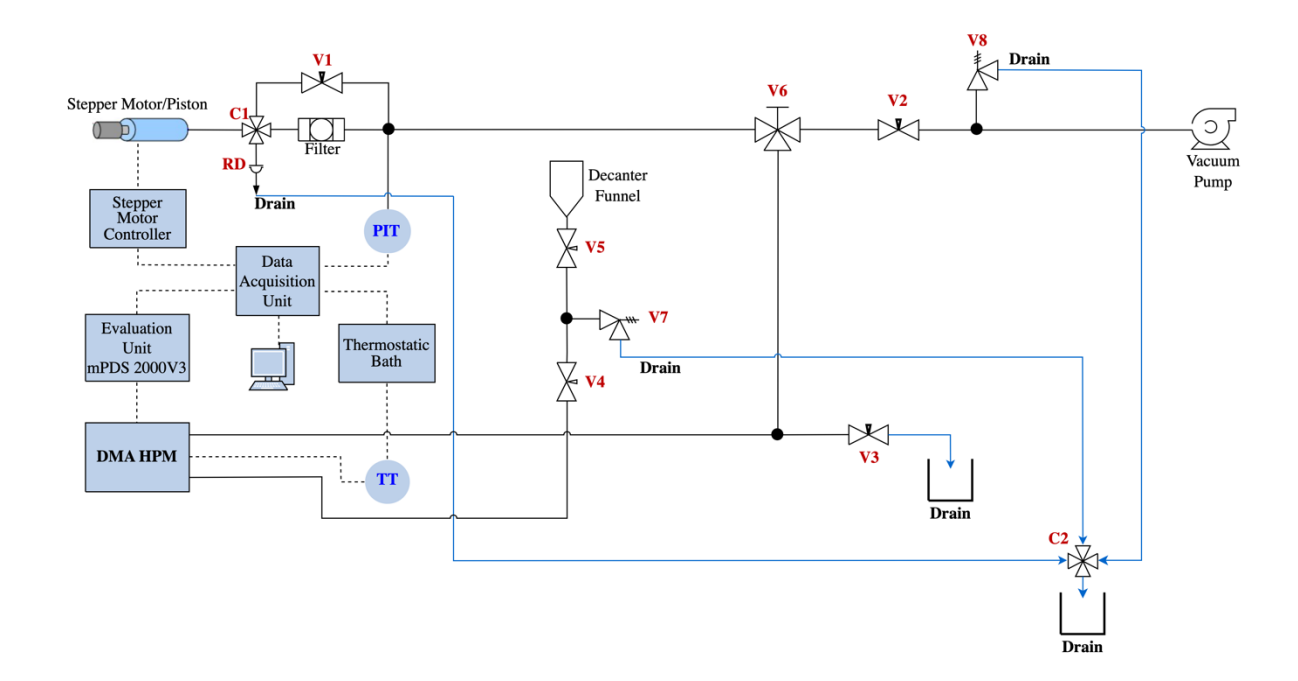


Figure 4.1. Scheme of vibrating tube densimeter (TermoCal laboratory). PIT: pressure indicator and transmitter Druck DPI 104; TT: temperature transmitter Pt100; V1-V5: high-pressure needle valves; V6: high-pressure three-way valve; V7 and V8: relief valves; RD: rupture disc; C1 and C2: crosses.

4.3.1.HPM DMA Unit

The HPM DMA Unit includes a mechanical unit and an electronic unit. A photo of this unit can be seen in **Figure 4.2**. The U-shaped oscillating tube is the heart of the mechanical unit, made from Hastelloy C-276, a well-known material known for its corrosion resistance and high strength. This tube is rigidly mounted on a heavy bronze block. This represents the counter mass of the oscillator.

The electronic unit is connected to the measuring cell by coaxial cables and serves as the driving force. Its primary function is to excite the vibrating tube, provoking it to resonate at its natural excitation frequency. This excitation occurs in a direction perpendicular to the plane containing the tube, ensuring precise control over the vibrational motion. The coaxial cables act as conduits for electronic excitation, delivering the necessary energy to the oscillator via two coils. An electronic circuit maintains a constant amplitude of the oscillations, ensuring consistent and reliable measurements. The induced vibration is transmitted to the cell by a metal foil attached to the base of the oscillator. This foil acts as a mechanical bridge, transferring the vibrational energy from the oscillator to the cell. The module determines the period of oscillation of the tube by interpreting this signal, which is directly related to the density of the fluid under study. The evaluation unit mPDS 2000V3, a frequency meter, measures the tube's vibration period with an uncertainty of 10⁻³ μs. Typical period values for the tube are around 2600 μs [131,136].

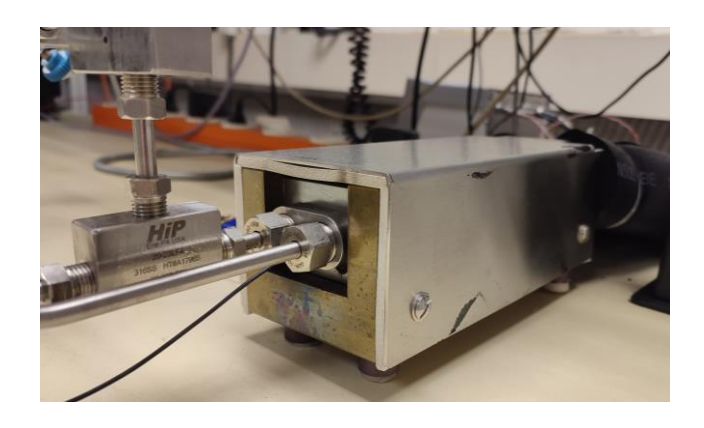


Figure 4.2. HPM DMA Unit photo.

4.3.2. Temperature Control System

Precise temperature control is essential for the vibrating tube unit. To achieve this, the unit should be contained in a thermostated environment. An external JULABO F25-HE thermostatic bath circulates a temperature-controlled fluid (silicone oil) through the cell's internal jacket. To minimise heat loss and maintain temperature stability, the rubber tubes of the circuit are insulated with thermal foam. The temperature control system is integrated into the bath itself and utilizes a Pt100 sensor inserted into the DMA HPM unit. This sensor is positioned within a cavity in the U-plane of the mechanical oscillator to measure the temperature of the sample. The Pt100 sensor has been calibrated against two calibrated Pt100 sensors at 13 temperature points from (273.15 to 413.15) K. The Pt100 sensors have been calibrated at the TermoCal facility, an accredited temperature calibration laboratory. The sensor's temperature measurement uncertainty is 0.02 K (95.5 % confidence). In **Equation 4.7** the interpolation function obtained from calibration is shown.

$$t_{real} = -1.8166 \cdot 10^{-7} \cdot (t_m - t)^3 + 3.0368 \cdot 10^{-5} \cdot (t_m - t)^2 - 3.8737 \cdot 10^{-3}$$

$$\cdot (t_m - t) - 3.2012$$
(4.7)

where t is the temperature measured with the Pt100 sensor in ${}^{\circ}$ C, and $t_{\rm m}$ is the average temperature measured with the two calibrated Pt100 sensors in ${}^{\circ}$ C.

The Pt100 sensor is a reliable temperature measurement device, utilising platinum as its conductive metal material. With a calibrated resistance of 100Ω at 273.15 K, the Pt100 offers several advantages over thermistors. Its wider temperature measurement range, extending beyond 413.15 K, allows for accurate readings. The Pt100 sensor also has a good chemical stability, linearity and high purity of its construction materials. These qualities make the Pt100 sensor a preferred choice for demanding temperature measurement applications.

4.3.3. Pressure Control System

The measuring fluid is pressurized by a HiP Model 68-5.75-15 pressure generator, as can be seen in **Figure 4.3**. This generator directly pressurizes the fluid line. A stepper motor (ACP&D type 6530-R211 with reducer) controls the piston within the generator, allowing precise volume and pressure adjustments. For safety, the system incorporates two relays: one for piston end-of-stroke and another for start-of-stroke. The piston was packed with Teflon which is a chemically, mechanically, and thermally stable material. Pressure within the system is monitored by a Druck DPI 104 transducer, capable of controlling pressures up to 140 MPa, with a resolution of 0.001 MPa throughout its entire measurement range (0.1-140 MPa). Furthermore, this sensor has been calibrated at the TermoCal facility, an accredited pressure calibration laboratory, with an uncertainty of 0.02 MPa (95.5 % confidence level).

The pressure circuit employs HiP stainless-steel tubing with a specific outer diameter (¼") throughout and HiP high-pressure needle valves with compatible connection sizes. These valves are directly coupled to the tubing via machined threads, creating a secure metal-to-metal seal under pressure.

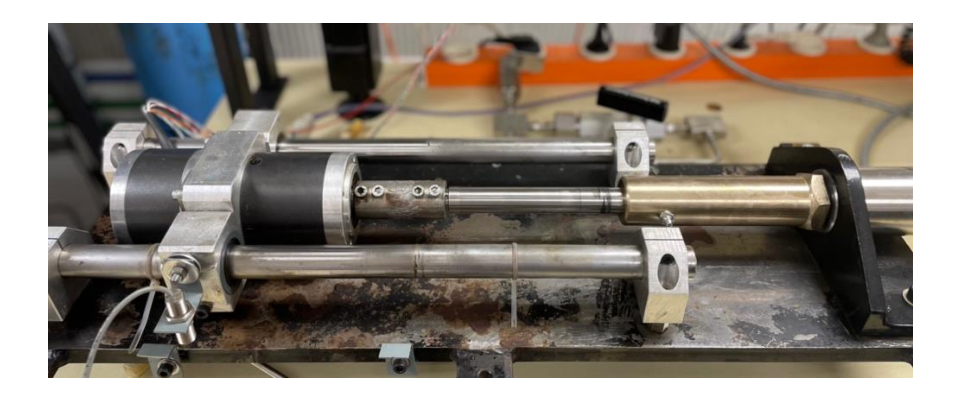


Figure 4.3. Pressure control system photo.

4.3.4. Pre-measurement Setup and Measurement Experimental Procedures

The initial step involves cleaning and removing any residual fluid from the densimeter system. To achieve this, water and isopropanol are introduced into the system to dilute the previously measured liquid. This dilution process is repeated until the densimeter is clean (two times for water and one time for isopropanol). The cleaning fluids are then evacuated using a vacuum line. This line includes a vacuum tube, a Leybold Vacuum Thermovac gauge, a liquid nitrogen cold trap, and a Leybold Trivac rotary vacuum pump. The evacuation process continues until the pressure within the densimeter reaches approximately 2 Pa, indicating a high vacuum state. This process facilitates the convenient introduction, removal, and pressurization of samples during measurements, particularly when the VTD operates under non-ambient conditions.

Experiments are conducted in a static mode, where the sample is injected into the vibrating tube using a piston-driven suction mechanism and the vacuum. Once the sample is introduced into the densimeter system, the piston movement ceases. During the measurement, the sample remains stationary within the tube at a predefined pressure. This static configuration is particularly advantageous for characterising pure fluids and their mixtures [134].

The entire measurement process is controlled by a program written in Agilent VEE Pro. This program utilizes a series of three hierarchical control loops: temperature, pressure, and period. Upon start-up, the program prompts the operator to specify the desired filename for the data (Excel format) and the temperature and pressure points for density measurements. The program then instructs the thermostatic bath to regulate the densimeter's temperature using the external Pt100 probe to reach the target value. A measurement loop continuously monitors the temperature until a stable state is achieved. That means that the standard deviation of the last ten measurements was less than 10⁻³. The program controls the pressure generator piston through a combination of on-off control with a deadband to avoid excessive adjustments. This allows for fine-tuned piston movement per stepper motor rotation. A Druck DPI 104 transducer continuously monitors the pressure, ensuring it reaches the desired value. Stability is achieved by minimising the standard deviation of the last ten pressure readings. Once the pressure loop stabilizes, the program initiates the densimeter period measurement loop. While this loop measures the period, it also verifies that the pressure remains stable. When the standard deviation of the last ten period measurements falls below 10⁻³ µs, the program records all monitored data to the previously opened Excel file. Following this recording, the program either moves to the next pressure point within the current isotherm or starts a new isotherm if the pressure sweep is complete [131].

4.4. Design Considerations for Safety

The main hazards associated with this experimental technique are related to the high pressure and temperature ranges, in addition to the risk associated with handling hazardous substances such as amines, carbon dioxide and nitrogen in liquid state. Therefore, it is necessary to design a safety system for the vibrating tube densimeter, including active and passive elements, according to the ALARP principle of the residual risk (as low as reasonably possible) [172].

The following methodology has been used to assess the risks associated with an experimental activity:

- 1. Identify the hazards (HP/LP interfaces, COSHH [156], equipment operating parameters).
- 2. Developing of Activity Risk Assessment Form (ARAF) document.
- 3. Implementing risk control.
- 4. Reviewing and recording the results of the above steps.
- 5. Check controls (maintenance and calibration).

The first step was described in detail in Section 3.1 in Chapter 3 and involves the preparation of a "Control of Substances Hazardous to Health (COSHH) Essentials" report from the detailed study of "Material Safety Data Sheets (MSDS)" for all substances involved in the measurement process [159]. In addition, the high pressure (HP) and low pressure (LP) interfaces are identified from the operating conditions in the equipment Piping and Instrumentation Diagram (P&ID). As a second step an experimental "Activity Risk Assessment (ARAF)" document [173] will be developed including identification of evacuation and waste management methods and procedures for safe equipment handling. In the third stage, incorporate safety controls like relief valves and rupture discs to ensure safe equipment operation, updating the ARAF consequently. A detailed description of the equipment, including the measurement procedure, ARAF document, COSHH report and the P&ID must always be available to the operator.

The overall risk to the standard operating procedure was identified in the activity risk assessment [173]. In this part, the active safety element was defined as a control in place. As a result, the implementation of a total of two relief valves in the HP/LP interfaces connected to another piece of equipment and a rupture disc between the stepper motor/piston and the filter were considered, as detailed in the P&ID of the VTD in **Figure 4.4**. The overall residual risk was moderate due to the low probability of injury or damage occurring and the fatal severity of the worst injury or damage in the absence of controls.

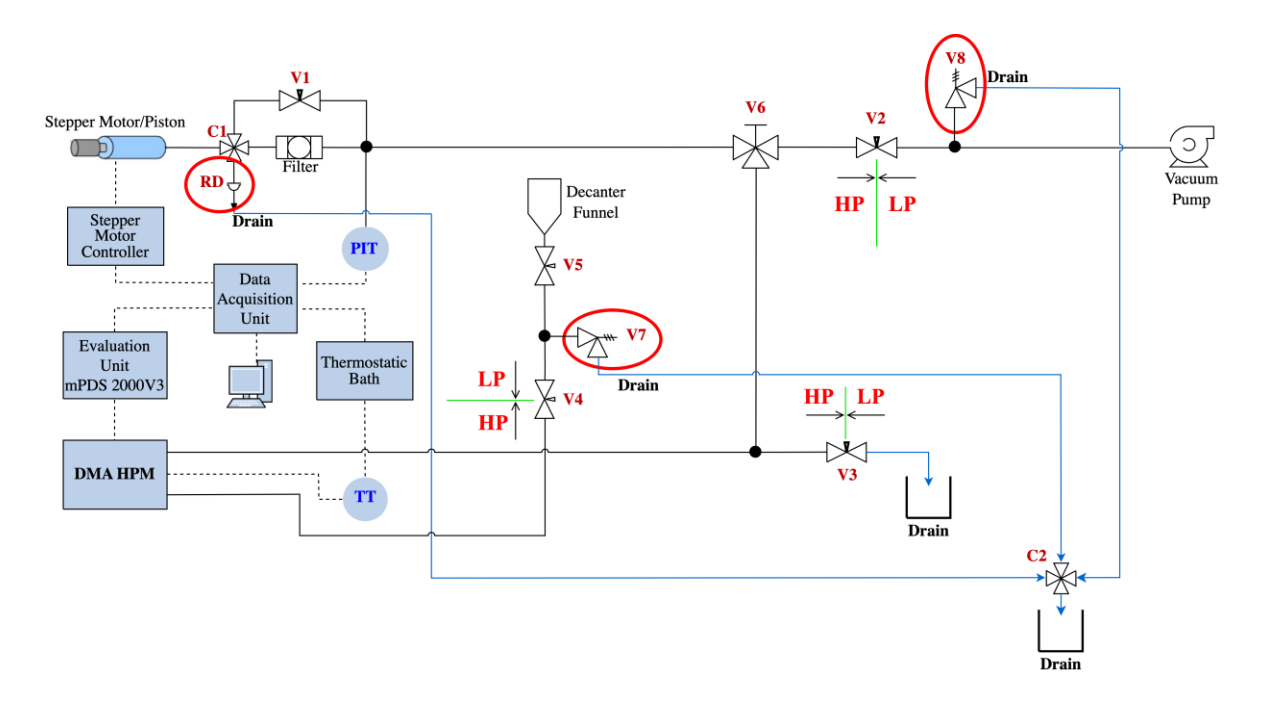


Figure 4.4. Scheme of vibrating tube densimeter (TermoCal laboratory). PIT: pressure indicator and transmitter Druck DPI 104; TT: temperature transmitter Pt100; V1-V5: high-pressure needle valves; V6: high-pressure three-way valve; V7 and V8: relief valves; RD: rupture disc; C1 and C2: crosses; Red circles: active elements implemented after activity risk assessment; HP: high-pressure interface and LP: low-pressure interface.

4.5. Calibration Procedure

As detailed in Section 4.2, the vibrating period τ , measured with a VTD correlates to density ρ , using **Equation 4.6** proposed by Lagourette et al. [164].

$$\rho(T,p) = A(T) \cdot \tau^2(T,p) - B(T,p) \tag{4.6}$$

Sousa et al. [165] and Lagourette et al. [164] aimed to reduce the number of fluids required for calibrating vibrating tube densimeters. This was motivated by the difficulty of finding in literature precise density values for two reference fluids across a wide range of temperatures and pressures. Their approach involved experimentally determining the evacuated tube's vibrating period $\tau_0(T)$. Lagourette et al. then proposed two methods (methods 1 and 2) for temperature and pressure-dependent density calibration. These methods rely on assumptions about how the densimeter's internal parameters change with temperature and pressure. Method 1 assumes A and B are temperature-dependent, but only parameter B varies (linearly) with pressure, leading to slightly better agreement with reference fluid densities during calibration, according to Lagourette et al. However, method 2 offers a stronger theoretical foundation and aligns with Sousa et al.'s proposal.

As described above, method 1 assumes that only parameter B varies significantly with pressure. This method requires only one additional fluid to measure the vibrating period as a function of temperature with knowledge of a reference fluid's volumetric behaviour (density as a function of temperature and pressure). Vacuum is typically chosen as the second "fluid" for this purpose [174,175]. In this sense, and taking into consideration that B(T,0) = B(T,0.1 MPa), Lagourette et al. [164] derived a density equation using water as the primary reference fluid, as given in **Equation 4.8**. Then the parameters A and B can be calculated using **Equations 4.9 and 4.10**.

$$\rho(T,p) = \rho_{w}(T,p) + \rho_{w}(T,0.1 \text{ MPa}) \left[\frac{\tau^{2}(T,p) - \tau_{w}^{2}(T,p)}{\tau_{w}^{2}(T,0.1 \text{ MPa}) - \tau_{0}^{2}(T)} \right]$$
(4.8)

$$A(T) = \frac{\rho_{\rm w}(T, 0.1 \text{ MPa})}{\tau_{\rm w}^2(T, 0.1 \text{ MPa}) - \tau_0^2(T)}$$
(4.9)

$$B(T,p) = \frac{\rho_{\rm w}(T,0.1 \text{ MPa})}{\tau_{\rm w}^2(T,0.1 \text{ MPa}) - \tau_0^2(T)} \cdot \tau_{\rm w}^2(T,p) - \rho_{\rm w}(T,p)$$
(4.10)

where ρ_w is the density of the water, τ_w is the vibrating period of the water, and τ_0 is the vibrating period in a vacuum state.

Parameters A and B in **Equation 4.6** are specific to the VTD being used and require calibration through measurements of the VTD's vibrating period under two conditions: once in a completely evacuated

state (vacuum) and again filled with a reference fluid (water in this case). This calibration ensures that A and B values are determined at the exact temperature and pressure conditions where the sample fluid's density will be measured [136,164]. Due to its well-characterised density, water was chosen as the reference fluid for this study. This selection is supported by the extensive data reported by Wagner and Pruss [176]. Their work covers a wide range of temperatures and pressures, enabling the development of accurate equations of state for pure water density. These equations present standard uncertainties as low as 0.001 % to 0.02 %.

Following the method 1 developed by Lagourette et al. [164] for calibrating VTDs supplied by Anton Paar, the densimeter was calibrated using water and vacuum over the whole working temperature and pressure ranges, i.e., at temperatures from (273.15 to 393.15) K and pressure up to 100 MPa. Lagourette et al. [164] highlight that parameter A(T) is only dependent on temperature T, while parameter B(T,p) is significantly influenced by both pressure p, and temperature T.

Figures 4.5 and 4.6 show the behaviour of the calibration parameters obtained using water and vacuum in this study. Figure 4.5 displays the ratio A(T)/B(T,p) plotted against pressure p, and Figure 4.6 depicts A(T) versus temperature T. As can be seen from these figures, A(T)/B(T,p) exhibits minimal variation with pressure. On the other hand, A(T) shows a linear decrease with increasing temperature. These trends are consistent with the conclusions reported by Lagourette et al. [164], Vega-Maza [131] and Lugo et al. [133].

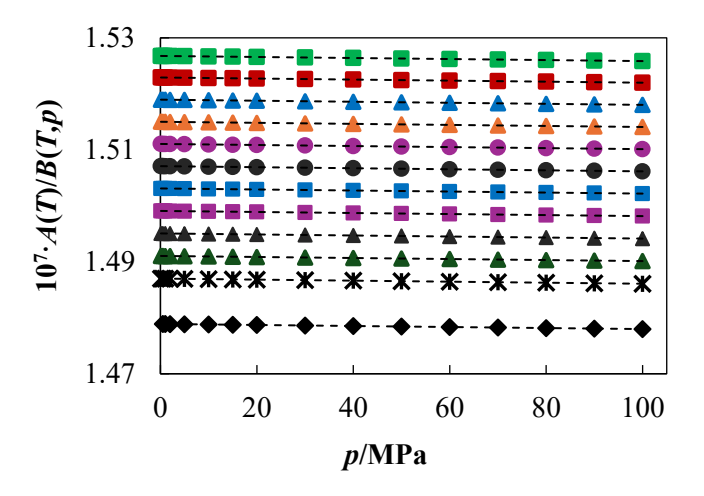


Figure 4.5. Coefficient A(T)/B(T,p) as a function of pressure p. Isotherms: (\blacksquare) T = 273.15 K, (\blacksquare) T = 283.15 K, (\blacktriangle) T = 293.15 K, (\blacktriangle) T = 303.15 K, (\spadesuit) T = 313.15 K, (\spadesuit) T = 323.15 K, (\blacksquare) T = 343.15 K, (\blacktriangle) T = 353.15 K, (\blacktriangle) T = 363.15 K, (\bigstar) T = 373.15 K, and (\spadesuit) T = 393.15 K. Dashed lines represent the linear function of each isotherm.

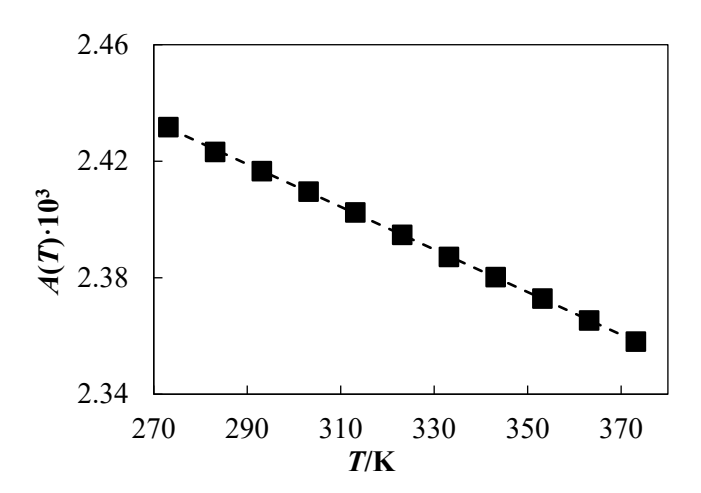


Figure 4.6. Parameter A(T) as a function of temperature T at pressure p = 0.1 MPa. Dashed line represents the linear function.

4.6. Uncertainty Budget

Uncertainty calculations for density measurement were carried out following the procedure described in the Guide to the Expression of Uncertainty in Measurement JCGM 100:2008 [177] and explained in [166]. The relative expanded uncertainty (U_r) in density measurements for CO₂-free amine solutions was 0.1 %, corresponding to a 95.5 % confidence level. Incorporating CO₂ loading into the amine solution increased this relative expanded uncertainty to 0.2 %, 95.5 % confidence level. An example of how the latter was calculated is shown below.

Table 4.1 presents the uncertainty budget for temperature and pressure, **Tables 4.2** and **4.3** for the calibration parameters A(T) and B(T,p), respectively, and **Table 4.4** for density measurement. All uncertainty budgets cover the entire temperature and pressure range, and water was used as the reference fluid. The density uncertainty analysis contemplates the uncertainties of the density of the water ρ_w , the vibrating period of the water τ_w , the vibrating period at vacuum state τ_0 , the temperature T, the pressure p, and the amine + H₂O mixture mass m, for the binary mixtures or the CO₂ loading α in terms of mol of CO₂ per mol of amine, in ternary and quaternary mixtures. **Equations 4.14** and **4.15** apply the Law of Propagation of Uncertainty with independent variables (see **Equation 4.11**) to calculate the combined uncertainty of density. Each independent property x_i has an associated sensitivity coefficient $C(x_i)$, calculated using **Equation 4.13**.

$$u_c^2(y) = \sum_{i=1}^N \left[\frac{\partial f}{\partial x_i} \right]^2 \cdot u^2(x_i)$$
 (4.11)

$$y = f(x_i, ..., x_N)$$
 (4.12)

$$C(x_{i}) = \left[\frac{\partial f}{\partial x_{i}}\right]^{2} \tag{4.13}$$

where $u_c(y)$ is the combined uncertainty of a defined property y. This combined uncertainty considers the individual standard uncertainties $u(x_i)$, associated with each of the N independent property x_i , that contribute to y as can be seen in **Equation 4.12**.

$$U_{c}(\rho(T,p)) = 2\left[\left(\frac{\partial\rho(T,p)}{\partial A(T)}\right)^{2} \cdot u^{2}(A(T)) + \left(\frac{\partial\rho(T,p)}{\partial\tau(T,p)}\right)^{2} \cdot u^{2}(\tau(T,p))\right] + \left(\frac{\partial\rho(T,p)}{\partial B(T,p)}\right)^{2} \cdot u^{2}(B(T,p))\right]^{1/2}$$

$$(4.14)$$

$$U_{c}(\rho(T,p)) = 2 \cdot \left[\left(\tau^{2}(T,p) \right)^{2} \cdot u^{2}(A(T)) + \left(2 \cdot A(T) \cdot \tau(T,p) \right)^{2} \cdot u^{2}(\tau(T,p)) + u^{2}(B(T,p)) \right]^{1/2}$$

$$(4.15)$$

Equations 4.14 and 4.15 are valid only if A(T) and B(T,p) are uncorrelated. The interdependence was tested by computing the correlation coefficient, which yielded a value of 0.1. Including this correlation in the law of propagation of uncertainty had no impact on the combined uncertainty of density. Therefore, Equations 4.14 and 4.15 were applied.

The expanded combined uncertainty (95.5 % confidence level) of the calibration parameter A(T) is calculated using **Equation 4.16** according to its definition in **Equation 4.9** and the law of propagating errors, see **Equation 4.11**. The reference pressure p_{ref} , was set at 0.1 MPa. However, for the isotherms measured at 373.15 K and 393.15 K, a reference pressure of 1 MPa was used because it was the lowest pressure attainable in those specific experiments. The sensitivity coefficient $C_A(x_i)$, used in this calculation are shown in **Equations 4.17 to 4.19**.

$$U_{c}(A(T)) = 2 \cdot \left[\left(\frac{\partial A(T)}{\partial \rho_{w}(T, p_{ref})} \right)^{2} \cdot u^{2} \left(\rho_{w}(T, p_{ref}) \right) + \left(\frac{\partial A(T)}{\partial \tau_{w}(T, p_{ref})} \right)^{2} \cdot u^{2} \left(\tau_{w}(T, p_{ref}) \right) + \left(\frac{\partial A(T)}{\partial \tau_{0}(T)} \right)^{2} \cdot u^{2} \left(\tau_{0}(T) \right) \right]^{1/2}$$

$$(4.16)$$

$$C_A\left(\rho_w(T, p_{ref})\right) = \frac{\partial A(T)}{\partial \rho_w(T, p_{ref})} = \frac{A(T)}{\rho_w(T, p_{ref})} \tag{4.17}$$

$$C_A\left(\tau_w(T, p_{ref})\right) = \frac{\partial A(T)}{\partial \tau_w(T, p_{ref})} = \frac{-2 \cdot A^2(T) \cdot \tau_w(T, p_{ref})}{\rho_w(T, p_{ref})} \tag{4.18}$$

$$C_A(\tau_0(T)) = \frac{\partial A(T)}{\partial \tau_0(T)} = \frac{2 \cdot A^2(T) \cdot \tau_0(T)}{\rho_w(T, p_{ref})} \tag{4.19}$$

The law of propagating errors, as described in **Equation 4.11**, is used to calculate the expanded combined uncertainty (95.5 % confidence level) of the calibration parameter B(T,p), which is shown in **Equation 4.20**. B(T,p) has been defined using **Equation 4.10**. The sensitivity coefficients $C_B(x_i)$, employed in this calculation are detailed in **Equations 4.21 to 4.23**.

$$U_{c}(B(T,p)) = 2\left[\left(\frac{\partial B(T,p)}{\partial \rho_{w}(T,p)}\right)^{2} \cdot u^{2}(\rho_{w}(T,p)) + \left(\frac{\partial B(T,p)}{\partial \tau_{w}(T,p)}\right)^{2} \cdot u^{2}(\tau_{w}(T,p))\right] + \left(\frac{\partial B(T,p)}{\partial \tau_{0}(T)}\right)^{2} \cdot u^{2}(\tau_{0}(T))\right]^{1/2}$$

$$(4.20)$$

$$C_B(\rho_w(T,p)) = \frac{\partial B(T,p)}{\partial \rho_w(T,p)} = \frac{A(T) \cdot \tau_w^2(T,p)}{\rho_w(T,p_{ref})} - 1 \tag{4.21}$$

$$C_B(\tau_w(T,p)) = \frac{\partial B(T,p)}{\partial \tau_w(T,p)} = \frac{-2 \cdot A^2(T) \cdot \tau_w(T,p_{ref}) \cdot \tau_0^2(T)}{\rho_w(T,p_{ref})}$$
(4.22)

$$C_B(\tau_0(T)) = \frac{\partial B(T, p)}{\partial \tau_0(T)} = \frac{2 \cdot A^2(T) \cdot \tau_0(T) \cdot \tau_w^2(T, p_{ref})}{\rho_w(T, p_{ref})}$$

$$\tag{4.23}$$

Table 4.1. Uncertainty budget for temperature T, and pressure p, in the range of temperature from (293.15 to 393.15) K and pressure from (0.1 to 100) MPa.

Source of	Uncertainty (x_i)	Units	Estimate uncertainty	Divisor	$u_{\rm c}(x_{\rm i})$
	Calibration		2·10-2	2	
u(T)	Resolution	K	1.10-2	$2\sqrt{3}$	1.10-2
	Repeatability		3.10-3	1	
<i>u</i> (<i>p</i>)	Calibration	MPa	2·10 ⁻²	2	1.10-2
<i>u(p)</i> _	Resolution	IVII a	1.10-2	$2\sqrt{3}$	1 10

Repeatability	$5 \cdot 10^{-2}$	1
---------------	-------------------	---

Table 4.2. Uncertainty budget for the calibration parameter A(T) in the density measurement in the range of temperature from (293.15 to 393.15) K and pressure from (0.1 to 100) MPa.

Source of	Uncertainty (x _i)	Units	Estimate uncertainty	Divisor	$u(x_i)$	$C_{\mathrm{A}}(x_{\mathrm{i}})$	u(A(T))
$u(ho_{ m w})$	Reference material	kg·m ⁻³	1.10-2	$\sqrt{3}$	6.10-3	2·10-6	1·10 ⁻⁸
$u(au_{ m w})$	Resolution	_ μs _	1.10-3	$2\sqrt{3}$	2.10-3	-3·10 ⁻⁵	-6·10 ⁻⁸
u(tw)	Repeatability		2·10-3	1	- 210		
$u(au_0)$	Resolution	. μs	1.10-3	$2\sqrt{3}$	2.10-3	3.10-5	6.10-8
$u(t_0)$	Repeatability	μο	2·10-3	1	2 10	3 10	0 10
$u_{c}(A(T))$	<i>k</i> = 1	kg·m ⁻³ ·μs ⁻²					9·10 ⁻⁸
$U_{c}(A(T))$	<i>k</i> = 2	kg·m ⁻³ ·μs ⁻²					2·10-7

Table 4.3. Uncertainty budget for the calibration parameter B(T,p) in the density measurement in the range of temperature from (293.15 to 393.15) K and pressure from (0.1 to 100) MPa.

Source of U	Incertainty (x_i)	Units	Estimate uncertainty	Divisor	$u(x_i)$	$C_{\rm B}(x_{\rm i})$	u(B(T,p))
$u(ho_{ m w})$	Reference material	kg·m ⁻³	1.10-2	$\sqrt{3}$	6.10-3	16	9·10 ⁻²
$u(au_{ m w})$	Resolution	μs _	1.10-3	$2\sqrt{3}$	2.10-3	-200	-4·10 ⁻¹
u(tw)	Repeatability		2·10-3	1	2 10		1 10
$u(au_0)$	Resolution	. μs	1.10-3	$2\sqrt{3}$	2.10-3	208	5·10 ⁻¹
$u(v_0)$	Repeatability	μο	2·10-3	1	2 10	200	3 10
$u_{c}(B(T,p))$	<i>k</i> = 1	kg·m ⁻³					5·10-1
$U_{c}(B(T,p))$	<i>k</i> = 2	kg·m ⁻³					1

Table 4.4. Uncertainty budget for density ρ , in the range of temperature from (293.15 to 393.15) K and pressure from (0.1 to 100) MPa.

Source of U	Incertainty (x_i)	Units	Estimate uncertainty	Divisor	$u(x_i)$	$C(x_i)$	$u(\rho(T,p))$
$u(\tau)$	Resolution	μs	1.10-3	$2\sqrt{3}$	- 2·10 ⁻³	13	3·10 ⁻²
u(t)	Repeatability	μο	2·10 ⁻³	1	_ 2 10	13	3 10
	Linearity		3·10 ⁻⁶	1			
u(m)	Resolution	kg	1.10-6	$2\sqrt{3}$	3.10-6	1	3·10 ⁻⁶
	Impurity		3·10 ⁻⁴	$2\sqrt{3}$	_		
		mol-					
$u(\alpha)$	CO ₂ -loading	CO ₂ /mo	$1 \cdot 10^{-3}$	1	$1 \cdot 10^{-3}$	192	$2 \cdot 10^{-1}$
		1-amine					
$u_{c}(A(T))$		kg·m ⁻ ³ ·μs ⁻²	6·10 ⁻¹	1	6·10-1	7·10 ⁶	6·10-1
$u_{c}(B(T,p))$	-	kg·m ⁻³	5·10-1	1	5·10-1	1	5·10-1
$u_{c}(\rho(T,p))$	k = 1	kg·m ⁻³					1
$U_{\rm c}(\rho(T,p))$	<i>k</i> = 2	kg·m ⁻³					2
$U_{\rm r}(ho(T,p))$	<i>k</i> = 2	%			$\rho = 1095.9$	kg·m ⁻³	0.2

Our CO₂-loaded amine solutions density measurements have an expanded uncertainty of 2 kg·m⁻³, assuming a 95.5 % confidence level. The calibration process, particularly the uncertainties associated with constants A(T) and B(T,p), contributes most significantly to this overall uncertainty. In addition, the uncertainty associated with the CO₂ loading in the equilibrium cell is an important contributor to the combined density uncertainty.

4.7. Experimental Validation

To ensure the accuracy of our density measurements, the apparatus, methodology and calibration were verified by measuring the density of toluene. These measurements covered the entire temperature and pressure range of interest in this study with 12 temperatures between (273.15 to 393.15) K and pressures up to 100 MPa, as detailed in **Table 4.5**. The experimental data obtained were then compared with an existing correlation and three experimental data references found in the literature [168,178,179].

Remarkably, the equation developed by Lemmon and Span [178] for toluene and integrated into the NIST REFPROP database [180], has an uncertainty of 0.01 % for saturated liquid density around 300 K and near atmospheric pressures.

Table 4.5. Experimental densities ρ , of toluene at different conditions of temperature T, and pressure p.

$\rho/(\mathrm{kg}\cdot\mathrm{m}^{-3})$								
n/MDa				T/K				
p/MPa	273.15	283.15	293.15	303.15	313.15	323.15		
0.1	885.4	876.5	867.2	857.8	848.5	839.0		
0.5	885.8	876.7	867.4	858.0	848.8	839.3		
1	886.1	876.9	867.7	858.4	849.2	839.7		
2	886.8	877.7	868.4	859.2	849.9	840.6		
5	888.8	879.8	870.7	861.5	852.5	843.3		
10	892.0	883.2	874.3	865.3	856.5	847.6		
15	895.1	886.5	877.7	868.9	860.3	851.7		
20	898.1	889.6	881.1	872.4	864.0	855.6		
30	903.9	895.6	887.4	879.1	871.0	862.9		
40	909.3	901.3	893.3	885.3	877.6	869.7		
50	914.5	906.7	898.9	891.3	883.7	876.1		
60	919.4	912.0	904.3	896.9	889.5	882.3		
70	924.1	916.9	909.5	902.2	894.9	887.8		
80	928.6	921.6	914.3	907.2	900.2	893.2		
90	933.0	926.1	919.0	912.0	905.1	898.4		
100	937.3	930.4	923.4	916.7	909.9	903.4		
				T/K				
	333.15	343.15	353.15	363.15	373.15	393.15		
0.1	829.4	819.9	810.2	800.3	790.3			
0.5	829.8	820.2	810.6	800.7	790.8	770.6		
1	830.3	820.7	811.1	801.3	791.4	771.3		
2	831.2	821.8	812.2	802.5	792.7	772.9		
5	834.1	824.8	815.5	806.0	796.4	777.2		
10	838.7	829.7	820.6	811.5	802.3	783.9		
15	843.0	834.2	825.5	816.6	807.8	790.1		
20	847.1	838.6	830.1	821.5	812.9	795.9		
30	854.9	846.7	838.6	830.5	822.4	806.5		

40	862.0	854.1	846.4	838.7	831.1	815.9	
50	868.6	861.1	853.7	846.2	838.9	824.5	
60	874.9	867.6	860.4	853.3	846.2	832.5	
70	880.9	873.8	866.8	859.9	853.2	839.8	
80	886.4	879.5	872.8	866.1	859.5	846.7	
90	891.7	885.0	878.5	871.9	865.5	853.1	
100	896.8	890.3	883.9	877.6	871.2	859.2	

^aExpanded uncertainties (k = 2): U(T) = 0.02 K; $U_r(p) = 0.0002$ and U(p) = 0.7 kg·m⁻³.

Table 4.6 summarizes the statistical analysis comparing our experimental density data to values reported in the literature for toluene. The absolute average relative deviation (AAD), maximum absolute relative deviation (MAD), and standard deviation (σ) were determined using **Equations 4.24**, **4.25 and 4.26**, respectively. Our experimental data show a good agreement with literature values, as indicated by the low relative deviations shown in **Figure 4.7** and the statistical analysis detailed in **Table 4.6**.

AAD,
$$\rho = \frac{1}{N} \sum_{i=1}^{N} \left(\frac{|\rho_{\text{exp,i}} - \rho_{\text{lit,i}}|}{\rho_{\text{exp,i}}} \right)$$
(4.24)

MAD,
$$\rho = \max\left(\frac{|\rho_{\text{exp,i}} - \rho_{\text{lit,i}}|}{\rho_{\text{exp,i}}}\right)$$
 (4.25)

$$\sigma = \sqrt{\left[\frac{1}{N}\right] \sum_{i=1}^{N} \left(\rho_{\text{exp},i} - \rho_{\text{lit},i}\right)^2}$$
(4.26)

where $\rho_{\text{exp,i}}$ is the *ith* density experimental value, $\rho_{\text{cal,i}}$ is the *ith* density literature value, and N is the total number of experimental points.

Table 4.6. Statistical parameters for density comparison.

Statistical		Literature	
parameters	Lemmon and Span [178]	Dymond et al. [179]	Ihmels and Gmehling [168]
AAD	0.02 %	0.06 %	0.05 %
MAD	0.09 %	0.09 %	0.1 %
σ	0.03 kg·m ⁻³	$0.06~\mathrm{kg}\cdot\mathrm{m}^{-3}$	$0.02~\mathrm{kg}\cdot\mathrm{m}^{-3}$

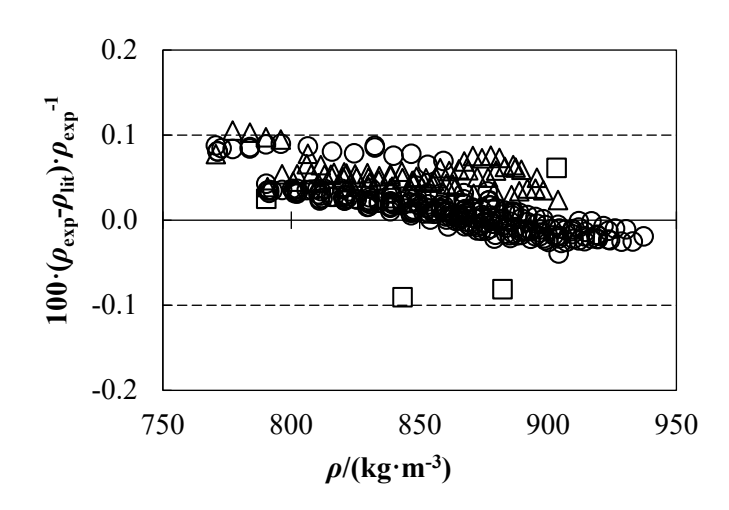


Figure 4.7. Relative deviations (%) of density measurements, ρ_{exp} , in comparison with literature values, ρ_{lit} . Literature for toluene: (\bigcirc) Lemmon and Span [178], (\square) Dymond et al. [179], and (\triangle) Ihmels and Gmehling [168]. Dashed lines represent the relative expanded uncertainty of our density measurements.

5. Flow Calorimeter

5.1. Introduction

Precise isobaric heat capacity data is essential for the successful advancement of carbon capture technologies. This data supports energy-efficient operation, enhances process control, and guides the selection of optimal materials, all crucial for effective climate change mitigation.

Flow calorimetry excels in this context by enabling continuous and accurate measurement of liquid isobaric heat capacity. By minimising heat loss and maintaining stable conditions, flow calorimeters deliver highly precise thermal property data. Furthermore, automation capabilities facilitate high-throughput analysis and minimise manual intervention. Furthermore, the isobaric heat capacity can be studied as a function of temperature and pressure.

This chapter explores the fundamental principles of flow calorimetry measurements, encompassing critical aspects such as safety considerations during design, calibration procedure, validation method, and a comprehensive analysis of associated measurement uncertainties.

5.2. Principle of Measurement

A flow calorimeter was used for the isobaric heat capacity measurements [131,181]. The operating principle of the flow calorimeter is based on a fluid circulating through a calorimetric cell at a constant flow rate. Simultaneous heating and cooling take place within the cell to maintain a fixed temperature difference (ΔT) of 0.5 K between the inlet and outlet temperatures, with an uncertainty of 0.01 K. By measuring the power supplied to the cell, the isobaric heat capacity is calculated. The calorimeter is quasi-adiabatic because the heat losses between the cell and the environment are numerically cancelled out with the experimental procedure.

Flow calorimeters use electrical resistance to heat a fluid. The resulting temperature change and power input are used to calculate the heat capacity of the fluid at constant pressure, as detailed in **Equations 5.1 and 5.2**. This method is based on the first law of thermodynamics. The theoretical basis of the isobaric heat capacity has been described previously in Section 2.2 of Chapter 2.

$$H(T_2, p) - H(T_1, p) = \frac{\dot{Q}_{net}}{\dot{m}}$$
 (5.1)

$$c_p = \left(\frac{\partial H}{\partial T}\right)_p = \lim_{T_2 \to T_1} \left\{ \frac{\dot{Q}_{net}}{\dot{m} \cdot (T_2 - T_1)} \right\}$$
 (5.2)

where H is the enthalpy, T is the temperature, p is the pressure, \dot{Q}_{net} is the net power exchange, and \dot{m} is the mass flow rate. Pressure drop effect will be considered below in 5.3.

Based on Equation 5.2 net power exchange (\dot{Q}_{net}) can be related to the isobaric heat capacity (c_p) as it is shown in Equation 5.3, over the working range of temperature and pressure.

$$c_p = \frac{\dot{Q}_{net}}{\dot{m} \cdot \Delta T} = \frac{\dot{Q}_{net}}{\dot{v} \cdot \rho \cdot \Delta T} \tag{5.3}$$

where \dot{m} is the mass flow rate that is determined using the volumetric flow rate \dot{v} set in the isocratic pump and the density ρ of the fluid at the pumping conditions (pressure and temperature). As can be seen from **Equation 5.3**, density data are a necessary input for this technique. These data were also measured using a vibrating tube densimeter Anton Paar DMA HPM described in Chapter 4 and the experimental data is reported in Chapter 7.

Isobaric heat capacity is temperature dependent. Hence, a small and fixed temperature difference (ΔT) of 0.5 K is maintained between the inlet and outlet temperatures. Net power exchange (\dot{Q}_{net}) was calculated as a linear function that correlates with the difference between the measured calorific power without flow (\dot{Q}_b) and with flow (\dot{Q}_m), as is shown in **Equation 5.4**, cancelling out the heat losses between the cell and the environment.

$$\dot{Q}_{net} = a + b \cdot (\dot{Q}_b - \dot{Q}_m) \tag{5.4}$$

where a and b are two parameters determined in a chemical calibration experiment with water as a fluid of well-known isobaric heat capacity.

Both \dot{Q}_b and \dot{Q}_m are electric powers (\dot{Q}) calculated using **Equation 5.7**, which is a result of combining Joule's Law (see **Equation 5.5**) and Ohm's Law (see **Equation 5.6**).

$$\dot{Q} = I^2 \cdot R \tag{5.5}$$

$$I = \frac{V}{R} \tag{5.6}$$

$$\dot{Q} = \frac{V^2}{R} \cdot (\% \text{ pulse}) \tag{5.7}$$

where I is the electric current, V is a constant voltage, R is the resistance and % pulse is the controlled percentage of pulse width in seconds supplied by an arbitrary waveform generator.

5.3. The Viscous Dissipation

Friction along the tube causes a pressure loss, so the process is not completely isobaric. Furthermore, viscous dissipation implies heat, which should be considered. Since the viscosities of the fluids used in this study are not high (less than 10 mPa·s) and the flow regime is laminar (Re \leq 200), the Poiseuille Law (see **Equation 5.8**) was applied to correct this effect and determine the dissipative energy loss (\dot{Q}_c). The magnitude of this correction is about 3 % in the final value of the isobaric heat capacity, which is higher than the relative uncertainty reported for the calorimeter. Therefore, the viscosity correction was considered when calculating the isobaric heat capacity.

$$\dot{Q}_c = \frac{\dot{m} \cdot \Delta p}{\rho} = \frac{\dot{m} \cdot 128 \cdot L \cdot \eta \cdot \dot{v}}{\rho \cdot \pi \cdot D^4} = \frac{128 \cdot L \cdot \eta \cdot \dot{v}^2}{\pi \cdot D^4}$$
(5.8)

where L is the tube length, which is 2.5 m; D is the tube diameter given by the supplier, which is 0.8 mm; \dot{v} is the volumetric flow rate; and η is the dynamic viscosity of the fluid at the calorimeter conditions. **Equation 5.3** can be rewritten as **Equation 5.9**, by adding the friction correction.

$$\dot{Q}_{net} = \left[a + b \cdot (\dot{Q}_b - \dot{Q}_m) \right] - \dot{Q}_c \tag{5.9}$$

As explained above, dynamic viscosity is then a necessary input to the friction correction term. The estimation of high-pressure viscosity was considered unnecessary due to the negligible error introduced by using ambient pressure viscosity. This error introduced into the isobaric heat capacity is only 0.03 % for the largest viscosity correction at the highest flow rate. This value is almost an order of magnitude smaller than the reported uncertainty.

5.4. Apparatus Description and Experimental Procedure

A double-piston Agilent HPLC 1100 series isocratic pump draws the liquid to be measured from the sample container at ambient pressure at programmable constant volumetric flow rate. This liquid is then pumped through the calorimetric cell. Under the specified temperature and pressure conditions, the density of the fluid is considered to calculate the isobaric heat capacity as a function of the volumetric flow rate, according to **Equation 5.3**. The total volume the circuit, excluding the pumps and sample container, is roughly 12 cm³. **Figure 5.1** shows a schematic diagram of the experimental set-up, and **Figure 5.2** shows a current photo of the flow calorimeter apparatus.

Before entering the calorimetric cell, the fluid passes through a 3.2 m coiled spiral tube immersed in a thermostatically controlled bath. This ensures that the fluid enters the measurement cell at a controlled temperature, regulated by the surrounding bath.

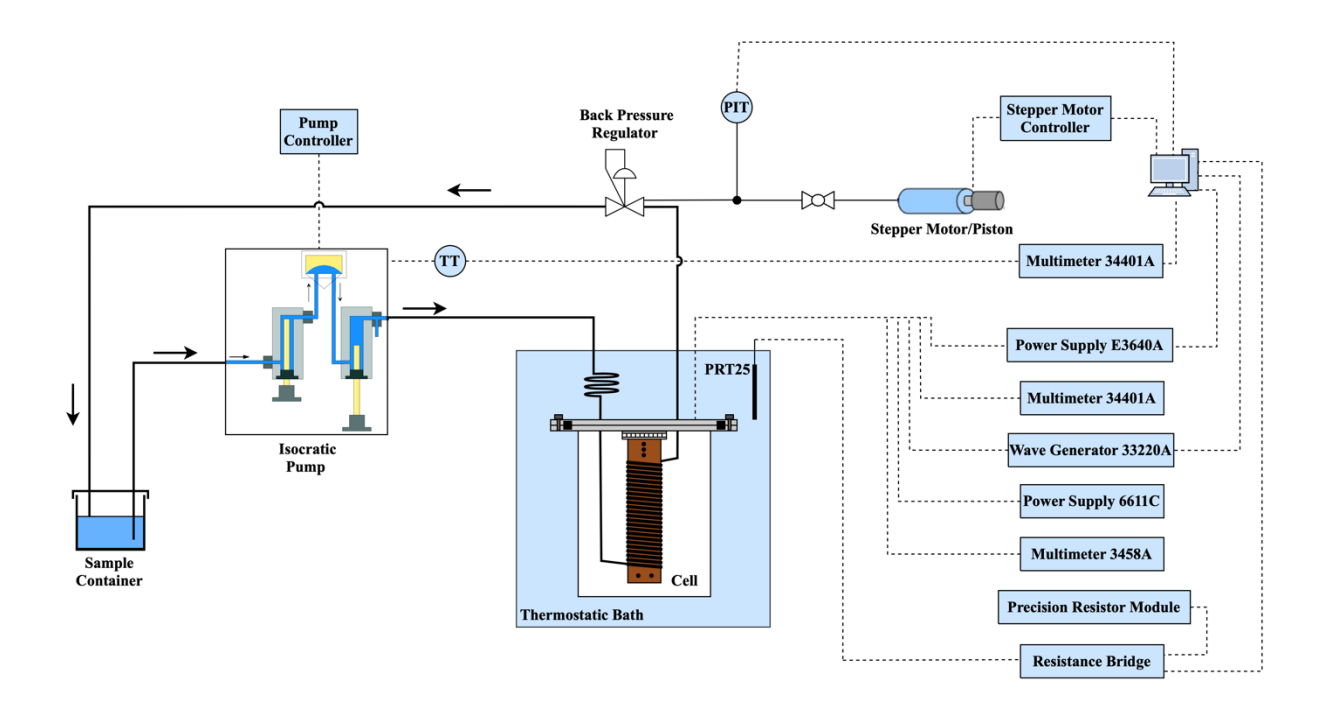


Figure 5.1. Scheme of the flow calorimeter (TermoCal laboratory). PIT: pressure indicator and transmitter Druck DPI; TT: temperature transmitter Pt100.

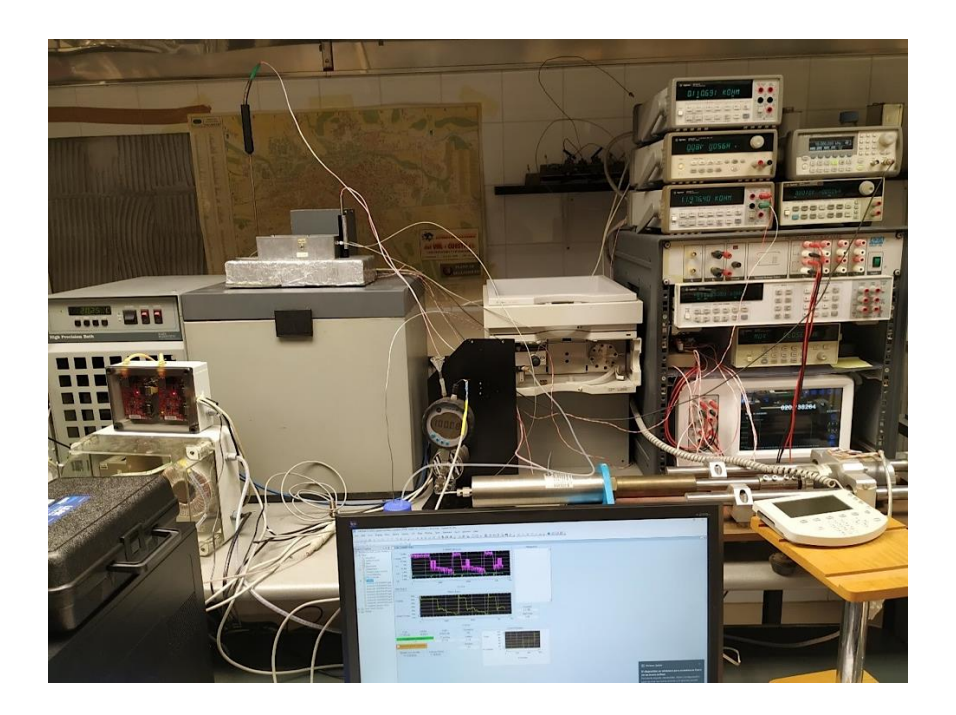


Figure 5.2. Flow calorimeter apparatus at the TermoCal UVa laboratory.

5.4.1. Calorimetric Cell

The calorimetric cell consists of a copper cylinder with a diameter of 14 mm. A thin stainless steel tube, of approximately 2.5 m long and an internal diameter of 0.8 mm, is coiled around a copper cylinder.

The copper cylinder containing the tube is silver-welded and placed in a sealed stainless-steel vessel with a lid. **Figure 5.3** shows a schematic diagram of the calorimetric cell.

As previously described in Section 5.2, the fluid temperature decreases by 0.5 K between the inlet (T_1) and the outlet (T_2) . This is achieved by controlling the T_2 temperature using a combination of cooling and heating. A thermoelectric cooler, a Peltier device, provides the cooling power, while an electrical resistance (100 Ω) delivers the heating power; both are located at the outlet (top) of the calorimetric cell. The Peltier device is powered by an Agilent E3640A power supply at constant current. On the other hand, the electrical resistance (100 Ω) is controlled by a constant frequency (10 kHz, 2 V_{pp}) provided by a variable time pulse generator Agilent 33220A, which compensates for all the energy contributions and sets the desired temperature rise.

When the fluid is flowing through the cell, the control resistance acts to maintain a steady temperature. The net power difference with and without flow is related to the change in enthalpy of the fluid and this to the isobaric heat capacity, as detailed in **Equations 5.3 and 5.4**.

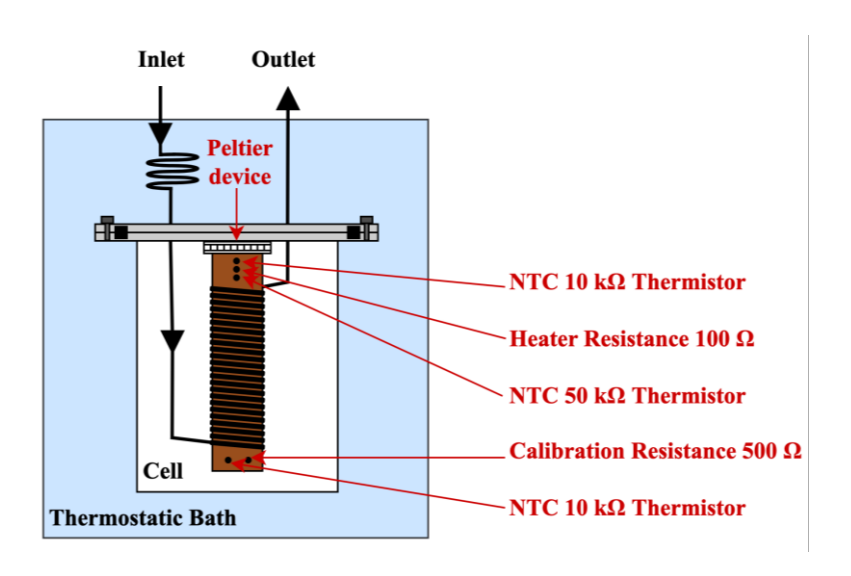


Figure 5.3. Schematic view of the calorimetric cell.

5.4.2. Temperature Control System

A thermostatic bath (Hart Scientific 7041) maintains the inlet temperature of the fluid and acts as a heat sink. The calorimetric cell is immersed in the thermostatic bath, as shown in **Figure 5.1**. Using water as the working fluid, this bath offers temperatures in the range (293.15 to 353.15) K with a stability of $\pm 10^{-3}$ K and a resolution of 10^{-3} K. The fluid inlet temperature (T_1), which is the temperature inside the bath is accurately determined using a Platinum Resistance Thermometer 25 Ω (PRT25) sensor connected to a resistance bridge (Multifunction Reference Thermometer Readout Additel 286) with a resolution of $2 \cdot 10^{-4}$ K.

A 10 k Ω control NTC thermistor, located in the upper part of the cell, measures the output temperature with a stability better than 1 mK. For this purpose, the electrical resistance of the 10 k Ω control NTC thermistor is measured using a multimeter (8½ digit 3458A).

5.4.3. Pressure Control System

The pressure of the entire fluid system is measured using a pressure indicator, Druck DPI 104 with an expanded relative uncertainty (k = 2) of 0.05 %. A Mity-Mite model S91XW back pressure regulator valve, installed in the circuit at the outlet of the measurement cell, maintains a pressure in the circuit higher than the pressure in the sample container. This pressure is established by the action of a variable volume piston HiP Model 87-6-5 controlled by a stepper motor ACP&D type 6530-24-4-0.4. The back pressure regulator valve isolates the measurement flow circuit and the hydraulic pressure control circuit. The fluid handling system includes medium-pressure fittings and tubes, as well as valves for medium-pressure filling connections.

5.4.4. Isocratic Pump

An Agilent 1100 Series precision double-piston isocratic pump was used to maintain a constant flow rate through the calorimetric cell. This pump, commonly used in HPLC chromatography applications, features a proprietary servo-controlled variable stroke drive, floating sapphire pistons and an active inlet valve. The liquid sample is fed and pumped to the high-pressure side. The pump assembly can generate pressures up to 40 MPa, , as shown in **Figure 5.4**. A damping unit is connected between the two piston chambers and a purge valve with a PTFE frit is fitted to the pump outlet for easy pump head priming. The isocratic pump offers a resolution of 10⁻³ mL·min⁻¹ at a flow rate from (0.001 to 10) mL·min⁻¹. The flow rate precision is typically 0.15 %, based on retention time, at 1 mL·min⁻¹ [182]. A four-wire Pt100 sensor connected to an Agilent 34401A multimeter is used to measure the temperature inside the pump.

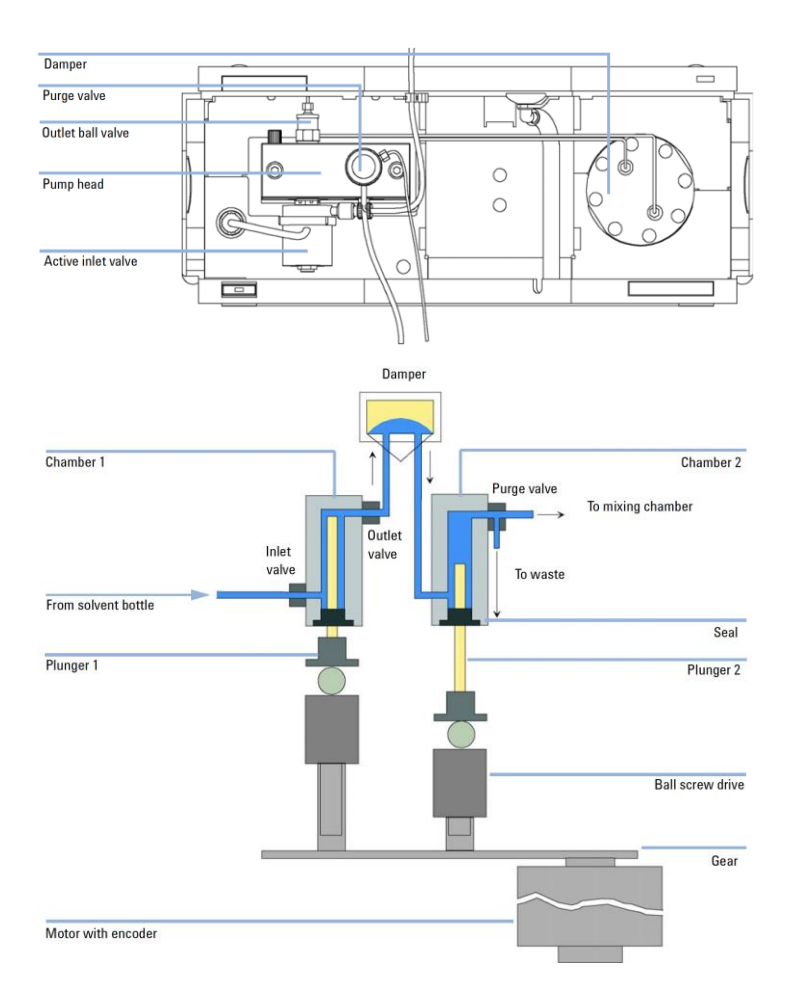


Figure 5.4. Isocratic pump main parts and the principle of operation (Source: [182]).

5.4.5. Pre-measurement Setup and Measurement Experimental Procedures

As a first step and before starting the measurement, the whole system was evacuated and cleaned with pure water. To ensure proper cleaning of the apparatus, approximately 50 cm³ of pure water was allowed to pass through the pump and the calorimetric cell as well as the entire tubing system. After this step, the flow calorimeter is ready to start the measurement.

Before each experiment, the control thermistor is calibrated by stabilising the temperature of the whole cell at the future target fluid outlet temperature (T_2), 0.5 K lower than its inlet temperature (T_1). This calibration is carried out against a PRT25 immersed in the bath, measured with the Additel resistance bridge. First, the temperature of the thermostatic bath is set 0.25 K below the desired measurement temperature; for example, at 293.15 K, the set temperature was 292.90 K, which is the output temperature T_2 of the cell. Once the temperature is stable, the stability criterion being a deviation ≤ 1 mK, the bath temperature is changed to a value of 0.25 K above the measurement temperature, i.e., following the example of the measurement at 293.15 K, this value was 293.40 K, which is the input temperature T_1 of the cell. Once this temperature value has stabilised, the experimental measurement

can proceed. In summary, the liquid sample enters the calorimetric cell at 293.40 K and is cooled to 292.90 K by the Peltier device.

As explained in Section 5.2, the heat capacity is determined by measuring the net power \dot{Q}_{net} , using **Equation 5.3**. Following **Equation 5.4**, this net power is determined by performing two experiments: the first one, an experiment without fluid flow (baseline) and the second one with fluid flow. In the baseline, the cooling power supplied by the Peltier device is set and kept constant throughout the experiment. The steady-state value of the heating power \dot{Q}_b , supplied by the control resistor and required to maintain the 0.5 K gradient is recorded and stored in Agilent VEE Pro software. After that, the second experiment start. The first of five sample flows is then set in the isocratic pump and the heating power \dot{Q}_m required to maintain the constant temperature gradient is stored.

This measurement procedure is repeated at five different volumetric flow rates, between 0.90 and 1.45 mL·min⁻¹, which is the optimum flow range for the measurement: if the flow rate is too low, the resolution is not good, and radial temperature gradients would appear due to the low velocity of the fluid; if the flow rate remains too high, the heat exchange would not take place properly. This is used to evaluate the repeatability of the measurement, as shown in **Figure 5.5**. This range was also demonstrated in [183] to be optimal for the types of fluids studied in this work.

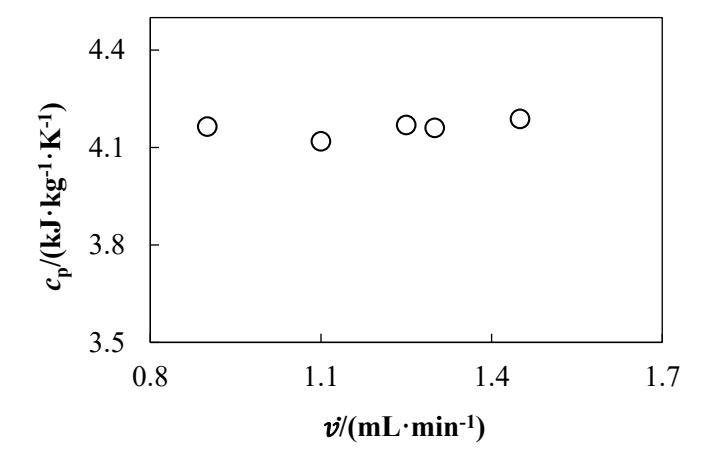


Figure 5.5. Experimental isobaric heat capacity c_p , of the 2-ethylaminoethanol (EAE) + H₂O mixture as a function of volumetric flow rate \dot{v} , at amine mass fraction of w = 0.2 and temperature T = 293.15 K.

5.5. Design Considerations for Safety

This experiment involves high pressure, high temperatures, and hazardous materials like liquid amines. To minimise risks (following the ALARP principle - As Low As Reasonably Possible) [172], a safety system was designed with both active and passive features for the flow calorimeter.

To ensure the safety of everyone involved in this experiment, a five-step process were follow:

- 1. **Identifying the Risks**: First, the interfaces between medium-pressure (MP) and low-pressure (LP) areas were examined, reviewing the equipment's operating parameters based on the Piping and Instrumentation Diagram (P&ID), as shown in **Figure 5.1**. Hazardous materials were considered based on "Control of Substances Hazardous to Health" (COSHH) report, detailed in Chapter 3 [156].
- 2. Creating a Safety Plan: Next, a detailed "Activity Risk Assessment" (ARAF) document was developed [173]. This plan outlines procedures for safe equipment handling, evacuation in case of emergencies, and proper waste management.
- 3. Implementing Safety Measures: The third step is to install safety controls, such as a back pressure valve to protect against overpressure. In addition, tubing and fittings must be suitable for medium pressures to minimise risks during operation. These aspects were already considered in the apparatus original design. The ARAF was updated.
- 4. **Keeping Records**: All crucial information, including a detailed equipment description, the measurement procedure, the ARAF document, the COSHH report, and the P&ID, are always readily available to the operator for reference.
- 5. **Regular Checks**: Finally, we regularly maintain and calibrate the safety controls to ensure they remain effective.

5.6. Calibration Procedure

5.4. Water was chosen as the calibration fluid due to its well-characterised isobaric heat capacity. These data are available in the NIST REFPROP database [180], which incorporates an empirical equation for calculating isobaric heat capacity developed by Lemmon and Span [178]. For this purpose, we measured the isobaric heat capacity of water at four temperatures: 293.15 K, 313.15 K, 333.15 K, and 353.15 K, and pressures up to 25 MPa. As demonstrated by Vega-Maza [131], parameter *a* is practically zero because heat losses are similar between flow and no-flow experiments. The value of *b* was determined for each temperature across the entire pressure range. The algorithm minimised the sum of the squares of the differences between the experimentally measured and literature values of isobaric heat capacity. **Table 5.1** summarizes the behaviour of parameter *b* at different temperatures. **Figure 5.6** shows how temperature affects the calibration curve.

Table 5.1. Temperature T dependence of the calibration parameter b.

T/K	b
293.15	2.0921
313.15	2.0925
333.15	2.1068
353.15	2.1481

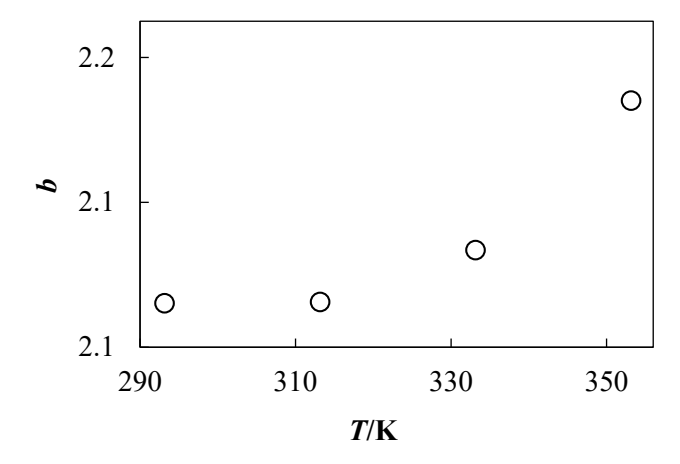


Figure 5.6. Temperature dependence of the calibration curve.

5.7. Uncertainty Budget

Uncertainty calculations for the experimental measurements were carried out according to the procedure described in the Guide to the Expression of Uncertainty in Measurement, JCGM 100:2008 [177]. Using a flow calorimeter, the relative expanded uncertainty (k=2) for the isobaric heat capacity measurements was better than 1 %, as detailed in **Table 5.2**. The full uncertainty analysis has previously been reported by [181,183]. The Law of Propagation of Uncertainty with independent variables shown in **Equations 5.10 and 5.11** has been applied to calculate the combined uncertainty from **Equation 5.3**, as detailed in **Equation 5.13**. Each independent property x_i has an associated sensitivity coefficient $C(x_i)$, calculated from **Equation 5.12**.

$$u_c^2(y) = \sum_{i=1}^N \left[\frac{\partial f}{\partial x_i} \right]^2 \cdot u^2(x_i)$$
 (5.10)

$$y = f(x_i, \dots, x_N) \tag{5.11}$$

$$C(x_{i}) = \left[\frac{\partial f}{\partial x_{i}}\right]^{2} \tag{5.12}$$

where $u_c(y)$ is the combined uncertainty of a defined property y. This combined uncertainty considers the individual standard uncertainties $u(x_i)$, associated with each of the N independent property x_i , that contribute to y, as can be seen in **Equation 5.14**.

$$U_{c}(c_{p}) = 2 \cdot \left[\left(\frac{\partial c_{p}}{\partial \dot{Q}_{net}} \right)^{2} \cdot u^{2} (\dot{Q}_{net}) + \left(\frac{\partial c_{p}}{\partial \dot{v}} \right)^{2} \cdot u^{2} (\dot{v}) + \left(\frac{\partial c_{p}}{\partial \rho} \right)^{2} \cdot u^{2} (\rho) + \left(\frac{\partial c_{p}}{\partial \Delta T} \right)^{2} \cdot u^{2} (\Delta T) \right]^{1/2}$$

$$(5.13)$$

The sensitivity coefficients $C(x_i)$ used in this calculation are given in **Equations 5.14 to 5.17**.

$$\frac{\partial c_p}{\partial \dot{Q}_{net}} = \frac{1}{\dot{v} \cdot \rho \cdot \Delta T} \tag{5.14}$$

$$\frac{\partial c_p}{\partial \dot{v}} = -\frac{\dot{Q}_{net}}{\dot{v}^2 \cdot \rho \cdot \Delta T} \tag{5.15}$$

$$\frac{\partial c_p}{\partial \rho} = -\frac{\dot{Q}_{net}}{\dot{v} \cdot \rho^2 \cdot \Delta T} \tag{5.16}$$

$$\frac{\partial c_p}{\partial \Delta T} = -\frac{\dot{Q}_{net}}{\dot{v} \cdot \rho \cdot (\Delta T)^2} \tag{5.17}$$

Table 5.2. Uncertainty budget for the isobaric heat capacity in the temperature range (293.15 to 353.15) K and pressure range (0.1 to 25) MPa.

Source of	Uncertainty (x_i)	Units	Estimate uncertainty	Divisor	$u(x_i)$	$C(x_i)$	$u(c_p)$
$u(c_p)$	Repeatability	kJ·kg ⁻¹ ·K ⁻¹	1.10-2	1	1.10-2	1	1.10-2
Resolution		4.10-6	$2\sqrt{3}$	1.10-6			
$u(\dot{Q}_{net})$	Repeatability	W	4.10-6	1	4.10-6	99	1.10-2
-	Non-linearity	-	1.10-4	1	1.10-4		
u(v) _	Precision	_ mL·s ⁻¹	3·10 ⁻⁵	1	3.10-5	78	2·10-3
	Resolution	- IIIL'S	2.10-5	$2\sqrt{3}$	5·10-6	78	2.10

$u_{\rm c}(ho)$	Densimeter	kg·m ⁻³	7.10-4	2	4.10-4	2	5·10-4
	Resolution		1.10-3	$2\sqrt{3}$	3.10-4		
$u_{\rm c}(\Delta T)$	Inlet Stability	K	1.10-3	$\sqrt{3}$	6.10-4	3	3.10-3
	Outlet Stability		1.10-3	$\sqrt{3}$	6.10-4		
$u_{\rm c}(c_{\rm p})$	<i>k</i> = 1	kJ·kg ⁻¹ ·K ⁻¹					2·10-2
$U_{\rm c}(c_{ m p})$	k = 2	kJ·kg ⁻¹ ·K ⁻¹					3·10-2
$U_{\rm r}(c_{ m p})$	k = 2	%		($c_p = 4.19 \text{ kJ} \cdot \text{kg}^{-1} \cdot \text{K}^{-1}$		1

Table 5.2 details the contributions to the uncertainty budget, noting that the main contributions are the non-linearity of the net power and the repeatability of the isobaric heat capacity. The influence of CO_2 load in the aqueous amine solution on the uncertainty of isobaric heat capacity has been studied and found to be negligible. Table 5.2 did not include them since this contribution to the final value of the combined uncertainty in the isobaric heat capacity is one order of magnitude smaller than other contributions such as the non-linearity of \dot{Q}_{net} .

5.8. Experimental Validation

Experimental validation of the flow calorimeter was carried out by experimentally measuring the heat capacity of toluene. This fluid is well-characterised in the literature, and Lemmon and Span [178] have developed an empirical correlation integrated into the NIST REFPROP database [180]. The empirical correlation allows the calculation of the isobaric heat capacity over a wide range of temperatures and pressures with a standard uncertainty of 0.5 %. The isobaric heat capacity of toluene was measured at three different temperatures: 293.15 K, 313.15 K, and 333.15 K, pressures up to 25 MPa and at five different volumetric flow rates from (3.0 to 3.5) mL·min⁻¹. The flows have been modified to adapt the measurement to isobaric capacities lower than those of aqueous amine solutions. This range was chosen based on the study carried out by Vega-Maza [131].

As detailed in **Table 5.3** and **Figure 5.7**, a maximum relative deviation of 0.9 % between the experimental isobaric heat capacity values and the reported values by Lemmon and Span [178] was observed, which is in good agreement with the associated uncertainties.

Table 5.3. Experimental isobaric heat capacity $c_p/(kJ\cdot kg^{-1}\cdot K^{-1})$, for toluene at different conditions of temperature T, and pressure p.

<i>T</i> /K	p/MPa	$c_{\rm p,exp}/({\rm kJ\cdot kg^{-1}\cdot K^{-1}})$	$c_{\text{p,lit}}/(\text{kJ}\cdot\text{kg}^{-1}\cdot\text{K}^{-1})$ [178]	RD%ª
	0.1	1.70	1.69	0.81
	5	1.69	1.68	0.53
293.15	10	1.69	1.68	0.76
293.13	15	1.68	1.67	0.38
	20	1.68	1.67	0.42
	25	1.67	1.67	0.37
	0.1	1.74	1.75	-0.64
	5	1.74	1.74	-0.41
212 15	10	1.73	1.74	-0.55
313.15	15	1.73	1.74	-0.30
	20	1.72	1.73	-0.61
	25	1.71	1.73	-0.90
	0.1	1.83	1.82	0.64
	5	1.81	1.81	-0.12
222 15	10	1.80	1.81	-0.28
333.15	15	1.79	1.80	-0.59
	20	1.78	1.79	-0.87
	25	1.78	1.79	-0.88

^aRD%: relative deviation in %.

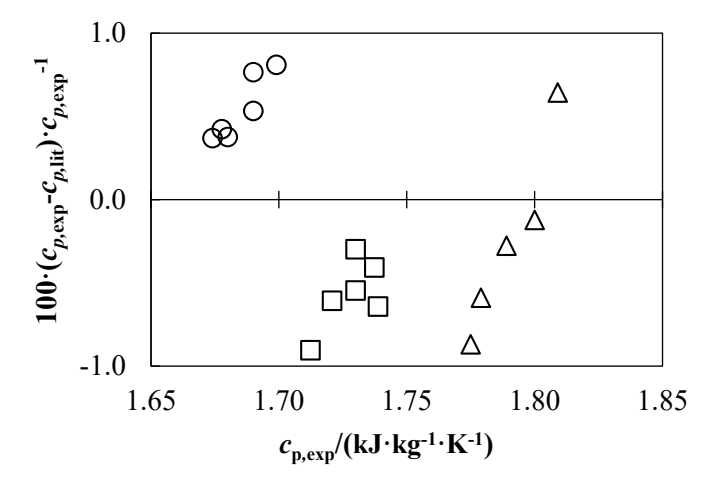
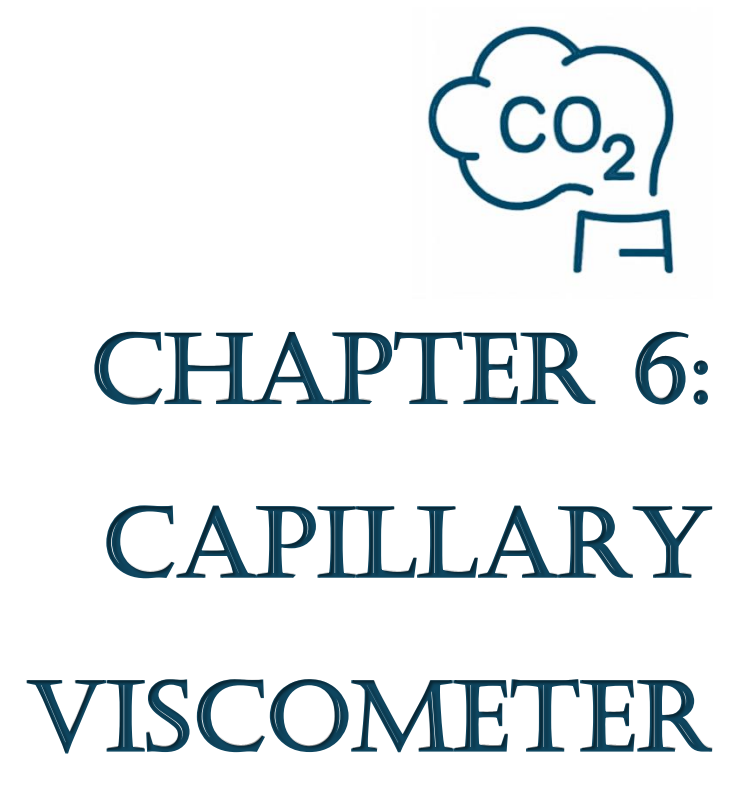


Figure 5.7. Relative deviations (%) between experimental isobaric heat capacity $c_{\rm p,exp}$, and literature isobaric heat capacity $c_{\rm p,lit}$, from Lemmon and Span [178]. Symbols: (\bigcirc) T = 293.15 K, (\square) T = 313.15 K, and (\triangle) T = 333.15 K.



6. Capillary Viscometer

6.1. Introduction

Accurate viscosity data is essential for optimising amine-based CO₂ capture processes, as it directly affects pumping, mass transfer, and contactor design. Unfortunately, a critical research gap exists; there is a shortage of precise experimental viscosity measurements for CO₂-loaded aqueous amine solutions, particularly those with two amines in the mixture. In this sense, this thesis tries to cover this gap providing experimental viscosity data of CO₂-loaded solutions, including amine blends solutions.

Viscosity measurements were conducted using an Ubbelohde capillary viscometer at Imperial College London's Thermophysics Laboratory, operating between 293.15 K and 353.15 K at atmospheric pressure. Following modifications, the expanded relative uncertainty was reduced to 1 % (95.5 % confidence level). To determine dynamic viscosity, density was required. For quaternary systems lacking prior experimental density data from the Anton Paar DMA HPM vibrating tube densimeter at the University of Valladolid, an Anton Paar DMA 445 densimeter tube densimeter (Anton Paar SVM 3001) was employed. Detailed descriptions of both apparatuses are provided in this chapter.

6.2. Apparatus Description

Kinematic viscosity v was measured using two certified glass U-tube SI Analytics Ubbelohde capillary viscometers: the 532 01/0a type for samples in the range of (0.8 to 5) mm²·s⁻¹, and the 532 13/1c type for samples in the range of (3 to 30) mm²·s⁻¹. A schematic view of the glass capillary viscometer can be seen in **Figure 6.1** and a photo is shown in **Figure 6.2**. This apparatus was calibrated with degassed deionized water and a viscosity standard oil from Paragon Scientific. The capillary viscometer was immersed in a silicon oil bath thermostat (Julabo 18 V) equipped with a Huber (CC-K6) chiller. The temperature was controlled within ± 0.01 K using a Julabo ME controller. For measuring the temperature, a calibrated secondary-standard platinum resistance thermometer (Fluke model 5615) with a resolution of 0.001 K was used with a digital readout (Fluke 1502A).

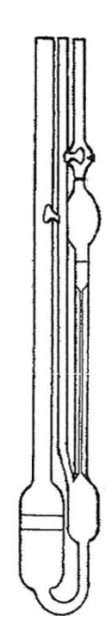


Figure 6.1. Schematic view of the glass capillary viscometer. Source: [150].

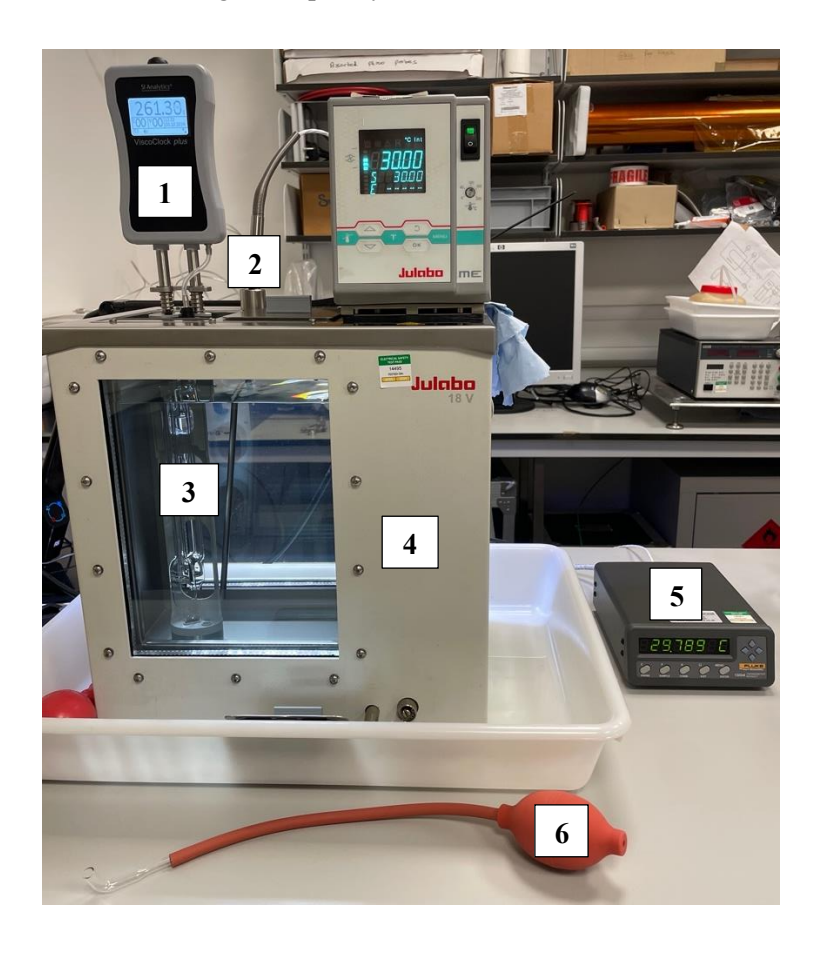


Figure 6.2. Photo of the Ubbelohde Capillary Viscometer apparatus. 1: electronic timing device ViscoClock Plus, 2: secondary-standard platinum resistance thermometer (Fluke model 5615), 3: capillary viscometer, 4: silicon oil bath thermostat (Julabo 18 V), 5: digital readout (Fluke 1502A), and 6: hand pump.

An electronic timing device, ViscoClock Plus, was used to monitor the liquid flow time in the capillary viscometers. The ViscoClock Plus, designed for SI Analytics, employs infrared light barriers to automatically determine the flow time. After thermostating, the sample is pushed into the measurement bulb using a hand pump, and the flow time is recorded automatically. The device can measure times up to 999.99 seconds with a resolution of 0.01 seconds [184].

The dynamic viscosity was calculated using **Equation 6.3**, **derived** from **Equations 6.1** and **6.2**. The liquid flow time in the capillary viscometer was measured using the electronic timing device ViscoClock Plus, as described before.

$$v = K \cdot t \tag{6.1}$$

$$\eta = \nu \cdot \rho \tag{6.2}$$

$$\eta = K \cdot t \cdot \rho \tag{6.3}$$

where, v is the kinematic viscosity in mm²·s⁻¹, K is the instrument constant provided by the capillary viscometer manufacturer (SI Analytics) in mm²·s⁻², t is the liquid flow time in seconds (s), η is the dynamic viscosity in mPa·s, and ρ is the density of the fluid in g·cm⁻³ at the same conditions of temperature and pressure.

6.3. Viscosity Uncertainty Budget

Viscosity measurements were carried out at atmospheric pressure and temperatures between (293.15 and 353.15) K. The combined expanded relative uncertainty (k = 2) of the viscosity measurements on CO₂-loaded solutions was 1 %. **Table 6.1** provides details associated with each contribution in the viscosity uncertainty for MDEA solution at 293.15 K and CO₂ loading 0.8 mol-CO₂/mol-MDEA. As can be observed, the main individual contribution is the uncertainty related to the flow time. This aspect was previously improved by using the ViscoClock Plus electronic timing device instead of the manual stopwatch, allowing an improvement of the liquid flow time repeatability. This modification has allowed us to reduce this value, resulting in an uncertainty lower than that typically described in the literature.

The Law of Propagation of Uncertainty with independent variables (see **Equations 6.4 and 6.5**) was used to calculate the dynamic viscosity combined uncertainty. Each independent property x_i has an associated sensitivity coefficient $C(x_i)$, calculated using **Equation 6.6**.

$$u_c^2(y) = \sum_{i=1}^N \left[\frac{\partial f}{\partial x_i} \right]^2 \cdot u^2(x_i)$$
 (6.4)

$$y = f(x_i, \dots, x_N) \tag{6.5}$$

$$C(x_{i}) = \left[\frac{\partial f}{\partial x_{i}}\right]^{2} \tag{6.6}$$

where $u_c(y)$ is the combined uncertainty of a defined property y. This combined uncertainty considers the individual standard uncertainties $u(x_i)$, associated with each of the N independent property x_i , that contributes to y, as can be seen in **Equation 6.12**.

The expanded combined uncertainty (95.5 % confidence level) of the dynamic viscosity was calculated using **Equation 6.7** according to its definition in **Equation 6.3** and the law of propagating errors in **Equation 6.4**. The sensitivity coefficients $C(x_i)$ used in this calculation are shown in **Equations 6.8 to 6.10**.

$$U_c(\eta) = 2 \cdot \left[\left(\frac{\partial \eta}{\partial K} \right)^2 \cdot u^2(K) + \left(\frac{\partial \eta}{\partial t} \right)^2 \cdot u^2(t) + \left(\frac{\partial \eta}{\partial \rho} \right)^2 \cdot u^2(\rho) \right]^{1/2}$$
(6.7)

$$C(K) = \frac{\partial \eta}{\partial K} = t \cdot \rho \tag{6.8}$$

$$C(t) = \frac{\partial \eta}{\partial t} = K \cdot \rho \tag{6.9}$$

$$C(\rho) = \frac{\partial \eta}{\partial \rho} = K \cdot t \tag{6.10}$$

Table 6.1. Uncertainty budget for the dynamic viscosity η , measurement in the range of temperature from (293.15 to 353.15) K, and atmospheric pressure.

Source	of Uncertainty (x _i)	Units	Estimate uncertainty	Divisor	$u(x_i)$	$C(x_i)$	$u(\eta)$
$u(\eta_{ref})$	Reference material	mPa·s	3·10 ⁻³	$\sqrt{3}$	2·10 ⁻³	1	2·10 ⁻³
u(T)	Resolution	. K	1.10-3	$2\sqrt{3}$	1.10-3	-5·10 ⁻²	-5·10 ⁻⁵
	Repeatability		1.10-3	1	- 110		
<i>u</i> (<i>t</i>)	Resolution	500	1.10-2	$2\sqrt{3}$	1	5·10 ⁻³	5·10-3
	Repeatability	sec	1	1	- 1	3.10	3.10

()	Resolution	lra-	1.10-6	$2\sqrt{3}$	_ 3·10 ⁻⁵	1	3·10 ⁻⁵
u(m) Impurity	_ kg _	1.10-4	$2\sqrt{3}$	_ 3.10	1	3.10	
u(K)	Calibration	mm ² ·s ⁻²	2·10 ⁻⁵	1	2·10-5	$8 \cdot 10^2$	1.10-2
$u(\alpha)$	CO ₂ loading	mol- CO ₂ /mol- amine	2·10-3	1	2·10-3	7·10-1	2·10-3
$u(\rho)^{\mathrm{a}}$		kg/m³	1.10-3	1	1.10-3	4	4.10-3
$u_{\rm c}(\eta)$	<i>k</i> = 1	mPa·s					1.10-2
$U_{\rm c}(\eta)$	<i>k</i> = 2	mPa·s					3·10-2
$U_{ m r}(\eta)$	<i>k</i> = 2	%			$\eta = 2.89$	mPa∙s	1

^aDensity measurements were carried out using a vibrating tube densimeter.

6.4. Experimental Validation

The viscosity measurements validation was carried out using two viscosity standard oils from Paragon Scientific. The viscosity standard oil used in the calibration of 532 01/0a type glass capillary viscometer was S3 for the range of kinematic viscosity (0.8 to 5) mm²·s⁻¹. For 532 13/1c type glass capillary viscometer, the viscosity standard oil N7.5 for the range of kinematic viscosity (3 to 30) mm²·s⁻¹ was used. **Table 6.2** contains the results of the flow time *t* in seconds *s* and the kinematic viscosity *v*. The relative deviations were calculated between the experimental kinematic viscosity values and the reported values by Paragon Scientific. As can be seen in **Table 6.2** and **Figure 6.3**, all relative deviations are within the reported uncertainty for viscosity measurements. The positive relative deviations observed are attributed to a minor difference in temperature. Specifically, the temperature reported for the standard calibration oils was up to 0.06 % higher than the actual temperature during viscosity measurements, as detailed in **Table 6.2**.

Table 6.2. Experimental kinematic viscosity v, and flow time t, of the standard calibration oils S3 and N7.5 at different temperatures T.

<i>T</i> /K	t/s	v/(mm ² ·s ⁻¹)	RD%ª			
I/K	S3 standard calibration oil					
292.96	918.96	4.58	0.7			
313.08	582.61	2.90	0.3			
323.08	482.07	2.40	0.2			

353.14	304.61	1.52	0.4					
	N7.5 standard calibration oil							
292.96	409.35	12.51	0.6					
297.94	346.48	10.59	0.6					
313.07	222.36	6.80	0.1					

^aRD%: relative deviation in %.

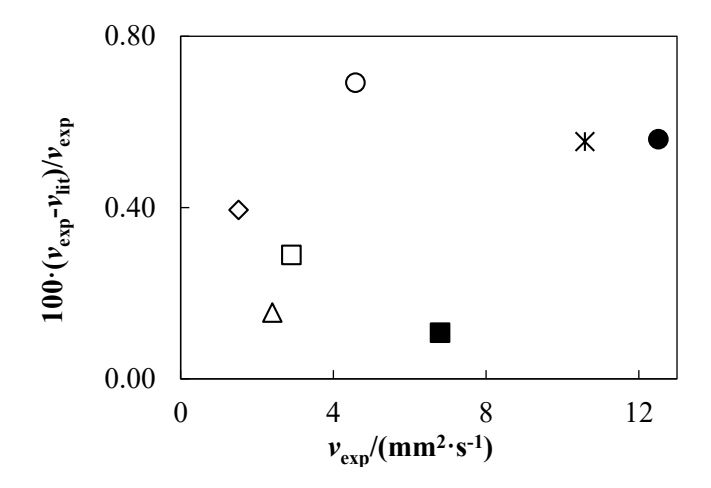


Figure 6.3. Relative deviations (%) of the experimental kinematic viscosity $v_{\rm exp}$, in comparison with reported values by Paragon Scientific $v_{\rm lit}$. Symbols for S3 standard calibration oil: (\bigcirc) T = 292.96 K, (\square) T = 313.08 K, (\triangle) T = 323.08 K, and (\diamondsuit) T = 353.14 K. Symbols for N7.5 standard calibration oil: (\blacksquare) T = 292.96 K, (*) T = 297.94 K, and (\blacksquare) T = 313.07 K.

6.5. Automatic Kinematic Viscometer Anton Paar SVM 3001

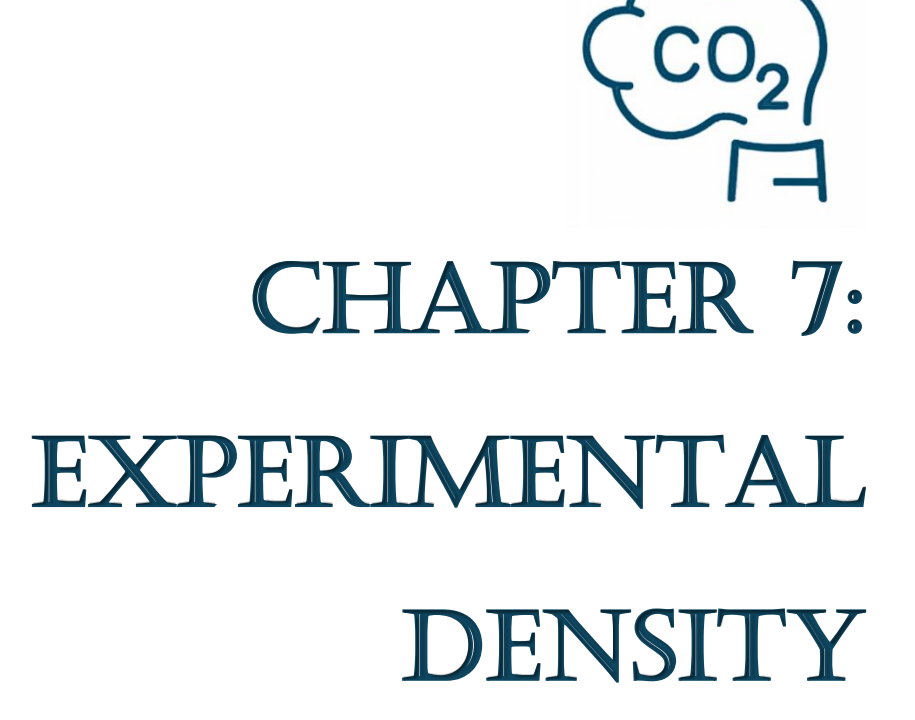
An DMA 445 vibrating tube densimeter, integrated into an automatic kinematic viscometer Anton Paar SVM 3001, was used for mixtures where experimental density data was measured using the Anton Paar DMA HPM vibrating tube densimeter. The SVM 3001 apparatus measures density in the range of (0 to 3000) kg·m⁻³. The repeatability for density was 0.5 kg·m⁻³, meanwhile the reproducibility was better than 1.1 kg·m⁻³. Temperature was measured with a repeatability of 0.005 °C and a resolution of 0.001 °C [185]. A photo of the equipment is shown in **Figure 6.4**.

The DMA 445 vibrating tube densimeter was calibrated with degassed ultrapure water and ambient air. As the SVM 3001 simultaneously measures density and kinematic viscosity, density values were monitored during the kinematic viscosity calibration. This monitoring revealed an average density deviation of 0.2 kg·m⁻³. The viscosity calibration process was carried out using five different viscosity standard oils from Paragon Scientific and 21 calibration points across the temperature working range.

Temperature was measured with an expanded uncertainty of 0.02 K at a 95.5 % confidence level. The expanded uncertainty (k = 2) for density measurements of CO₂-unloaded solutions was determined to be $0.3 \text{ kg} \cdot \text{m}^{-3}$. For CO₂-loaded amine solutions, the overall expanded uncertainty (k = 2) of density was estimated to be $0.6 \text{ kg} \cdot \text{m}^{-3}$, highlighting the significant contribution of CO₂ loading to the combined uncertainty. If the SVM 3001 indicated the presence of bubbles inside the vibrating tube, the measurement sequence was stopped. This occurrence was noted specifically at high temperatures and CO₂ loadings.



Figure 6.4. Photo of the automatic kinematic viscometer Anton Paar SVM 3001.



7. Experimental Density

7.1. Introduction

Experimental density of CO₂-loaded and CO₂-unloaded aqueous amine solutions is interesting for the amine-based CO₂ capture process, allowing the design of new equipment and the optimisation of existing ones, contributing to the improvement of models that allow the simulation of this process and to complete the thermodynamic characterisation of the mixtures involved.

In this work the following chemical samples were used: monoethanolamine (MEA), diethanolamine (DEA), 2-(ethylamino)ethanol (EAE), methyldiethanolamine (MDEA), 2-(dimethylamino)ethanol (DMEA), 2-diethylaminoethanol (DEAE), 2-amino-2-methyl-1-propanol (AMP), 3-(methylamino)propylamine (MAPA), 1-methylpiperazine (1-MPZ), piperazine (PZ), water (H₂O) and carbon dioxide (CO₂).

Density measurements were achieved on:

- Five binary systems: DEAE + H₂O, EAE + H₂O, MAPA + H₂O, 1-MPZ + H₂O and AMP + H₂O.
- Four ternary systems: $MEA + H_2O + CO_2$, $MDEA + H_2O + CO_2$, $AMP + H_2O + CO_2$ and $DEA + H_2O + CO_2$.
- One quaternary system: $DMEA + MAPA + H_2O + CO_2$.

The measurement range covered 16 different pressures between (0.1 and 100) MPa and six temperatures between (293.15 and 393.15) K. For binary systems, four amine mass fractions were measured from 0.1 to 0.4. Ternary systems were measured only at total amine mass fraction (CO₂-free basis) of 0.3 and the quaternary system at 0.4 total amine mass fraction. The behaviour of systems containing CO₂ has been studied at different CO₂ concentrations, with maximum values from (0.5 to 0.9) mol-CO₂/mol-amine, according with the type of system.

Aqueous solutions are not liquid at temperatures above or equal to 373.15 K at atmospheric pressure, so experimental data were obtained at pressures above 1 MPa when the temperature reached values of 373.15 K and 393.15 K. A vibrating tube densimeter Anton Paar DMA HPM was used to measure the density, explained in detail in Chapter 4. The relative expanded combined uncertainty (k = 2) in density measurements was less than 0.1 % for the CO₂-unloaded solutions and 0.2 % for the CO₂-loaded solutions.

A modified version of the Tammann-Tait equation, which includes molality dependence, has been shown to be suitable for correlating experimental density data as a function of pressure, temperature

and molality. The suitability of molality units for accurately deriving empirical density correlations in various aqueous amine solutions has been demonstrated instead of mass or molar fractions. The modified Tammann-Tait equation, originally proposed by Al Ghafri et al. [186,187] for brine densities, has also been shown to be effective in correlating the densities of binary amine + H₂O systems. This correlation achieved good average absolute relative deviations (AAD \leq 0.03 %) compared to experimental density. Furthermore, this equation can be successfully fitted to density data for ternary mixtures (amine + H₂O + CO₂), achieving average absolute relative deviations lower than 0.02 % compared to experimental density.

A literature search was carried out to compare our experimental density data with data reported in the literature. All density data found for binary systems in the literature were measured at temperatures equal to or lower than 353.15 K and atmospheric pressure, except for Zúñiga-Moreno et al. [94] which measures up to 20 MPa. The comparison with the scarce references available in the literature was mostly within the expanded relative uncertainty of the density.

Also, a comparison was made between the experimental density data from our study and previously published data available in literature for CO_2 -loaded aqueous amine solutions. The range of CO_2 loading α , of the compared data has gone from (0.1 to 0.4) mol- CO_2 /mol-amine. To the best of our knowledge, at temperatures (T > 353.15 K), pressures (p > 0.1 MPa), and CO_2 loading ($\alpha > 0.5$ mol- CO_2 /mol-amine), there are no density experimental data reported in literature for the studied systems when amine mass percent is 30 % in CO_2 -free aqueous amine solution. Therefore, a comparison of density under these conditions was not possible.

Several systems and compositions are used in this work, so in order to achieve greater clarity, the components of the studied mixtures have been numbered as follows: amine(1), $H_2O(2)$ and $CO_2(3)$.

7.2. Binary Mixtures. CO₂-Unloaded Aqueous Amine Solutions

 $7.2.1.DEAE + H_2O$

7.2.1.1. Experimental Density

The results of the density measurements for the aqueous amine solutions are presented in **Table 7.1** for DEAE + H₂O. In order to analyze the influence of pressure, amine mass fraction, and temperature, the experimental density data were plotted as a function of these variables for all the systems analyzed, as can be seen in **Figures 7.1 to 7.3**.

Table 7.1. Experimental densities ρ , for DEAE(1) + H₂O(2) mixture at different conditions of temperature T, pressure p, amine mass fraction w_1 , and equivalent amine molality b_1 .

$\rho/(\mathrm{kg}\cdot\mathrm{m}^{-3})$										
	T/K									
p/MPa	293.15	313.15	333.15	353.15	373.15	393.15				
	$w_1 = 0.1000 \ (b_1 = 0.9485 \ \text{mol} \cdot \text{kg}^{-1})$									
0.1	995.2	987.9	977.4	964.9						
0.5	995.3	988.1	977.6	965.1						
1	995.5	988.2	977.8	965.3	950.7	934.4				
2	995.8	988.6	978.3	965.7	951.2	935.0				
5	997.1	989.9	979.6	967.1	952.7	936.6				
10	999.1	991.9	981.7	969.3	954.9	939.1				
15	1001.2	993.9	983.7	971.4	957.3	941.6				
20	1003.2	995.9	985.7	973.6	959.5	944.1				
30	1007.1	999.8	989.7	977.7	964.0	948.8				
40	1010.9	1003.6	993.7	981.8	968.3	953.4				
50	1014.7	1007.4	997.5	985.8	972.5	957.9				
60	1018.4	1011.0	1001.2	989.6	976.5	962.3				
70	1022.1	1014.7	1004.9	993.5	980.5	966.5				
80	1025.7	1018.2	1008.5	997.2	984.5	970.6				
90	1029.3	1021.7	1012.1	1000.9	988.2	974.6				
100	1032.8	1025.2	1015.6	1004.4	992.0	978.5				
	$w_1 = 0.20$	$000 (b_1 = 2)$.1333 mo	l·kg ⁻¹)						
0.1	993.1	983.2	970.7	956.4						
0.5	993.2	983.4	970.9	956.6						
1	993.4	983.5	971.1	956.8	940.8	923.2				
2	993.7	983.9	971.5	957.3	941.3	923.8				
5	994.9	985.2	972.9	958.7	942.8	925.5				
10	996.8	987.1	975.0	961.0	945.3	928.2				
15	998.7	989.1	977.1	963.2	947.7	930.9				
20	1000.6	991.1	979.1	965.4	950.1	933.5				
30	1004.2	994.9	983.1	969.7	954.7	938.5				
40	1007.8	998.6	987.1	973.8	959.2	943.3				
50	1011.4	1002.2	990.9	977.9	963.5	948.0				
60	1014.9	1005.8	994.6	981.8	967.7	952.6				

70	1018.3	1009.3	998.2	985.7	971.7	956.9
80	1021.6	1012.7	1001.8	989.4	975.7	961.1
90	1024.9	1016.1	1005.3	993.1	979.6	965.3
100	1028.2	1019.4	1008.7	996.6	983.3	969.3
	$w_1 = 0.30$	$000 (b_1 = 3)$.6571 mol	l·kg ⁻¹)		
0.1	989.5	976.8	962.2	946.4		
0.5	989.6	976.9	962.4	946.6		
1	989.7	977.1	962.6	946.8	929.2	910.4
2	990.1	977.5	963.1	947.3	929.7	911.0
5	991.3	978.8	964.5	948.8	931.4	912.9
10	993.2	980.8	966.7	951.2	934.0	915.9
15	995.1	982.8	968.9	953.6	936.7	918.8
20	997.0	984.8	971.0	955.9	939.2	921.6
30	1000.6	988.7	975.2	960.3	944.2	927.0
40	1004.1	992.4	979.2	964.8	948.9	932.2
50	1007.6	996.1	983.1	969.0	953.4	937.1
60	1011.0	999.7	986.9	973.0	957.8	941.9
70	1014.4	1003.2	990.6	977.0	962.0	946.5
80	1017.7	1006.6	994.2	980.8	966.2	951.0
90	1020.9	1010.0	997.7	984.5	970.2	955.2
100	1024.0	1013.2	1001.2	988.1	974.1	959.4
	$w_1 = 0.40$	$000 (b_1 = 5)$.6890 mol	l·kg ⁻¹)		
0.1	983.1	968.5	952.3	934.9		
0.5	983.2	968.6	952.5	935.1		
1	983.4	968.8	952.8	935.4	916.7	896.8
2	983.8	969.2	953.2	935.9	917.3	897.5
5	985.0	970.6	954.7	937.5	919.1	899.6
10	987.0	972.7	957.1	940.1	921.9	902.8
15	988.9	974.7	959.4	942.7	924.8	906.0
20	990.9	976.9	961.6	945.2	927.6	909.0
30	994.6	980.9	966.0	949.9	932.8	914.9
40	998.3	984.7	970.2	954.5	937.8	920.5
50	1001.8	988.5	974.3	958.9	942.6	925.7
60	1005.3	992.2	978.2	963.2	947.2	930.7
70	1008.6	995.8	982.0	967.3	951.6	935.5
80	1012.0	999.2	985.7	971.2	956.0	940.2

90	1015.1	1002.6	989.3	975.1	960.1	944.6
100	1018.3	1006.0	992.8	978.8	964.1	949.0

^aExpanded uncertainties (k = 2): U(T) = 0.02 K; $U_r(p) = 0.0002$; $U_r(w) = 0.0004$ and $U(\rho) = 0.7$ kg·m⁻³.

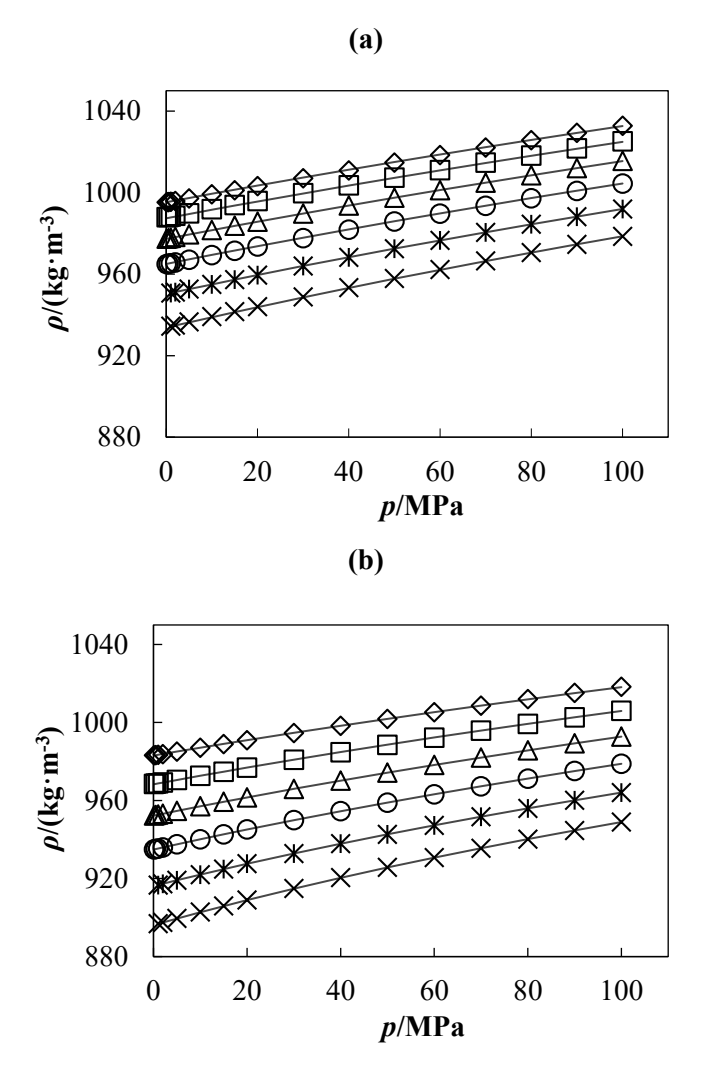


Figure 7.1. Experimental density ρ , of the system DEAE(1) + H₂O(2) as a function of pressure p, at amine mass fraction of (a) $w_1 = 0.1$ and (b) $w_1 = 0.4$. Isotherms: (\diamondsuit) T = 293.15 K, (\square) T = 313.15 K, (\triangle) T = 333.15 K, (\bigcirc) T = 353.15 K, (\ast) T = 373.15 K, and (\times) T = 393.15 K. Solid lines represent the calculated values using modified Tammann-Tait (**Equations 7.1 to 7.4**) with the parameters given in **Tables 7.11 and 7.12**.

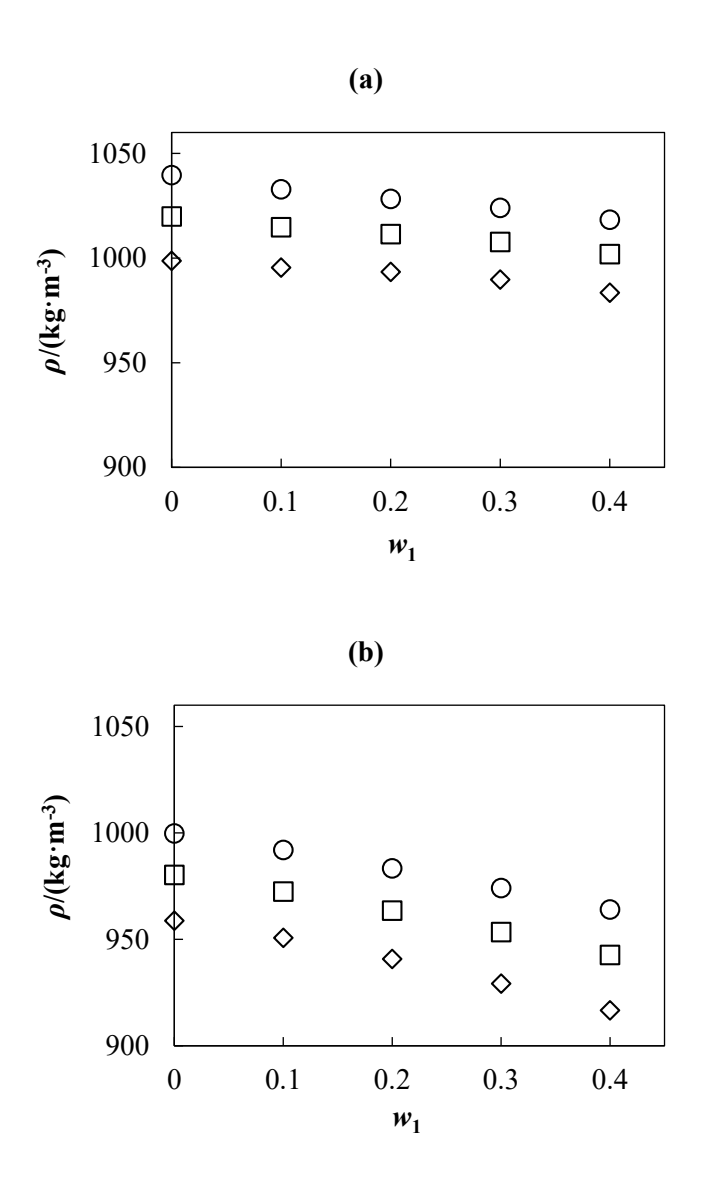


Figure 7.2. Experimental density ρ , of the system DEAE(1) + H₂O(2) as a function of amine mass fraction w_1 , at temperatures of (a) T = 293.15 K and (b) T = 373.15 K. Isobars: (\diamondsuit) p = 1 MPa, (\square) p = 50 MPa, and (\bigcirc) p = 100 MPa. Experimental data of pure water ($w_1 = 0$) from NIST REFPROP database [180].

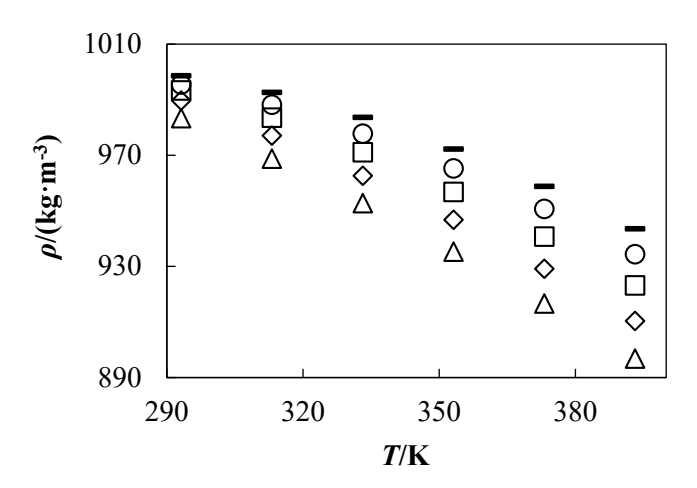


Figure 7.3. Experimental density ρ , of the system DEAE(1) + H₂O(2) as a function of temperature T, at pressure p = 1 MPa. Amine mass fractions: (—) $w_1 = 0$, (\bigcirc) $w_1 = 0.1$, (\square) $w_1 = 0.2$, (\diamondsuit) $w_1 = 0.3$, and (\triangle) $w_1 = 0.4$. Experimental data of pure water ($w_1 = 0$) from NIST REFPROP database [180].

7.2.1.2. Comparison with Literature

The experimental conditions of the references used for the comparison of DEAE aqueous solutions are shown in **Table 7.2**. The relative deviations of our measurements and the experimental density values reported in the literature are plotted in **Figure 7.4**. Karunarathne et al. [62] reports eight common data points for comparison, with relative deviation within the uncertainty of our measurements. Lebrette et al. [60] published twelve common data points and all of them are consistent with our uncertainty.

Table 7.2. Measurement conditions of literature data used to compare the experimental density of DEAE(1) + $H_2O(2)$ mixture measured in this work.

Reference	Densimeter	Conditions	Number of Points	$U_{ m r}^{ m a}$
Karunarathne et al. [62]	Anton Paar DMA 4500	$w_1 = 0.30; 0.40$ T = (293.15 - 353.15) K p = 0.1 MPa	8	1 %
Lebrette et al. [60]	Anton Paar DMA 45	$w_1 = 0.1006; 0.2009;$ 0.2941; 0.3941 T = (313.15 - 353.15) K p = 0.1 MPa	12	NA ^b

^aRelative expanded uncertainty (k = 2), %.

^bNA: Not Available.

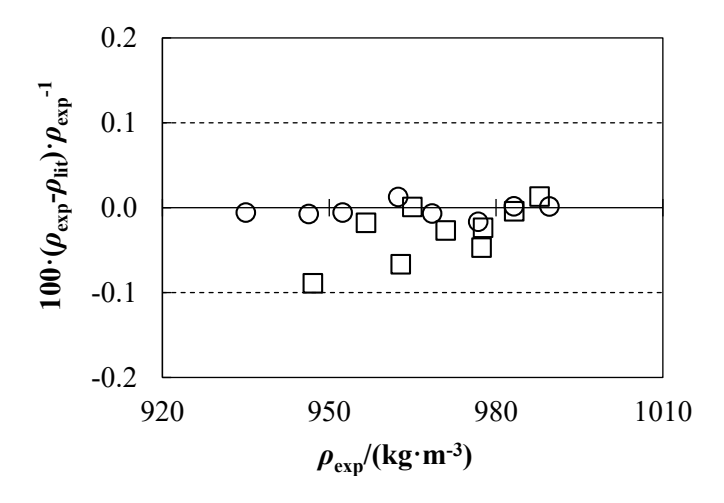


Figure 7.4. Relative deviations (%) of density measurements ρ_{exp} , in comparison with literature values ρ_{lit} . Literature for DEAE + H₂O: (\bigcirc) Karunarathne et al. [62] and (\square) Lebrette et al. [60]. Dashed lines represent the relative expanded uncertainty of our density measurements.

7.2.2. EAE $+ H_2O$

7.2.2.1. Experimental Density

The results of the density measurements for the aqueous amine solutions are presented in **Table 7.3** for $EAE + H_2O$. In order to analyse the influence of pressure, amine mass fraction, and temperature, the experimental density data were plotted as a function of these variables, as can be seen in **Figures 7.5 to 7.7.**

Table 7.3. Experimental densities ρ , for EAE(1) + H₂O(2) mixture at different conditions of temperature T, pressure ρ , amine mass fraction w_1 , and equivalent amine molality b_1 .

$\rho/(\mathrm{kg \cdot m^{-3}})$										
T/K										
p/MPa	293.15	313.15	333.15	353.15	373.15	393.15				
$w_1 = 0.1000 \ (b_1 = 1.2463 \ \text{mol} \cdot \text{kg}^{-1})$										
0.1	995.6	988.6	978.5	966.4						
0.5	995.6	988.7	978.7	966.5						
1	995.8	988.8	978.9	966.7	952.6	936.9				
2	996.1	989.3	979.3	967.2	953.1	937.4				
5	997.4	990.5	980.6	968.5	954.6	939.0				
10	999.4	992.5	982.7	970.7	956.8	941.4				
15	1001.5	994.5	984.8	972.8	959.1	943.9				
20	1003.5	996.5	986.8	975.0	961.3	946.3				

30	1007.5	1000.4	990.7	979.1	965.8	951.0
40	1011.3	1004.3	994.7	983.2	970.0	955.5
50	1015.1	1008.0	998.5	987.1	974.1	959.9
60	1018.9	1011.7	1002.2	990.9	978.1	964.3
70	1022.6	1015.3	1005.9	994.8	982.1	968.3
80	1026.2	1018.9	1009.5	998.4	986.0	972.5
90	1029.8	1022.4	1013.0	1002.1	989.7	976.4
100	1033.3	1025.9	1016.5	1005.6	993.4	980.3
	$w_1 = 0.20$	$000 (b_1 = 2)$.8048 mo	l·kg ⁻¹)		
0.1	995.3	986.4	974.6	961.3		
0.5	995.3	986.4	974.8	961.4		
1	995.5	986.5	975.0	961.5	946.4	929.8
2	995.8	986.9	975.4	962.0	946.9	930.3
5	997.0	988.1	976.7	963.4	948.3	931.9
10	998.9	990.0	978.8	965.5	950.7	934.5
15	1000.8	991.9	980.7	967.6	953.0	936.9
20	1002.6	993.8	982.7	969.7	955.2	939.4
30	1006.2	997.5	986.6	973.9	959.7	944.2
40	1009.8	1001.2	990.5	977.9	963.9	948.8
50	1013.3	1004.8	994.2	981.9	968.1	953.3
60	1016.8	1008.3	997.8	985.7	972.2	957.7
70	1020.2	1011.8	1001.4	989.4	976.1	961.9
80	1023.5	1015.2	1004.9	993.0	980.1	965.9
90	1026.8	1018.5	1008.4	996.6	983.7	969.9
100	1030.1	1021.8	1011.7	1000.1	987.4	973.9
	$w_1 = 0.30$	$000 (b_1 = 4)$.8085 mol	l·kg ⁻¹)		
0.1	995.2	983.6	970.1	955.4		
0.5	995.2	983.7	970.3	955.5		
1	995.3	983.8	970.5	955.7	939.5	921.9
2	995.6	984.2	970.9	956.2	940.0	922.6
5	996.8	985.4	972.1	957.5	941.5	924.2
10	998.6	987.3	974.3	959.8	943.9	926.8
15	1000.4	989.1	976.3	961.9	946.3	929.5
20	1002.1	991.0	978.2	964.2	948.6	932.1
30	1005.6	994.7	982.1	968.2	953.2	937.0
40	1009.0	998.3	986.0	972.4	957.5	941.8

50	1012.3	1001.8	989.7	976.3	961.8	946.4
60	1015.6	1005.2	993.3	980.1	965.9	950.9
70	1018.8	1008.6	996.8	983.9	969.9	955.1
80	1022.0	1011.9	1000.3	987.6	973.7	959.3
90	1025.1	1015.1	1003.7	991.1	977.6	963.4
100	1028.2	1018.3	1007.0	994.6	981.3	967.3
	$w_1 = 0.40$	$002 (b_1 = 7)$.4842 mol	·kg ⁻¹)		
0.1	993.1	979.4	964.3	948.5		
0.5	993.2	979.5	964.5	948.6		
1	993.3	979.7	964.7	948.8	931.7	913.5
2	993.6	980.1	965.2	949.3	932.3	914.1
5	994.8	981.2	966.5	950.7	933.8	915.9
10	996.6	983.2	968.6	953.0	936.3	918.7
15	998.4	985.1	970.7	955.3	938.8	921.4
20	1000.2	987.0	972.8	957.6	941.2	924.1
30	1003.7	990.7	976.7	961.8	946.0	929.3
40	1007.1	994.3	980.6	966.0	950.5	934.2
50	1010.4	997.8	984.4	970.1	954.9	939.0
60	1013.6	1001.3	988.1	973.9	959.1	943.6
70	1016.8	1004.7	991.6	977.8	963.2	948.0
80	1020.0	1008.0	995.1	981.5	967.2	952.3
90	1023.0	1011.2	998.5	985.1	971.0	956.4
100	1026.0	1014.3	1001.9	988.6	974.8	960.4

^aExpanded uncertainties (k = 2): U(T) = 0.02 K; $U_r(p) = 0.0002$; $U_r(w) = 0.0004$ and $U(\rho) = 0.7$ kg·m⁻³.

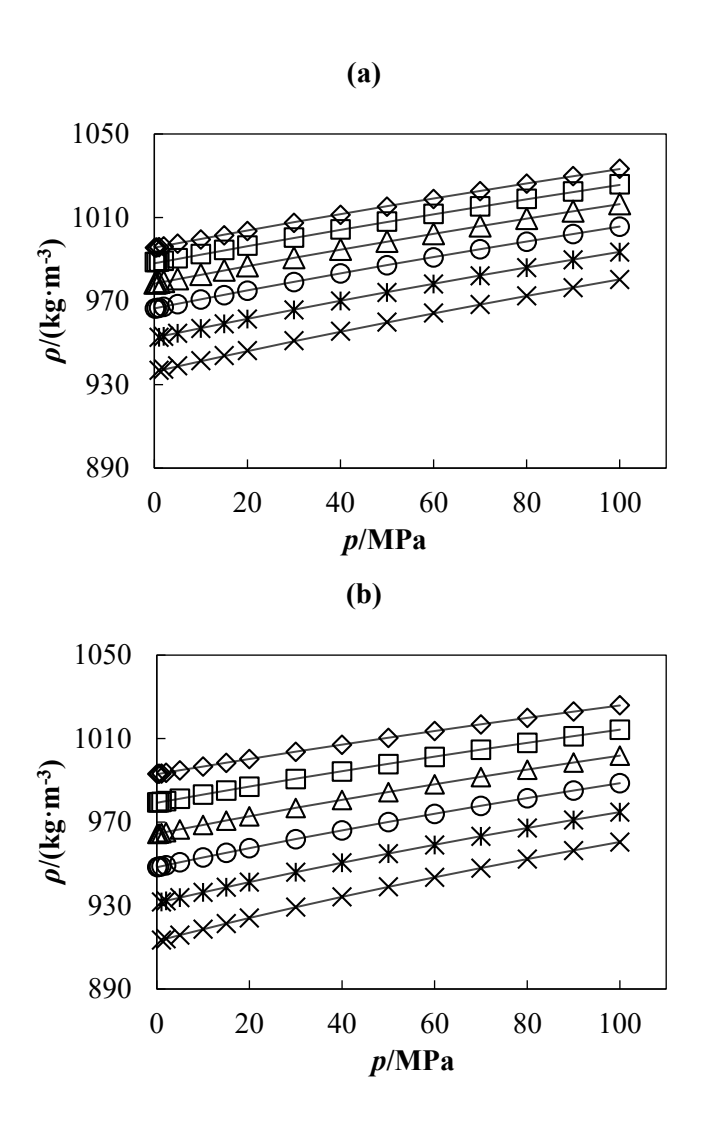


Figure 7.5. Experimental density ρ , of the system EAE(1) + H₂O(2) as a function of pressure p, at amine mass fraction of (a) $w_1 = 0.1$ and (b) $w_1 = 0.4$. Isotherms: (\diamondsuit) T = 293.15 K, (\square) T = 313.15 K, (\triangle) T = 333.15 K, (\square) T = 353.15 K, (\square) T = 373.15 K, and (\square) T = 393.15 K. Solid lines represent the calculated values using modified Tammann-Tait (**Equations 7.1 to 7.4**) with the parameters given in **Tables 7.11 and 7.12.**

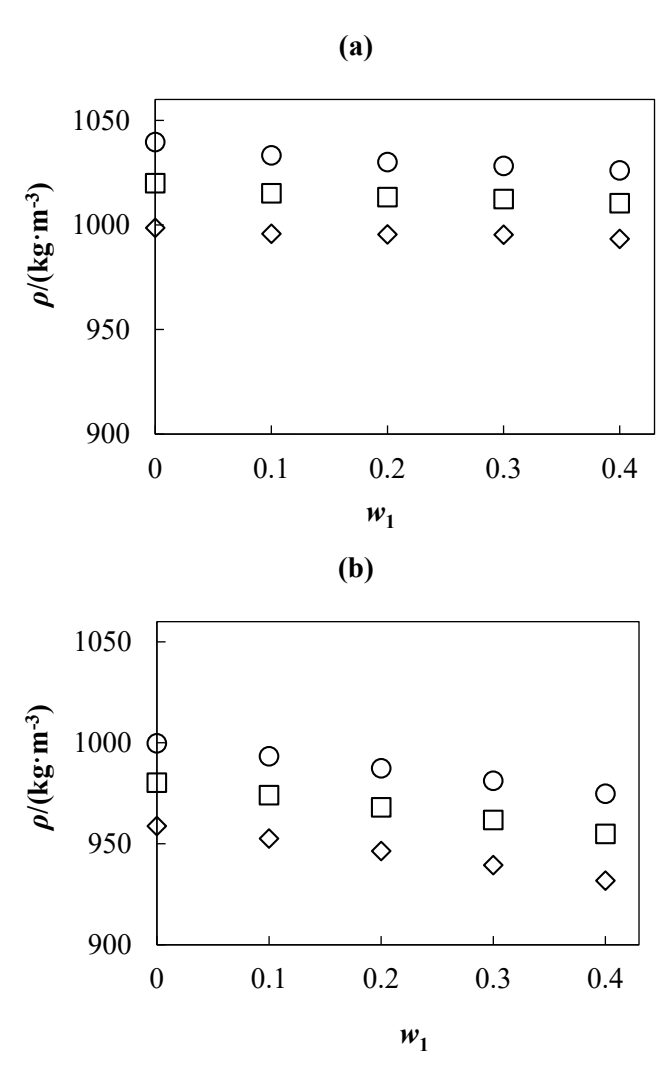


Figure 7.6. Experimental density ρ , of the system EAE(1) + H₂O(2) as a function of amine mass fraction w_1 , at temperatures of (a) T = 293.15 K and (b) T = 373.15 K. Isobars: (\diamondsuit) p = 1 MPa, (\square) p = 50 MPa, and (\bigcirc) p = 100 MPa. Experimental data of pure water ($w_1 = 0$) from NIST REFPROP database [180].

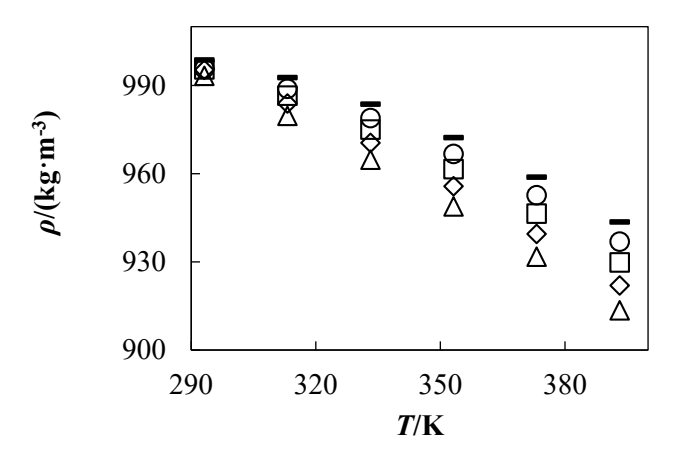


Figure 7.7. Experimental density ρ , of the system EAE(1) + H₂O(2) as a function of temperature T, at pressure p = 1 MPa. Amine mass fractions: (—) $w_1 = 0$, (○) $w_1 = 0.1$, (□) $w_1 = 0.2$, (◇) $w_1 = 0.3$, and (△) $w_1 = 0.4$. Experimental data of pure water ($w_1 = 0$) from NIST REFPROP database [180].

7.2.2.2. Comparison with Literature

The experimental conditions of the references used for the comparison of EAE aqueous solutions are shown in **Table 7.4**. The relative deviations of our measurements and the experimental density values reported in the literature are plotted in **Figure 7.8** for EAE + H₂O system. An average relative deviation below 0.04 % was found for Viet et al. [72], which agrees with our uncertainty. Pandey & Mondal [73] report nine common points for comparison with a declared relative uncertainty of 0.3 %. The deviations are within their experimental uncertainty, as can be seen in **Figure 7.8**.

Table 7.4. Measurement conditions of literature data used to compare the experimental density of $EAE(1) + H_2O(2)$ mixtures measured in this work.

Reference	Densimeter	Conditions	Number of Points	$U_{ m r}^{ m a}$
Pandey & Mondal [73]	Anton Paar DMA 35	$w_1 = 0.10; 0.20; 0.30$ T = (293.15 - 333.15) K p = 0.1 MPa	9	0.3 %
Viet et al. [72]	Stabinger-type kinematic viscometer- densimeter (SVM 3001, Anton Paar)	$w_1 = 0.20$; 0.40 T = (293.15 - 313.15) K p = 0.1 MPa	4	0.4 %

^aRelative expanded uncertainty (k = 2), %.

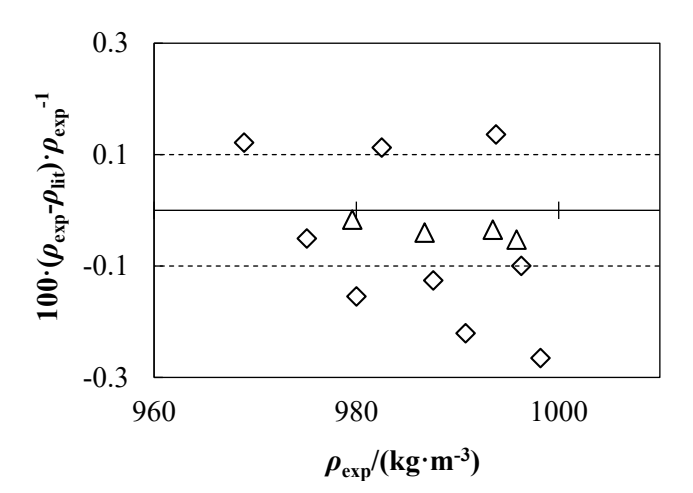


Figure 7.8. Relative deviations (%) of density measurements ρ_{exp} , in comparison with literature values ρ_{lit} . Literature for EAE + H₂O: (\diamondsuit) Pandey & Mondal [73] and (\triangle) Viet et al. [72]. Dashed lines represent the relative expanded uncertainty of our density measurements.

7.2.3. $MAPA + H_2O$

7.2.3.1. Experimental Density

The results of the density measurements for the aqueous amine solutions are presented in **Table 7.5** for MAPA + H₂O. To analyse the influence of pressure, amine mass fraction, and temperature, the experimental density data were plotted as a function of these variables, as can be seen in **Figures 7.9 to 7.11.**

Table 7.5. Experimental densities ρ , for MAPA(1) + H₂O(2) mixture at different conditions of temperature T, pressure ρ , amine mass fraction w_1 , and equivalent amine molality b_1 .^a

-						
		,	o/(kg·m ⁻³))		
			T /	K		
p/MPa	293.15	313.15	333.15	353.15	373.15	393.15
	$w_1 = 0.10$	$000 (b_1 = 1)$.2608 mo	l·kg ⁻¹)		
0.1	991.0	983.8	973.6	961.5		
0.5	991.0	983.9	973.8	961.7		
1	991.2	984.0	974.0	961.9	947.8	932.2
2	991.5	984.4	974.4	962.3	948.3	932.7
5	992.8	985.6	975.7	963.6	949.7	934.2
10	994.8	987.6	977.8	965.8	951.9	936.6
15	996.8	989.6	979.8	967.8	954.1	939.1
20	998.7	991.5	981.8	970.0	956.4	941.4
30	1002.6	995.4	985.7	974.0	960.8	946.1
40	1006.4	999.2	989.6	978.1	964.9	950.6
50	1010.2	1002.9	993.3	981.9	969.0	954.9
60	1013.8	1006.5	997.0	985.8	973.0	959.2
70	1017.4	1010.1	1000.6	989.5	976.9	963.3
80	1021.0	1013.6	1004.2	993.1	980.7	967.3
90	1024.5	1017.0	1007.7	996.7	984.5	971.3
100	1027.9	1020.4	1011.1	1000.3	988.1	975.1
	$w_1 = 0.20$	$000 (b_1 = 2)$.8369 mo	l·kg ⁻¹)		
0.1	987.4	977.8	965.8	952.4		
0.5	987.3	977.9	966.1	952.6		
1	987.4	978.0	966.3	952.8	937.7	921.1
2	987.8	978.4	966.7	953.2	938.1	921.6
5	988.9	979.5	967.9	954.5	939.6	923.2

10	990.7	981.4	969.9	956.6	941.8	925.6
15	992.5	983.3	971.8	958.7	944.0	928.1
20	994.2	985.1	973.7	960.7	946.3	930.5
30	997.6	988.6	977.5	964.7	950.6	935.1
40	1001.0	992.2	981.2	968.7	954.7	939.6
50	1004.4	995.5	984.8	972.5	958.8	944.0
60	1007.7	999.0	988.3	976.1	962.7	948.3
70	1010.9	1002.3	991.8	979.8	966.6	952.4
80	1014.1	1005.6	995.2	983.4	970.4	956.4
90	1017.3	1008.8	998.5	986.8	974.0	960.2
100	1020.4	1011.9	1001.8	990.2	977.5	964.0
	$w_1 = 0.30$	$000 (b_1 = 4)$.8623 mo	$1 \cdot kg^{-1}$		
0.1	985.3	972.8	958.6	943.4		
0.5	985.3	972.8	958.8	943.6		
1	985.4	972.9	959.0	943.8	927.4	909.8
2	985.7	973.3	959.4	944.2	927.9	910.4
5	986.8	974.4	960.6	945.6	929.3	912.0
10	988.5	976.2	962.5	947.7	931.6	914.5
15	990.1	977.9	964.4	949.7	933.9	917.0
20	991.7	979.7	966.4	951.8	936.1	919.5
30	995.0	983.1	970.0	955.7	940.5	924.2
40	998.1	986.5	973.6	959.6	944.7	928.8
50	1001.2	989.8	977.2	963.4	948.7	933.2
60	1004.2	993.0	980.6	967.1	952.7	937.5
70	1007.2	996.2	984.0	970.7	956.5	941.6
80	1010.2	999.3	987.2	974.1	960.3	945.7
90	1013.0	1002.3	990.5	977.5	963.9	949.5
100	1015.9	1005.3	993.6	980.9	967.4	953.3
	$w_1 = 0.40$	$007 (b_1 = 7)$.5840 mo	l·kg ⁻¹)		
0.1	981.5	966.3	950.0	933.3		
0.5	981.6	966.3	950.2	933.4		
1	981.7	966.5	950.4	933.6	915.9	897.4
2	982.0	966.8	950.8	934.1	916.4	897.9
5	983.1	967.9	952.1	935.4	917.9	899.5
10	984.7	969.7	954.1	937.6	920.3	902.2
15	986.4	971.5	956.0	939.7	922.6	904.8

20	988.0	973.3	957.9	941.8	924.9	907.4
30	991.2	976.7	961.6	945.8	929.4	912.3
40	994.3	980.1	965.3	949.8	933.7	917.0
50	997.4	983.3	968.8	953.6	937.8	921.5
60	1000.4	986.6	972.2	957.3	941.8	925.9
70	1003.3	989.7	975.6	960.9	945.7	930.1
80	1006.2	992.7	978.9	964.5	949.5	934.2
90	1009.0	995.8	982.1	967.9	953.2	938.2
100	1011.8	998.7	985.2	971.2	956.7	942.0

^aExpanded uncertainties (k = 2): U(T) = 0.02 K; $U_r(p) = 0.0002$; $U_r(w) = 0.0004$ and $U(\rho) = 0.7$ kg·m⁻³.

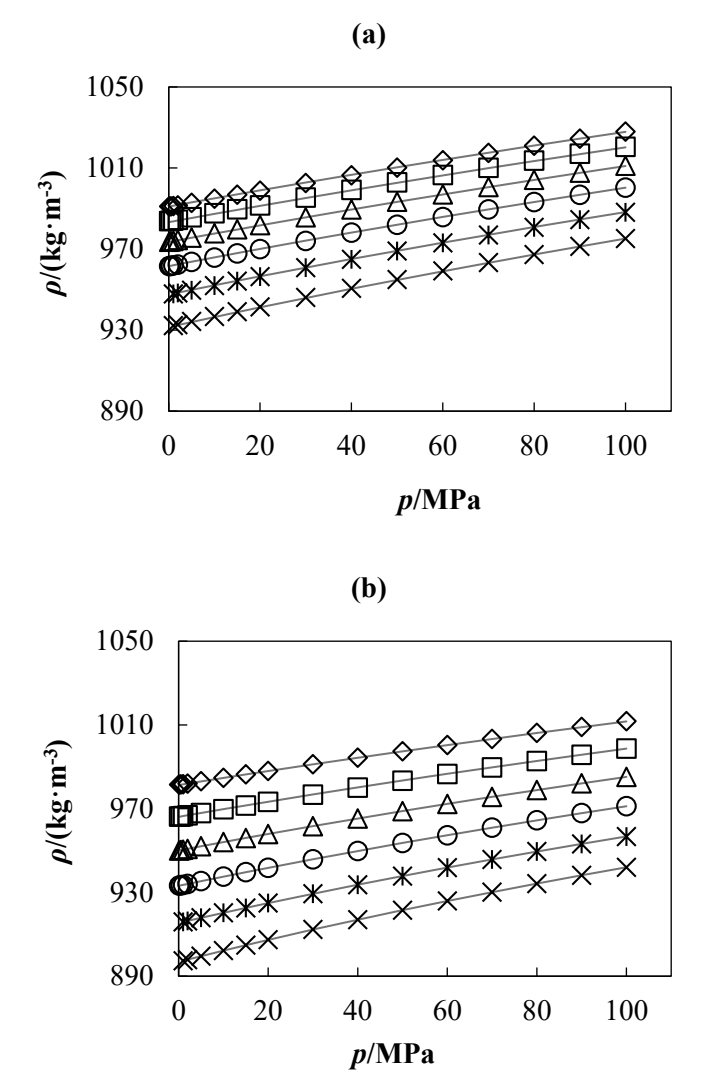


Figure 7.9. Experimental density ρ , of the system MAPA(1) + H₂O(2) as a function of pressure p, at amine mass fraction of (a) $w_1 = 0.1$ and (b) $w_1 = 0.4$. Isotherms: (\diamondsuit) T = 293.15 K, (\square) T = 313.15 K, (\triangle) T = 333.15 K, (\square) T = 353.15 K, (\square) T = 373.15 K, and (\square) T = 393.15 K. Lines represent the calculated values using modified Tammann-Tait (**Equations 7.1 to 7.4**) with the parameters given in **Tables 7.11 and 7.12**.

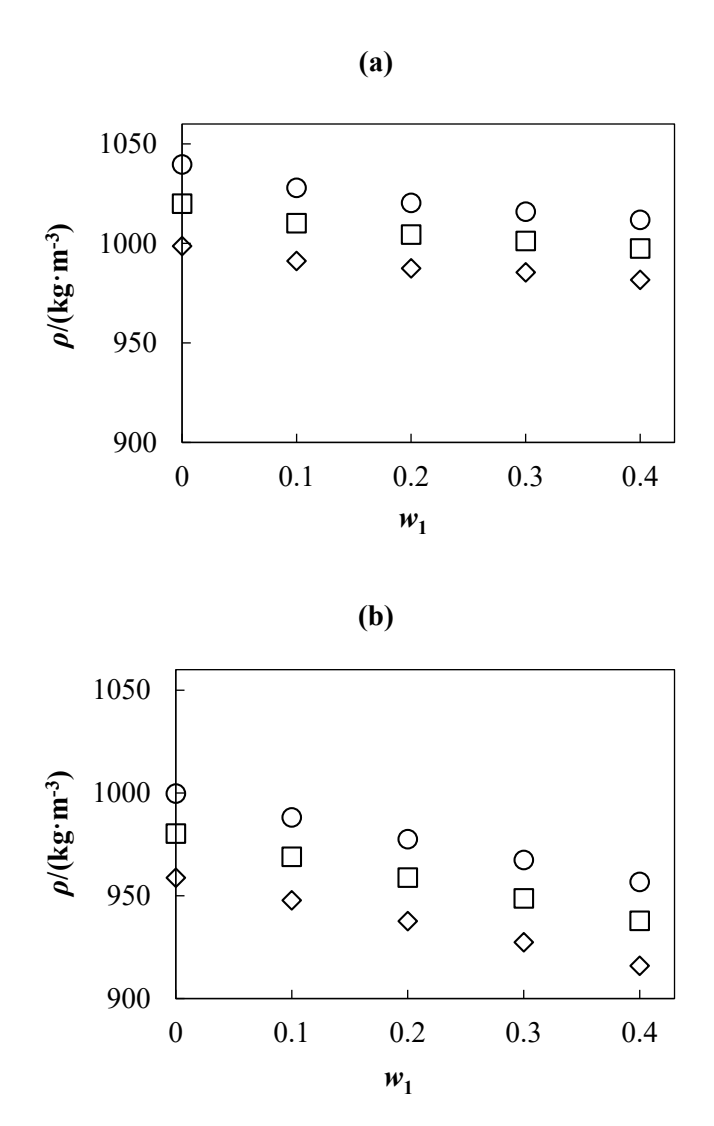


Figure 7.10. Experimental density ρ , of the system MAPA(1) + H₂O(2) as a function of amine mass fraction w_1 , at temperatures of (a) T = 293.15 K and (b) T = 373.15 K. Isobars: (\diamondsuit) p = 1 MPa, (\square) p = 50 MPa, and (\bigcirc) p = 100 MPa. Experimental data of pure water ($w_1 = 0$) from NIST REFPROP database [180].

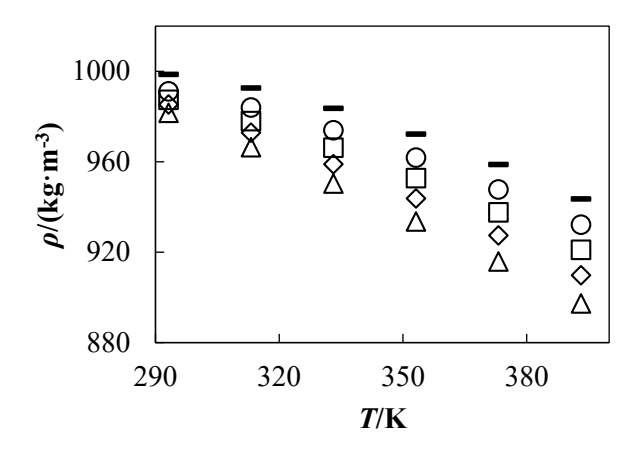


Figure 7.11. Experimental density ρ , of the system MAPA(1) + H₂O(2) as a function of temperature T, at pressure p = 1 MPa. Amine mass fractions: (—) $w_1 = 0$, (\bigcirc) $w_1 = 0.1$, (\square) $w_1 = 0.2$, (\diamondsuit) $w_1 = 0.3$, and (\triangle) $w_1 = 0.4$. Experimental data of pure water ($w_1 = 0$) from NIST REFPROP database [180].

7.2.3.2. Comparison with Literature

Table 7.6 presents a review of the experimental data found in the literature for the MAPA + H₂O. The relative deviations of our measurements and the experimental density values reported in the literature are plotted in **Figure 7.12** for MAPA + H₂O. As can be observed in **Table 7.6** for the comparison of experimental densities of MAPA + H₂O, Monteiro et al. [76] report three common points and Wang et al. [77] report eight. All of them with negative relative deviations above the uncertainty of our measurements (see **Figure 7.12**). This is because the amine mass fractions reported in the literature were slightly lower than those reported in this work, so the experimental densities reported in these references are slightly lower.

Table 7.6. Measurement conditions of literature data used to compare the experimental density of $MAPA(1) + H_2O(2)$ mixture measured in this work.

Reference	Densimeter	Conditions	Number of Points	$U_{ m r}^{ m a}$
Monteiro et al. [76]	Anton Paar DMA 4500	$w_1 = 0.09$ T = (293.15 - 333.15) K p = 0.1 MPa	3	0.006 %
Wang et al. [77]	Anton Paar DMA 5000 M	$w_1 = 0.09; 0.29$ T = (293.15 - 353.15) K p = 0.1 MPa	8	0.001 %

^aRelative expanded uncertainty (k = 2), %.

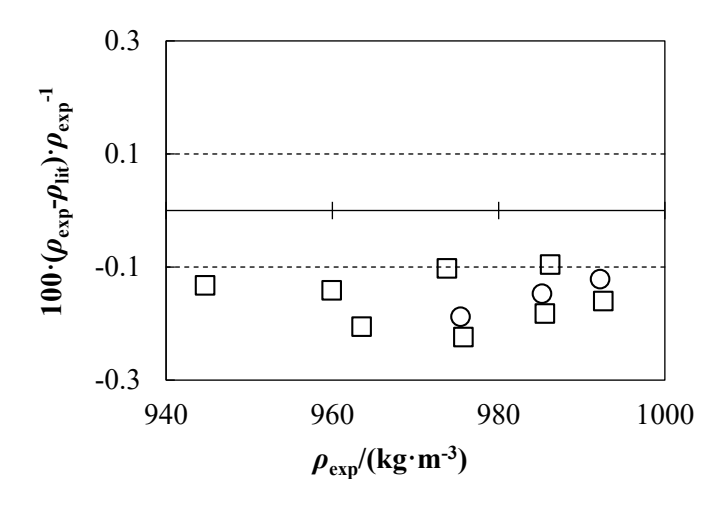


Figure 7.12. Relative deviations (%) of density measurements ρ_{exp} , in comparison with literature values ρ_{lit} . Literature for MAPA + H₂O: (\bigcirc) Monteiro et al. [76] and (\square) Wang et al. [77]. Dashed lines represent the relative expanded uncertainty of our density measurements.

7.2.4. $1-MPZ + H_2O$

7.2.4.1. Experimental Density

The results of the density measurements for the aqueous amine solutions are presented in **Table 7.7** for $1\text{-MPZ} + \text{H}_2\text{O}$. To analyse the influence of pressure, amine mass fraction, and temperature, the experimental density data were plotted as a function of these variables, as can be seen in **Figures 7.13** to 7.15.

Table 7.7. Experimental densities ρ , for 1-MPZ(1) + H₂O(2) mixture at different conditions of temperature T, pressure p, amine mass fraction w_1 , and equivalent amine molality b_1 .^a

		0/	(kg·m ⁻³)			
		p /	(kg·m)			
			T/K			
p/MPa	293.15	313.15	333.15	353.15	373.15	393.15
	$w_1 = 0.10$	$000 (b_1 = 1)$.1092 mo	l·kg ⁻¹)		
0.1	998.0	991.1	981.1	969.2		
0.5	998.1	991.3	981.4	969.4		
1	998.2	991.4	981.6	969.6	955.6	940.1
2	998.6	991.8	982.0	970.0	956.1	940.5
5	999.8	993.0	983.3	971.3	957.5	942.1
10	1001.9	995.0	985.4	973.5	959.7	944.5
15	1003.9	997.0	987.4	975.6	962.0	946.9
20	1005.9	999.0	989.4	977.6	964.2	949.3

30	1009.8	1002.9	993.3	981.8	968.6	954.0
40	1013.6	1006.6	997.2	985.8	972.8	958.5
50	1017.4	1010.3	1001.0	989.7	976.9	962.8
60	1021.1	1014.0	1004.7	993.5	980.9	967.1
70	1024.7	1017.6	1008.3	997.3	984.8	971.2
80	1028.3	1021.1	1011.9	1000.9	988.6	975.3
90	1031.9	1024.6	1015.3	1004.4	992.3	979.2
100	1035.4	1028.0	1018.8	1008.0	996.0	983.0
	$w_1 = 0.20$	$000 (b_1 = 2)$.4957 mol	l·kg ⁻¹)		
0.1	1001.7	992.8	981.3	968.0		
0.5	1001.8	992.9	981.5	968.2		
1	1001.9	993.1	981.7	968.4	953.3	936.7
2	1002.2	993.5	982.1	968.8	953.8	937.2
5	1003.4	994.6	983.3	970.1	955.2	938.8
10	1005.2	996.5	985.3	972.3	957.4	941.3
15	1007.0	998.3	987.3	974.3	959.8	943.7
20	1008.8	1000.1	989.2	976.4	962.0	946.2
30	1012.3	1003.7	993.0	980.4	966.3	950.9
40	1015.7	1007.3	996.7	984.3	970.5	955.5
50	1019.1	1010.8	1000.3	988.2	974.5	959.8
60	1022.5	1014.2	1003.9	991.9	978.5	964.1
70	1025.8	1017.6	1007.3	995.5	982.3	968.2
80	1029.0	1020.9	1010.8	999.1	986.2	972.3
90	1032.2	1024.1	1014.1	1002.6	989.8	976.0
100	1035.4	1027.2	1017.4	1005.9	993.5	980.0
	$w_1 = 0.30$	$000 (b_1 = 4)$.2825 mol	l·kg ⁻¹)		
0.1	1007.6	995.8	981.8	966.9		
0.5	1007.7	995.8	982.1	967.0		
1	1007.8	995.9	982.2	967.2	950.8	932.9
2	1008.1	996.3	982.7	967.6	951.3	933.4
5	1009.2	997.4	983.8	968.9	952.7	935.0
10	1010.8	999.2	985.8	971.1	955.0	937.6
15	1012.5	1001.0	987.8	973.2	957.3	940.1
20	1014.2	1002.7	989.7	975.3	959.6	942.6
30	1017.4	1006.2	993.4	979.3	964.0	947.4
40	1020.6	1009.6	997.1	983.2	968.2	952.0

50	1023.7	1012.9	1000.6	987.0	972.3	956.5
60	1026.8	1016.2	1004.0	990.7	976.3	960.9
70	1029.8	1019.4	1007.4	994.4	980.2	965.0
80	1032.8	1022.5	1010.7	997.8	983.9	969.1
90	1035.8	1025.4	1013.9	1001.3	987.6	973.1
100	1038.7	1028.5	1017.2	1004.7	991.3	976.9
	$w_1 = 0.40$	$003 (b_1 = 6)$.6649 mo	l·kg ⁻¹)		
0.1	1012.9	997.9	981.5	964.6		
0.5	1013.0	997.9	981.7	964.8		
1	1013.1	998.1	981.9	965.0	946.8	927.7
2	1013.4	998.4	982.3	965.4	947.3	928.3
5	1014.5	999.5	983.6	966.8	948.8	930.0
10	1016.1	1001.3	985.6	969.0	951.2	932.7
15	1017.8	1003.1	987.6	971.1	953.6	935.3
20	1019.5	1004.9	989.5	973.2	956.0	938.0
30	1022.6	1008.4	993.3	977.4	960.6	943.0
40	1025.8	1011.8	997.0	981.4	965.0	947.8
50	1028.9	1015.1	1000.6	985.3	969.2	952.5
60	1031.9	1018.3	1004.1	989.1	973.3	956.9
70	1034.8	1021.5	1007.4	992.7	977.2	961.2
80	1037.8	1024.6	1010.8	996.3	981.1	965.5
90	1040.7	1027.7	1014.1	999.8	984.8	969.5
100	1043.5	1030.7	1017.2	1003.2	988.5	973.5

^aExpanded uncertainties (k = 2): U(T) = 0.02 K; $U_r(p) = 0.0002$; $U_r(w) = 0.0004$ and $U(\rho) = 0.7$ kg·m⁻³.

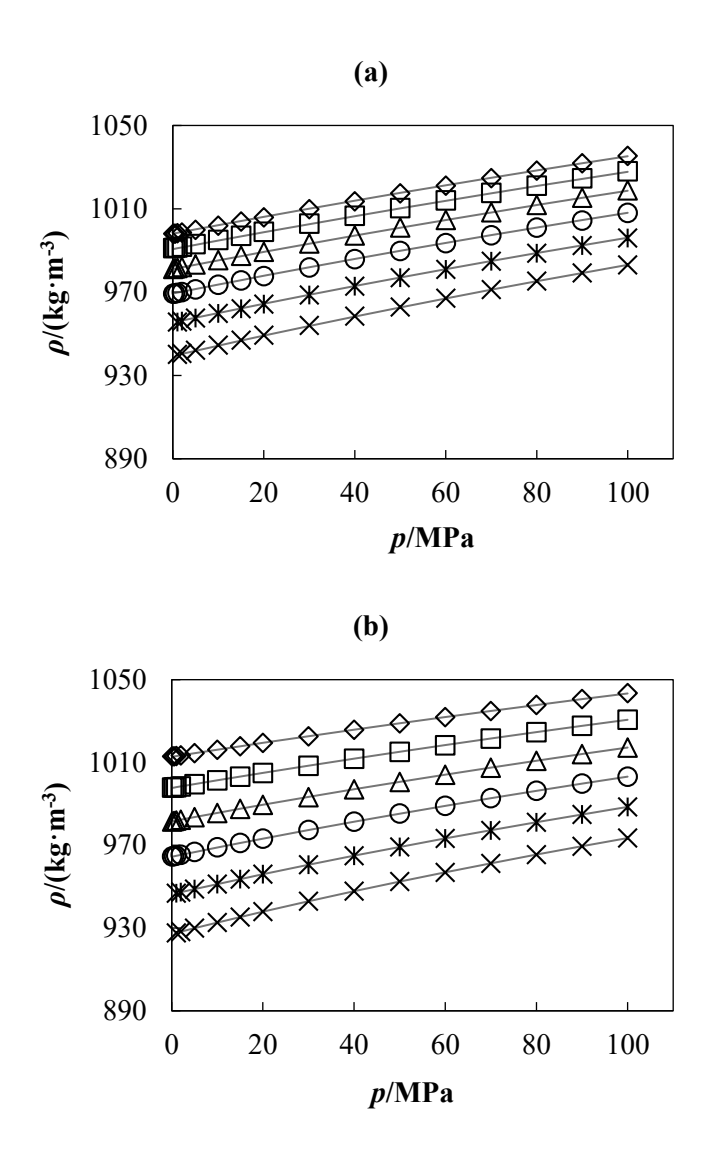


Figure 7.13. Experimental density ρ , of the system 1-MPZ(1) + H₂O(2) as a function of pressure p, at amine mass fraction of (a) $w_1 = 0.1$ and (b) $w_1 = 0.4$. Isotherms: (\diamondsuit) T = 293.15 K, (\square) T = 313.15 K, (\triangle) T = 333.15 K, (\bigcirc) T = 353.15 K, (\ast) T = 373.15 K, and (\times) T = 393.15 K. Solid lines represent the calculated values using modified Tammann-Tait (**Equations 7.1 to 7.4**) with the parameters given in **Tables 7.11 and 7.12**.

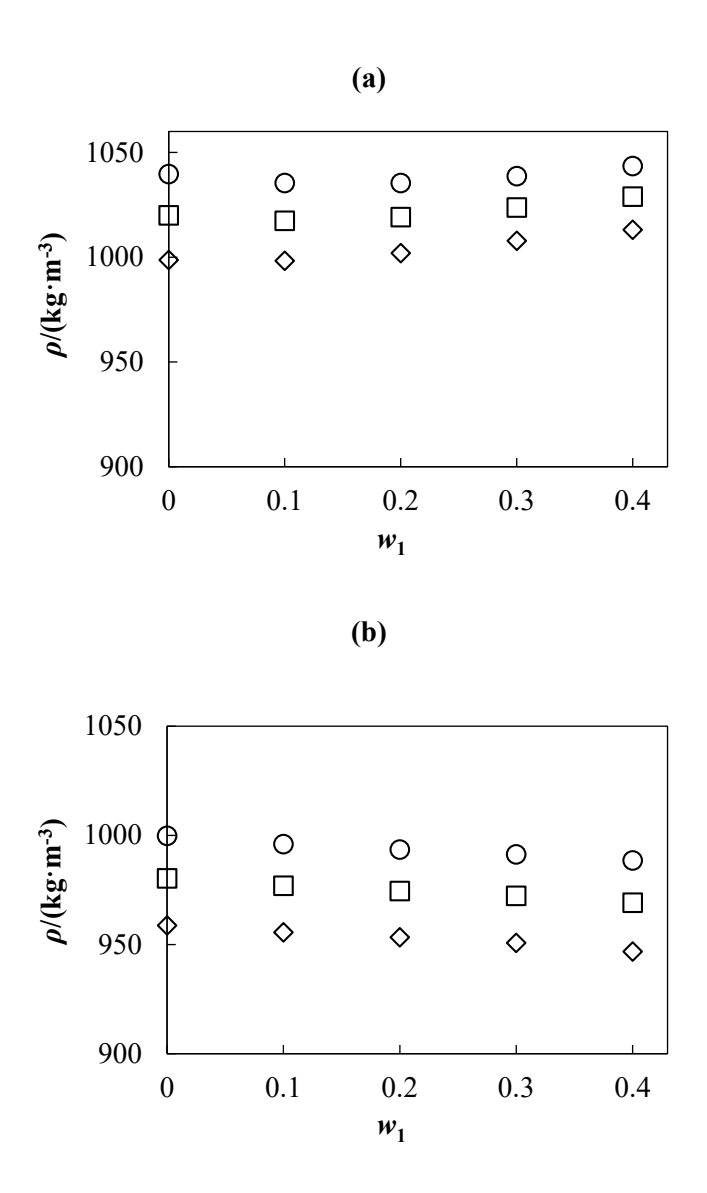


Figure 7.14. Experimental density ρ , of the system 1-MPZ(1) + H₂O(2) as a function of amine mass fraction w_1 , at temperatures of (a) T = 293.15 K and (b) T = 373.15 K. Isobars: (\diamondsuit) p = 1 MPa, (\square) p = 50 MPa, and (\bigcirc) p = 100 MPa. Experimental data of pure water ($w_1 = 0$) from NIST REFPROP database [180].

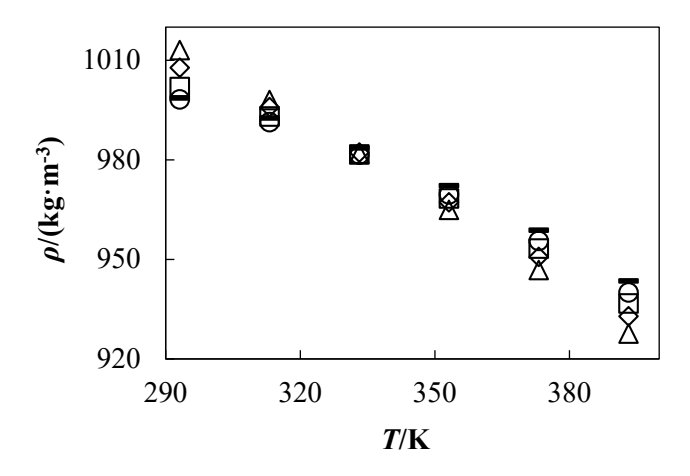


Figure 7.15. Experimental density ρ , of the system 1-MPZ(1) + H₂O(2) as a function of temperature T, at pressure p = 1 MPa. Amine mass fractions: (—) $w_1 = 0$, (\bigcirc) $w_1 = 0.1$, (\square) $w_1 = 0.2$, (\diamondsuit) $w_1 = 0.3$, and (\triangle) $w_1 = 0.4$. Experimental data of pure water ($w_1 = 0$) from NIST REFPROP database [180].

7.2.4.2. Comparison with Literature

The details of the experimental conditions of the measurements carried out by Rayer et al. [78] and Vamja et al. [38] can be found in **Table 7.8**. The relative deviations of our measurements and the experimental density values reported in the literature are plotted in **Figure 7.16**. In the case of the comparison with the densities reported by Rayer et al. [78] for the 1-MPZ + H₂O mixture, as can be seen in **Figure 7.16**, all points were within our uncertainty. In Vamja et al. [38] study six of the eight comparison points are above the uncertainty.

Table 7.8. Measurement conditions of literature data used to compare the experimental density of 1- $MPZ(1) + H_2O(2)$ mixture measured in this work.

Reference	Densimeter	Conditions	Number of Points	$U_{ m r}{}^{ m a}$
Rayer et al. [78]	Anton Paar DMA 4500	$w_1 = 0.3029; 0.3920$ T = (313.15 - 333.15) K p = 0.1 MPa	4	NA ^b
Vamja et al. [38]	Anton Paar DMA 4500	$w_1 = 0.1; 0.2; 0.3; 0.4$ T = (313.15 - 333.15) K p = 0.1 MPa	8	0.06 %

^aRelative expanded uncertainty (k = 2), %.

^bNA: Not Available.

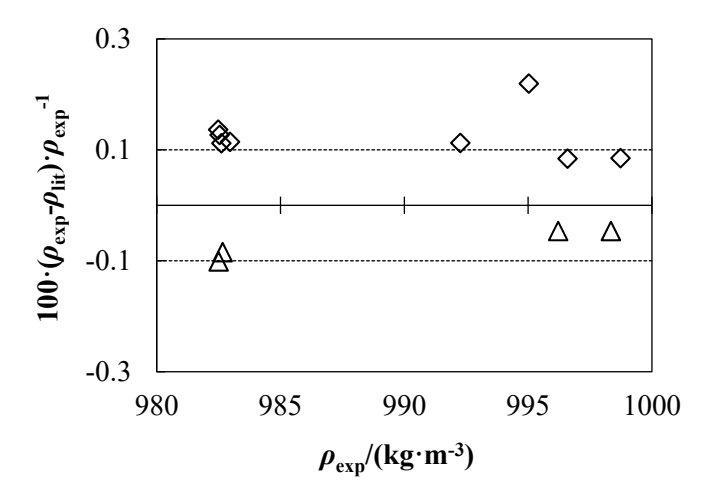


Figure 7.16. Relative deviations (%) of density measurements ρ_{exp} , in comparison with literature values ρ_{lit} . Literature for 1-MPZ + H₂O: (\triangle) Rayer et al. [78] and (\diamondsuit) Vamja et al. [38]. Dashed lines represent the relative expanded uncertainty of our density measurements.

7.2.5. $AMP + H_2O$

7.2.5.1. Experimental Density

The results of the density measurements for the aqueous amine solutions are presented in **Table 7.9** for AMP + H₂O. To analyse the influence of pressure, amine mass fraction, and temperature, the experimental density data were plotted as a function of these variables, as can be seen in **Figures 7.17** to 7.19.

Table 7.9. Experimental densities ρ , for AMP(1) + H₂O(2) mixture at different conditions of temperature T, pressure p, amine mass fraction w_1 , and equivalent amine molality b_1 .

$ ho/(\mathrm{kg}\cdot\mathrm{m}^{-3})$										
T/K										
p/MPa	293.15	313.15	333.15	353.15	373.15	393.15				
	$w_1 =$	$0.1001 (b_1$	= 1.2481 1	mol·kg ⁻¹)						
0.1	997.3	990.4	980.4	968.2						
0.5	997.3	990.5	980.6	968.4						
1	997.5	990.7	980.7	968.6	954.4	938.7				
2	997.8	991.1	981.2	969.0	954.9	939.2				
5	999.1	992.3	982.4	970.3	956.3	940.7				
10	1001.2	994.3	984.6	972.5	958.6	943.3				
15	1003.2	996.3	986.6	974.6	960.8	945.6				
20	1005.2	998.3	988.6	976.7	963.1	948.0				
30	1009.1	1002.2	992.5	980.9	967.4	952.7				

40	1013.0	1006.0	996.5	984.9	971.7	957.2
50	1016.8	1009.8	1000.3	988.8	975.8	961.6
60	1020.6	1013.5	1004.0	992.6	979.8	965.9
70	1024.2	1017.2	1007.6	996.5	983.8	970.0
80	1027.9	1020.7	1011.2	1000.1	987.6	974.1
90	1031.5	1024.2	1014.8	1003.7	991.3	978.0
100	1035.0	1027.6	1018.2	1007.3	995.0	981.9
	$w_1 =$	$0.2002 (b_1$	= 2.8081	mol·kg ⁻¹)		
0.1	998.1	989.4	977.8	964.5		
0.5	998.1	989.5	978.0	964.6		
1	998.3	989.6	978.2	964.8	949.7	933.1
2	998.6	990.0	978.6	965.2	950.2	933.7
5	999.8	991.1	979.9	966.5	951.6	935.3
10	1001.7	993.1	982.0	968.7	953.9	937.8
15	1003.6	995.0	984.0	970.8	956.2	940.3
20	1005.4	996.8	985.9	972.9	958.4	942.7
30	1009.0	1000.5	989.7	977.0	962.8	947.4
40	1012.5	1004.2	993.6	981.0	967.1	952.0
50	1016.0	1007.7	997.3	984.9	971.2	956.5
60	1019.5	1011.2	1000.9	988.7	975.2	960.7
70	1022.9	1014.7	1004.4	992.4	979.1	964.9
80	1026.2	1018.0	1007.9	996.0	983.0	969.1
90	1029.5	1021.4	1011.3	999.6	986.7	972.9
100	1032.7	1024.6	1014.6	1003.0	990.2	976.7
	$w_1 =$	$0.3001 (b_1$	= 4.8111	mol·kg ⁻¹)		
0.1	999.6	988.2	974.8	960.1		
0.5	999.6	988.3	975.0	960.3		
1	999.7	988.4	975.2	960.5	944.3	926.8
2	1000.0	988.8	975.6	961.0	944.8	927.4
5	1001.2	989.9	976.8	962.3	946.3	929.0
10	1003.0	991.8	978.9	964.5	948.6	931.6
15	1004.8	993.7	980.9	966.6	950.9	934.2
20	1006.5	995.5	982.8	968.8	953.3	936.7
30	1009.9	999.1	986.7	972.8	957.7	941.5
40	1013.2	1002.6	990.4	976.9	962.0	946.2
50	1016.5	1006.1	994.1	980.8	966.2	950.8

60	1019.9	1009.5	997.7	984.5	970.3	955.2
70	1023.0	1012.9	1001.1	988.3	974.2	959.4
80	1026.1	1016.1	1004.6	991.8	978.1	963.5
90	1029.2	1019.3	1007.9	995.4	981.8	967.4
100	1032.3	1022.4	1011.2	998.8	985.5	971.4
	$w_1 =$	$0.4002 (b_1$	= 7.4852	mol·kg ⁻¹)		
0.1	999.1	985.4	970.3	954.6		
0.5	999.1	985.5	970.6	954.8		
1	999.2	985.6	970.8	955.0	938.0	919.8
2	999.6	986.0	971.2	955.4	938.5	920.4
5	1000.7	987.2	972.5	956.8	940.0	922.1
10	1002.5	989.1	974.6	959.1	942.4	924.9
15	1004.3	991.0	976.6	961.3	944.9	927.5
20	1006.0	992.9	978.6	963.5	947.3	930.1
30	1009.4	996.5	982.5	967.7	951.9	935.2
40	1012.7	1000.0	986.4	971.9	956.3	940.1
50	1016.0	1003.5	990.1	975.8	960.6	944.7
60	1019.2	1006.9	993.6	979.6	964.7	949.2
70	1022.3	1010.2	997.1	983.4	968.7	953.6
80	1025.4	1013.4	1000.6	987.1	972.7	957.7
90	1028.4	1016.5	1003.9	990.6	976.5	961.8
100	1031.4	1019.7	1007.2	994.1 980.1	965.7	

^aExpanded uncertainties (k = 2): U(T) = 0.02 K; $U_r(p) = 0.0002$; $U_r(w) = 0.0004$ and $U(\rho) = 0.7$ kg·m⁻³.

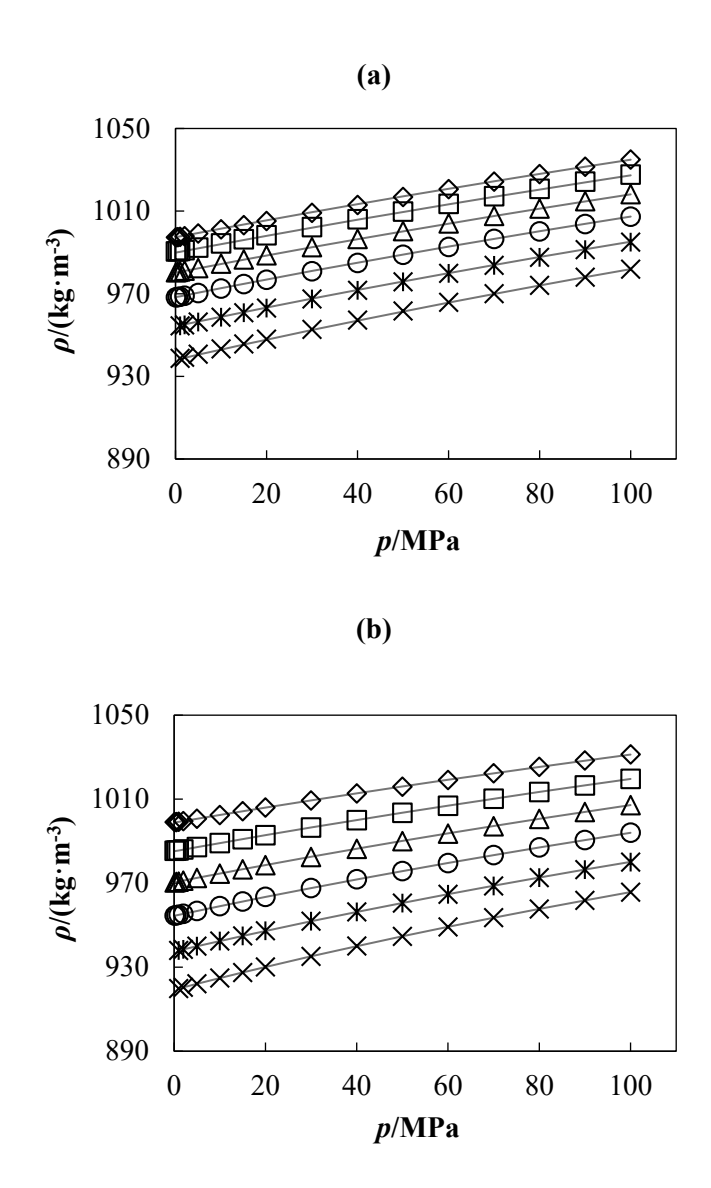


Figure 7.17. Experimental density ρ , of the system AMP(1) + H₂O(2) as a function of pressure p, at amine mass fraction of (a) $w_1 = 0.1$ and (b) $w_1 = 0.4$. Isotherms: (\diamondsuit) T = 293.15 K, (\square) T = 313.15 K, (\triangle) T = 333.15 K, (\bigcirc) T = 353.15 K, (\ast) T = 373.15 K, and (\times) T = 393.15 K. Lines represent the calculated values using modified Tammann-Tait (**Equations 7.1 to 7.4**) with the parameters given in **Tables 7.11 and 7.12**.

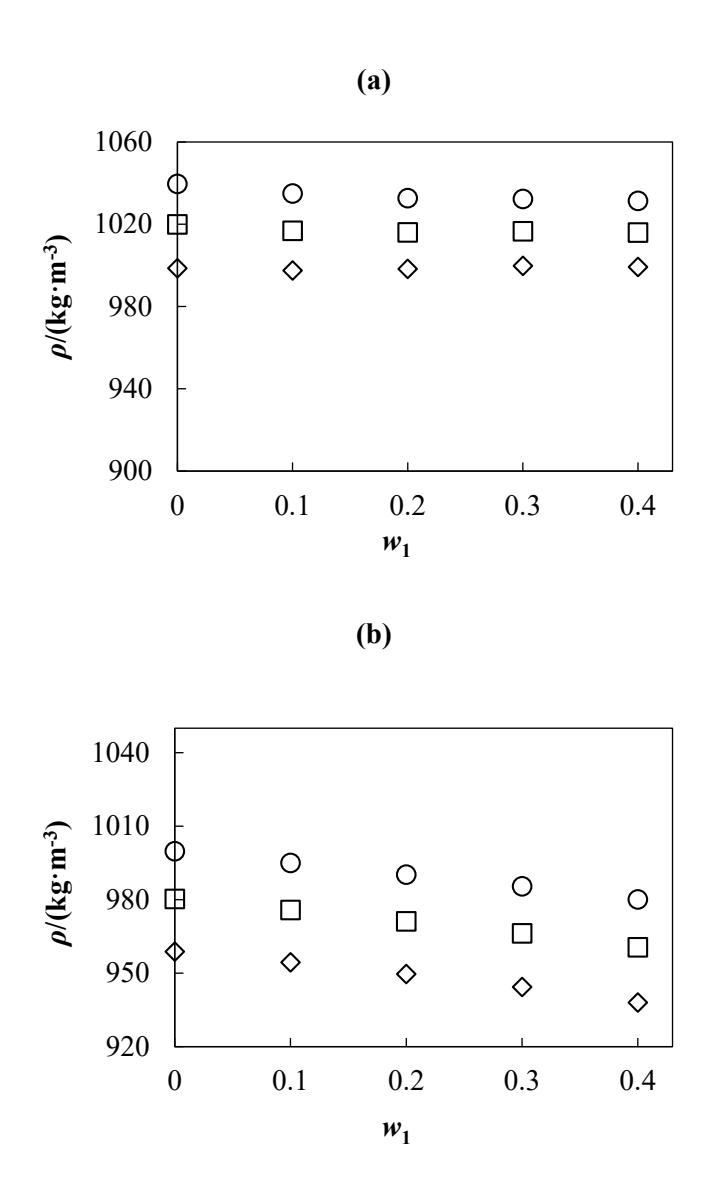


Figure 7.18. Experimental density ρ , of the system AMP(1) + H₂O(2) as a function of amine mass fraction w_1 , at temperatures of (a) T = 293.15 K and (b) T = 373.15 K. Isobars: (\diamondsuit) p = 1 MPa, (\square) p = 50 MPa, and (\bigcirc) p = 100 MPa. Experimental data of pure water ($w_1 = 0$) from NIST REFPROP database [180].

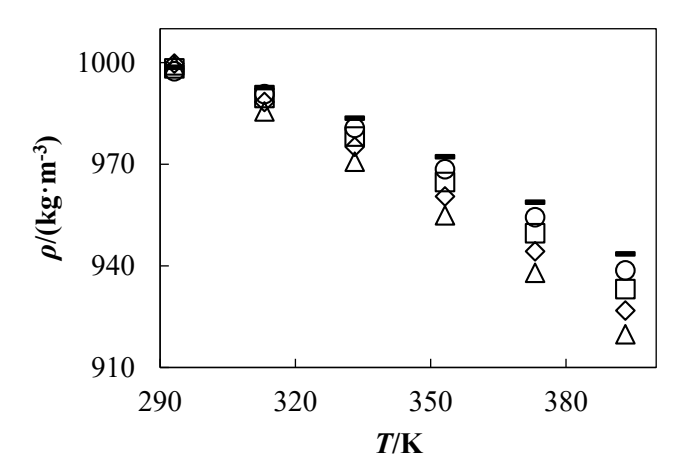


Figure 7.19. Experimental density ρ , of the system AMP(1) + H₂O(2) as a function of temperature T, at pressure p = 1 MPa. Amine mass fractions: (—) $w_1 = 0$, (\bigcirc) $w_1 = 0.1$, (\square) $w_1 = 0.2$, (\diamondsuit) $w_1 = 0.3$, and (\triangle) $w_1 = 0.4$. Experimental data of pure water ($w_1 = 0$) from NIST REFPROP database [180].

7.2.5.2. Comparison with Literature

The relative deviations obtained from the comparison of the experimental densities of AMP + H_2O with 11 references from the literature were generally within the uncertainty of our densimeter, as can be seen in **Figure 7.20**. Zúñiga-Moreno et al. [94] reported measurements at pressures other than atmospheric, yielding results consistent with our measurements. The highest deviations (slightly above the uncertainty) were obtained in the comparison with the data reported by Zúñiga-Moreno et al. [94] at a temperature of 353.15 K and amine mass fraction of 0.3. This result is due to the small difference in the measurement conditions since, as can be seen in **Table 7.10**, these authors measure the density at a temperature of 352.96 K and an amine mass fraction of 0.282.

Table 7.10. Measurement conditions of literature data used to compare the experimental density of $AMP(1) + H_2O(2)$ mixture measured in this work.

Reference	Densimeter	Conditions	Number of Points	$U_{ m r}^{ m a}$
Zúñiga-Moreno et al. [94]	Anton Paar DMA 60/512P	$w_1 = 0.200; 0.282; 0.400$ T = (313.13 - 352.96) K p = (0.5 - 20) MPa	57	0.02 %
Stec et al. [83]	Kyoto Electronics KEM DA-645	$w_1 = 0.300$ T = (293.15 - 333.15) K p = 0.1 MPa	3	NA ^b
Rezaei et al. [93]	Anton Paar Stabinger SVM3000	$w_1 = 0.300$ T = (313.15 - 333.15) K p = 0.1 MPa	2	0.1 %

	~ .	$w_1 = 0.40$		
Das et al. [90]	Gay-Lussac	T = 313 K	1	0.01 %
	pycnometer	p = 0.1 MPa		
Chainainn Pr	Anton Paar DMA-	$w_1 = 0.300; 0.400$		
Shojaeian &		T = (293.15 - 333.15) K	6	0.02 %
Haghtalab [81]	58	p = 0.1 MPa		
Samanta &	Cov. Lugge	$w_1 = 0.300$		
Bandyopadhyay	Gay-Lussac	T = (313.15 - 333.15) K	2	0.01 %
[82]	pycnometer	p = 0.1 MPa		
	Anton Paar DMA-	$w_1 = 0.208$		
Henni et al. [85]	4500	T = (313.15 - 333.15) K	2	NA ^b
	4300	p = 0.1 MPa		
	Anton Paar DMA	$w_1 = 0.097$		
Chan et al. [86]	Anton Paar DMA 45	T = 353.15 K	1	NA ^b
	43	p = 0.1 MPa		
	Gay-Lussac	$w_1 = 0.2; 0.3$		
Li & Lie [89]	•	T = (313.15 - 353.15) K	6	NA ^b
	pycnometer	p = 0.1 MPa		
Aguila-	Anton Paar DMA	$w_1 = 0.298; 0.399$		
Hernández et al.	45	T = (313.15 - 333.15) K	4	NA ^b
[91]	43	p = 0.1 MPa		
Mandal et al.	Gay-Lussac	$w_1 = 0.3$		
	-	T = (293.15 - 313.15) K	2	NA ^b
[92]	pycnometer	p = 0.1 MPa		

^aRelative expanded uncertainty (k = 2), %.

^bNA: Not Available.

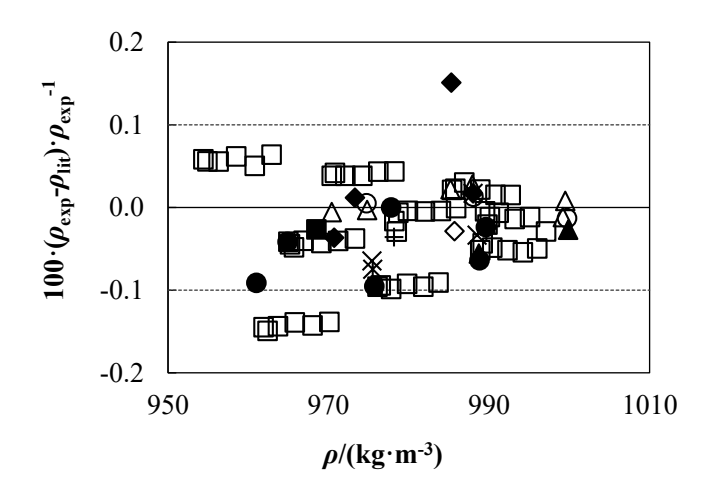


Figure 7.20. Relative deviations (%) of density measurements ρ_{exp} , in comparison with literature values ρ_{lit} . Literature for AMP + H₂O: (\square) Zúñiga-Moreno et al. [94], (\bigcirc) Stec et al. [83], (\times) Rezaei et al. [93], (\diamondsuit) Das et al. [90], (\triangle) Shojaeian & Haghtalab [81], (*) Samanta & Bandyopadhyay [82], (+) Henni et al. [85], (\blacksquare) Chan et al. [86], (\bullet) Li & Lie [89], (\spadesuit) Aguila-Hernández et al. [91], and (\blacktriangle) Mandal et al. [92]. Dashed lines represent the relative expanded uncertainty of our density measurements.

7.2.6. Discussion

The experimental densities of the aqueous amine solutions show the highest to lowest values in the following order: 1-MPZ > AMP > EAE > DEAE > MAPA under the same conditions of pressure, temperature, and amine mass fraction. This difference increases with amine mass fraction, temperature and pressure, reaching a maximum of 3 % difference between the densities of the extreme values, which are the highest density corresponding to the $1\text{-MPZ} + \text{H}_2\text{O}$ mixture and the lowest density corresponding to the MAPA + H₂O mixture, under the same measurement conditions.

EAE and DEAE are two ethanolamines with a similar structure, EAE is a secondary amine and DEAE a tertiary amine. In the comparison of the densities of aqueous solutions of these amines, we found that under the same measurement conditions, EAE + H_2O has a higher density than DEAE + H_2O . This can be explained by the molecular interactions between these amines and water. The molecular interaction between DEAE and H_2O reflects the compaction of the mixture due to a strong hydrogen bonding interaction [64]. This is a consequence of ability of DEAE to attract hydrogens and the donating ability of H_2O . On the other hand, EAE does not have the ability to form strong hydrogen bonds in the interaction with H_2O because this molecule is a secondary amine and has the facility to donate hydrogens rather than accept them [70]. Consequently, EAE + H_2O exhibits lower molecular compaction compared to DEAE + H_2O , resulting in a smaller volume and a higher density. The density difference between these two solutions reached up to 2 %.

The density of these mixtures increases with pressure while maintaining very similar trends for all systems, as can be observed in Figures 7.1, 7.5, 7.9, 7.13, and 7.17. An increase in temperature leads to a decrease in density. This change resembles a linear behaviour for all aqueous mixtures studied, as can be seen in Figures 7.3, 7.7, 7.11, 7.15, and 7.19. Regarding the trend of density with amine mass fraction, two types of behaviours were observed. In the first case, according to Figures 7.2, 7.6, 7.10 and 7.18, it is observed that as the amine mass fraction increases, the density decreases for aqueous solutions of DEAE, EAE, MAPA, and AMP. In the second type of behaviour, as can be seen in Figures 7.14 and 7.15, there is a change in the slope of the curve that describes the trend of density as a function of temperature when the amine mass fraction varies from 0.1 to 0.4 for 1-MPZ aqueous solutions. At temperatures approximately lower than 325 K, the density increases with increasing amine mass fraction, while at temperatures above approximately 325 K, the behaviour is different; an increase in density is caused by a decrease in amine mass fraction. The explanation for this behaviour was given by Rayer et al. [78], who studied the experimental density of 1-MPZ aqueous solutions over the entire range of molar compositions. In this study, it is proposed that the self-association of pure 1-MPZ amine decreases when it is mixed with water. This is due to the hydrogen bonding interactions between 1-MPZ and water, as well as the ability of 1-MPZ molecules to fill the cavities within the loose structure of water. The magnitude of the contributions of these different types of interactions will vary with the amine, the composition of the mixture, and the temperature. Therefore, for this system $(1-MPZ + H_2O)$ at amine mass fractions greater than 0.5, the behaviour trend changes and there are not observed changes in the trend of the curves that describe the density as a function of temperature at fixed amine mass fraction values.

Mixtures like methyldiethanolamine (MDEA) + H_2O , monoethanolamine (MEA) + H_2O , diethanolamine (DEA) + H_2O and triethanolamine (TEA) + H_2O exhibit an increase in density with the rise of amine mass fraction, while 2-(dimethylamino)ethanol (DMEA) + H_2O shows the opposite effect [104,188].

7.2.7. Experimental Density Data Fitting

The experimental density was correlated (see **Equations 7.1 to 7.4**) using a Tammann–Tait equation [189] that was modified to render density as a function of temperature, pressure, and the amine molality b (mol-amine/kg-H₂O). These equations replicate the density correlation model for brines as proposed by Al Ghafri et al. [186,187]. Parameter's standard error analysis was used to reduce overfitting and optimise the parameter set for CO₂-unloaded solutions.

The reference density, ρ_{ref} , is computed with **Equation 7.2**. $\rho_o(T)$ represents the density of saturated liquid water under the vapor pressure conditions at the specified temperature. The vapor pressure and density of water are obtained from the NIST REFPROP database [180].

$$\rho(T, p, b) = \frac{\rho_{\text{ref}}(T, b)}{1 - C(b) \cdot \ln\left(\frac{B(T, b) + p}{B(T, b) + p_{\text{ref}}(T)}\right)}$$
(7.1)

$$[\rho_{ref}(T,b) - \rho_{0}(T)]$$

$$= \alpha_{11} \cdot b \cdot (T/T_{c}) + \alpha_{12} \cdot b \cdot (T/T_{c})^{3/2} + \alpha_{21} \cdot b^{3/2} \cdot (T/T_{c}) + \alpha_{22}$$

$$\cdot b^{3/2} \cdot (T/T_{c})^{3/2} + \alpha_{23} \cdot b^{3/2} \cdot (T/T_{c})^{2} + \alpha_{31} \cdot b^{2} \cdot (T/T_{c}) + \alpha_{32} \cdot b^{2}$$

$$\cdot (T/T_{c})^{3/2} + \alpha_{33} \cdot b^{2} \cdot (T/T_{c})^{2}$$

$$(7.2)$$

$$B(T,b) = \beta_{00} + \beta_{01} \cdot (T/T_c) + \beta_{02} \cdot (T/T_c)^2 + \beta_{03} \cdot (T/T_c)^3 + \beta_{10} \cdot b + \beta_{11} \cdot b$$

$$\cdot (T/T_c) + \beta_{12} \cdot b \cdot (T/T_c)^2$$
(7.3)

$$C(b) = \gamma_0 + \gamma_2 \cdot b^2 \tag{7.4}$$

The critical temperature of pure water, T_c , was 647.10 K in **Equations 7.2 and 7.3**. Firstly, the coefficients β_{00} , β_{01} , β_{02} , β_{03} , and γ_0 in **Equations 7.2 and 7.3** for molality ($b = 0 \text{ mol·kg}^{-1}$) were determined. Then, the remaining coefficients in ρ_{ref} , B and C in **Equations 7.2**, **7.3 and 7.4** were optimised. All fittings were carried out in MATLAB R2023b [190] by minimising the sum of the squares of the differences between the experimental and calculated density values, implementing a Levenberg-Marquardt algorithm [191].

In order to evaluate the goodness-of-fit with this modified Tammann-Tait equation, the following statistical parameters were determined: absolute average relative deviation (AAD) calculated using **Equation 7.5**, maximum absolute relative deviation (MAD) calculated using **Equation 7.6**, and standard deviation (σ) calculated using **Equation 7.7**.

AAD,
$$X = \frac{1}{N} \sum_{i=1}^{N} \frac{|X_{\text{exp,i}} - X_{\text{cal,i}}|}{X_{\text{exp,i}}}$$
 (7.5)

$$MAD, X = \max\left(\frac{|X_{\exp,i} - X_{\text{cal,i}}|}{X_{\exp,i}}\right)$$
(7.6)

$$\sigma, X = \sqrt{\left[\frac{1}{N-m}\right] \sum_{i=1}^{N} \left(X_{\text{exp,i}} - X_{\text{cal,i}}\right)^2}$$
(7.7)

where $X_{\text{exp,i}}$ is the *i*th experimental value of a defined property X, $X_{\text{cal,i}}$ is the *i*th calculated value using the correlation at the same condition, N is the total number of experimental points, and m is the number of fitting parameters.

As a result of the first optimisation, the coefficients β_{00} , β_{01} , β_{02} , β_{03} , and γ_0 in **Equations 7.3 and 7.4** for pure water ($b_1 = 0 \text{ mol·kg}^{-1}$) were determined. **Table 7.11** shows these coefficients, which are the same

for all aqueous amine solutions. The fitting resulted in relative density deviations for pure water below 0.01 %.

Table 7.11. Parameters β_{00} , β_{01} , β_{02} , β_{03} , and γ_0 for pure water ($b_1 = 0 \text{ mol·kg}^{-1}$) in **Equations 7.3 and 7.4**.

eta_{00}	$oldsymbol{eta}_{01}$	eta_{02}	eta_{03}	γο
-2894.127	16489.61	-27612.67	14807.00	0.1326506

The remaining coefficients in **Equations 7.2, 7.3 and 7.4** optimised in the second fitting are shown in **Table 7.12**. The modified correlation satisfactorily represents the density over the entire range of temperature, pressure, and amine molality. **Figures 7.21 to 7.25** show the fitting residuals for the binary systems studied, which mostly agree with the density uncertainty without exhibiting any systematic trend in either molality or density.

Table 7.12. Coefficients in Equations 7.2, 7.3 and 7.4, and statistical parameters AAD, MAD and σ .

Dayamataya			Binary Mixtures		
Parameters	DEAE + H ₂ O	$EAE + H_2O$	$MAPA + H_2O$	$1-MPZ + H_2O$	$AMP + H_2O$
α_{11}	-34.461	-39.462	-77.608	-50.657	-25.398
α_{12}	27.7161	38.529	75.430	56.124	24.764
a_{21}	357.50	299.02	353.11	360.57	269.37
α_{22}	-852.38	-730.34	-849.46	-858.12	-661.13
α_{23}	499.32	446.54	515.95	511.88	404.87
α_{31}	-81.138	-65.622	-76.122	-76.420	-56.509
α_{32}	187.18	160.48	186.35	182.50	137.59
α_{33}	-104.28	-97.859	-114.52	-109.30	-83.300
β_{10}	1059.8	987.32	403.23	395.67	909.88
$oldsymbol{eta}_{11}$	391.78	352.69	-1331.8	-1270.3	332.43
$oldsymbol{eta}_{12}$	-1296.5	-1178.5	1107.7	1029.3	-1096.3
γ ₂	6.4148 · 10-4	3.4143·10 ⁻⁴	3.7682·10 ⁻⁴	5.0526·10 ⁻⁴	3.4966·10 ⁻⁴
AAD	0.03 %	0.02 %	0.02 %	0.02 %	0.02 %
MAD	0.2 %	0.1 %	0.1 %	0.1 %	0.1 %
$\sigma/(\text{kg}\cdot\text{m}^{-3})$	0.4	0.3	0.3	0.2	0.3

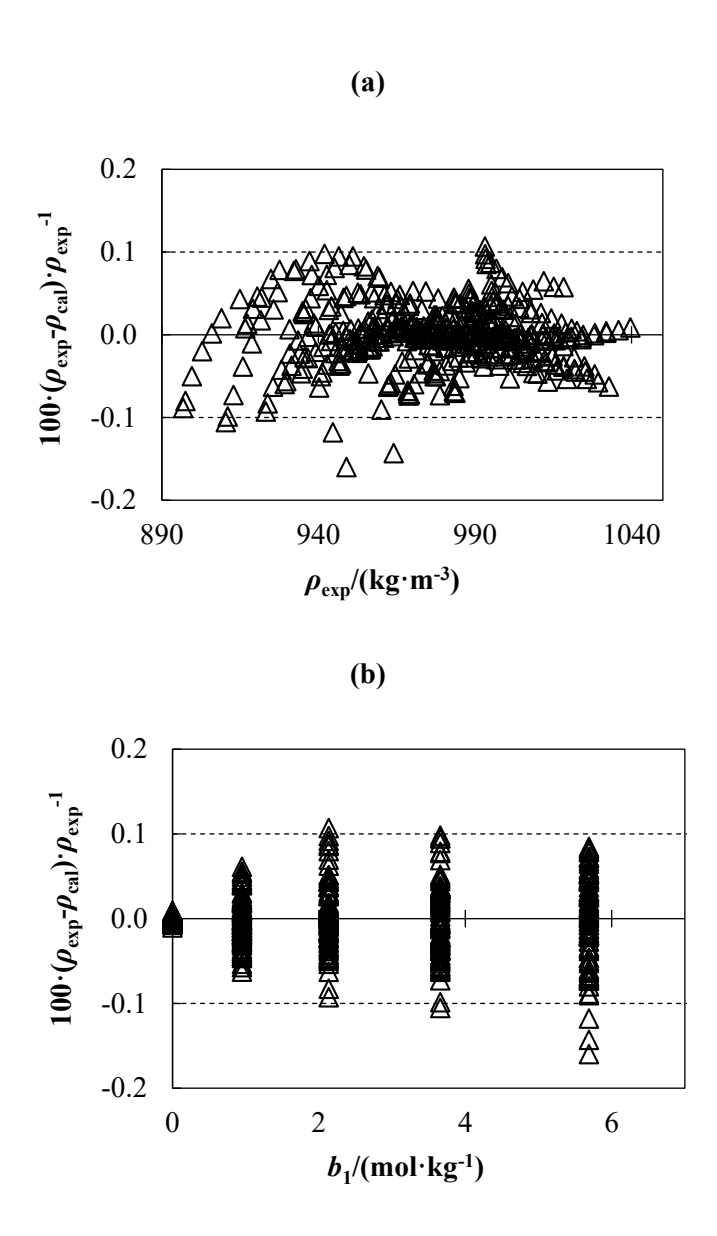


Figure 7.21. Relative deviations (%) for DEAE(1) + $H_2O(2)$ mixture of experimental density measurements, ρ_{exp} , in comparison with calculated density, ρ_{cal} , using **Equations 7.1 to 7.4**. (a) Relative deviations vs ρ_{exp} and (b) Relative deviations vs b_1 . Dashed lines represent the relative expanded uncertainty of our density measurements.

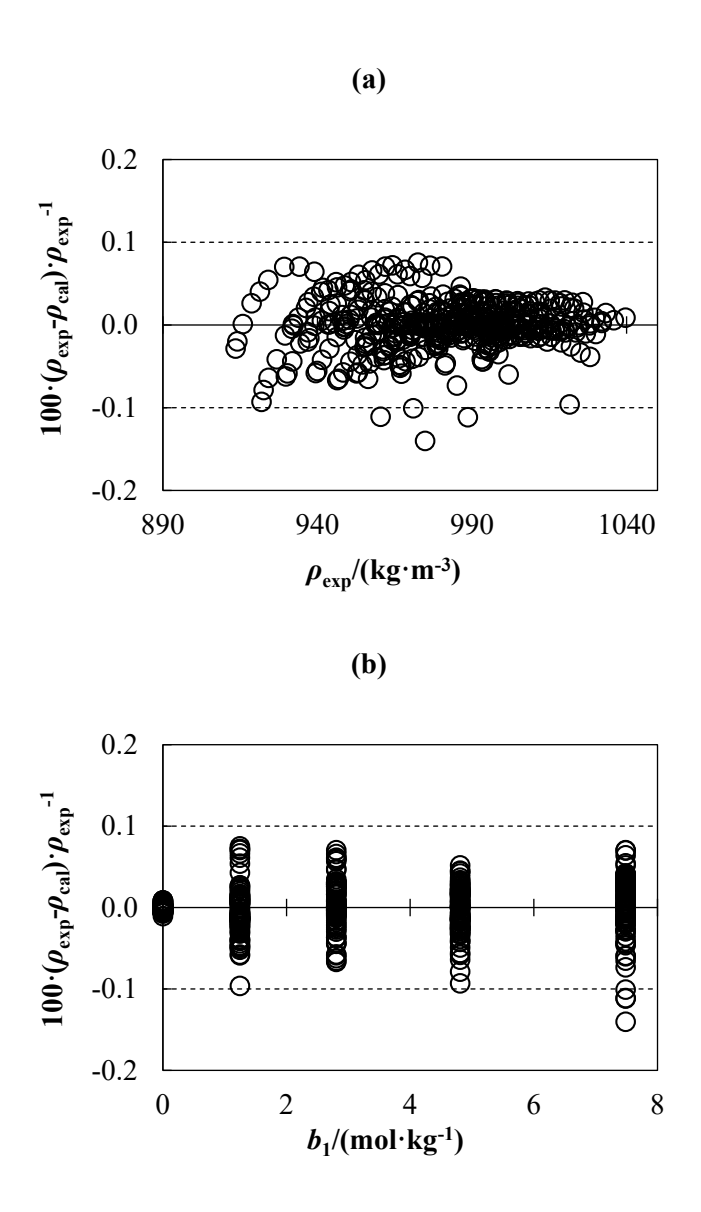


Figure 7.22. Relative deviations (%) for EAE(1) + $H_2O(2)$ mixture of experimental density measurements, ρ_{exp} , in comparison with calculated density, ρ_{cal} , using **Equations 7.1 to 7.4**. (a) Relative deviations vs ρ_{exp} and (b) Relative deviations vs b_1 . Dashed lines represent the relative expanded uncertainty of our density measurements.

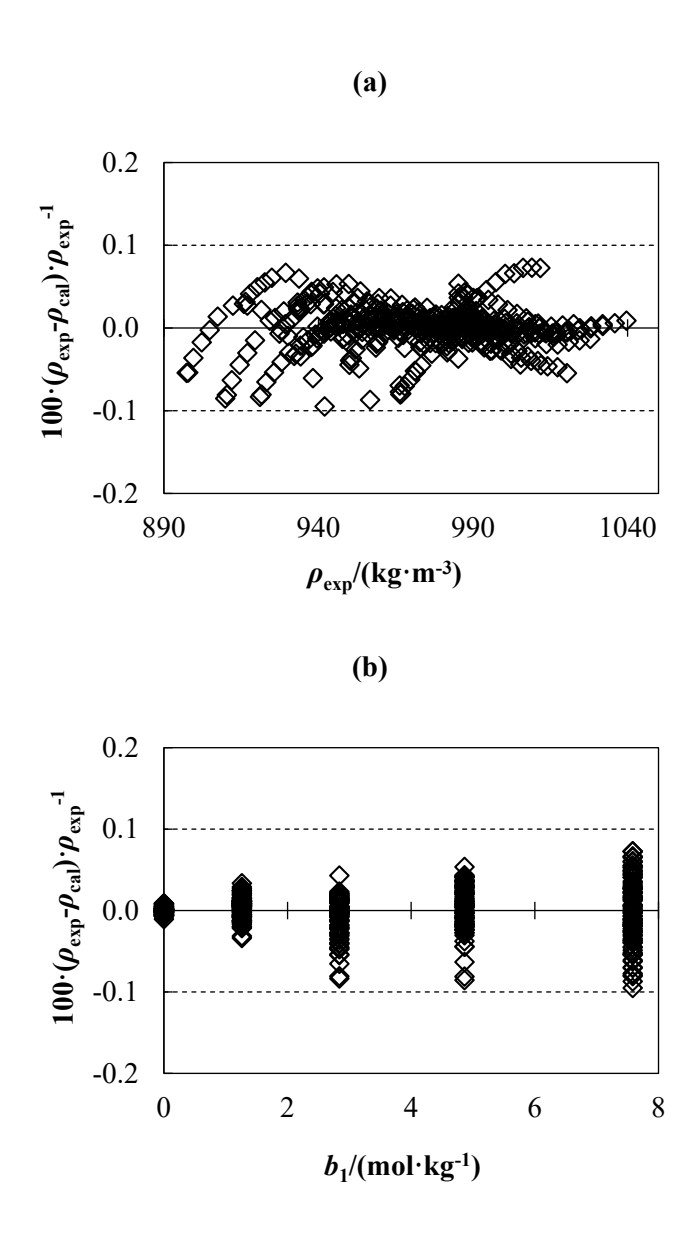


Figure 7.23. Relative deviations (%) for MAPA(1) + $H_2O(2)$ mixture of experimental density measurements, ρ_{exp} , in comparison with calculated density, ρ_{cal} , using **Equations 7.1 to 7.4**. (a) Relative deviations vs ρ_{exp} and (b) Relative deviations vs b_1 . Dashed lines represent the relative expanded uncertainty of our density measurements.

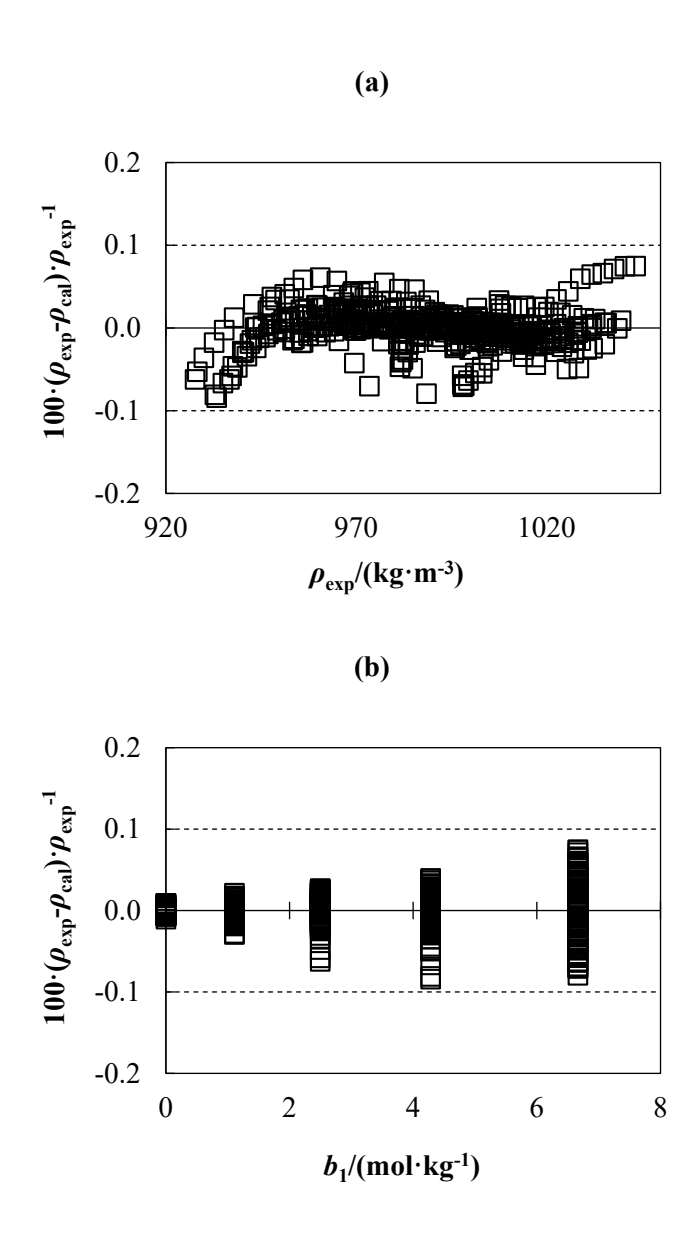


Figure 7.24. Relative deviations (%) for 1-MPZ(1) + H₂O(2) mixture of experimental density measurements, $\rho_{\rm exp}$, in comparison with calculated density, $\rho_{\rm cal}$, using **Equations 7.1 to 7.4**. (a) Relative deviations vs $\rho_{\rm exp}$ and (b) Relative deviations vs b_1 . Dashed lines represent the relative expanded uncertainty of our density measurements.

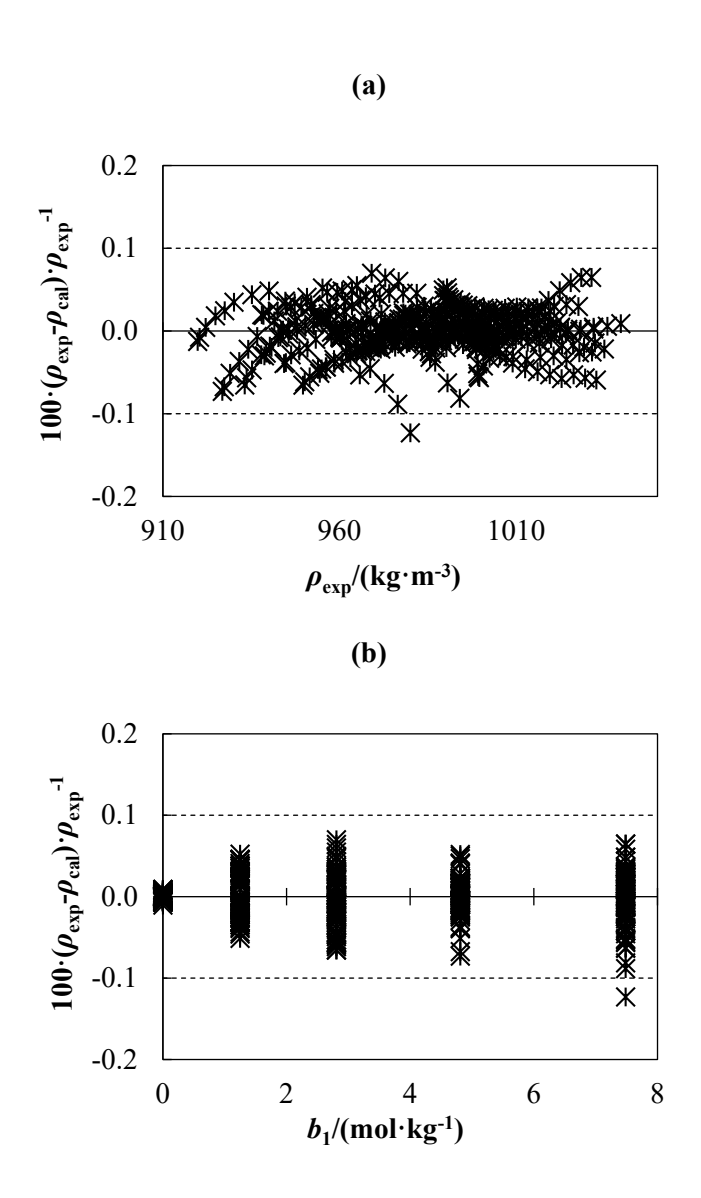


Figure 7.25. Relative deviations (%) for AMP(1) + $H_2O(2)$ mixture of experimental density measurements, ρ_{exp} , in comparison with calculated density, ρ_{cal} , using **Equations 7.1 to 7.4**. (a) Relative deviations vs ρ_{exp} and (b) Relative deviations vs b_1 . Dashed lines represent the relative expanded uncertainty of our density measurements.

7.2.7.1. Comparison of Calculated Density with Experimental Literature Data

Calculated density values for the studied binary mixtures, derived from **Equations 7.1 to 7.4**, were compared against literature data given in Table 1.2 in Chapter 1, effectively expanding the experimental density comparison range presented in this chapter. The following results were obtained.

• For the DEAE + H₂O mixture, 5 references were used for comparison, with a total of 87 data points. The average absolute relative deviation was 0.05 %, with a maximum of 0.1 % (see Figure 7.26).

- For the EAE + H₂O mixture, 4 references were used for comparison, with a total of 76 data points. The average absolute relative deviation was 0.1 %, with a maximum of 0.3 % (see Figure 7.27).
- For the MAPA + H₂O mixture, 3 references were used for comparison, with a total of 57 data points. The average absolute relative deviation was 0.09 %, with a maximum of 0.2 % (see Figure 7.28).
- For the 1-MPZ + H₂O mixture, 2 references were used for comparison, with a total of 62 data points. The average absolute relative deviation was 0.09 %, with a maximum of 0.3 % (see **Figure 7.29**).
- For the AMP + H₂O mixture, 6 references were used for comparison, with a total of 457 data points. The average absolute relative deviation was 0.3 %, with a maximum of 0.9 % (see **Figure 7.30**).

The reasons for the observed discrepancies between calculated and literature densities are unclear, particularly in the AMP + H₂O mixture.

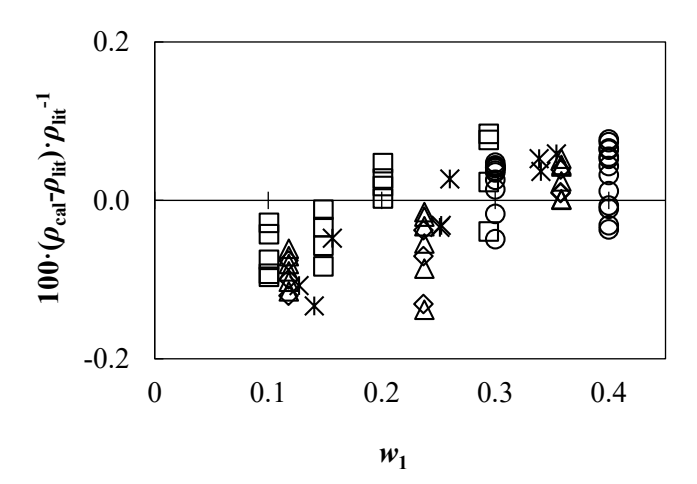


Figure 7.26. Relative deviations (%) vs amine mass fraction w_1 for DEAE(1) + H₂O(2) mixture of calculated density ρ_{cal} , using **Equations 7.1 to 7.4**, in comparison with density literature values ρ_{lit} . Literature: (\bigcirc) Karunarathne et al. [62], (\square) Lebrette et al. [60], (\diamondsuit) Xu et al. [59], (\triangle) Pinto et al. [63], and (*) Hawrylak et al. [64].

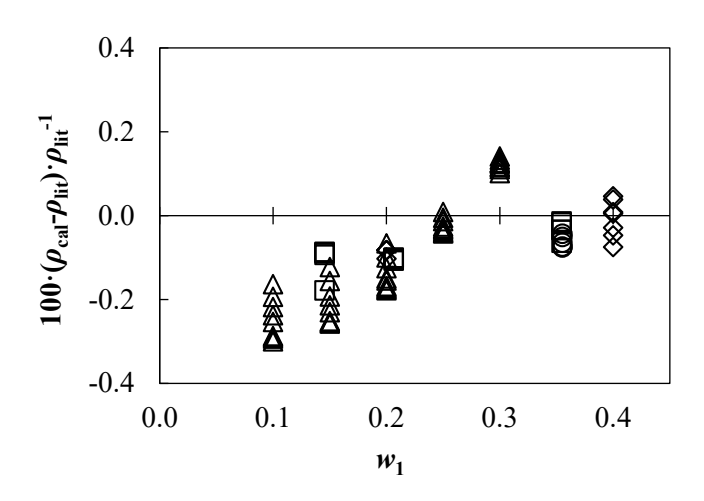


Figure 7.27. Relative deviations (%) vs amine mass fraction w_1 for EAE(1) + H₂O(2) mixture of calculated density ρ_{cal} , using **Equations 7.1 to 7.4**, in comparison with density literature values ρ_{lit} . Literature: (\bigcirc) Zhu et al. [70], (\square) Chowdhury et al. [71], (\diamondsuit) Viet et al. [72], and (\triangle) Pandey & Mondal [73].

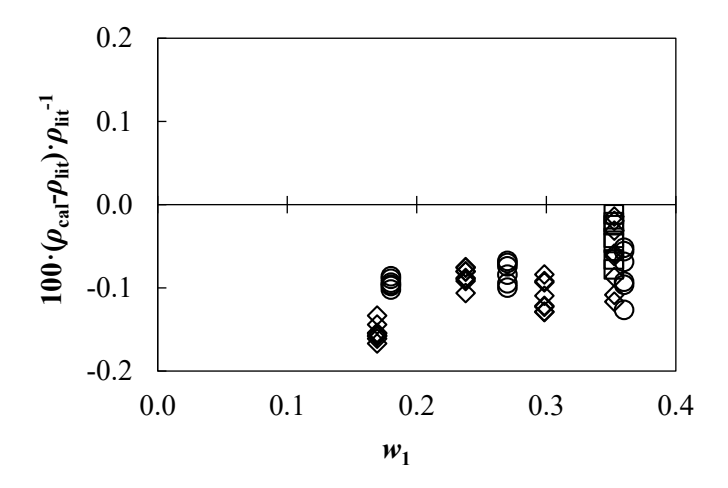


Figure 7.28. Relative deviations (%) vs amine mass fraction w_1 for MAPA(1) + H₂O(2) mixture of calculated density ρ_{cal} , using **Equations 7.1 to 7.4**, in comparison with density literature values ρ_{lit} . Literature: (\bigcirc) Monteiro et al. [76], (\square) Pinto et al. [63], and (\diamondsuit) Wang et al. [77].

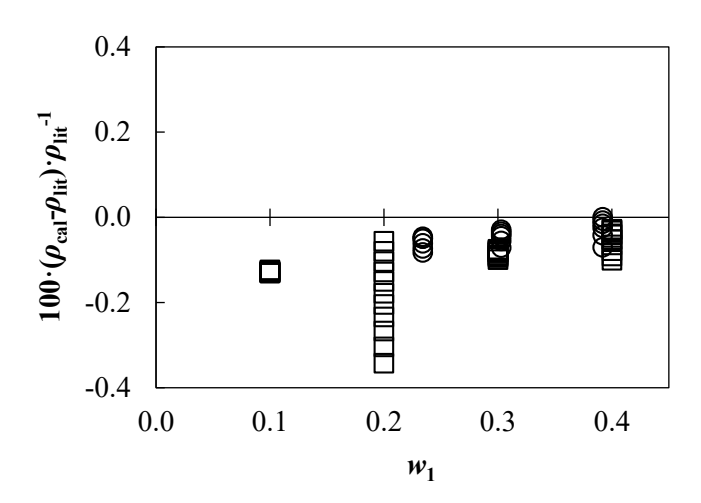


Figure 7.29. Relative deviations (%) vs amine mass fraction w_1 for 1-MPZ(1) + H₂O(2) mixture of calculated density ρ_{cal} , using **Equations 7.1 to 7.4**, in comparison with density literature values ρ_{lit} . Literature: (\bigcirc) Rayer et al. [78], and (\square) Vamja et al. [38].

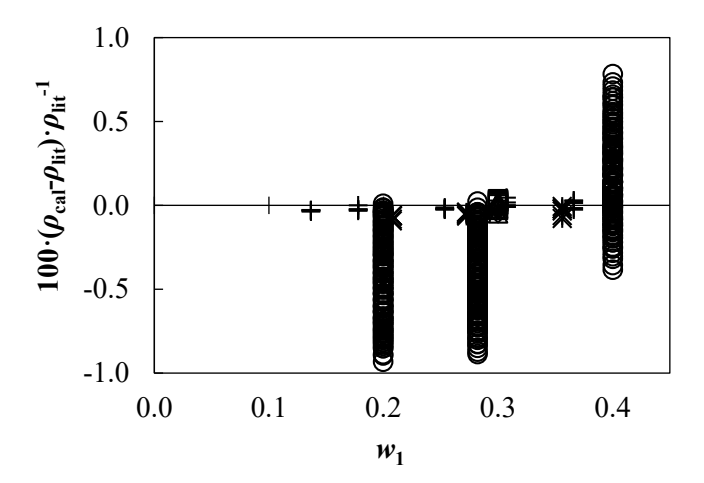


Figure 7.30. Relative deviations (%) vs amine mass fraction w_1 for 1-MPZ(1) + H₂O(2) mixture of calculated density ρ_{cal} , using **Equations 7.1 to 7.4**, in comparison with density literature values ρ_{lit} . Literature: (\bigcirc) Zúñiga-Moreno et al. [94], (\square) Shojaeian & Haghtalab [81], (\diamondsuit) Samanta & Bandyopadhyay [82], (\triangle) Stee et al. [83], (*) Henni et al. [85], and (+) Chan et al. [86].

7.3. Ternary Mixtures. CO₂-Loaded Aqueous Amine Solutions

7.3.1.
$$MEA + H_2O + CO_2$$

7.3.1.1. Experimental Density

The results of the density measurements of the aqueous amine solutions are presented in **Table 7.13** for MEA + H_2O + CO_2 . In order to analyse the impact of pressure, CO_2 loading, and temperature, the

experimental density data were plotted as a function of these variables for all the studied systems, as can be observed in Figures 7.31 to 7.33.

Table 7.13. Experimental densities ρ , for the system MEA(1) + H₂O(2) + CO₂(3) with amine mass fraction (CO₂-free basis) w_1 = 0.3002, at different conditions of temperature T, pressure p, CO₂ loading α in terms of mol-CO₂/mol-MEA, and equivalent CO₂ molality b_3 .

$\rho/(\text{kg}\cdot\text{m}^{-3})$							
			T/	K			
p/MPa	293.15	313.15	333.15	353.15	373.15	393.15	
	$\alpha = 0.10$	$0 (b_3 = 0.4)$.94 mol·kg	g ⁻¹)			
0.1	1032.7	1023.4	1012.1	999.8			
0.5	1032.7	1023.4	1012.3	1000.0			
1	1032.9	1023.5	1012.5	1000.1			
2	1033.2	1023.9	1012.9	1000.6			
5	1034.3	1025.0	1014.1	1001.8	987.9	972.9	
10	1036.1	1026.8	1016.0	1003.8	990.1	975.3	
20	1039.7	1030.4	1019.8	1007.7	994.3	979.8	
30	1043.1	1034.0	1023.4	1011.6	998.4	984.2	
40	1046.6	1037.4	1027.1	1015.4	1002.3	988.5	
50	1050.0	1040.9	1030.6	1019.1	1006.2	992.6	
60	1053.2	1044.2	1034.0	1022.6	1010.0	996.6	
70	1056.5	1047.5	1037.4	1026.1	1013.6	1000.5	
80	1059.7	1050.7	1040.7	1029.6	1017.3	1004.3	
90	1062.9	1053.9	1044.0	1033.0	1020.8	1008.0	
100	1066.0	1057.1	1047.3	1036.2	1024.3	1011.6	
	$\alpha = 0.20$	$0 (b_3 = 0.9)$	89 mol·kg	g ⁻¹)			
0.1	1052.3	1043.6	1032.2	1020.1			
0.5	1052.3	1043.6	1032.4	1020.3			
1	1052.4	1043.5	1032.6	1020.5			
2	1052.7	1043.8	1033.0	1020.9			
5	1053.9	1044.9	1034.1	1022.1	1008.5	994.0	
10	1055.7	1046.7	1036.1	1024.1	1010.7	996.3	
20	1059.2	1050.2	1039.7	1027.9	1014.8	1000.7	
30	1062.6	1053.7	1043.3	1031.6	1018.8	1005.0	
40	1065.9	1057.1	1046.9	1035.3	1022.6	1009.0	
50	1069.3	1060.5	1050.4	1038.9	1026.4	1013.0	

60	1072.6	1063.9	1053.7	1042.4	1030.1	1017.0
70	1075.8	1067.1	1057.0	1045.9	1033.7	1020.8
80	1078.9	1070.3	1060.3	1049.3	1037.2	1024.5
90	1082.1	1073.5	1063.5	1052.6	1040.7	1028.1
100	1085.1	1076.5	1066.7	1055.8	1044.1	1031.7
	$\alpha = 0.40$	$0 (b_3 = 1.9)$	78 mol·kg	g ⁻¹)		
0.1	1091.3	1082.1	1071.1	1059.3		
0.5	1091.3	1081.9	1071.3	1059.4		
1	1091.4	1082.2	1071.5	1059.6		
2	1091.7	1082.5	1071.8	1060.0		
5	1092.8	1083.6	1072.9	1061.1	1048.1	1033.7
10	1094.6	1085.4	1074.8	1063.0	1050.1	1036.0
20	1098.0	1088.8	1078.3	1066.7	1053.9	1040.1
30	1101.3	1092.2	1081.8	1070.2	1057.8	1044.1
40	1104.6	1095.5	1085.2	1073.8	1061.3	1048.1
50	1107.8	1098.8	1088.6	1077.2	1064.9	1051.9
60	1111.0	1102.0	1091.8	1080.7	1068.6	1055.6
70	1114.1	1105.3	1095.1	1084.0	1071.9	1059.3
80	1117.3	1108.4	1098.2	1087.3	1075.3	1062.8
90	1120.3	1111.4	1101.4	1090.4	1078.6	1066.3
100	1123.2	1114.4	1104.5	1093.6	1081.9	1069.7
	$\alpha = 0.60$	$9 (b_3 = 3.0)$	11 mol·kg	g ⁻¹)		
0.1	1126.5	1117.0	1105.9	1093.8		
0.5	1126.6	1117.1	1106.0	1094.0		
1	1126.8	1117.2	1106.2	1094.0		
2	1127.0	1117.5	1106.6	1094.4		
5	1128.1	1118.5	1107.6	1095.6	1082.0	1066.8
10	1129.8	1120.2	1109.4	1097.4	1084.0	1069.0
20	1133.2	1123.6	1112.9	1101.0	1087.9	1073.1
30	1136.4	1126.9	1116.3	1104.5	1091.6	1077.2
40	1139.7	1130.2	1119.6	1108.0	1095.2	1081.1
50	1142.9	1133.4	1122.9	1111.4	1098.8	1084.9
60	1146.1	1136.5	1126.1	1114.7	1102.3	1088.8
70	1149.2	1139.6	1129.2	1118.0	1105.7	1092.4
80	1152.2	1142.7	1132.3	1121.1	1109.1	1095.9
90	1155.2	1145.7	1135.4	1124.2	1112.2	1099.3

100 1158.2 1148.7 1138.3 1127.3 1115.5 1102.8

^aExpanded uncertainty (k = 2): U(T) = 0.02 K; $U_r(p) = 0.0002$; $U_r(w) = 0.0004$; $U_r(\alpha) = 0.003$ and $U(\rho) = 2 \text{ kg} \cdot \text{m}^{-3}$.

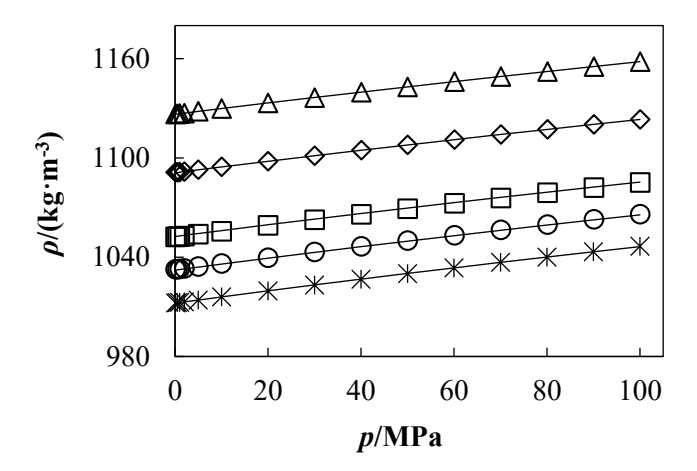


Figure 7.31. Experimental density ρ , of the system MEA(1) + H₂O(2) + CO₂(3) as a function of pressure ρ , at temperature T=293.15 K. CO₂ loadings: (*) $\alpha=0$ mol-CO₂/mol-MEA, (\bigcirc) $\alpha=0.1$ mol-CO₂/mol-MEA, (\bigcirc) $\alpha=0.2$ mol-CO₂/mol-MEA, and (\triangle) $\alpha=0.6$ mol-CO₂/mol-MEA. Experimental density data of aqueous amine solution (CO₂-free basis) from [104]. Lines represent the calculated values using modified Tammann-Tait (**Equations 7.1 to 7.4**) with the parameters given in **Table 7.21**.

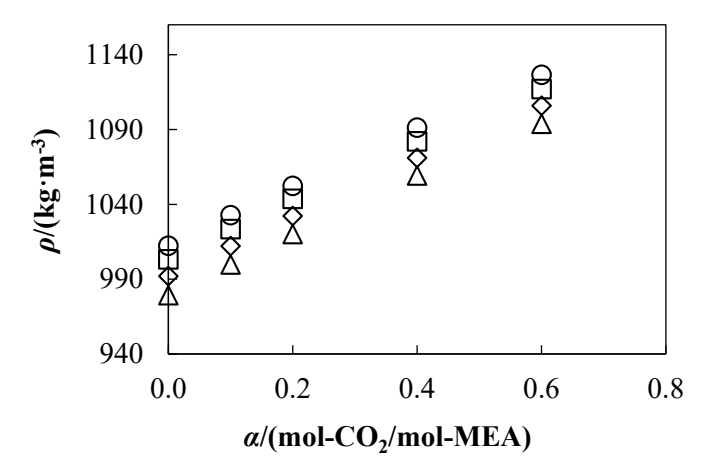


Figure 7.32. Experimental density ρ , of the system MEA(1) + H₂O(2) + CO₂(3) as a function of CO₂ loading α , at pressure p = 0.1 MPa. Isotherms: (\bigcirc) T = 293.15 K, (\bigcirc) T = 313.15 K, (\bigcirc) T = 333.15 K, and (\triangle) T = 353.15 K. Experimental density data of aqueous amine solution (CO₂-free basis) from [104].

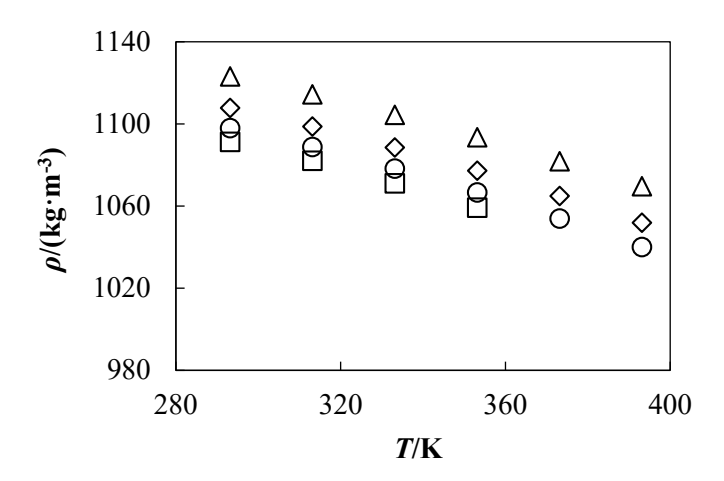


Figure 7.33. Experimental density ρ , of the system MEA(1) + H₂O(2) + CO₂(3) as a function of temperature T, at CO₂ loading $\alpha = 0.4$ mol-CO₂/mol-MEA. Isobars: (\square) p = 0.1 MPa, (\bigcirc) p = 20 MPa, (\bigcirc) p = 50 MPa, and (\triangle) p = 100 MPa.

7.3.1.2. Comparison with Literature

Table 7.14 details the temperature, pressure, and CO₂ loading conditions reported in the references used for the comparison of our density data. As shown in **Figure 7.34**, the relative deviations are within 0.7 %, which is within the uncertainties reported in the literature. The high uncertainty value in CO₂ loading was the main contributor to the deviations observed in the comparison.

Table 7.14. Measurement conditions of literature data used to compare the experimental density of MEA(1) + $H_2O(2)$ + $CO_2(3)$ mixture measured in this work. CO_2 loading α in terms of mol- CO_2 /molamine.

Reference	Densimeter	Conditions	Number of Points	$U_{\rm r}(\alpha)^{\rm a}$	$U_{ m r}(ho)^{ m b}$
Amundsen et al. [108]	Anton Paar DMA 4500	T = (313.15 - 353.15) K p = 0.1 MPa $\alpha = 0.1 - 0.4$	6	2 %	0.4 %
Han et al. [109]	Anton Paar DMA 4500	T = (313.15 - 353.15) K p = 0.1 MPa $\alpha = 0.1 - 0.2$	6	2 %	0.3 %
Jayarathna et al. [113]	Anton Paar DMA HP	T = (313.15 - 333.15) K p = 0.8 MPa $\alpha = 0.1 - 0.4$	6	0.5 %	0.4 %
Hartono et al. [110]	Anton	T = (293.15 - 353.15) K p = 0.1 MPa	12	5 %	0.002 %

	Paar DMA	$\alpha = 0.1 - 0.4$			
	4500 M				
Spiotz et al	KEM Kyoto	T = (293.15 - 333.15) K			
Spietz et al.	Electronics	p = 0.1 MPa	9	4 %	0.005 %
F . J	DA-645	$\alpha = 0.1 - 0.4$			

^aRelative expanded uncertainty in CO₂ loading (k = 2), %.

^bRelative expanded uncertainty in density (k = 2), %.

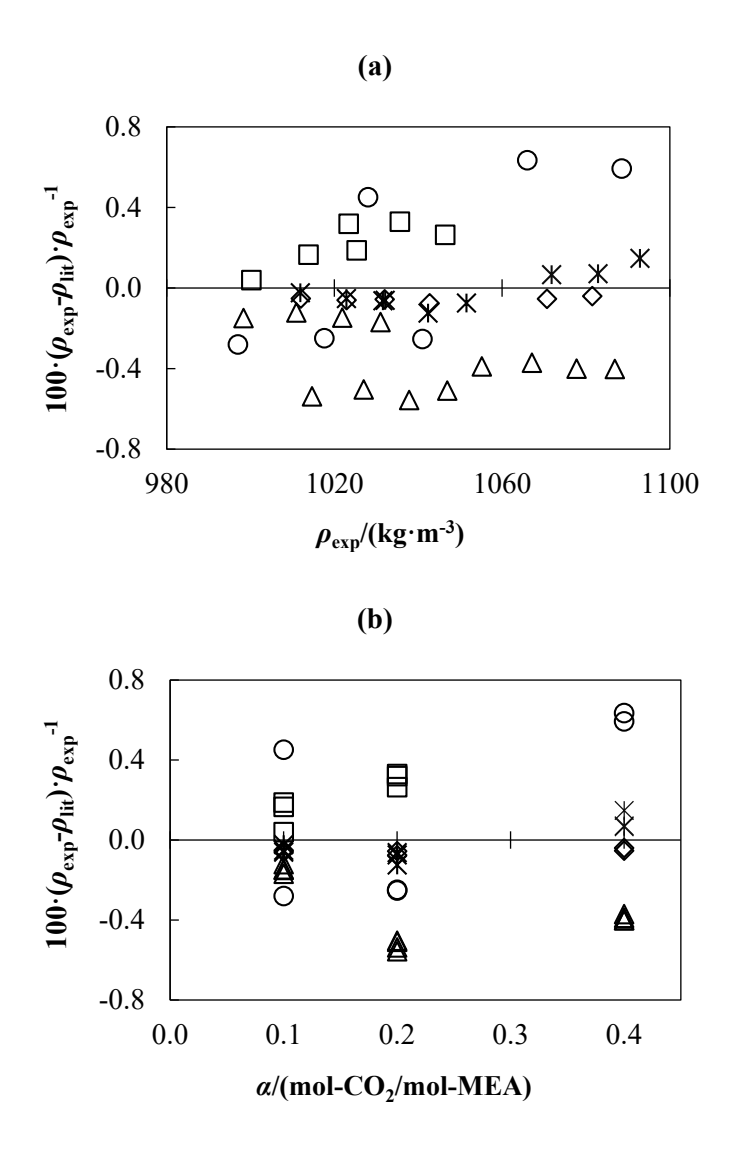


Figure 7.34. Relative deviations (%) of density measurements ρ_{exp} , in comparison with literature values ρ_{lit} . (a) Relative deviations vs ρ_{exp} , y (b) Relative deviations vs α . Literature for MEA + H₂O + CO₂: (\bigcirc) Amundsen et al. [108], (\square) Han et al. [109], (\diamondsuit) Jayarathna et al. [113], (\triangle) Hartono et al. [110], and (*) Spietz et al. [117].

7.3.2. $MDEA + H_2O + CO_2$

7.3.2.1. Experimental Density

The results of the density measurements of the aqueous amine solutions are presented in **Table 7.15** for MDEA + H₂O + CO₂. In order to analyse the impact of pressure, CO₂ loading, and temperature, the experimental density data were plotted as a function of these variables for all the studied systems, as can be observed in **Figures 7.35 to 7.37**.

Table 7.15. Experimental densities ρ , for the system MDEA(1) + H₂O(2) + CO₂(3) with amine mass fraction (CO₂-free basis) $w_1 = 0.3000$, at different conditions of temperature T, pressure p, CO₂ loading α in terms of mol-CO₂/mol-MDEA, and equivalent CO₂ molality b_3 .

$ ho/(\mathrm{kg}\cdot\mathrm{m}^{-3})$									
	T/K								
p/MPa	293.15	313.15	333.15	353.15	373.15	393.15			
$\alpha = 0.100 \ (b_3 = 0.253 \ \text{mol} \cdot \text{kg}^{-1})$									
0.1	1035.8	1026.0	1014.0	1000.6					
0.5	1035.8	1026.1	1014.2	1000.8					
1	1036.0	1026.2	1014.4	1000.9					
2	1036.3	1026.6	1014.8	1001.3					
5	1037.5	1027.7	1016.0	1002.6	987.7	971.4			
10	1039.4	1029.6	1018.0	1004.7	990.0	973.9			
15	1041.2	1031.5	1019.9	1006.8	992.2	976.3			
20	1043.0	1033.3	1021.9	1008.8	994.4	978.7			
30	1046.6	1037.0	1025.6	1012.8	998.7	983.3			
40	1050.1	1040.6	1029.4	1016.7	1002.8	987.8			
50	1053.6	1044.1	1033.1	1020.6	1006.8	992.1			
60	1057.0	1047.6	1036.6	1024.3	1010.8	996.3			
70	1060.4	1051.0	1040.1	1027.9	1014.5	1000.4			
80	1063.8	1054.4	1043.6	1031.5	1018.3	1004.4			
90	1067.0	1057.7	1046.9	1035.0	1022.1	1008.2			
100	1070.2	1060.9	1050.2	1038.4	1025.6	1012.0			
$\alpha = 0.200 \ (b_3 = 0.507 \ \text{mol} \cdot \text{kg}^{-1})$									
0.1	1044.4	1034.3	1022.1	1008.8					
0.5	1044.4	1034.4	1022.3	1008.9					
1	1044.6	1034.5	1022.5	1009.1					
2	1044.9	1034.9	1022.9	1009.5					

5	1046.1	1036.0	1024.1	1010.7	995.9	979.6
10	1048.0	1037.9	1026.1	1012.8	998.1	982.1
15	1049.8	1039.8	1028.1	1014.9	1000.3	984.4
20	1051.6	1041.6	1030.0	1016.9	1002.5	986.8
30	1055.2	1045.3	1033.8	1020.8	1006.9	991.4
40	1058.8	1048.8	1037.5	1024.7	1010.9	995.9
50	1062.3	1052.4	1041.1	1028.5	1014.9	1000.2
60	1065.8	1055.9	1044.6	1032.2	1018.7	1004.4
70	1069.1	1059.3	1048.1	1035.8	1022.6	1008.4
80	1072.5	1062.7	1051.5	1039.4	1026.3	1012.3
90	1075.6	1065.9	1054.8	1042.7	1029.8	1016.2
100	1079.0	1068.9	1058.0	1046.2	1033.5	1019.9
	$\alpha = 0.40$	$0 (b_3 = 1.0)$	014 mol·k	(g^{-1})		
0.1	1060.4	1049.9	1037.6	1024.2		
0.5	1060.4	1049.9	1037.8	1024.4		
1	1060.6	1050.1	1037.9	1024.5		
2	1060.9	1050.4	1038.3	1024.9		
5	1062.1	1051.5	1039.5	1026.2	1011.4	994.7
10	1063.9	1053.4	1041.5	1028.3	1013.6	997.2
15	1065.8	1055.3	1043.4	1030.3	1015.7	999.6
20	1067.6	1057.1	1045.3	1032.2	1017.9	1001.9
30	1071.2	1060.8	1049.0	1036.1	1022.1	1006.6
40	1074.8	1064.3	1052.7	1039.9	1026.1	1010.9
50	1078.3	1067.8	1056.3	1043.6	1030.0	1015.2
60	1081.8	1071.3	1059.8	1047.3	1033.8	1019.4
70	1085.2	1074.8	1063.3	1050.9	1037.6	1023.4
80	1088.5	1078.1	1066.7	1054.3	1041.3	1027.3
90	1091.8	1081.3	1069.9	1057.8	1044.8	1031.1
100	1095.1	1084.6	1073.2	1061.1	1048.3	1034.8
	$\alpha = 0.60$	$0 (b_3 = 1.5)$	521 mol·k	(g ⁻¹)		
0.1	1076.4	1065.7	1053.4	1040.1		
0.5	1076.4	1065.8	1053.6	1040.3		
1	1076.6	1065.9	1053.7	1040.4		
2	1076.9	1066.3	1054.2	1040.8		
5	1078.1	1067.4	1055.3	1042.0	1027.1	1009.8
10	1079.9	1069.2	1057.3	1044.0	1029.3	1012.2

15	1081.8	1071.1	1059.1	1046.0	1031.4	1014.7
20	1083.6	1072.9	1061.0	1048.0	1033.5	1017.0
30	1087.2	1076.5	1064.7	1051.8	1037.7	1021.7
40	1090.8	1080.0	1068.3	1055.6	1041.6	1026.1
50	1094.2	1083.5	1071.8	1059.3	1045.6	1030.4
60	1097.7	1086.9	1075.3	1062.8	1049.4	1034.5
70	1101.1	1090.3	1078.7	1066.3	1053.1	1038.5
80	1104.4	1093.6	1082.0	1069.7	1056.7	1042.5
90	1107.7	1096.9	1085.3	1073.1	1060.2	1046.2
100	1111.0	1100.1	1088.5	1076.3	1063.6	1049.9
	$\alpha = 0.80$	$8 (b_3 = 2.0)$	048 mol·k	(g^{-1})		
0.1	1092.2	1081.5	1069.3	1056.0		
0.5	1092.3	1081.6	1069.5	1056.1		
1	1092.4	1081.8	1069.7	1056.3		
2	1092.7	1082.1	1070.1	1056.7		
5	1093.8	1083.2	1071.2	1057.9	1042.5	1024.0
10	1095.7	1085.0	1073.2	1059.9	1044.7	1026.6
15	1097.5	1086.8	1075.0	1061.8	1046.9	1029.1
20	1099.2	1088.6	1076.8	1063.8	1049.0	1031.6
30	1102.7	1092.1	1080.4	1067.6	1053.2	1036.3
40	1106.2	1095.6	1084.0	1071.3	1057.2	1040.8
50	1109.6	1098.9	1087.4	1075.0	1061.0	1045.1
60	1113.1	1102.3	1090.8	1078.5	1064.9	1049.3
70	1116.3	1105.6	1094.1	1081.9	1068.5	1053.4
80	1119.6	1108.9	1097.4	1085.3	1072.1	1057.4
90	1122.8	1112.1	1100.8	1088.6	1075.6	1061.2
100	1125.9	1115.2	1103.8	1091.9	1079.0	1064.9
	$\alpha = 0.89$	$6 (b_3 = 2.2)$	271 mol·k	(g ⁻¹)		
0.1	1108.5	1098.2	1086.0	1072.3		
0.5	1108.5	1098.3	1086.2	1072.3		
1	1108.6	1098.4	1086.4	1072.5		
2	1108.9	1098.7	1086.7	1072.9		
5	1110.0	1099.8	1087.8	1074.1	1057.6	1037.4
10	1111.8	1101.5	1089.7	1076.1	1059.9	1040.1
15	1113.5	1103.3	1091.6	1078.0	1062.0	1042.7
20	1115.2	1105.0	1093.4	1080.0	1064.2	1045.2

30	1118.5	1108.5	1096.9	1083.7	1068.4	1050.1
40	1121.9	1111.7	1100.4	1087.4	1072.4	1054.7
50	1125.1	1115.0	1103.8	1091.1	1076.3	1059.2
60	1128.3	1118.3	1107.1	1094.5	1080.3	1063.6
70	1131.5	1121.5	1110.4	1098.0	1083.9	1067.7
80	1134.6	1124.7	1113.6	1101.3	1087.6	1071.8
90	1137.7	1127.8	1116.8	1104.7	1091.1	1075.8
100	1140.7	1130.7	1119.9	1107.9	1094.6	1079.6

^aExpanded uncertainty (k = 2): U(T) = 0.02 K; $U_r(p) = 0.0002$; $U_r(w) = 0.0004$; $U_r(\alpha) = 0.003$ and $U(\rho) = 2$ kg·m⁻³.

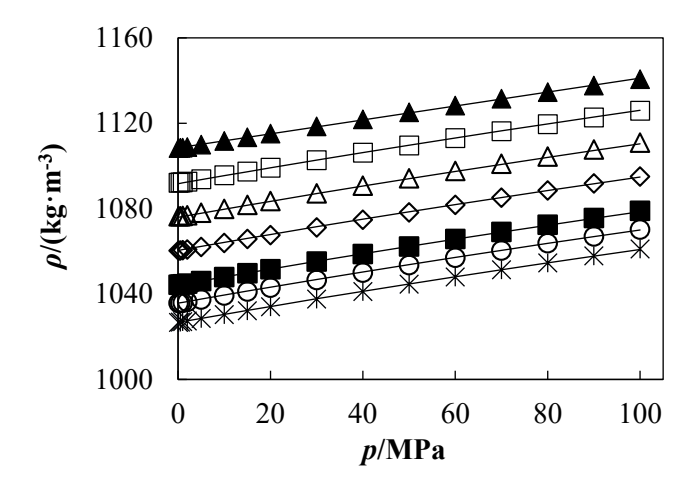


Figure 7.35. Experimental density ρ , of the system MDEA(1) + H₂O(2) + CO₂(3) as a function of pressure p, at temperature T = 293.15 K. CO₂ loadings: (*) $\alpha = 0$ mol-CO₂/mol-MDEA, (\bigcirc) $\alpha = 0.1$ mol-CO₂/mol-MDEA, (\bigcirc) $\alpha = 0.2$ mol-CO₂/mol-MDEA, (\bigcirc) $\alpha = 0.4$ mol-CO₂/mol-MDEA, (\bigcirc) $\alpha = 0.6$ mol-CO₂/mol-MDEA, and (\triangle) $\alpha = 0.9$ mol-CO₂/mol-MDEA. Experimental density data of aqueous amine solution (CO₂-free basis) from [104]. Lines represent the calculated values using modified Tammann-Tait (**Equations 7.1 to 7.4**) with the parameters given in **Table 7.21**.

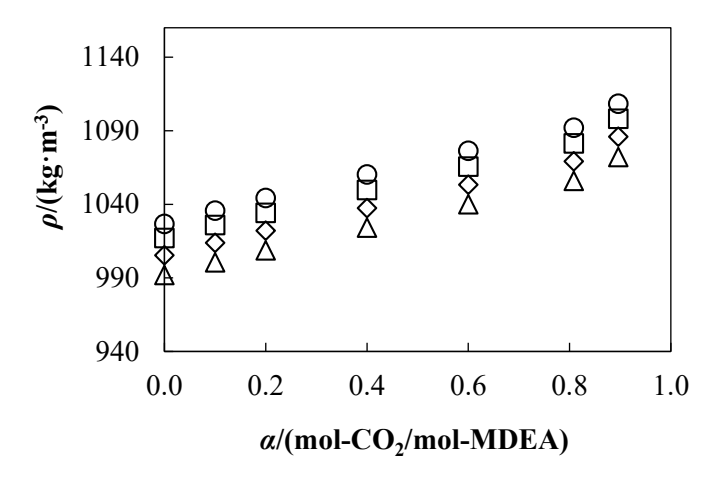


Figure 7.36. Experimental density ρ , of the system MDEA(1) + H₂O(2) + CO₂(3) as a function of CO₂ loading α , at pressure p = 0.1 MPa. Isotherms: (\bigcirc) T = 293.15 K, (\bigcirc) T = 313.15 K, (\diamondsuit) T = 333.15 K, and (\triangle) T = 353.15 K. Experimental density data of aqueous amine solution (CO₂-free basis) from [104].

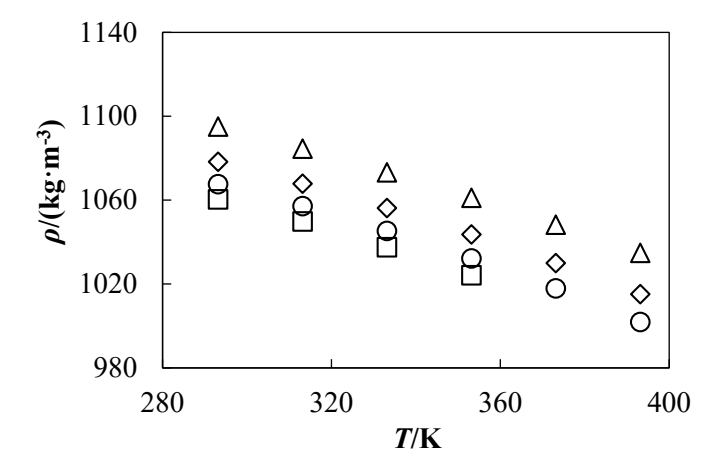


Figure 7.37. Experimental density ρ , of the system MDEA(1) + H₂O(2) + CO₂(3) as a function of temperature T, at CO₂ loading $\alpha = 0.4$ mol-CO₂/mol-MDEA. Isobars: (\square) p = 0.1 MPa, (\bigcirc) p = 20 MPa, (\bigcirc) p = 50 MPa, and (\triangle) p = 100 MPa.

7.3.2.2. Comparison with Literature

Table 7.16 details the temperature, pressure, and CO₂ loading conditions reported in the references used for the comparison of our density data. As shown in **Figure 7.38**, the relative deviations are within 0.7 %, which is within the uncertainties reported in the literature. The high uncertainty value in CO₂ loading was the main contributor to the deviations observed in the comparison.

Table 7.16. Measurement conditions of literature data used to compare the experimental density of MDEA(1) + $H_2O(2) + CO_2(3)$ mixture measured in this work. CO_2 loading α in terms of mol- CO_2 /molamine.

Reference	Densimeter	Conditions	Number of Points	$U_{\rm r}(\alpha)^{\rm a}$	$U_{ m r}(ho)^{ m b}$
Uan at al	Anton	T = (313.15 - 353.15) K			
Han et al. [126]	Paar DMA 4500	p = 0.1 MPa $\alpha = 0.1 - 0.4$	9	2 %	1 %

^aRelative expanded uncertainty in CO₂ loading (k = 2), %.

^bRelative expanded uncertainty in density (k = 2), %.

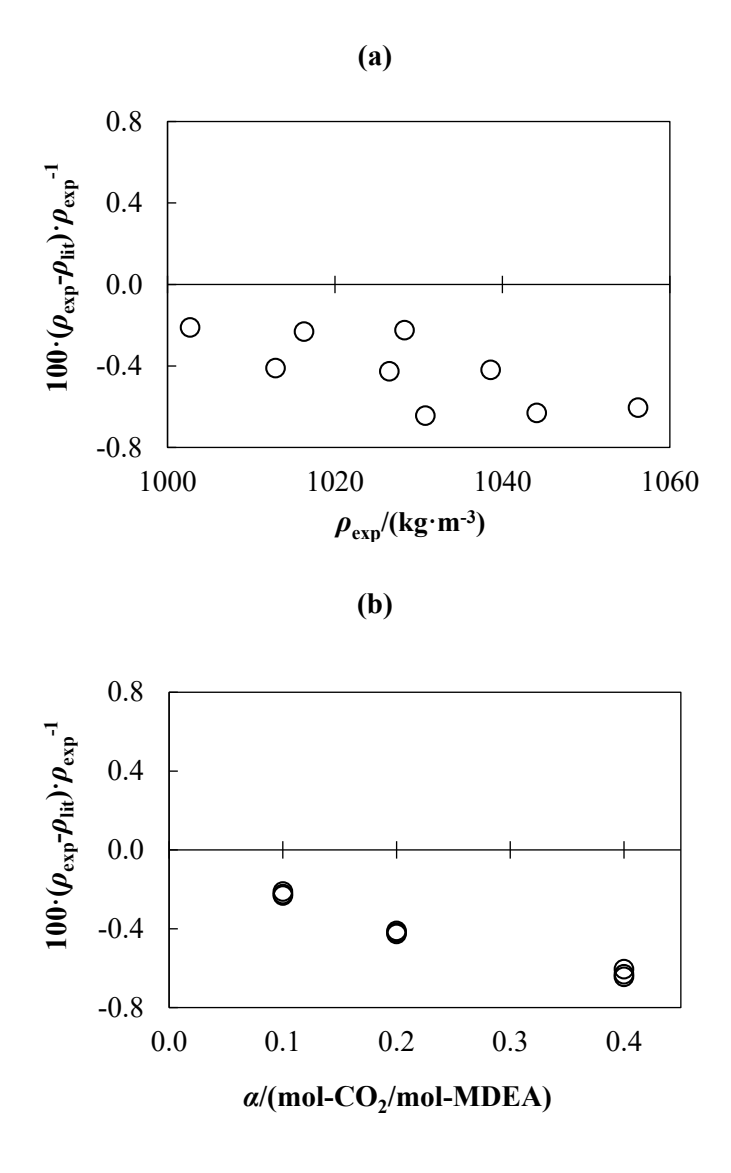


Figure 7.38. Relative deviations (%) of density measurements ρ_{exp} , in comparison with literature values ρ_{lit} . (a) Relative deviations vs ρ_{exp} , y (b) Relative deviations vs α . Literature for MDEA + H₂O + CO₂: (\bigcirc) Han et al. [126].

7.3.3. $AMP + H_2O + CO_2$

7.3.3.1. Experimental Density

The results of the density measurements of the aqueous amine solutions are presented in **Table 7.17** for AMP + H₂O + CO₂. In order to analyse the impact of pressure, CO₂ loading, and temperature, the experimental density data were plotted as a function of these variables for all the studied systems, as can be observed in **Figures 7.39 to 7.41**.

Table 7.17. Experimental densities ρ , for the system AMP(1) + H₂O(2) + CO₂(3) with amine mass fraction (CO₂-free basis) $w_1 = 0.3015$, at different conditions of temperature T, pressure p, CO₂ loading α in terms of mol-CO₂/mol-AMP, and equivalent CO₂ molality b_3 .

$\rho/(\mathrm{kg}\cdot\mathrm{m}^{-3})$								
p/MPa	T/K							
p/Mi a	293.15	313.15	333.15	353.15	373.15	393.15		
	$\alpha = 0$	$.100 (b_3 =$	0.334 mo	l·kg ⁻¹)				
0.1	1016.5	1004.2	989.9	974.8				
0.5	1016.6	1004.3	990.1	975.0				
1	1016.7	1004.4	990.3	975.2				
2	1017.0	1004.8	990.7	975.7				
5	1018.1	1006.0	991.9	977.0	961.0	943.9		
10	1020.0	1007.9	994.1	979.1	963.3	946.5		
15	1021.7	1009.7	996.1	981.3	965.6	949.0		
20	1023.5	1011.6	998.0	983.4	967.9	951.4		
30	1026.9	1015.3	1001.9	987.5	972.3	956.2		
40	1030.3	1018.9	1005.7	991.5	976.6	960.9		
50	1033.6	1022.4	1009.4	995.4	980.7	965.3		
60	1036.8	1025.9	1013.0	999.2	984.8	969.6		
70	1040.0	1029.2	1016.5	1003.0	988.7	973.8		
80	1043.2	1032.5	1020.0	1006.6	992.5	977.9		
90	1046.2	1035.7	1023.5	1010.1	996.3	981.7		
100	1049.2	1038.9	1026.7	1013.5	999.9	985.6		
	$\alpha = 0$	$.200 (b_3 =$	0.667 mo	$l \cdot kg^{-1}$				
0.1	1032.7	1019.5	1004.4	988.9				
0.5	1032.8	1019.6	1004.6	989.1				
1	1033.0	1019.7	1004.8	989.3				

2	1033.3	1020.1	1005.2	989.7		
5	1034.5	1021.2	1006.4	991.0	974.9	957.9
10	1036.3	1023.2	1008.5	993.2	977.2	960.4
15	1038.1	1025.1	1010.6	995.3	979.5	962.9
20	1039.8	1026.9	1012.5	997.4	981.7	965.3
30	1043.3	1030.7	1016.4	1001.5	986.1	970.1
40	1046.6	1034.3	1020.3	1005.6	990.3	974.6
50	1050.0	1037.9	1024.0	1009.4	994.3	978.9
60	1053.4	1041.4	1027.6	1013.2	998.4	983.0
70	1056.5	1044.8	1031.2	1017.0	1002.2	987.3
80	1059.7	1048.1	1034.7	1020.5	1006.0	991.4
90	1062.8	1051.4	1038.1	1024.2	1009.8	995.2
100	1065.8	1054.6	1041.5	1027.5	1013.4	999.0
	$\alpha = 0$).400 (<i>b</i> ₃ =	= 1.334 m	ol·kg ⁻¹)		
0.1	1062.4	1047.1	1030.9	1014.9		
0.5	1062.5	1047.2	1031.1	1015.1		
1	1062.7	1047.4	1031.3	1015.3		
2	1063.0	1047.8	1031.7	1015.7		
5	1064.2	1048.9	1032.9	1017.0	1000.8	983.6
10	1066.0	1050.9	1035.0	1019.1	1003.0	986.1
15	1067.9	1052.8	1037.0	1021.2	1005.2	988.5
20	1069.7	1054.8	1039.0	1023.2	1007.4	990.9
30	1073.2	1058.5	1042.9	1027.2	1011.6	995.4
40	1076.7	1062.2	1046.8	1031.2	1015.8	999.9
50	1080.2	1065.9	1050.4	1035.1	1019.7	1004.2
60	1083.6	1069.4	1054.1	1038.8	1023.7	1008.3
70	1086.8	1072.9	1057.7	1042.5	1027.4	1012.3
80	1090.1	1076.3	1061.3	1046.1	1031.2	1016.3
90	1093.3	1079.7	1064.7	1049.7	1034.8	1020.2
100	1096.4	1083.0	1068.1	1053.2	1038.4	1023.8
	$\alpha = 0$	0.501 (b ₃ =	= 1.669 m	ol·kg ⁻¹)		
0.1	1075.2	1059.7	1043.3	1027.5		
0.5	1075.2	1059.8	1043.6	1027.6		
1	1075.4	1059.9	1043.7	1027.9		
2	1075.7	1060.3	1044.2	1028.2		

1076.9	1061.5	1045.4	1029.5	1013.3	996.1
1078.8	1063.4	1047.4	1031.6	1015.5	998.5
1080.6	1065.3	1049.4	1033.6	1017.7	1000.9
1082.4	1067.2	1051.4	1035.7	1019.8	1003.2
1086.0	1071.0	1055.2	1039.6	1024.0	1007.7
1089.5	1074.7	1059.1	1043.6	1028.1	1012.1
1092.9	1078.2	1062.8	1047.3	1032.0	1016.4
1096.4	1081.8	1066.4	1051.0	1035.9	1020.5
1099.7	1085.3	1069.9	1054.7	1039.6	1024.6
1103.0	1088.7	1073.4	1058.3	1043.4	1028.4
1106.1	1092.1	1077.0	1061.7	1046.9	1032.3
1109.3	1095.3	1080.3	1065.2	1050.5	1036.0
	1078.8 1080.6 1082.4 1086.0 1089.5 1092.9 1096.4 1099.7 1103.0 1106.1	1078.81063.41080.61065.31082.41067.21086.01071.01089.51074.71092.91078.21096.41081.81099.71085.31103.01088.71106.11092.1	1078.8 1063.4 1047.4 1080.6 1065.3 1049.4 1082.4 1067.2 1051.4 1086.0 1071.0 1055.2 1089.5 1074.7 1059.1 1092.9 1078.2 1062.8 1096.4 1081.8 1066.4 1099.7 1085.3 1069.9 1103.0 1088.7 1073.4 1106.1 1092.1 1077.0	1078.8 1063.4 1047.4 1031.6 1080.6 1065.3 1049.4 1033.6 1082.4 1067.2 1051.4 1035.7 1086.0 1071.0 1055.2 1039.6 1089.5 1074.7 1059.1 1043.6 1092.9 1078.2 1062.8 1047.3 1096.4 1081.8 1066.4 1051.0 1099.7 1085.3 1069.9 1054.7 1103.0 1088.7 1073.4 1058.3 1106.1 1092.1 1077.0 1061.7	1078.8 1063.4 1047.4 1031.6 1015.5 1080.6 1065.3 1049.4 1033.6 1017.7 1082.4 1067.2 1051.4 1035.7 1019.8 1086.0 1071.0 1055.2 1039.6 1024.0 1089.5 1074.7 1059.1 1043.6 1028.1 1092.9 1078.2 1062.8 1047.3 1032.0 1096.4 1081.8 1066.4 1051.0 1035.9 1099.7 1085.3 1069.9 1054.7 1039.6 1103.0 1088.7 1073.4 1058.3 1043.4 1106.1 1092.1 1077.0 1061.7 1046.9

^aExpanded uncertainty (k = 2): U(T) = 0.02 K; $U_r(p) = 0.0002$; $U_r(w) = 0.0004$; $U_r(\alpha) = 0.003$ and $U(\rho) = 2 \text{ kg} \cdot \text{m}^{-3}$.

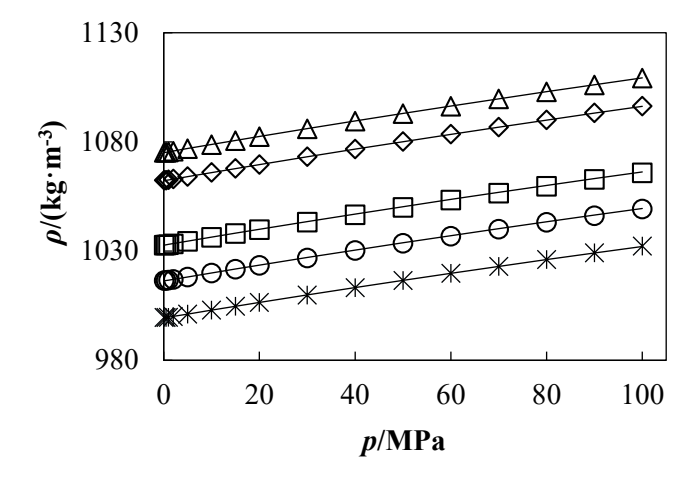


Figure 7.39. Experimental density ρ , of the system AMP(1) + H₂O(2) + CO₂(3) as a function of pressure p, at temperature T = 293.15 K. CO₂ loadings: (*) α = 0 mol-CO₂/mol-AMP, (\bigcirc) α = 0.1 mol-CO₂/mol-AMP, (\bigcirc) α = 0.2 mol-CO₂/mol-AMP, and (\triangle) α = 0.5 mol-CO₂/mol-AMP. Experimental density data of aqueous amine solution (CO₂-free basis) reported in this work. Lines represent the calculated values using modified Tammann-Tait (**Equations 7.1 to 7.4**) with the parameters given in **Table 7.21**.

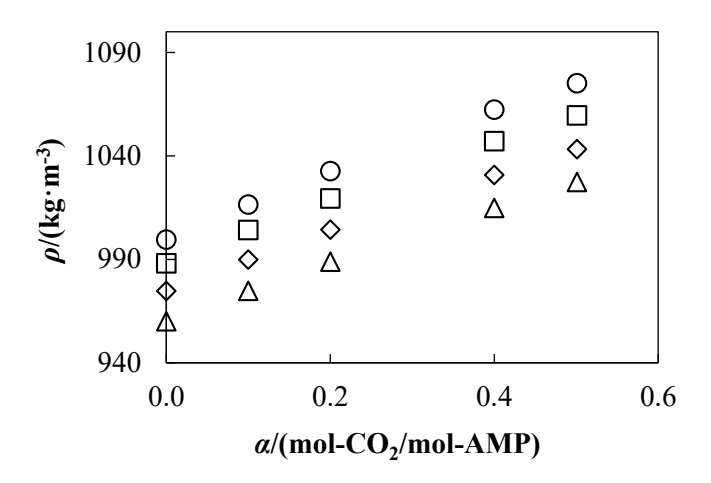


Figure 7.40. Experimental density ρ , of the system AMP(1) + H₂O(2) + CO₂(3) as a function of CO₂ loading α , at pressure p = 0.1 MPa. Isotherms: (\bigcirc) T = 293.15 K, (\bigcirc) T = 313.15 K, (\diamondsuit) T = 333.15 K, and (\triangle) T = 353.15 K. Experimental density data of aqueous amine solution (CO₂-free basis) reported in this work.

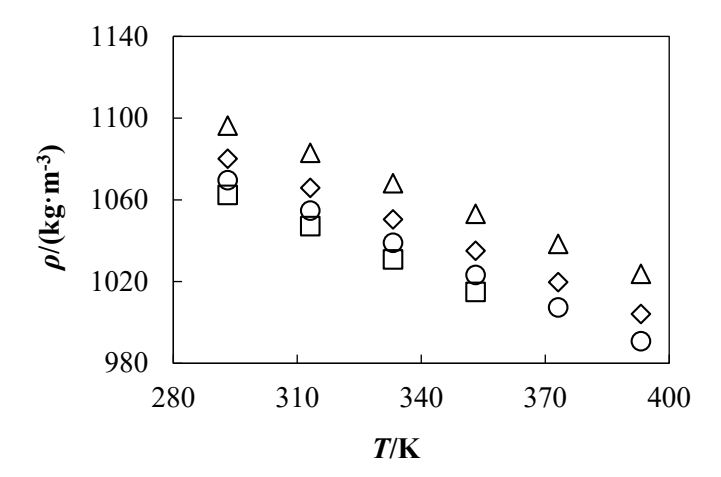


Figure 7.41. Experimental density ρ , of the system AMP(1) + H₂O(2) + CO₂(3) as a function of temperature T, at CO₂ loading $\alpha = 0.4$ mol-CO₂/mol-AMP. Isobars: (\square) p = 0.1 MPa, (\bigcirc) p = 20 MPa, (\bigcirc) p = 50 MPa, and (\triangle) p = 100 MPa.

7.3.3.2. Comparison with Literature

Table 7.18 details the temperature, pressure, and CO₂ loading conditions reported in the references used for the comparison of our density data. As shown in **Figure 7.42**, the relative deviations are within 0.2 %, which is within the uncertainties reported in the literature. The high uncertainty value in CO₂ loading was the main contributor to the deviations observed in the comparison.

Table 7.18. Measurement conditions of literature data used to compare the experimental density of AMP + $H_2O + CO_2$ mixture measured in this work. CO_2 loading α in terms of mol- CO_2 /mol-amine.

Reference	Densimeter	Conditions	Number of Points	$U_{\rm r}(\alpha)^{\rm a}$	$U_{ m r}(ho)^{ m b}$
Stec et al.	Kyoto	T = (293.15 - 333.15) K			
[83]	Electronics KEM DA-645	p = 0.1 MPa $\alpha = 0.1 - 0.4$	12	NA ^c	NA ^c

^aRelative expanded uncertainty in CO₂ loading (k = 2), %.

^cNA: Not Available.

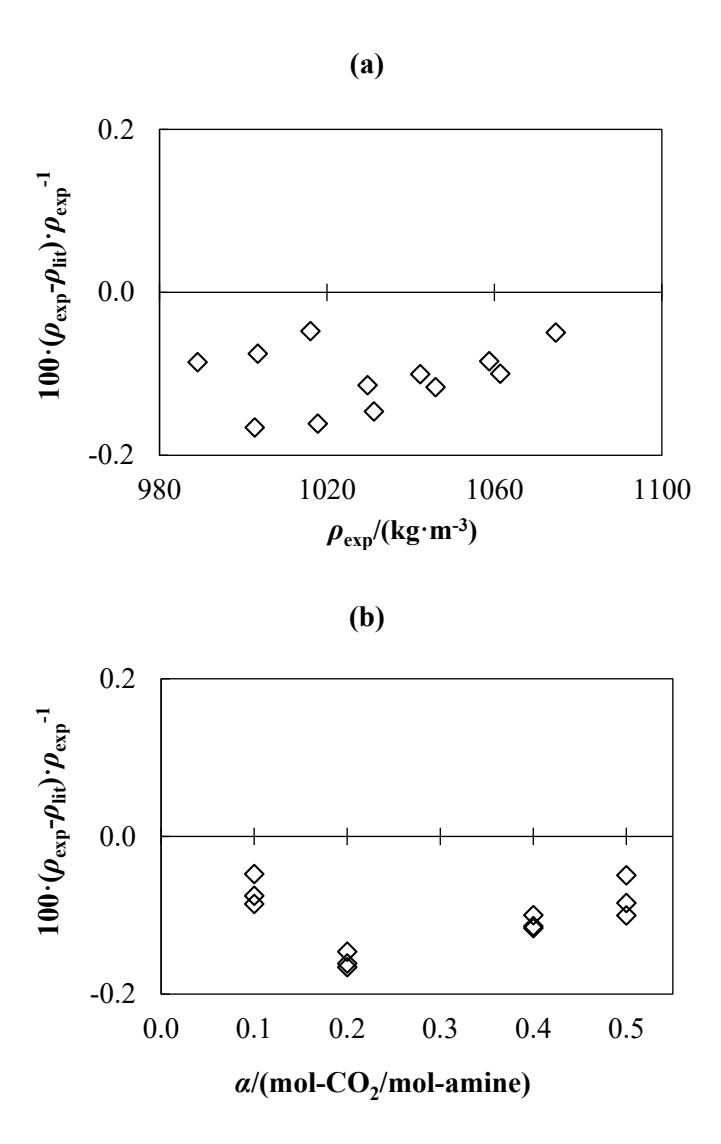


Figure 7.42. Relative deviations (%) of density measurements ρ_{exp} , in comparison with literature values ρ_{lit} . (a) Relative deviations vs ρ_{exp} , y (b) Relative deviations vs α . Literature for AMP + H₂O + CO₂: (\diamondsuit) Stee et al. [83].

^bRelative expanded uncertainty in density (k = 2), %.

7.3.4. DEA + $H_2O + CO_2$

7.3.4.1. Experimental Density

The results of the density measurements of the aqueous amine solutions are presented in **Table 7.19** for DEA + H_2O + CO_2 . In order to analyse the impact of pressure, CO_2 loading, and temperature, the experimental density data were plotted as a function of these variables for all the studied systems, as can be observed in **Figures 7.43 to 7.45**.

Table 7.19. Experimental densities ρ , for the system DEA(1) + H₂O(2) + CO₂(3) with amine mass fraction (CO₂-free basis) $w_1 = 0.3001$, at different conditions of temperature T, pressure p, CO₂ loading α in terms of mol-CO₂/mol-DEA, and equivalent CO₂ molality b_3 .

$ ho/(\mathrm{kg}\cdot\mathrm{m}^{-3})$								
p/MPa	T/K							
privit a	293.15	313.15	333.15	353.15	373.15	393.15		
	$\alpha = 0$	$.100 (b_3 =$	0.282 mo	l·kg ⁻¹)				
0.1	1047.2	1038.6	1027.7	1015.5				
0.5	1047.3	1038.6	1027.9	1015.6				
1	1047.4	1038.8	1028.1	1015.8				
2	1047.7	1039.1	1028.4	1016.2				
5	1048.9	1040.3	1029.6	1017.4	1003.6	988.4		
10	1050.7	1042.1	1031.6	1019.4	1005.8	990.8		
15	1052.6	1044.0	1033.5	1021.4	1007.9	993.0		
20	1054.4	1045.8	1035.5	1023.4	1010.1	995.2		
30	1057.9	1049.5	1039.1	1027.3	1014.1	999.6		
40	1061.5	1053.0	1042.8	1031.1	1018.1	1003.9		
50	1064.9	1056.5	1046.4	1034.8	1022.0	1008.1		
60	1068.4	1060.0	1050.0	1038.4	1025.9	1012.1		
70	1071.7	1063.3	1053.3	1042.0	1029.4	1016.1		
80	1075.0	1066.6	1056.8	1045.4	1033.3	1019.9		
90	1078.2	1069.9	1060.0	1048.9	1036.8	1023.7		
100	1081.4	1073.1	1063.3	1052.2	1040.2	1027.4		
	$\alpha = 0$	$.200 (b_3 =$	0.563 mo	l·kg ⁻¹)				
0.1	1059.2	1050.3	1039.4	1027.1				
0.5	1059.2	1050.4	1039.6	1027.2				
1	1059.3	1050.5	1039.7	1027.4				

2	1059.7	1050.9	1040.1	1027.9		
5	1060.8	1052.0	1041.3	1029.0	1015.2	1000.0
10	1062.7	1053.9	1043.3	1031.1	1017.4	1002.4
15	1064.5	1055.8	1045.2	1033.1	1019.5	1004.6
20	1066.3	1057.6	1047.0	1035.1	1021.6	1006.8
30	1069.8	1061.2	1050.7	1038.9	1025.6	1011.2
40	1073.3	1064.7	1054.4	1042.7	1029.6	1015.3
50	1076.7	1068.2	1057.9	1046.3	1033.4	1019.5
60	1080.2	1071.6	1061.4	1049.9	1037.3	1023.5
70	1083.5	1075.0	1064.8	1053.5	1040.9	1027.4
80	1086.9	1078.3	1068.2	1057.0	1044.5	1031.2
90	1090.0	1081.6	1071.5	1060.4	1048.1	1034.8
100	1093.3	1084.8	1074.7	1063.6	1051.5	1038.6
	$\alpha = 0$.	.400 $(b_3 =$	= 1.127 mol	l·kg ⁻¹)		
0.1	1082.4	1073.1	1061.7	1049.3		
0.5	1082.5	1073.2	1061.9	1049.4		
1	1082.7	1073.3	1062.1	1049.6		
2	1083.0	1073.7	1062.5	1050.0		
5	1084.2	1074.8	1063.6	1051.2	1037.2	1021.6
10	1086.0	1076.7	1065.6	1053.1	1039.3	1023.8
15	1087.8	1078.5	1067.5	1055.1	1041.4	1026.0
20	1089.6	1080.3	1069.3	1057.0	1043.4	1028.2
30	1093.2	1083.9	1072.9	1060.8	1047.4	1032.6
40	1096.7	1087.4	1076.5	1064.6	1051.3	1036.7
50	1100.1	1090.8	1080.1	1068.2	1055.1	1040.7
60	1103.5	1094.3	1083.5	1071.7	1058.8	1044.7
70	1106.8	1097.6	1086.9	1075.2	1062.4	1048.6
80	1110.1	1100.9	1090.3	1078.6	1066.0	1052.3
90	1113.3	1104.1	1093.6	1082.0	1069.5	1055.9
100	1116.5	1107.3	1096.8	1085.3	1072.8	1059.5
	$\alpha = 0$.	$.600 (b_3 =$	1.689 mol	l·kg ⁻¹)		
0.1	1102.9	1093.1	1081.4	1068.7		
0.5	1102.9	1093.1	1081.6	1068.8		
1	1103.0	1093.3	1081.8	1069.0		
2	1103.4	1093.6	1082.2	1069.4		

5	1104.5	1094.7	1083.3	1070.6	1055.6	1039.1
10	1106.3	1096.5	1085.2	1072.6	1058.1	1041.9
15	1108.1	1098.3	1087.1	1074.5	1060.3	1044.2
20	1109.9	1100.1	1088.9	1076.4	1062.3	1046.4
30	1113.3	1103.7	1092.4	1080.1	1066.3	1050.8
40	1116.8	1107.1	1096.0	1083.8	1070.2	1055.0
50	1120.2	1110.5	1099.5	1087.4	1073.9	1059.1
60	1123.6	1113.9	1102.9	1090.8	1077.7	1063.0
70	1126.8	1117.1	1106.2	1094.3	1081.3	1067.0
80	1130.0	1120.3	1109.5	1097.7	1084.9	1070.6
90	1133.2	1123.5	1112.7	1101.0	1088.2	1074.3
100	1136.4	1126.7	1115.9	1104.3	1091.6	1077.8

^aExpanded uncertainty (k = 2): U(T) = 0.02 K; $U_r(p) = 0.0002$; $U_r(w) = 0.0004$; $U_r(\alpha) = 0.003$ and $U(\rho) = 2 \text{ kg} \cdot \text{m}^{-3}$.

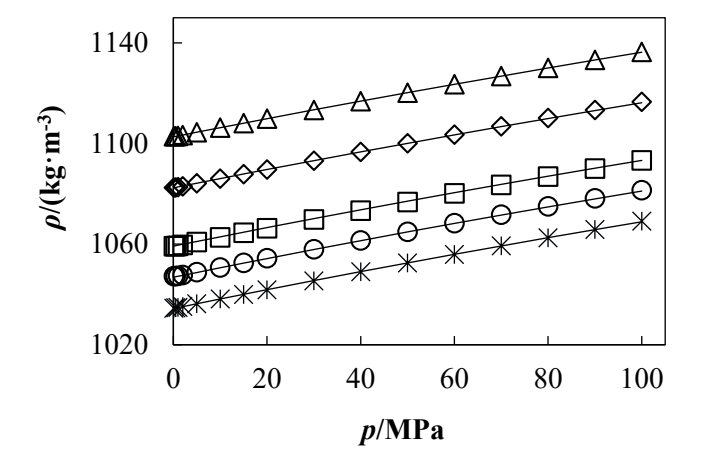


Figure 7.43. Experimental density ρ , of the system DEA(1) + H₂O(2) + CO₂(3) as a function of pressure p, at temperature T = 293.15 K. CO₂ loadings: (*) $\alpha = 0$ mol-CO₂/mol-DEA, (\bigcirc) $\alpha = 0.1$ mol-CO₂/mol-DEA, (\bigcirc) $\alpha = 0.2$ mol-CO₂/mol-DEA, (\bigcirc) $\alpha = 0.4$ mol-CO₂/mol-DEA, and (\triangle) $\alpha = 0.6$ mol-CO₂/mol-DEA. Experimental density data of aqueous amine solution (CO₂-free basis) from [188]. Lines represent the calculated values using modified Tammann-Tait (**Equations 7.1 to 7.4**) with the parameters given in **Table 7.21**.

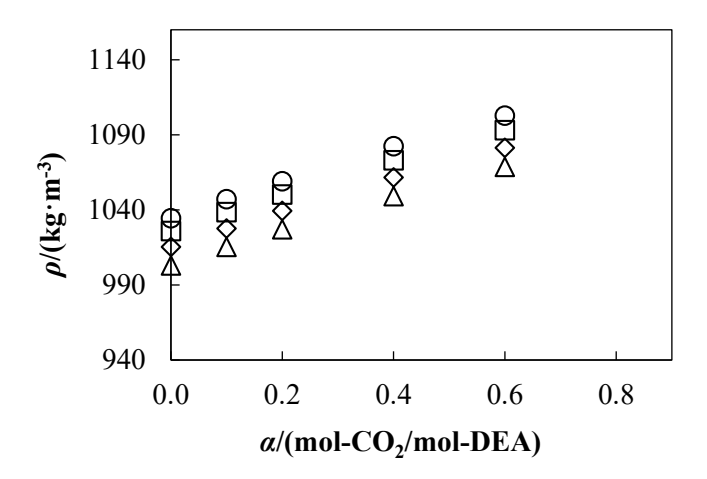


Figure 7.44. Experimental density ρ , of the system DEA(1) + H₂O(2) + CO₂(3) as a function of CO₂ loading α , at pressure p = 0.1 MPa. Isotherms: (\bigcirc) T = 293.15 K, (\bigcirc) T = 313.15 K, (\diamondsuit) T = 333.15 K, and (\triangle) T = 353.15 K. Experimental density data of aqueous amine solution (CO₂-free basis) from [188].

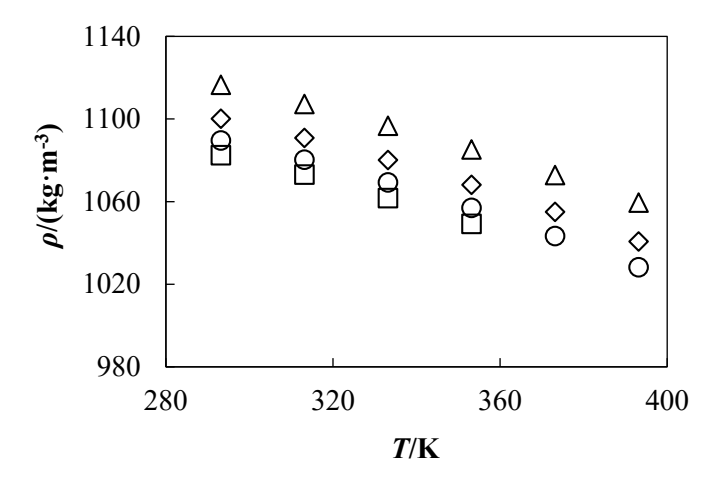


Figure 7.45. Experimental density ρ , of the system DEA(1) + H₂O(2) + CO₂(3) as a function of temperature T, at CO₂ loading $\alpha = 0.4$ mol-CO₂/mol-DEA. Isobars: (\square) p = 0.1 MPa, (\bigcirc) p = 20 MPa, (\bigcirc) p = 50 MPa, and (\triangle) p = 100 MPa.

7.3.4.2. Comparison with Literature

Table 7.20 details the temperature, pressure, and CO₂ loading conditions reported in the references used for the comparison of our density data. As shown in **Figure 7.46**, the relative deviations are within 0.2 %, which is within the uncertainties reported in the literature. The high uncertainty value in CO₂ loading was the main contributor to the deviations observed in the comparison.

Table 7.20. Measurement conditions of literature data used to compare the experimental density of DEA $+ H_2O + CO_2$ mixture measured in this work. CO_2 loading α in terms of mol-CO₂/mol-amine.

Reference	Densimeter	Conditions	Number of Points	$U_{\rm r}(lpha)^{ m a}$	$U_{ m r}(ho)^{ m b}$
Han et al. [126]	Anton Paar DMA 4500	T = (313.15 - 353.15) K p = 0.1 MPa $\alpha = 0.1 - 0.4$	9	2 %	1 %

^aRelative expanded uncertainty in CO₂ loading (k = 2), %.

^bRelative expanded uncertainty in density (k = 2), %.

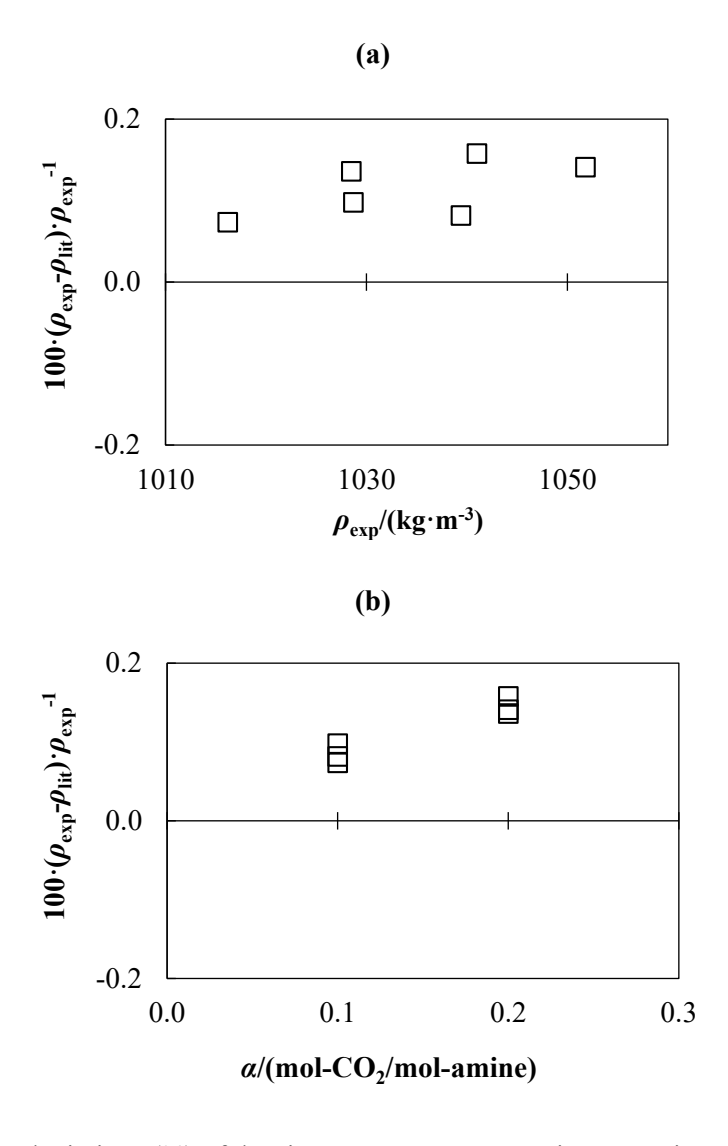


Figure 7.46. Relative deviations (%) of density measurements ρ_{exp} , in comparison with literature values ρ_{lit} . (a) Relative deviations vs ρ_{exp} , y (b) Relative deviations vs α . Literature for DEA + H₂O + CO₂: (\square) Han et al. [126].

7.3.5. Discussion

For all the ternary systems studied, an increase in temperature caused a decrease in the measured density, as can be seen in **Figures 7.33**, **7.37**, **7.41**, **and 7.45**. Pressure exhibited the opposite effect to temperature on density (see **Figures 7.31**, **7.35**, **7.39**, **and 7.43**). All solutions showed an increase in density as the CO₂ loading increased in terms of mol-CO₂/mol-amine, with MEA experiencing the most notable increase with an 11 % increase in density when the CO₂ loading increases from (0 to 0.6) mol-CO₂/mol-amine, as illustrated in **Figure 7.32**. While for the rest of the solutions the change was 8 % for MDEA solutions when the loading varies from (0 to 0.9) mol-CO₂/mol-amine (see **Figure 7.36**), 7 % for AMP solutions when the loading varies from (0 to 0.5) mol-CO₂/mol-amine (see **Figure 7.40**), and 6 % for DEA solutions when the loading varies from (0 to 0.9) mol-CO₂/mol-amine (see **Figure 7.40**).

Bicarbonate ions form a more compact hydration shell with the aqueous solution than carbamate ions due to the much larger diameter of the latter. This leads to a reduction in the molar volume attributable to CO₂ in the reaction of aqueous amine solutions with CO₂, where bicarbonate is the main product [83,107]. According to this approach, it would be logical to think that the density of aqueous amine solutions that produce bicarbonate as a result of their reaction with CO₂ is higher than that of amines that produce carbamates, since a decrease in the volume of the solution containing CO₂ would favour an increase in density. However, another significant aspect, the mechanism of this reaction, must also be taken into account. For example, MEA, a primary amine, forms carbamate, requiring two MEA molecules per CO₂ molecule. This translates into an increase in the amount of amine and CO₂ required in the reaction and therefore the density of the solution. On the other hand, MDEA, a tertiary amine, forms bicarbonate in its reaction in an aqueous solution with CO₂, with a molar ratio of 1:1 with CO₂, which leads to a decrease in the amount of amine and CO2 required and, in the density, compared to MEA solutions. This analysis is applied under identical conditions of CO₂ loading and amine mass fraction based on the amine and H₂O binary solution. Similar conclusions are reached by performing the same analysis with a CO₂-loaded aqueous DEA solution, a secondary amine that forms carbamate, and a CO₂-loaded aqueous AMP solution, a sterically hindered amine that, although it has a primary amino group, the carbamate it forms is very unstable, and bicarbonate is the main product of the reaction [32].

In summary, aqueous amine solutions (MDEA, AMP,...) that produce bicarbonate as the main product in their reaction with CO₂ have a lower density than aqueous amine solutions (MEA, DEA,...) that produce carbamate. A decrease in the solution density allows the optimisation of the size of the equipment involved in the CO₂ capture process with amines.

7.3.6. Experimental Density Data Fitting

The experimental density for CO₂-loaded aqueous amine solutions was also correlated (see **Equations 7.1 to 7.4**) using a Tammann–Tait equation [189] that was modified to render density as a function of temperature, pressure, and the CO₂ molality *b* (mol-CO₂/kg-H₂O). Parameter's standard error analysis was used to reduce overfitting and optimise the parameter set.

The reference density, ρ_{ref} , is computed with **Equation 7.2**. $\rho_{o}(T)$ is the density of the CO₂-unloaded aqueous amine solution at the reference pressure (p = 5 MPa) and at the given temperature. The experimental density data for MEA + H₂O, MDEA + H₂O, and DEA + H₂O mixtures used in the ternary solutions fitting were taken from the literature [104,188], and the density data for the AMP + H₂O mixture is reported in this work (see Section 7.3.3).

$$\rho(T, p, b) = \frac{\rho_{\text{ref}}(T, b)}{1 - C \cdot \ln\left(\frac{B(T, b) + p}{B(T, b) + p_{\text{ref}}(T)}\right)}$$
(7.1)

$$[\rho_{ref}(T,b) - \rho_{0}(T)]$$

$$= \alpha_{11} \cdot b \cdot (T/T_{c}) + \alpha_{12} \cdot b \cdot (T/T_{c})^{3/2} + \alpha_{21} \cdot b^{3/2} \cdot (T/T_{c}) + \alpha_{22}$$

$$\cdot b^{3/2} \cdot (T/T_{c})^{3/2} + \alpha_{23} \cdot b^{3/2} \cdot (T/T_{c})^{2} + \alpha_{31} \cdot b^{2} \cdot (T/T_{c}) + \alpha_{32} \cdot b^{2}$$

$$\cdot (T/T_{c})^{3/2} + \alpha_{33} \cdot b^{2} \cdot (T/T_{c})^{2}$$

$$(7.2)$$

$$B(T,b) = \beta_{00} + \beta_{01} \cdot (T/T_c) + \beta_{02} \cdot (T/T_c)^2 + \beta_{03} \cdot (T/T_c)^3 + \beta_{11} \cdot b \cdot (T/T_c) + \beta_{12}$$

$$\cdot b \cdot (T/T_c)^2$$
(7.3)

$$C = \gamma_0 \tag{7.4}$$

The implementation procedure was the same as for binary amine + H₂O solutions following the methodology proposed in Section 7.3.7. In order to evaluate the goodness-of-fit with this modified Tammann-Tait equation, the following statistical parameters were determined: absolute average relative deviation (AAD) calculated using **Equation 7.5**, maximum absolute relative deviation (MAD) calculated using **Equation 7.6**, and standard deviation (σ) calculated using **Equation 7.7**.

In the first fitting, which allowed the determination of the coefficients β_{00} , β_{01} , β_{02} , β_{03} , and γ_0 in **Equations 7.2 and 7.3** for the aqueous amine solution without CO₂ loading ($b_3 = 0 \text{ mol·kg}^{-1}$), relative deviations between the experimental and calculated values were obtained to be less than 0.02 %. The second fitting allowed the optimisation of the rest of the coefficients. The numerical values of all of them are shown in **Table 7.21**, along with the statistical parameters ADD, MAD and σ calculated using **Equations 7.5, 7.6, and 7.7**, respectively. The fitting residuals can be observed in **Figures 7.47 to 7.50** for MEA + H₂O + CO₂, MDEA + H₂O + CO₂, and DEA + H₂O + CO₂, respectively.

All residuals are in good agreement with the density uncertainty. No systematic deviations are observed in either molality or density.

Table 7.21. Parameters in **Equations 7.1 to 7.4**, and statistical parameters AAD, MAD and σ .

Parameters _	Tei	Ternary Mixtures (amine + H ₂ O + CO ₂)					
rarameters _	MEA	MDEA	AMP	DEA			
α_{11}	150.19	182.88	250.20	162.0011			
α_{12}	-110.90	-151.88	-218.86	-108.012			
α_{21}	960.16	1625.5	3388.9	1589.2			
α_{22}	-2529.8	-4458.1	-8985.3	-4123.05			
α_{23}	1696.2	3021.6	5931.7	2669.08			
α_{31}	-417.57	-998.66	-1901.4	-928.08			
α_{32}	1110.7	2732.4	5000.9	2423.9			
α_{33}	-755.46	-1857.01	-3285.2	-1592.5			
β_{00}	-1822.5	-1747.6	65.00018	-1694.6			
eta_{01}	12114	11755	2244.3	11160			
eta_{02}	-22001	-21651	-5108.7	-19836			
eta_{03}	12549	12512	2899.9	11023			
β_{11}	87.795	41.596	-66.369	67.972			
eta_{12}	-74.138	-27.453	166.48	-56.753			
γο	1.1929·10 ⁻¹	1.1154·10 ⁻¹	1.1142·10 ⁻¹	1.1723 · 10 ⁻¹			
AAD	0.02 %	0.02 %	0.01 %	0.01 %			
MAD	0.09 %	0.2 %	0.05 %	0.1 %			
$\sigma/(\text{kg}\cdot\text{m}^{-3})$	0.2	0.3	0.2	0.2			

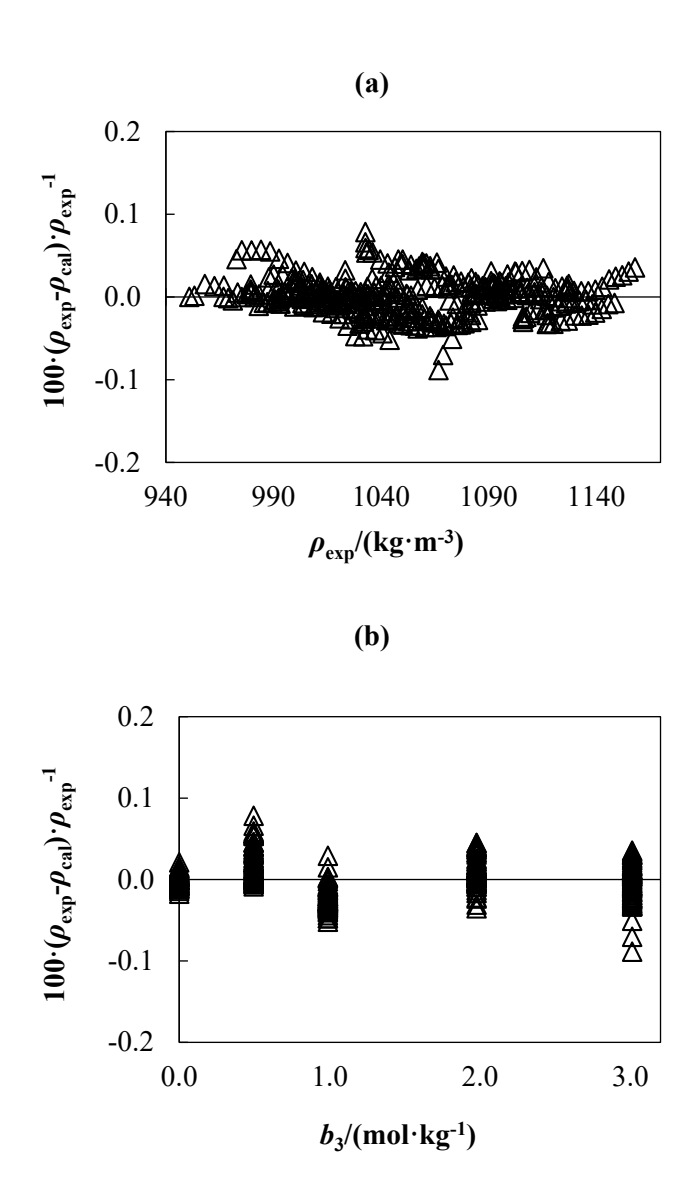


Figure 7.47. Relative deviations (%) for MEA(1) + H₂O(2) + CO₂(3) mixture of experimental density measurements, ρ_{exp} , in comparison with calculated density, ρ_{cal} , using **Equations 7.1 to 7.4**. (a) Relative deviations vs ρ_{exp} and (b) Relative deviations vs b_3 .

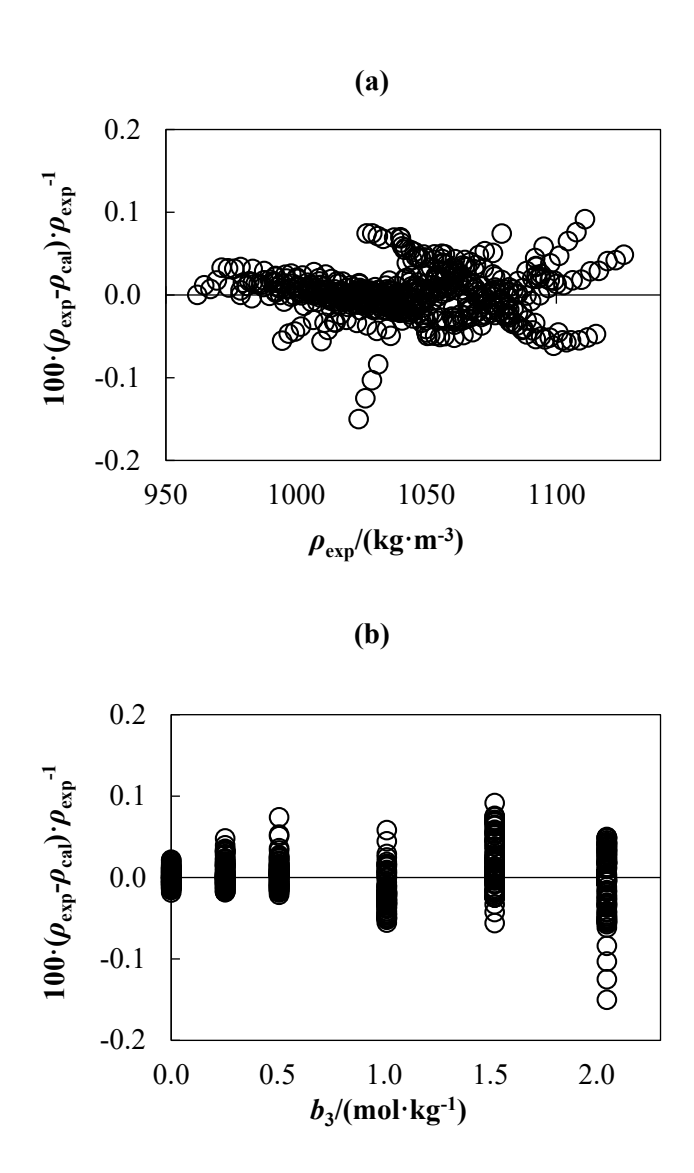


Figure 7.48. Relative deviations (%) for MDEA(1) + $H_2O(2) + CO_2(3)$ mixture of experimental density measurements, ρ_{exp} , in comparison with calculated density, ρ_{cal} , using **Equations 7.1 to 7.4**. (a) Relative deviations vs ρ_{exp} and (b) Relative deviations vs b_3 .

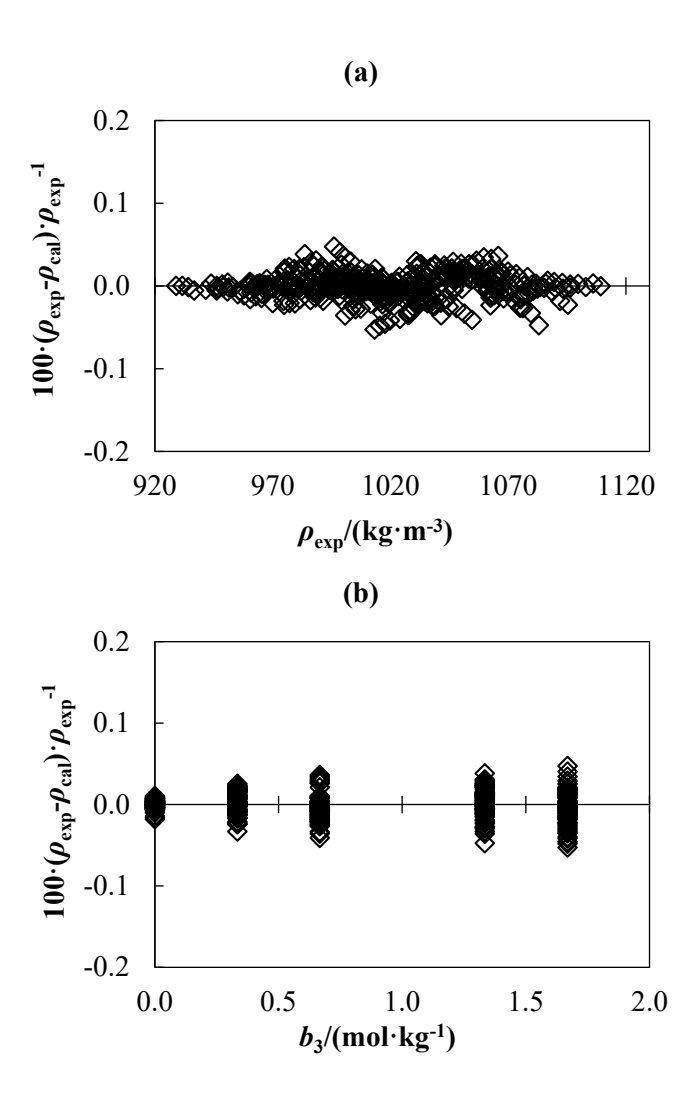
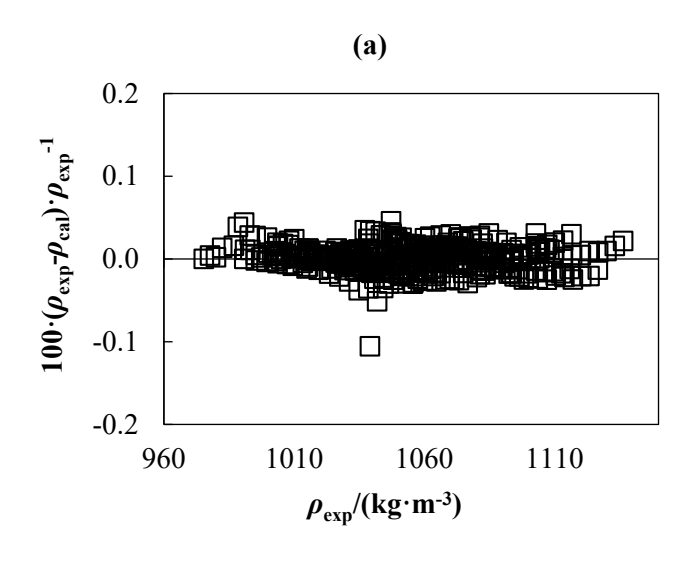


Figure 7.49. Relative deviations (%) for AMP(1) + $H_2O(2) + CO_2(3)$ mixture of experimental density measurements, ρ_{exp} , in comparison with calculated density, ρ_{cal} , using **Equations 7.1 to 7.4**. (a) Relative deviations vs ρ_{exp} and (b) Relative deviations vs b_3 .



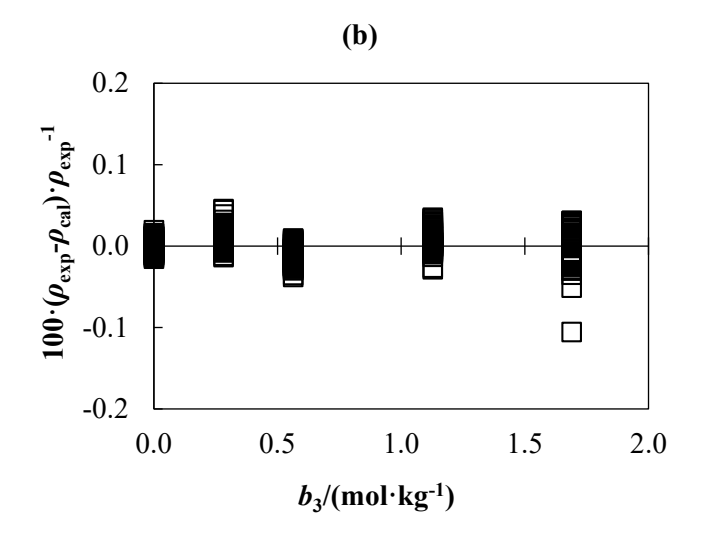


Figure 7.50. Relative deviations (%) for DEA(1) + H₂O(2) + CO₂(3) mixture of experimental density measurements, ρ_{exp} , in comparison with calculated density, ρ_{cal} , using **Equations 7.1 to 7.4**. (a) Relative deviations vs ρ_{exp} and (b) Relative deviations vs b_3 .

7.3.6.1. Comparison of Calculated Density with Experimental Literature Data

Density values for the ternary mixtures, calculated using **Equations 7.1 to 7.4**, were compared to literature data (Chapter 1, Table 1.3), expanding the experimental density comparison presented in this chapter. The results of this comparison are shown below.

• For the MEA + H₂O + CO₂ mixture, comparisons were made using 6 references, totalling 188 data points. The average absolute relative deviation was 0.4 %, with a maximum of 1 % (see **Figure 7.51**).

- For the MDEA + H₂O + CO₂ mixture, comparisons were made using 2 references, totalling 67 data points. The average absolute relative deviation was 0.6 %, with a maximum of 1 % (see **Figure 7.52**).
- For the AMP + H₂O + CO₂ mixture, comparisons were made using 1 reference, totalling 30 data points. The average absolute relative deviation was 0.2 %, with a maximum of 0.3 % (see Figure 7.53).
- For the DEA + H₂O + CO₂ mixture, comparisons were made using 2 references, totalling 70 data points. The average absolute relative deviation was 0.2 %, with a maximum of 0.7 % (see **Figure 7.54**).

For the ternary mixtures, calculated density and literature values discrepancies result from experimental uncertainties, notably in CO₂ loading. Variations in amine mass fraction, due to the lack of a dependent model, also affect the observed relative deviation differences.

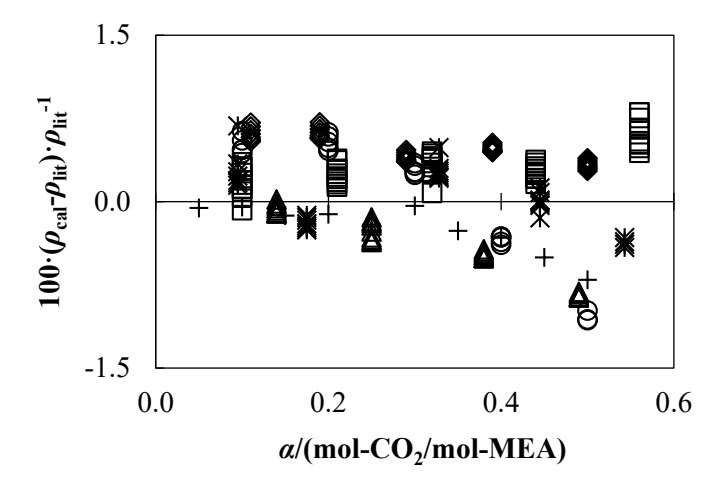


Figure 7.51. Relative deviations (%) vs CO₂ loading α for MEA(1) + H₂O(2) + CO₂(3) mixture of calculated density ρ_{cal} , using **Equations 7.1 to 7.4**, in comparison with density literature values ρ_{lit} . Literature: (\bigcirc) Amundsen et al. [108], (\square) Han et al. [109], (\diamondsuit) Hartono et al. [110], (\triangle) Zhang et al. [112], (*) Karunarathne et al. [115], and (+) Weiland et al. [107].

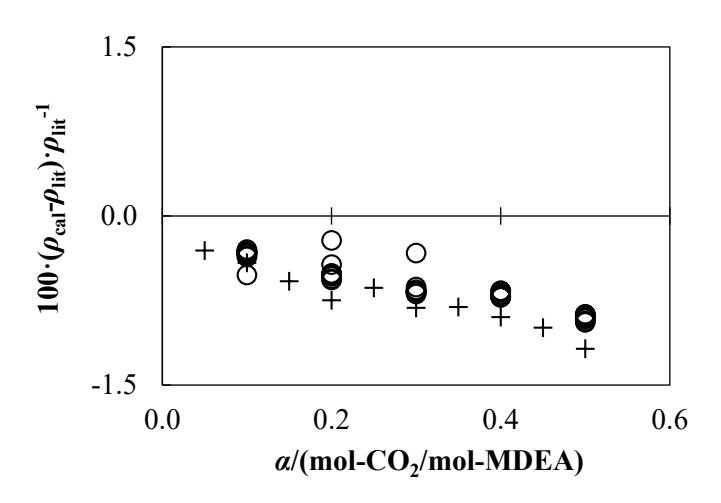


Figure 7.52. Relative deviations (%) vs CO₂ loading α for MDEA(1) + H₂O(2) + CO₂(3) mixture of calculated density ρ_{cal} , using **Equations 7.1 to 7.4**, in comparison with density literature values ρ_{lit} . Literature: (\bigcirc) Han et al. [126], and (+) Weiland et al. [107].

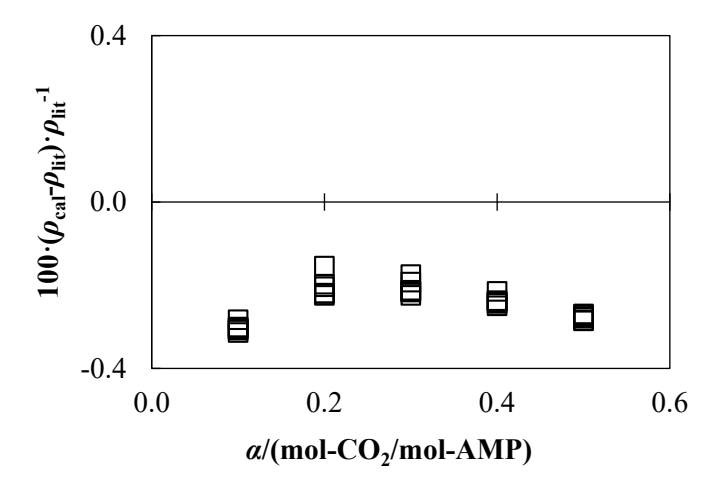


Figure 7.53. Relative deviations (%) vs CO₂ loading α for AMP(1) + H₂O(2) + CO₂(3) mixture of calculated density ρ_{cal} , using **Equations 7.1 to 7.4**, in comparison with density literature values ρ_{lit} . Literature: (\square) Stee et al. [83].

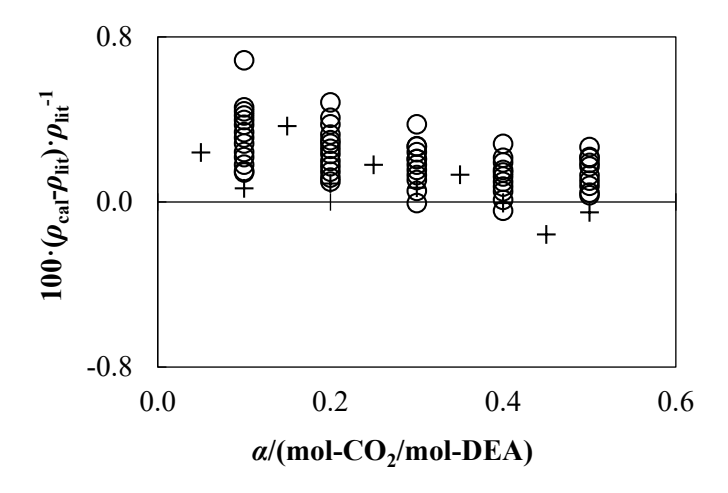


Figure 7.54. Relative deviations (%) vs CO₂ loading α for DEA(1) + H₂O(2) + CO₂(3) mixture of calculated density ρ_{cal} , using **Equations 7.1 to 7.4**, in comparison with density literature values ρ_{lit} . Literature: (\bigcirc) Han et al. [126], and (+) Weiland et al. [107].

7.4. Quaternary Mixtures. Aqueous Solution of Two Amines Loaded with CO2

The experimental densities of the quaternary mixture formed by an aqueous solution of two amines loaded with CO₂ have been measured in a wide range of temperatures, pressures, and CO₂ loading. Since experimental data for the mixture without CO₂ loading were not available, the experimental densities could not be correlated using the modified Tammann-Tait equation. An exhaustive search of the literature revealed that, to the best of our knowledge, there are no references that report densities of this mixture at the concentrations studied, so the comparison with the literature was not possible.

7.4.1. DMEA + MAPA +
$$H_2O + CO_2$$

7.4.1.1. Experimental Density

The results of the density measurements of the aqueous amine solutions are presented in **Table 7.22** for DMEA + MAPA + H₂O + CO₂ with DMEA mass fraction (CO₂-free basis) $w_{\text{DMEA}} = 0.3000$ and MAPA mass fraction (CO₂-free basis) $w_{\text{MAPA}} = 0.1000$. In order to analyse the impact of pressure, CO₂ loading, and temperature, the experimental density data were plotted as a function of these variables for all the studied systems, as can be observed in **Figures 7.55 to 7.57**.

Table 7.22. Experimental densities ρ , for the system DMEA + MAPA + H₂O + CO₂ with amine mass fraction (CO₂-free basis) w = 0.4000, at different conditions of temperature T, pressure p, CO₂ loading α in terms of mol-CO₂/mol-amines.^a

$ ho/(\mathrm{kg}\cdot\mathrm{m}^{-3})$							
n/MDa	T/K						
p/MPa	293.15	313.15	333.15	353.15	373.15	393.15	
		O	$\alpha = 0.206$				
0.1	1019.3	1006.2	991.8	976.7			
0.5	1019.4	1006.3	992.0	976.8			
1	1019.4	1006.4	992.2	977.0			
2	1019.7	1006.8	992.6	977.4			
5	1020.8	1007.9	993.9	978.8	962.4	945.1	
10	1022.6	1009.8	996.0	980.9	964.9	947.8	
15	1024.3	1011.6	997.9	983.1	967.2	950.4	
20	1026.0	1013.4	999.9	985.2	969.5	953.0	
30	1029.3	1017.0	1003.7	989.3	974.0	957.9	
40	1032.6	1020.5	1007.4	993.4	978.4	962.6	
50	1035.8	1023.9	1011.0	997.2	982.5	967.1	
60	1038.9	1027.2	1014.6	1001.0	986.6	971.6	
70	1042.0	1030.4	1018.0	1004.7	990.5	975.8	
80	1045.0	1033.6	1021.3	1008.2	994.3	979.9	
90	1047.9	1036.7	1024.7	1011.7	998.0	983.9	
100	1050.8	1039.7	1027.8	1015.0	1001.6	987.7	
		O	$\alpha = 0.401$				
0.1	1053.1	1040.5	1026.4	1011.6			
0.5	1053.2	1040.5	1026.6	1011.8			
1	1053.3	1040.7	1026.8	1012.0			
2	1053.6	1041.0	1027.2	1012.4			
5	1054.7	1042.1	1028.4	1013.7	997.7	980.7	
10	1056.4	1043.9	1030.3	1015.7	1000.0	983.3	
15	1058.0	1045.6	1032.2	1017.7	1002.3	985.8	
20	1059.7	1047.4	1034.1	1019.8	1004.4	988.2	
30	1062.9	1050.8	1037.7	1023.6	1008.7	992.8	
40	1066.1	1054.2	1041.3	1027.5	1012.7	997.3	

50	1069.2	1057.4	1044.7	1031.2	1016.7	1001.7
60	1072.3	1060.7	1048.2	1034.7	1020.5	1005.9
70	1075.3	1063.8	1051.4	1038.3	1024.3	1009.9
80	1078.2	1066.9	1054.7	1041.7	1028.0	1013.8
90	1081.1	1070.0	1057.9	1045.0	1031.5	1017.5
100	1083.9	1072.9	1060.9	1048.3	1034.9	1021.2
		o	a = 0.600			
0.1	1085.7	1072.9	1059.0	1044.6		
0.5	1085.7	1073.0	1059.2	1044.8		
1	1085.9	1073.1	1059.4	1044.9		
2	1086.2	1073.5	1059.7	1045.3		
5	1087.2	1074.5	1060.9	1046.5	1030.9	1013.8
10	1088.9	1076.2	1062.7	1048.5	1033.0	1016.2
15	1090.5	1077.9	1064.5	1050.4	1035.1	1018.6
20	1092.1	1079.6	1066.3	1052.3	1037.2	1020.8
30	1095.3	1083.0	1069.8	1055.9	1041.2	1025.3
40	1098.4	1086.2	1073.2	1059.6	1045.0	1029.7
50	1101.5	1089.3	1076.5	1063.1	1048.8	1033.7
60	1104.5	1092.5	1079.8	1066.5	1052.4	1037.8
70	1107.4	1095.6	1083.0	1069.9	1056.0	1041.7
80	1110.4	1098.6	1086.2	1073.1	1059.6	1045.5
90	1113.2	1101.6	1089.2	1076.4	1063.0	1049.1
100	1116.2	1104.5	1092.2	1079.6	1066.2	1052.7
		o	a = 0.802			
0.1	1113.2	1101.5	1088.5	1074.9		
0.5	1113.3	1101.6	1088.7	1075.1		
1	1113.4	1101.7	1088.8	1075.2		
2	1113.8	1102.0	1089.2	1075.6		
5	1114.8	1103.0	1090.3	1076.8	1061.6	1044.1
10	1116.4	1104.6	1092.1	1078.6	1063.6	1046.4
15	1117.9	1106.3	1093.8	1080.4	1065.6	1048.7
20	1119.5	1107.9	1095.4	1082.2	1067.6	1051.0
30	1122.5	1111.0	1098.8	1085.7	1071.4	1055.4
40	1125.5	1114.1	1102.0	1089.2	1075.1	1059.6
50	1128.5	1117.2	1105.2	1092.6	1078.7	1063.7

60	1131.5	1120.2	1108.3	1095.7	1082.3	1067.5
70	1134.4	1123.2	1111.4	1099.0	1085.6	1071.3
80	1137.2	1126.1	1114.4	1102.1	1089.0	1075.0
90	1140.0	1128.9	1117.4	1105.3	1092.3	1078.6
100	1142.7	1131.8	1120.3	1108.3	1095.5	1082.0

^aExpanded uncertainty (k = 2): U(T) = 0.02 K; $U_r(p) = 0.0002$; $U_r(w) = 0.0004$; $U_r(\alpha) = 0.003$ and $U(\rho) = 2$ kg·m⁻³.

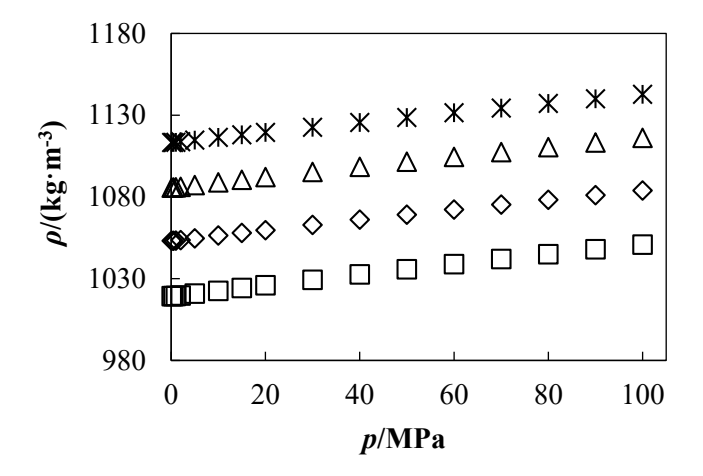


Figure 7.55. Experimental density ρ , of the system DMEA-MAPA(1) + H₂O(2) + CO₂(3) as a function of pressure p, at temperature T = 293.15 K. CO₂ loadings: (\square) $\alpha = 0.2$ mol-CO₂/mol-amine, (\diamondsuit) $\alpha = 0.4$ mol-CO₂/mol-amine, (\triangle) $\alpha = 0.6$ mol-CO₂/mol-amine, and (*) $\alpha = 0.8$ mol-CO₂/mol-amine.

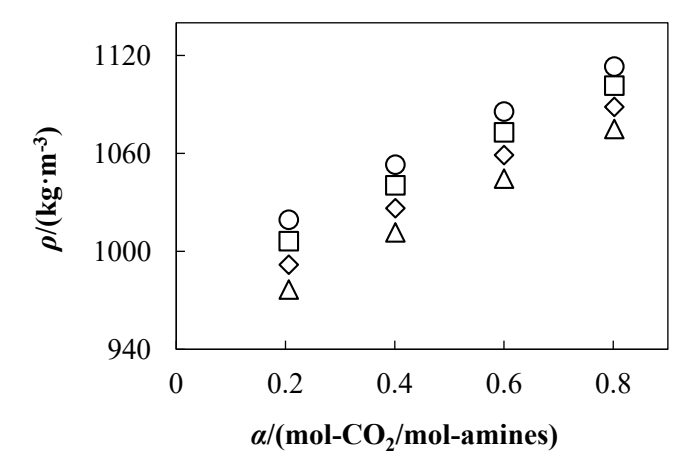


Figure 7.56. Experimental density ρ , of the system DMEA-MAPA(1) + H₂O(2) + CO₂(3) as a function of CO₂ loading α , at pressure p = 0.1 MPa. Isotherms: (\bigcirc) T = 293.15 K, (\bigcirc) T = 313.15 K, (\diamondsuit) T = 333.15 K, and (\triangle) T = 353.15 K.

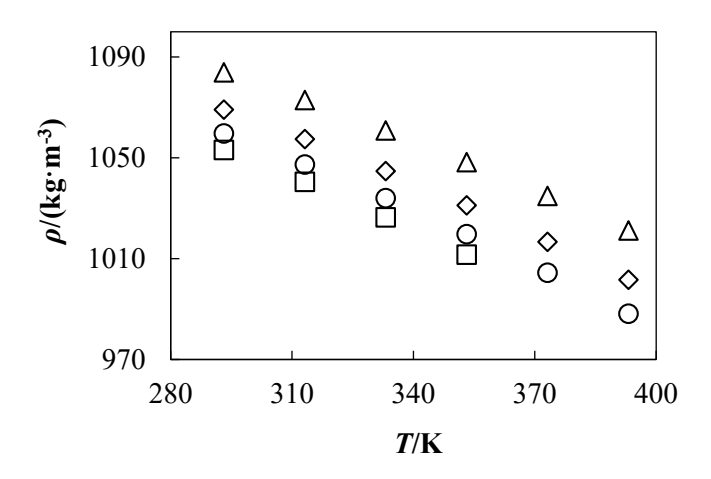


Figure 7.57. Experimental density ρ , of the system DMEA-MAPA(1) + H₂O(2) + CO₂(3) as a function of temperature T, at CO₂ loading $\alpha = 0.4$ mol-CO₂/mol-amine. Isobars: (\square) p = 0.1 MPa, (\bigcirc) p = 20 MPa, (\bigcirc) p = 50 MPa, and (\triangle) p = 100 MPa.

As for the rest of the solutions studied, the experimental density increased with pressure and decreased with temperature, as shown in **Figures 7.55 and 7.57**. An increase in CO₂ loading resulted in a 10 % increase in density when the CO₂ loading changed from (0.2 to 0.8) mol-CO₂/mol-amines, as detailed in **Figure 7.56**.



8. Experimental Isobaric Heat Capacity

8.1. Introduction

The isobaric heat capacity data obtained for the CO₂-unloaded and CO₂-loaded aqueous amine solutions systems is valuable for optimising the energy efficiency of amine-based CO₂ capture processes. It can also contribute to improving models used to simulate these processes and complete the thermodynamic characterisation of these mixtures.

In this work the following chemicals samples were used: monoethanolamine (MEA), diethanolamine (DEA), 2-(ethylamino)ethanol (EAE), methyldiethanolamine (MDEA), 2-(dimethylamino)ethanol (DMEA), 2-diethylaminoethanol (DEAE), 2-amino-2-methyl-1-propanol (AMP), 3-(methylamino)propylamine (MAPA), 1-methylpiperazine (1-MPZ), piperazine (PZ), water (H₂O) and carbon dioxide (CO₂). This chapter focuses on the isobaric heat capacity measurements of five binary (amine + H₂O) and three ternary (amine + H₂O + CO₂) systems.

Isobaric heat capacity measurements were achieved on:

- Five binary systems: DEAE + H₂O, EAE + H₂O, MAPA + H₂O, 1-MPZ + H₂O and AMP + H₂O.
- Three ternary systems: $MEA + H_2O + CO_2$, $MDEA + H_2O + CO_2$, and $AMP + H_2O + CO_2$.

The measurements covered a pressure range of up to 25 MPa for binary solutions and 20 MPa for ternary solutions, with temperatures ranging from 293.15 K to 353.15 K. For binary systems, four amine mass fractions were measured (0.1 to 0.4), except for the AMP + H₂O system where only a single mass fraction of 0.3 was studied. The ternary systems were only measured at an amine mass fraction of 0.3. The effect of varying CO₂ concentrations on these last systems was also studied.

Density plays a crucial role in calculating isobaric heat capacity, as detailed in Equation 5.3 in Chapter 5. This property was used for the mass flow determination and all the experimental data was measured in this work. On the other hand, viscosity is a critical factor in the friction correction term used for isobaric heat capacity calculations, as explained in Section 5.3 in Chapter 5. We relied on existing experimental viscosity data from various sources for the aqueous amine mixtures studied. The source of the experimental viscosity data is explained below.

- DEAE + H₂O: Data from Maham et al. [67] and Karunarathne et al. [62].
- EAE + H₂O: Data from Pandey & Mondal [73] and Viet et al. [72].
- MAPA + H₂O: Data from Monteiro et al. [76].
- 1-MPZ + H₂O: Data from Rayer et al. [78] and Vamja et al. [38].

- AMP + H₂O: Data from Mandal et al. [92] and Kummamuru et al. [100].
- MEA + H₂O + CO₂: Hartono et al. [110], Weiland et al. [107] and Zhang et al. [112].
- MDEA + H₂O + CO₂: Weiland et al. [107] and our viscosity measurements.
- AMP + $H_2O + CO_2$: our viscosity measurements.

These references provided viscosity data relevant to our study conditions: atmospheric pressure, temperatures ranging from 293.15 K to 353.15 K, and amine mass fractions of 0.1, 0.2, 0.3, and 0.4 in binary systems and the corresponding conditions of CO₂ loading in ternary systems.

Estimating viscosity at high pressures was unnecessary for our purposes. Using the available ambient-pressure viscosity data introduced a negligible error of only 0.03 % to the isobaric heat capacity, even at the highest flow rate where the viscosity correction was largest. This error is significantly smaller than the reported uncertainty in our measurements, being nearly an order of magnitude lower.

The isobaric heat capacity of the binary systems was correlated as a function of temperature and amine mass fraction using the empirical equation proposed by Al-Ghawas et al. [105]. For the ternary systems the symbolic regression software TuringBot [201] was employed to develop new correlation that describe the behavior of the studied fluid. As a result, the statistical parameters obtained were in good agreement with the experimental uncertainty. In addition, our data showed good agreement with the limited references available in the literature, considering the associated uncertainties.

To enhance clarity for the variety of systems and compositions studied in this work, we have adopted a numbering scheme for the mixture components: amine(1), H₂O(2) and CO₂(3).

8.2. Binary Mixtures. CO₂-Unloaded Aqueous Amine Solutions

8.2.1. DEAE + H_2O

8.2.1.1. Experimental Isobaric Heat Capacity

Isobaric heat capacities were measured at four temperatures from 293.15 K to 353.15 K, pressures up to 25 MPa, and amine mass fractions of 0.1, 0.2, 0.3, and 0.4. The experimental values are shown in **Table 8.1** for DEAE + H₂O. In order to analyse the influence of temperature, pressure, and amine mass fraction on isobaric heat capacities, the experimental data were plotted as a function of temperature at fixed pressure with different amine mass fractions (see **Figure 8.1**), as a function of pressure at fixed temperature (313.15 K) with different amine mass fractions (see **Figure 8.2**), and finally, as a function of amine mass fraction at atmospheric pressure (see **Figure 8.3**).

Table 8.1. Experimental isobaric heat capacity $c_p/(kJ\cdot kg^{-1}\cdot K^{-1})$, for DEAE(1) + H₂O(2) mixture at different conditions of temperature T, pressure p, and amine mass fraction w_1 .^a

$c_p/(\mathrm{kJ}\cdot\mathrm{kg}^{-1}\cdot\mathrm{K}^{-1})$								
	T/K							
p/MPa	293.15	313.15	333.15	353.15				
-		$w_1 = 0.10$	000					
0.1	4.22	4.21	4.23	4.19				
5	4.22	4.21	4.22	4.19				
10	4.18	4.19	4.20	4.20				
15	4.18	4.20	4.21	4.18				
20	4.17	4.19	4.21	4.18				
25	4.16	4.18	4.22	4.18				
		$w_1 = 0.20$	000					
0.1	4.24	4.19	4.23	4.23				
5	4.28	4.19	4.21	4.22				
10	4.26	4.17	4.19	4.22				
15	4.26	4.23	4.19	4.24				
20	4.24	4.20	4.20	4.23				
25	4.26	4.18	4.21	4.23				
		$w_1 = 0.30$	000					
0.1	4.14	4.11	4.13	4.20				
5	4.12	4.13	4.11	4.15				
10	4.12	4.13	4.10	4.13				
15	4.13	4.10	4.10	4.18				
20	4.13	4.11	4.11	4.16				
25	4.17	4.12	4.12	4.10				
		$w_1 = 0.40$	000					
0.1	3.96	4.00	4.02	4.09				
5	3.92	3.96	4.02	4.07				
10	3.94	3.95	4.01	4.04				
15	3.91	3.97	4.00	4.05				
20	3.89	3.97	4.04	4.07				
25	3.85	3.99	4.01	4.07				

^aExpanded uncertainties (k = 2): U(T) = 0.02 K, $U_r(p) = 0.0005$, $U_r(w) = 0.0004$ and $U_r(c_p) = 0.01$.

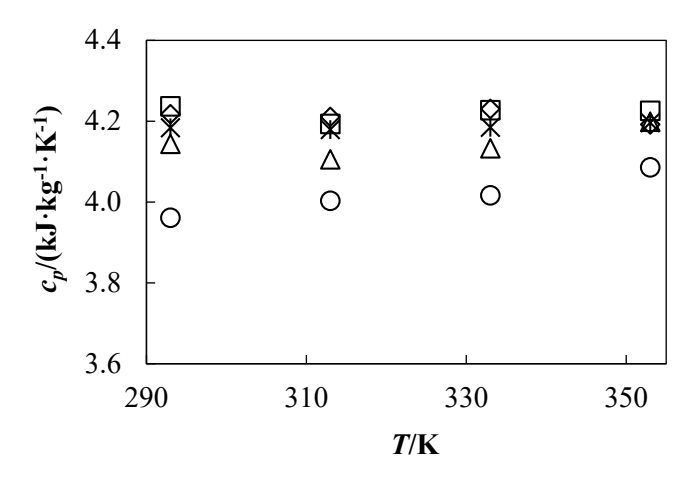


Figure 8.1. Experimental isobaric heat capacity c_p , for DEAE(1) + H₂O(2) mixture as a function of temperature T, at pressure p = 0.1 MPa. Amine mass fraction: (*) $w_1 = 0$, (\diamondsuit) $w_1 = 0.1$, (\square) $w_1 = 0.2$, (\triangle) $w_1 = 0.3$, and (\bigcirc) $w_1 = 0.4$. Experimental isobaric heat capacity data of pure water ($w_1 = 0$) from NIST REFPROP database [180].

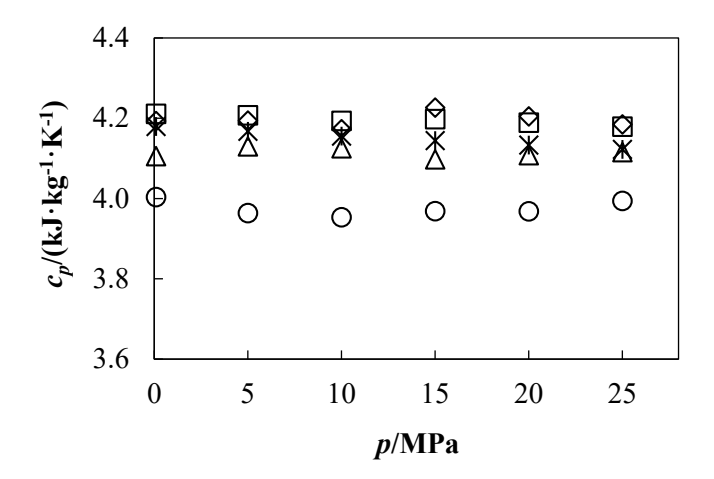


Figure 8.2. Experimental isobaric heat capacity c_p , for DEAE(1) + H₂O(2) mixture as a function of pressure p, at temperature T = 313.15 K. Amine mass fraction: (*) $w_1 = 0$, (\diamondsuit) $w_1 = 0.1$, (\square) $w_1 = 0.2$, (\triangle) $w_1 = 0.3$, and (\bigcirc) $w_1 = 0.4$. Experimental isobaric heat capacity data of pure water ($w_1 = 0$) from NIST REFPROP database [180].

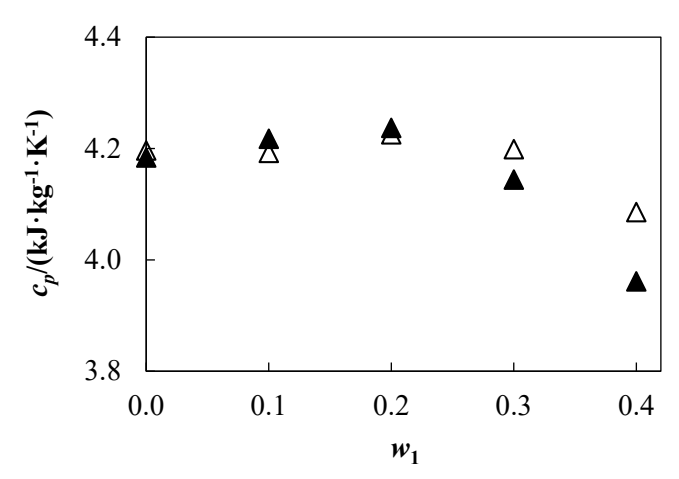


Figure 8.3. Experimental isobaric heat capacity c_p , for DEAE(1) + H₂O(2) mixture as a function of amine mass fraction w_1 , at pressure p = 0.1 MPa. Isotherms: (\triangle) T = 293.15 K, and (\blacktriangle) T = 353.15 K. Experimental isobaric heat capacity data of pure water ($w_1 = 0$) from NIST REFPROP database [180].

8.2.1.2. Comparison with Literature

Only one reference in the literature was found that provides experimental data on isobaric heat capacity for DEAE aqueous solutions. This property is reported by Cabani et al. [69] in the form of apparent molal heat capacity on a molality basis per gram of water ($J \cdot mol^{-1} \cdot K^{-1}$). As detailed in **Table 8.2** the average value of apparent molal heat capacity, Φ_{c_p} , at 313.15 K for a molal concentration range between (0.35 and 0.99) mol·kg⁻¹ is 540 ±8 J·mol⁻¹·K⁻¹ for DEAE + H₂O. Our experimental isobaric heat capacity data were converted to units of apparent molal heat capacity ($J \cdot mol^{-1} \cdot K^{-1}$) using **Equation 8.1**, as proposed by the same research group in a prior publication [193].

$$\Phi_{c_{pm}} = \left(\frac{1}{b_1} + M_1\right) c_p - \frac{1}{b_1} c_{p,w} \tag{8.1}$$

where M_1 is the amine molar mass, b_1 is the amine molality and $c_{p,w}$ is the water specific isobaric heat capacity at a given temperature obtained from NIST REFPROP database [180].

Table 8.2. Measurement conditions of literature data used to compare the experimental isobaric heat capacity data of DEAE + H₂O measured in this work.

Binary mixture	$b_1/(\text{mol}\cdot\text{kg}^{-1})$	$\Phi_{c_{pm,lit}}/(\mathbf{J}\cdot\mathbf{mol}^{-1}\cdot\mathbf{K}^{-1})$	$\Phi_{c_{pm,\exp}}/(\mathbf{J}\cdot\mathbf{mol}^{-1}\cdot\mathbf{K}^{-1})$	RDª
$DEAE + H_2O$	0.35 - 0.99	540 ±8	525 ±5	3 %

^aRelative deviation.

Upon conversions, relative deviations of 3 % was found, as shown in **Table 8.2**. These deviations are considered acceptable, given the expected uncertainties and the fact that the reported apparent molal heat capacity represents an average value across a range of molal concentrations.

$8.2.2.EAE + H_2O$

8.2.2.1. Experimental Isobaric Heat Capacity

Isobaric heat capacities were measured at four temperatures from 293.15 K to 353.15 K, pressures up to 25 MPa, and amine mass fractions of 0.1, 0.2, 0.3, and 0.4. The experimental values are shown in **Table 8.3** for EAE + H₂O. In order to analyse the influence of temperature, pressure, and amine mass fraction on isobaric heat capacities, the experimental data were plotted as a function of temperature at fixed pressure with different amine mass fractions (see **Figure 8.4**), as a function of pressure at fixed temperature (313.15 K) with different amine mass fractions (see **Figure 8.5**), and finally, as a function of amine mass fraction at atmospheric pressure (see **Figure 8.6**).

Table 8.3. Experimental isobaric heat capacity $c_p/(kJ\cdot kg^{-1}\cdot K^{-1})$, for EAE(1) + H₂O(2) mixture at different conditions of temperature T, pressure p, and amine mass fraction w_1 .

$c_p/(\mathrm{kJ} \cdot \mathrm{kg}^{\text{-}1} \cdot \mathrm{K}^{\text{-}1})$							
		T	/K				
p/MPa	293.15	313.15	333.15	353.15			
		$w_1 = 0.100$	00				
0.1	4.23	4.19	4.22	4.26			
5	4.18	4.18	4.21	4.25			
10	4.23	4.19	4.19	4.23			
15	4.24	4.15	4.19	4.24			
20	4.22	4.15	4.21	4.22			
25	4.21	4.15	4.20	4.24			
$w_1 = 0.2000$							
0.1	4.18	4.18	4.23	4.26			
5	4.19	4.18	4.23	4.25			
10	4.15	4.17	4.23	4.26			
15	4.20	4.17	4.22	4.25			
20	4.20	4.17	4.22	4.28			
25	4.15	4.19	4.22	4.25			
		$w_1 = 0.300$	00				
0.1	4.11	4.12	4.18	4.21			
5	4.09	4.10	4.17	4.20			
10	4.10	4.09	4.15	4.20			
15	4.08	4.10	4.16	4.19			
20	4.09	4.09	4.17	4.20			

25	4.13	4.10	4.17	4.22
		$w_1 = 0.40$	02	
0.1	3.97	4.00	4.06	4.12
5	3.98	3.94	4.04	4.11
10	3.98	3.99	4.06	4.08
15	3.96	3.96	4.06	4.08
20	3.97	3.97	4.05	4.09
25	3.99	3.96	4.06	4.10

^aExpanded uncertainties (k = 2): U(T) = 0.02 K, $U_r(p) = 0.0005$, $U_r(w) = 0.0004$ and $U_r(c_p) = 0.01$.

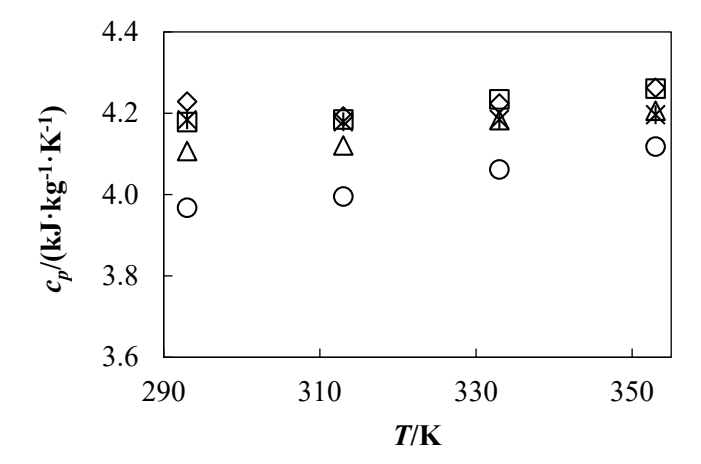


Figure 8.4. Experimental isobaric heat capacity c_p , for EAE(1) + H₂O(2) mixture as a function of temperature T, at pressure p = 0.1 MPa. Amine mass fraction: (*) $w_1 = 0$, (\diamondsuit) $w_1 = 0.1$, (\square) $w_1 = 0.2$, (\triangle) $w_1 = 0.3$, and (\bigcirc) $w_1 = 0.4$. Experimental isobaric heat capacity data of pure water ($w_1 = 0$) from NIST REFPROP database [180].

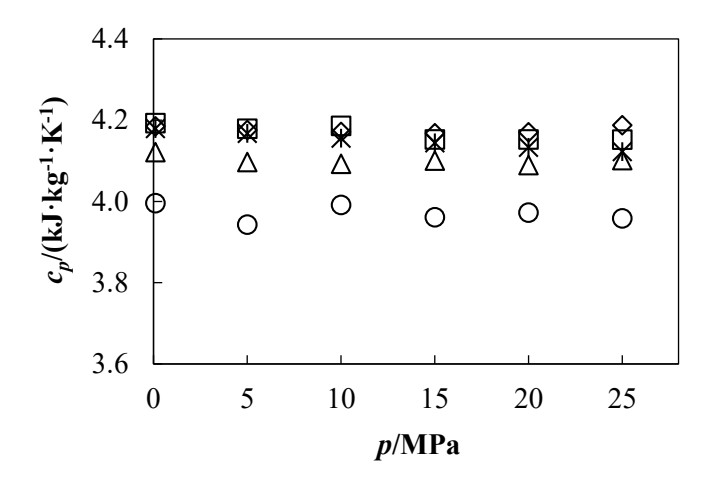


Figure 8.5. Experimental isobaric heat capacity c_p , for EAE(1) + H₂O(2) mixture as a function of pressure p, at temperature T = 313.15 K. Amine mass fraction: (*) $w_1 = 0$, (\$\infty\$) $w_1 = 0.1$, (\$\square\$) $w_1 = 0.2$,

(\triangle) $w_1 = 0.3$, and (\bigcirc) $w_1 = 0.4$. Experimental isobaric heat capacity data of pure water ($w_1 = 0$) from NIST REFPROP database [180].

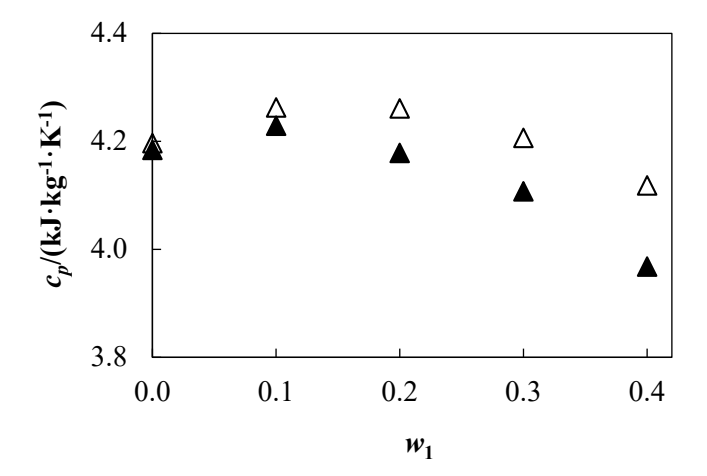


Figure 8.6. Experimental isobaric heat capacity c_p , for EAE(1) + H₂O(2) mixture as a function of amine mass fraction w_1 , at pressure p = 0.1 MPa. Isotherms: (\triangle) T = 293.15 K, and (\blacktriangle) T = 353.15 K. Experimental isobaric heat capacity data of pure water ($w_1 = 0$) from NIST REFPROP database [180].

8.2.2.2. Comparison with Literature

Cabani et al. [69] also provides experimental data on isobaric heat capacity for EAE aqueous solutions. In order to carry out the comparison, the same methodology was followed as that used for the DEAE solutions, explained in Section 8.2.1.2. As detailed in **Table 8.4** the average value of apparent molal heat capacity, Φ_{c_p} , at 313.15 K for a molal concentration range between (0.36 and 0.98) mol·kg⁻¹ is 391 $\pm 10 \text{ J·mol}^{-1} \cdot \text{K}^{-1}$ for EAE + H₂O.

Table 8.4. Measurement conditions of literature data used to compare the experimental isobaric heat capacity data of EAE + H₂O measured in this work.

Binary mixtures	<i>b</i> ₁ /(mol·kg ⁻¹)	$\Phi_{c_{pm,lit}}/(\mathbf{J}\cdot\mathbf{mol}^{-1}\cdot\mathbf{K}^{-1})$	$\Phi_{c_{pm,\text{exp}}}/(\mathbf{J}\cdot\mathbf{mol}^{-1}\cdot\mathbf{K}^{-1})$	RDª
$EAE + H_2O$	0.36 - 0.98	391 ±10	382 ±4	2 %

^aRelative deviation.

A 2 % difference was observed for EAE + H₂O after conversion (see **Table 8.4**). This deviation is considered acceptable due to inherent uncertainties and because the reported apparent molal heat capacity represents an average across a range of molal concentrations.

8.2.3. $MAPA + H_2O$

8.2.3.1. Experimental Isobaric Heat Capacity

Isobaric heat capacities were measured at four temperatures from 293.15 K to 353.15 K, pressures up to 25 MPa, and amine mass fractions of 0.1, 0.2, 0.3, and 0.4. The experimental values are shown in **Table 8.5** for MAPA + H₂O. In order to analyse the influence of temperature, pressure, and amine mass fraction on isobaric heat capacities, the experimental data were plotted as a function of temperature at fixed pressure with different amine mass fractions (see **Figure 8.7**), as a function of pressure at fixed temperature (313.15 K) with different amine mass fractions (see **Figure 8.8**), and finally, as a function of amine mass fraction at atmospheric pressure (see **Figure 8.9**).

Table 8.5. Experimental isobaric heat capacity $c_p/(kJ\cdot kg^{-1}\cdot K^{-1})$, for MAPA(1) + H₂O(2) mixture at different conditions of temperature T, pressure p, and amine mass fraction w_1 .

		/a * 1 ==	· 1s		
$c_p/(\mathrm{kJ} \cdot \mathrm{kg}^{\text{-}1} \cdot \mathrm{K}^{\text{-}1})$					
<i>T</i> /K					
p/MPa	293.15	313.15	333.15	353.15	
		$w_1 = 0.1000$)		
0.1	4.21	4.20	4.24	4.29	
5	4.21	4.17	4.22	4.27	
10	4.18	4.16	4.22	4.25	
15	4.22	4.16	4.20	4.25	
20	4.24	4.16	4.21	4.26	
25	4.21	4.18	4.21	4.26	
		$w_1 = 0.2000$)		
0.1	4.18	4.17	4.25	4.30	
5	4.15	4.17	4.24	4.28	
10	4.16	4.15	4.23	4.27	
15	4.16	4.14	4.24	4.28	
20	4.13	4.17	4.23	4.27	
25	4.17	4.18	4.25	4.28	
$w_1 = 0.3000$					
0.1	4.09	4.16	4.20	4.23	
5	4.07	4.11	4.20	4.22	
10	4.06	4.14	4.17	4.20	
15	4.08	4.13	4.16	4.22	
20	4.08	4.14	4.17	4.19	
25	4.06	4.13	4.15	4.18	
$w_1 = 0.4007$					

0.1	3.92	3.99	4.07	4.11
5	3.92	3.97	4.06	4.13
10	3.94	3.99	4.07	4.14
15	3.90	3.94	4.09	4.16
20	3.96	3.98	4.08	4.19
25	3.88	3.97	4.08	4.18

^aExpanded uncertainties (k = 2): U(T) = 0.02 K, $U_r(p) = 0.0005$, $U_r(w) = 0.0004$ and $U_r(c_p) = 0.01$.

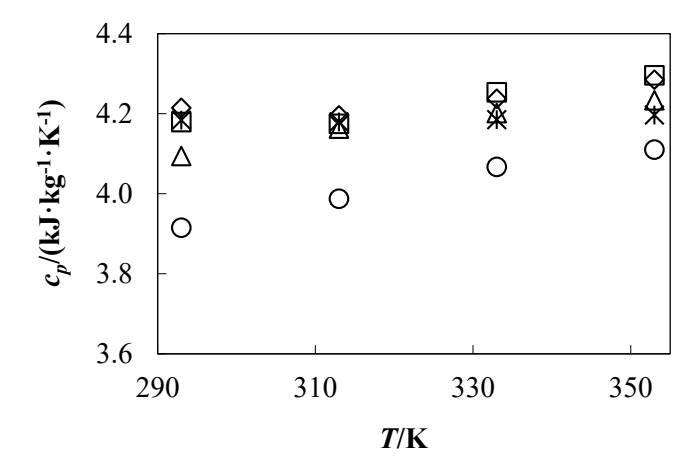


Figure 8.7. Experimental isobaric heat capacity c_p , for MAPA(1) + H₂O(2) mixture as a function of temperature T, at pressure p = 0.1 MPa. Amine mass fraction: (*) $w_1 = 0$, (\diamondsuit) $w_1 = 0.1$, (\square) $w_1 = 0.2$, (\triangle) $w_1 = 0.3$, and (\bigcirc) $w_1 = 0.4$. Experimental isobaric heat capacity data of pure water ($w_1 = 0$) from NIST REFPROP database [180].

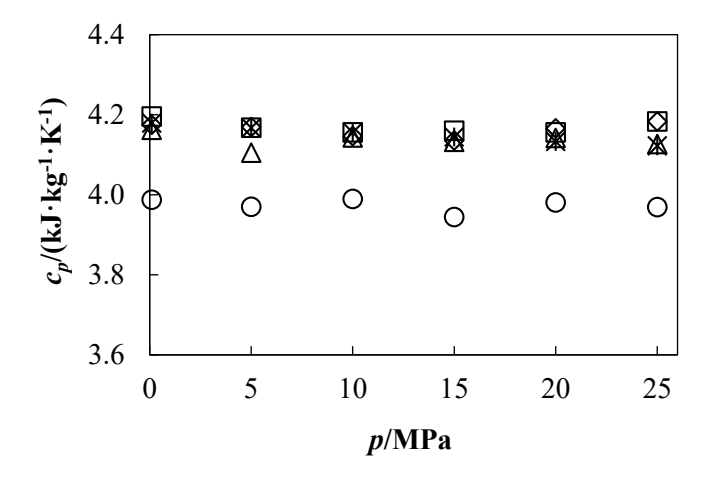


Figure 8.8. Experimental isobaric heat capacity c_p , for MAPA(1) + H₂O(2) mixture as a function of pressure p, at temperature T = 313.15 K. Amine mass fraction: (*) $w_1 = 0$, (\diamondsuit) $w_1 = 0.1$, (\square) $w_1 = 0.2$, (\triangle) $w_1 = 0.3$, and (\bigcirc) $w_1 = 0.4$. Experimental isobaric heat capacity data of pure water ($w_1 = 0$) from NIST REFPROP database [180].

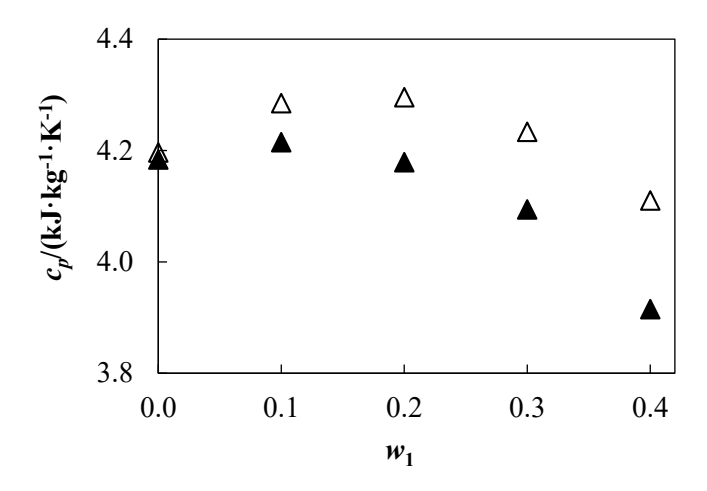


Figure 8.9. Experimental isobaric heat capacity c_p , for MAPA(1) + H₂O(2) mixture as a function of amine mass fraction w_1 , at pressure p = 0.1 MPa. Isotherms: (\triangle) T = 293.15 K, and (\blacktriangle) T = 353.15 K. Experimental isobaric heat capacity data of pure water ($w_1 = 0$) from NIST REFPROP database [180].

8.2.4. $1-MPZ + H_2O$

8.2.4.1. Experimental Isobaric Heat Capacity

Isobaric heat capacities were measured at four temperatures from 293.15 K to 353.15 K, pressures up to 25 MPa, and amine mass fractions of 0.1, 0.2, 0.3, and 0.4. The experimental values are shown in **Table 8.6** for 1-MPZ + H₂O. In order to analyse the influence of temperature, pressure, and amine mass fraction on isobaric heat capacities, the experimental data were plotted as a function of temperature at fixed pressure with different amine mass fractions (see **Figure 8.10**), as a function of pressure at fixed temperature (313.15 K) with different amine mass fractions (see **Figure 8.11**), and finally, as a function of amine mass fraction at atmospheric pressure (see **Figure 8.12**).

Table 8.6. Experimental isobaric heat capacity $c_p/(kJ\cdot kg^{-1}\cdot K^{-1})$, for 1-MPZ(1) + H₂O(2) mixture at different conditions of temperature T, pressure p, and amine mass fraction w_1 .

$c_p/(\mathrm{kJ}\cdot\mathrm{kg}^{-1}\cdot\mathrm{K}^{-1})$					
	T/K				
p/MPa	293.15	313.15	333.15	353.15	
		$w_1 = 0.1001$			
0.1	4.19	4.17	4.17	4.20	
5	4.16	4.15	4.17	4.21	
10	4.14	4.16	4.16	4.18	
15	4.14	4.14	4.16	4.18	
20	4.17	4.14	4.14	4.17	
25	4.09	4.15	4.16	4.18	

		$w_1 = 0.2002$	2	
0.1	4.02	4.04	4.11	4.13
5	4.03	4.05	4.11	4.16
10	4.04	4.05	4.12	4.16
15	4.01	4.06	4.11	4.13
20	4.04	4.07	4.12	4.17
25	4.03	4.06	4.13	4.14
		$w_1 = 0.3001$	[
0.1	3.97	4.01	4.07	4.15
5	3.96	4.01	4.07	4.13
10	3.96	4.00	4.07	4.13
15	3.95	4.00	4.06	4.11
20	3.96	3.97	4.07	4.13
25	3.97	4.01	4.08	4.12
		$w_1 = 0.4002$	2	
0.1	3.76	3.85	3.93	4.03
5	3.78	3.79	3.93	4.03
10	3.73	3.80	3.92	4.03
15	3.77	3.79	3.93	4.03
20	3.77	3.80	3.93	4.02
25	3.79	3.81	3.94	4.02

^aExpanded uncertainties (k = 2): U(T) = 0.02 K, $U_r(p) = 0.0005$, $U_r(w) = 0.0004$ and $U_r(c_p) = 0.01$.

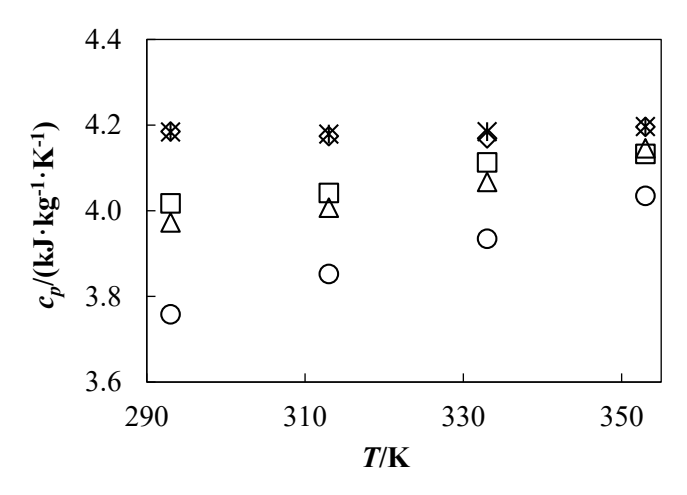


Figure 8.10. Experimental isobaric heat capacity c_p , for 1-MPZ(1) + H₂O(2) mixture as a function of temperature T, at pressure p = 0.1 MPa. Amine mass fraction: (*) $w_1 = 0$, (\diamondsuit) $w_1 = 0.1$, (\square) $w_1 = 0.2$, (\triangle) $w_1 = 0.3$, and (\bigcirc) $w_1 = 0.4$. Experimental isobaric heat capacity data of pure water ($w_1 = 0$) from NIST REFPROP database [180].

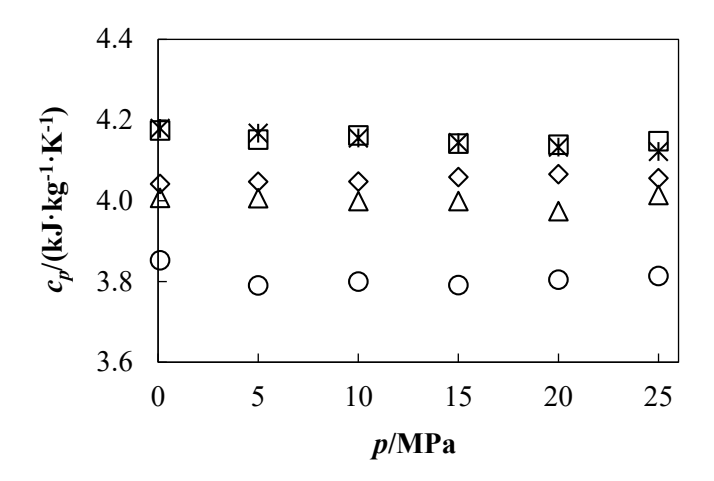


Figure 8.11. Experimental isobaric heat capacity c_p , for 1-MPZ(1) + H₂O(2) mixture as a function of pressure p, at temperature T = 313.15 K. Amine mass fraction: (*) $w_1 = 0$, (\diamondsuit) $w_1 = 0.1$, (\square) $w_1 = 0.2$, (\triangle) $w_1 = 0.3$, and (\bigcirc) $w_1 = 0.4$. Experimental isobaric heat capacity data of pure water ($w_1 = 0$) from NIST REFPROP database [180].

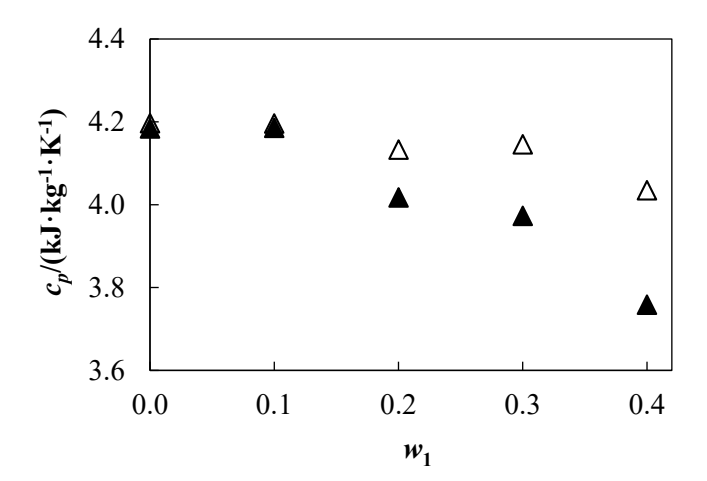


Figure 8.12. Experimental isobaric heat capacity c_p , for 1-MPZ(1) + H₂O(2) mixture as a function of amine mass fraction w_1 , at pressure p = 0.1 MPa. Isotherms: (\triangle) T = 293.15 K, and (\blacktriangle) T = 353.15 K. Experimental isobaric heat capacity data of pure water ($w_1 = 0$) from NIST REFPROP database [180].

8.2.4.2. Comparison with Literature

For the 1-MPZ + H₂O binary mixture, we found only one reference in the literature carried out by Poozesh et al. [79] reporting molar isobaric heat capacities in a range of amine mole fractions from $x_{\text{amine}} = (0.099 \text{ to } 1) \text{ mol/mol}$, temperatures from T = (298.15 to 353.15) K, and at atmospheric pressure p = 0.1 MPa. The expanded relative uncertainty (k = 2) in molar isobaric heat capacity c_{pm} reported in Poozesh et al. [79] study was 1 %. From this study [79] three comparable data points have been found in terms of measurement conditions with respect to our work, as shown in **Figure 8.13**. Relative deviations of less than 1 % have been obtained in the comparison, which is in good agreement with the reported uncertainty for the measurement.

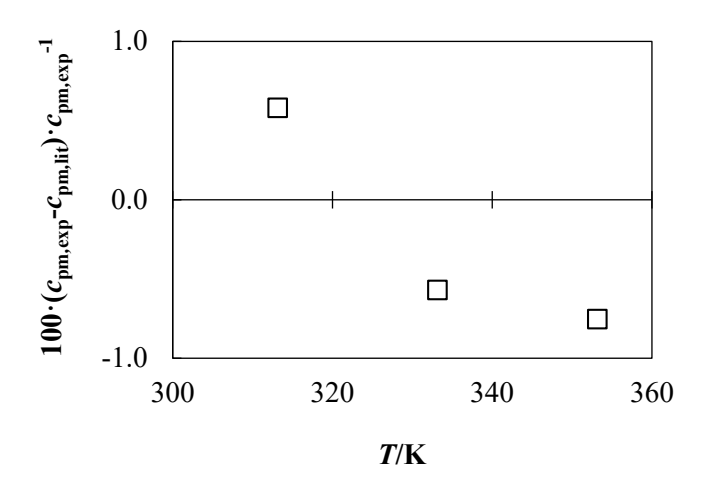


Figure 8.13. Relative deviations (%) of molar isobaric heat capacity measurements $c_{pm,exp}$, in comparison with literature values $c_{pm,lit}$. Literature for 1-MPZ + H₂O: (\square) Poozesh et al. [79].

8.2.5. $AMP + H_2O$

8.2.5.1. Experimental Isobaric Heat Capacity

Isobaric heat capacities were measured at four temperatures from 293.15 K to 353.15 K, pressures up to 20 MPa, and amine mass fractions of 0.3. The experimental values are shown in **Table 8.7** for AMP + H₂O. The system was studied at a specific mass fraction to enable the use of data from the CO₂-free solution. This data was involved in developing a model to describe how CO₂ loading affects the solution, as it will be discussed in Section 8.3.4.

Table 8.7. Experimental isobaric heat capacity $c_p/(kJ\cdot kg^{-1}\cdot K^{-1})$, for AMP(1) + H₂O(2) mixture at amine mass fraction $w_1 = 0.3015$ and different conditions of temperature T, and pressure p.

$c_p/(\mathrm{kJ}\!\cdot\!\mathrm{kg}^{ ext{-}1}\!\cdot\!\mathrm{K}^{ ext{-}1})$					
	T/K				
p/MPa	293.15	313.15	333.15	353.15	
0.1	3.91	4.07	4.12	4.18	
10	3.91	4.11	4.13	4.18	
20	3.95	4.07	4.16	4.16	

^aExpanded uncertainties (k = 2): U(T) = 0.02 K, $U_r(p) = 0.0005$, $U_r(w) = 0.0004$ and $U_r(c_p) = 0.01$.

8.2.6. Discussion

Poling et al. [139] suggest that at a reduced temperature below 0.7, there is no strong dependence of temperature on liquid heat capacity. This is valid for the reduced range of temperatures studied for the binary mixtures. **Figure 8.1** shows that the isobaric heat capacity increases by an average of 4 % from

(293.15 to 353.15) K in the DEAE + H_2O mixture for a $w_{DEAE} = 0.4$. While, for the EAE + H_2O mixture, **Figure 8.4** shows average increases of 2 %, 3 %, and 3 % for $w_{EAE} = 0.2$, 0.3, and 0.4, respectively.

Regarding MAPA aqueous solutions (**Figure 8.7**), the change with temperature was noticeable for all mass fractions, with increases from 2 % to 6 % at w_{MAPA} range from 0.1 to 0.4. For the 1-MPZ + H₂O binary solution, as can be seen in **Figure 8.10**, an increase in temperature resulted in increases in c_p of 3 %, 4 %, and 7 % for $w_{1-\text{MPZ}} = 0.2$, 0.3, and 0.4, respectively. This behaviour agrees with the fact that temperature has a slight influence on the isobaric heat capacity of pure amines [79,146,148,194,195]. For the 1-MPZ solution ($w_{1-\text{MPZ}} = 0.1$), the change in c_p as a function of temperature is less than the measurement uncertainty. DEAE aqueous solutions with $w_{\text{DEAE}} = 0.2$ showed a minimum in c_p at a temperature of 313.15 K.

The effect of pressure on c_p at a fixed temperature of 313.15 K for these mixtures is shown in **Figures 8.2, 8.5, 8.8, and 8.11** for aqueous solutions of DEAE, EAE, MAPA, or 1-MPZ amines, respectively. For the DEAE + H₂O system, a decrease of 2 % can be observed for $w_{DEAE} = 0.3$ at 353.15 K, and 3 % for $w_{DEAE} = 0.4$ at 293.15 K. For the MAPA + H₂O mixture, a decrease of 2 % was observed for $w_{MAPA} = 0.3$ at 293.15 K, and an increase of 2 % for $w_{MAPA} = 0.4$ at 353.15 K. The 1-MPZ aqueous solution at $w_{1-MPZ} = 0.1$ experienced a 2 % decrease in c_p at a temperature of 293.15 K. For the rest of the amine mass fractions and temperature conditions, the change in c_p with pressure is within the measurement uncertainty.

As the amine mass fraction increases from 0.1 to 0.4, the isobaric heat capacity decreases, as can be seen in **Figures 8.3, 8.6, 8.9, and 8.12**. In these terms, c_p decreases by an average of 4 % for DEAE + H_2O and for EAE + H_2O , 3 % for MAPA + H_2O , and 7 % for 1-MPZ + H_2O mixtures. A maximum (see **Figures 8.3, 8.6, 8.9, and 8.12**) in c_p was observed when $w_{amine} = 0.1$ for aqueous solutions of EAE, MAPA, or 1-MPZ, while for DEAE solutions the maximum was found at $w_{amine} = 0.2$.

While c_p was measured for a wider range of amine mass fractions and pressures for other solutions, data for the AMP + H₂O mixture was limited to a single amine mass fraction (0.3) and a narrower pressure range. This focus was chosen to allow for a more detailed analysis of the influence of CO₂ loading on this mixture, which will be discussed in Section 8.3.4. For the AMP + H₂O mixture, the change in isobaric heat capacity with temperature was within 7 %, while with pressure it remained within the measurement uncertainty.

8.2.7. Experimental Isobaric Heat Capacity Data Fitting

Experimental isobaric heat capacities for the binary mixtures were correlated with temperature T, and amine mass fraction w_1 , using **Equation 8.2**. These empirical equations were initially proposed by Al-Ghawas et al. [105] for densities of aqueous amine solutions. This model has been successfully used to

correlate isobaric heat capacity as a function of temperature and amine mass fraction in aqueous amino acid solutions in the study by Song et al. [202] and more recently in the work by Kim et al. [203] on aqueous solutions of 2-(isopropylamino)ethanol.

$$c_p(T, w_1) = k_{11} + k_{12} \cdot w_1 + (k_{21} + k_{22} \cdot w_1 + k_{23} \cdot w_1^2) \cdot T$$
(8.2)

where k_{11} , k_{12} , k_{21} , k_{22} and k_{23} are the fitting parameters; w_1 is the amine mass fraction; and T is the temperature.

First, the coefficients k_{11} and k_{21} in **Equation 8.2** were optimised for the amine mass fraction $w_1 = 0$ (pure water). The isobaric heat capacity data for pure water were taken from the NIST REFPROP database [180]. Once these values were determined, the remaining parameters k_{12} , k_{22} and k_{23} were fitted. The Levenberg-Marquardt algorithm [191] implemented in MATLAB R2023b [190] was used to optimise both fits. The objective function was to minimise the difference between the sum of the squares of the experimental and calculated isobaric heat capacity values. The isobaric heat capacity measurements were fitted to a 5-parameter correlation model. The goodness-of-fit was determined by calculating the statistical parameters: average absolute relative deviation (AAD), maximum absolute relative deviation (MAD) and standard deviation (σ). All these equations were shown previously in Equations 7.5, 7.6 and 7.7 in Chapter 7.

All the fitted coefficients are shown in **Table 8.8**, along with the statistical parameters AAD, MAD, and σ . As can be seen in **Figure 8.14**, the fitting residuals are within the measurement uncertainty in most cases, except for two points belonging to the DEAE + H₂O and four points for 1-MPZ + H₂O that deviate slightly above 1 %. No systematic deviations are observed in either the isobaric heat capacity or the amine mass fraction.

Table 8.8. Fitted parameters k_{11} , k_{12} , k_{21} , k_{22} and k_{23} in **Equation 8.2**, and statistical parameters AAD, MAD, and σ .

	Mixtures			
Parameters	$DEAE + H_2O$	$EAE + H_2O$	$MAPA + H_2O$	$1-MPZ + H_2O$
k_{11}	4.116	4.116	4.116	4.116
k_{12}	-1.111	-2.050	-2.728	-3.729
k_{21}	$2.182 \cdot 10^{-4}$	$2.182 \cdot 10^{-4}$	$2.182 \cdot 10^{-4}$	$2.182 \cdot 10^{-4}$
k_{22}	$5.476 \cdot 10^{-3}$	$8.407 \cdot 10^{-3}$	$1.106 \cdot 10^{-2}$	$1.131 \cdot 10^{-2}$
k_{23}	$-8.291 \cdot 10^{-3}$	-8.039·10 ⁻³	-9.651·10 ⁻³	-4.875·10 ⁻³
AAD	0.4 %	0.2 %	0.3 %	0.5 %
MAD	1 %	0.7 %	0.9 %	1 %
$\sigma/(kJ\cdot kg^{-1}\cdot K^{-1})$	0.03	0.02	0.02	0.03

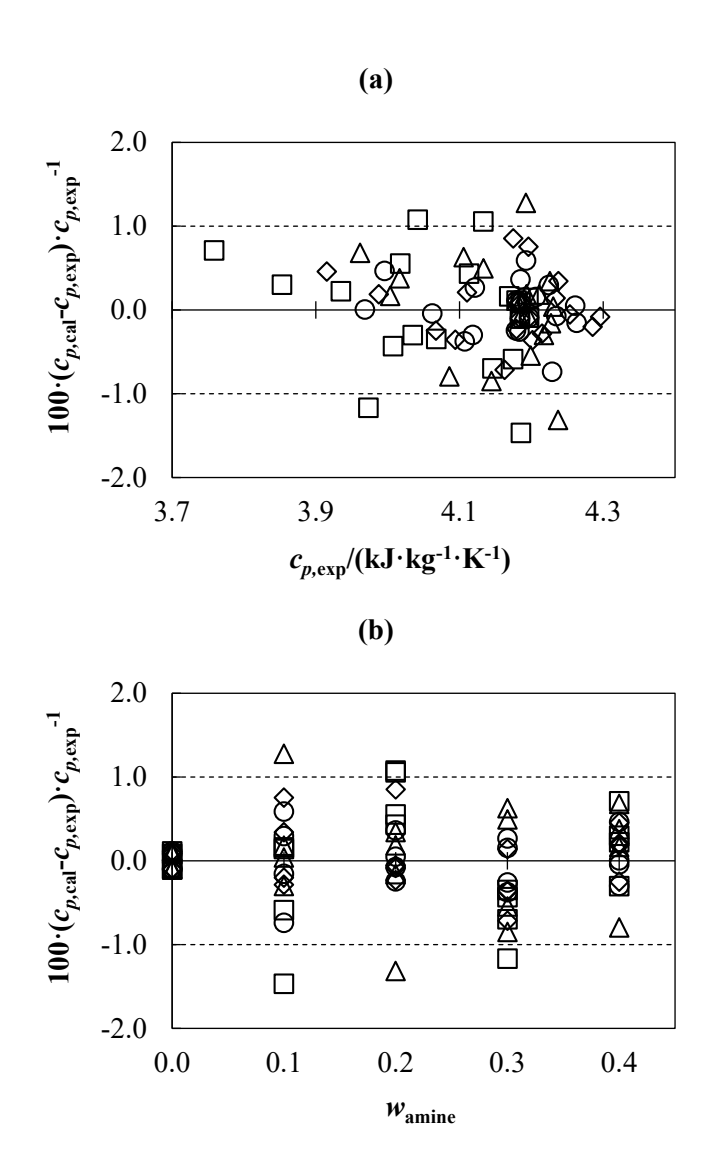


Figure 8.14. Relative deviations (%) between experimental isobaric heat capacity $c_{p,\text{exp}}$, and calculated isobaric heat capacity $c_{p,\text{cal}}$, using **Equation 8.2**. (a) Relative deviations vs $c_{p,\text{exp}}$, y (b) Relative deviations vs w_{amine} . Mixtures: (\triangle) DEAE + H₂O, (\bigcirc) EAE + H₂O, (\bigcirc) MAPA + H₂O, and (\square) 1-MPZ + H₂O. Dashed lines represent the relative expanded uncertainty of our measurements.

8.2.7.1. Comparison of Calculated Isobaric Heat Capacity with Experimental Literature Data

Only one literature source, Poozesh et al. [79], provided isobaric heat capacity data for the systems under studied (specifically $1\text{-MPZ} + H_2O$) across a broad range of molar composition and temperature (see Section 8.2.4.2). To enhance our comparison, we calculated 9 additional temperature points using **Equation 8.2**. This expanded dataset showed an average absolute relative deviation of 2 %, with a maximum of 3 %, as illustrated in **Figure 8.15**. The source of the observed deviations is not clearly understood, and this represents an aspect requiring in-depth investigation.

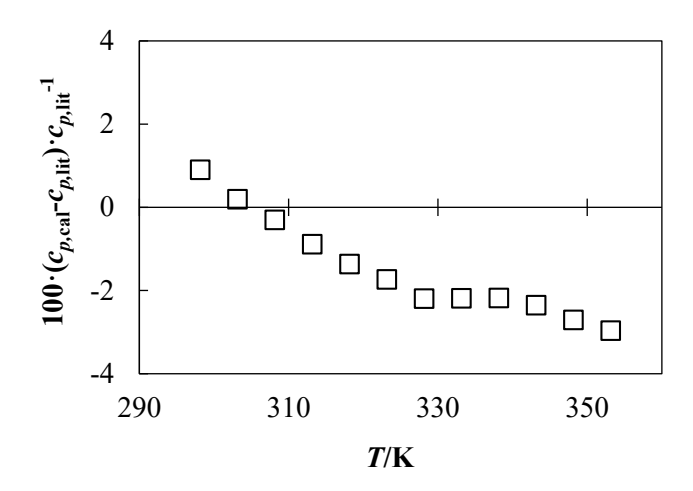


Figure 8.15. Relative deviations (%) vs temperature T for 1-MPZ + H₂O mixture of calculated isobaric heat capacity $c_{p,\text{cal}}$ using **Equation 8.2**, in comparison with isobaric heat capacity literature values $c_{p,\text{lit}}$. Literature: (\square) Poozesh et al. [79].

8.3. Ternary Mixtures. CO₂-Loaded Aqueous Amine Solutions

8.3.1.
$$MEA + H_2O + CO_2$$

8.3.1.1. Experimental Isobaric Heat Capacity

Isobaric heat capacities were measured at four temperatures from 293.15 K to 353.15 K, three pressures from (0.1 to 20) MPa, and different CO_2 loading. The experimental values are shown in **Table 8.9** for MEA + $H_2O + CO_2$. The influence of the temperature, pressure, and CO_2 loading can be seen in **Figures 8.16 to 8.18**.

Table 8.9. Experimental isobaric heat capacity c_p , for the system MEA(1) + H₂O(2) + CO₂(3) with amine mass fraction (CO₂-free basis) $w_1 = 0.3002$, at different conditions of temperature T, pressure p, and CO₂ loading α .^a

	$c_p/(\mathrm{kJ}\cdot\mathrm{kg}^{-1}\cdot\mathrm{K}^{-1})$				
		T/K			
p/MPa	293.15	313.15	333.15	353.15	
		$\alpha = 0.200$			
0.1	3.61	3.62	3.69	3.78	
10	3.60	3.67	3.71	3.78	
20	3.65	3.66	3.71	3.80	
	$\alpha = 0.300$				
0.1	3.53	3.55	3.65	3.72	
10	3.54	3.55	3.67	3.73	

CHAPTER 8: EXPERIMENTAL ISOBARIC HEAT CAPACITY

20	3.57	3.58	3.69	3.75
		$\alpha = 0.400$		
0.1	3.47	3.46	3.53	
10	3.49	3.48	3.55	
20	3.48	3.52	3.57	
		$\alpha = 0.609$		
0.1	3.29	3.33	3.45	
10	3.33	3.34	3.47	
20	3.30	3.35	3.52	

^aExpanded uncertainties (k = 2): U(T) = 0.02 K, $U_r(p) = 0.0005$, $U_r(w) = 0.0004$, $U_r(\alpha) = 0.003$ and $U_r(c_p) = 0.01$.

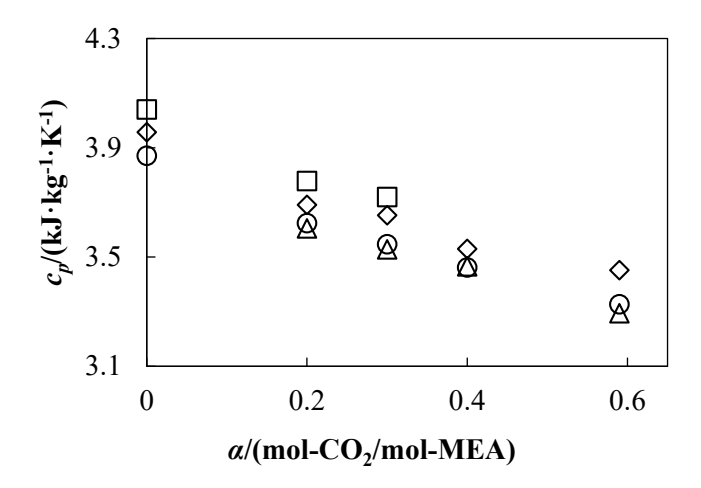


Figure 8.16. Experimental isobaric heat capacity c_p , of the system MEA(1) + H₂O(2) + CO₂(3) as a function of CO₂ loading α , at pressure p = 0.1 MPa. Isotherms: (\triangle) T = 293.15 K, (\bigcirc) T = 313.15 K, (\bigcirc) T = 353.15 K. Experimental isobaric heat capacity data of aqueous amine solution (CO₂-free basis) from [183].

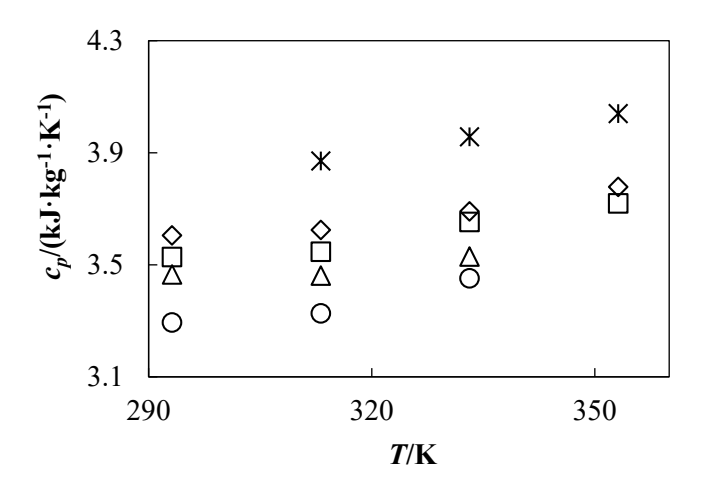


Figure 8.17. Experimental isobaric heat capacity c_p , of the system MEA(1) + H₂O(2) + CO₂(3) as a function of temperature T, at pressure p = 0.1 MPa. CO₂ loadings: (*) $\alpha = 0$ mol-CO₂/mol-MEA, (\diamondsuit) $\alpha = 0.2$ mol-CO₂/mol-MEA, (\square) $\alpha = 0.3$ mol-CO₂/mol-MEA, (\square) $\alpha = 0.4$ mol-CO₂/mol-MEA, and (\square) $\alpha = 0.6$ mol-CO₂/mol-MEA. Experimental isobaric heat capacity data of aqueous amine solution (CO₂-free basis) from [183].

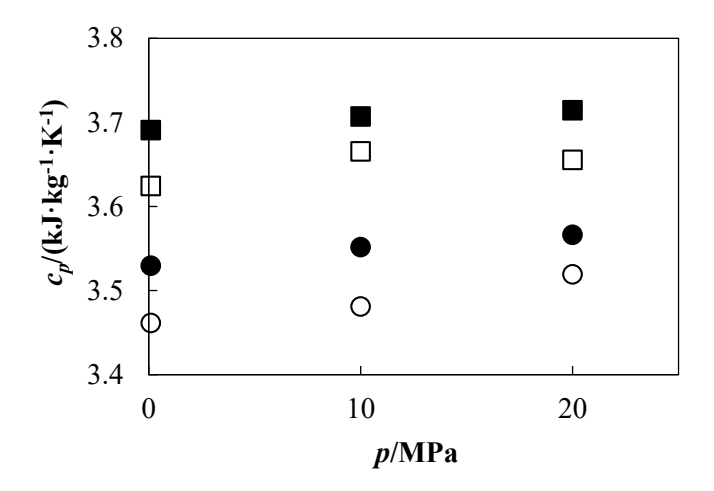


Figure 8.18. Experimental isobaric heat capacity c_p , of the system MEA(1) + H₂O(2) + CO₂(3) as a function of pressure p. CO₂ loadings: (\bullet) $\alpha = 0.2$ mol-CO₂/mol-MEA and T = 333.15 K, (\blacksquare) $\alpha = 0.4$ mol-CO₂/mol-MEA and T = 333.15 K, (\square) $\alpha = 0.2$ mol-CO₂/mol-MEA and T = 313.15 K, and (\bigcirc) $\alpha = 0.4$ mol-CO₂/mol-MEA and T = 313.15 K.

8.3.2. $MDEA + H_2O + CO_2$

8.3.2.1. Experimental Isobaric Heat Capacity

Isobaric heat capacities were measured at four temperatures from 293.15 K to 353.15 K, three pressures from (0.1 to 20) MPa, and different CO₂ loading. The experimental values are shown in **Table 8.10** for

CHAPTER 8: EXPERIMENTAL ISOBARIC HEAT CAPACITY

MDEA + H_2O + CO_2 . The influence of the temperature, pressure, and CO_2 loading can be seen in Figures 8.19 to 8.21.

Table 8.10. Experimental isobaric heat capacity c_p , for the system MDEA(1) + H₂O(2) + CO₂(3) with amine mass fraction (CO₂-free basis) $w_1 = 0.3000$, at different conditions of temperature T, pressure p, and CO₂ loading α .^a

	$c_p/($	kJ·kg ⁻¹ ·K	1)	
		T/K		
p/MPa	293.15	313.15	333.15	353.15
		$\alpha = 0.200$		
0.1	3.62	3.73	3.79	3.88
10	3.68	3.72	3.76	3.94
20	3.71	3.74	3.82	3.96
		$\alpha = 0.300$		
0.1	3.51	3.56	3.62	3.75
10	3.56	3.51	3.74	3.76
20	3.56	3.54	3.83	3.83
		$\alpha = 0.600$		
0.1	3.38	3.47	3.56	
10	3.40	3.46	3.54	
20	3.44	3.48	3.53	

^aExpanded uncertainties (k = 2): U(T) = 0.02 K, $U_r(p) = 0.0005$, $U_r(w) = 0.0004$, $U_r(\alpha) = 0.003$ and $U_r(c_p) = 0.01$.

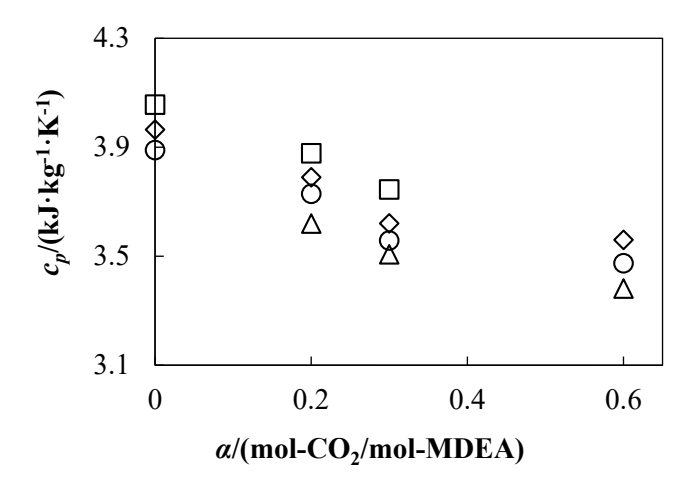


Figure 8.19. Experimental isobaric heat capacity c_p , of the system MDEA(1) + H₂O(2) + CO₂(3) as a function of CO₂ loading α , at pressure p = 0.1 MPa. Isotherms: (\triangle) T = 293.15 K, (\bigcirc) T = 313.15 K,

CHAPTER 8: EXPERIMENTAL ISOBARIC HEAT CAPACITY

(\diamondsuit) T = 333.15 K, and (\square) T = 353.15 K. Experimental density data of aqueous amine solution (CO₂-free basis) from [183].

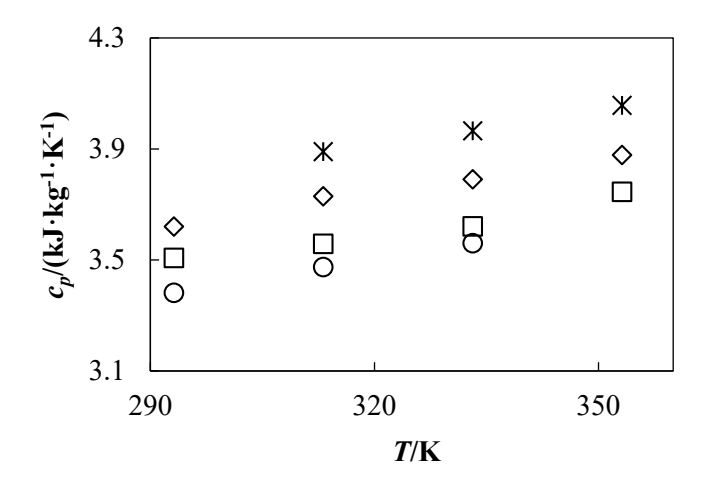


Figure 8.20. Experimental isobaric heat capacity c_p , of the system MDEA(1) + H₂O(2) + CO₂(3) as a function of temperature T, at pressure p = 0.1 MPa. CO₂ loadings: (*) $\alpha = 0$ mol-CO₂/mol-MDEA, (\diamondsuit) $\alpha = 0.2$ mol-CO₂/mol-MDEA, (\square) $\alpha = 0.3$ mol-CO₂/mol-MDEA, and (\square) $\alpha = 0.6$ mol-CO₂/mol-MDEA. Experimental isobaric heat capacity data of aqueous amine solution (CO₂-free basis) from [183].

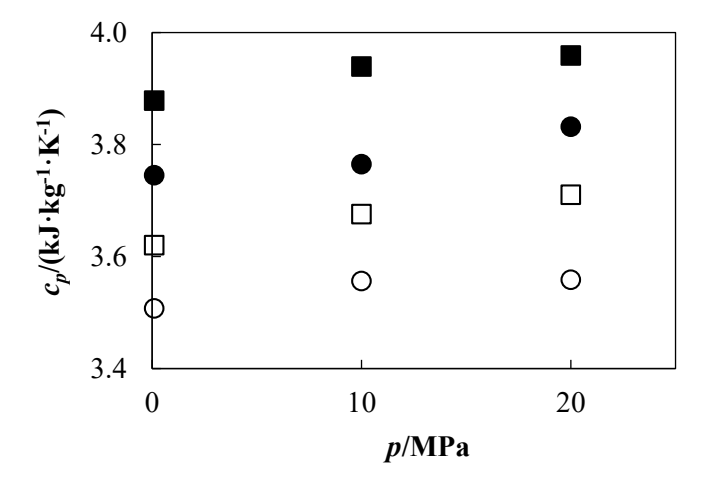


Figure 8.21. Experimental isobaric heat capacity c_p , of the system MDEA(1) + H₂O(2) + CO₂(3) as a function of pressure p. CO₂ loadings: (\bullet) α = 0.2 mol-CO₂/mol-MDEA and T = 353.15 K, (\blacksquare) α = 0.3 mol-CO₂/mol-MDEA and T = 353.15 K, (\square) α = 0.2 mol-CO₂/mol-MDEA and T = 293.15 K, and (\bigcirc) α = 0.3 mol-CO₂/mol-MDEA and T = 293.15 K.

8.3.3. $AMP + H_2O + CO_2$

8.3.3.1. Experimental Isobaric Heat Capacity

Isobaric heat capacities were measured at four temperatures from 293.15 K to 353.15 K, three pressures from (0.1 to 20) MPa, and different CO₂ loading. The experimental values are shown in **Table 8.11** for AMP + H₂O + CO₂. The influence of the temperature, pressure, and CO₂ loading can be seen in **Figures 8.22 to 8.24**.

Table 8.11. Experimental isobaric heat capacity c_p , for the system AMP(1) + H₂O(2) + CO₂(3) with amine mass fraction (CO₂-free basis) $w_1 = 0.3015$, at different conditions of temperature T, pressure p, and CO₂ loading α .^a

	$c_p/($	(kJ·kg ⁻¹ ·K ⁻	1)	
		T/K		
p/MPa	293.15	313.15	333.15	353.15
		$\alpha = 0.100$		
0.1	3.89	3.94	4.03	4.11
10	3.98	4.07	4.10	4.13
20	4.11	4.10	4.18	4.12
		$\alpha = 0.200$		
0.1	3.67	3.79	3.83	3.86
10	3.79	3.92	3.96	3.95
20	3.91	3.98	4.06	4.03

^aExpanded uncertainties (k = 2): U(T) = 0.02 K, $U_r(p) = 0.0005$, $U_r(w) = 0.0004$, $U_r(\alpha) = 0.003$ and $U_r(c_p) = 0.01$.

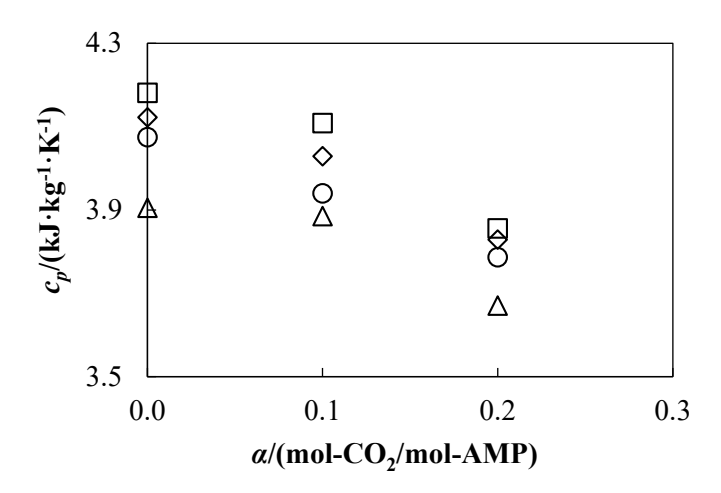


Figure 8.22. Experimental isobaric heat capacity c_p , of the system AMP(1) + H₂O(2) + CO₂(3) as a function of CO₂ loading α , at pressure p = 0.1 MPa. Isotherms: (\triangle) T = 293.15 K, (\bigcirc) T = 313.15 K,

(\diamondsuit) T = 333.15 K, and (\square) T = 353.15 K. Experimental density data of aqueous amine solution (CO₂-free basis) reported in this work.

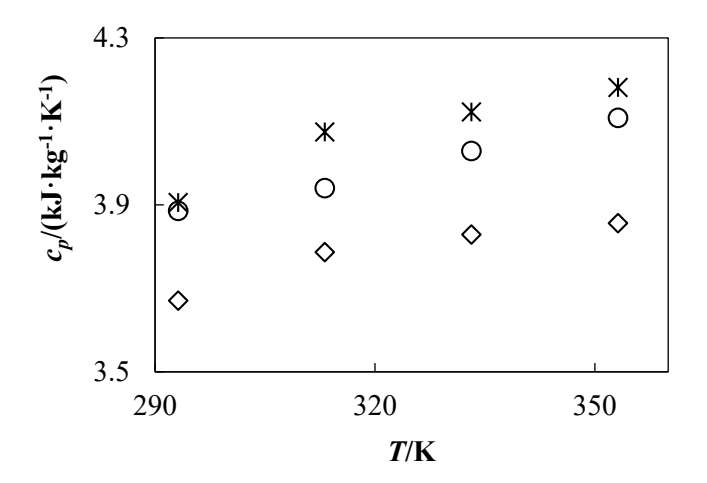


Figure 8.23. Experimental isobaric heat capacity c_p , of the system AMP(1) + H₂O(2) + CO₂(3) as a function of temperature T, at pressure p = 0.1 MPa. CO₂ loadings: (*) $\alpha = 0$ mol-CO₂/mol-AMP, (\bigcirc) $\alpha = 0.1$ mol-CO₂/mol-AMP, and (\bigcirc) $\alpha = 0.2$ mol-CO₂/mol-AMP. Experimental isobaric heat capacity data of aqueous amine solution (CO₂-free basis) reported in this work.

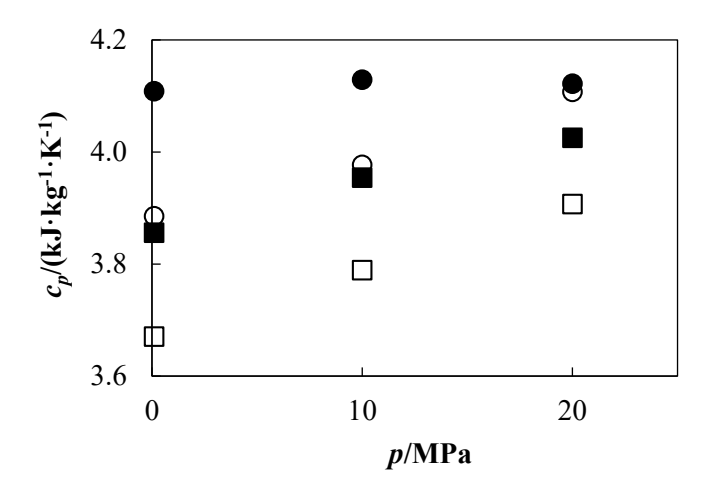


Figure 8.24. Experimental isobaric heat capacity c_p , of the system AMP(1) + H₂O(2) + CO₂(3) as a function of pressure p. CO₂ loadings: (\blacksquare) $\alpha = 0.1$ mol-CO₂/mol-AMP and T = 353.15 K, (\bullet) $\alpha = 0.2$ mol-CO₂/mol-AMP and T = 353.15 K, (\bigcirc) $\alpha = 0.1$ mol-CO₂/mol-AMP and T = 293.15 K, and (\square) $\alpha = 0.2$ mol-CO₂/mol-AMP and T = 293.15 K.

8.3.4. Discussion

Tables 8.9 and 8.10 show some missing data points. This is due to a Le Chatelier effect observed at the highest CO₂ loading. When temperature increases at high CO₂ loading, the equilibrium between the aqueous amine solution and CO₂ shifts towards the endothermic reaction, favouring the conversion of

CHAPTER 8: EXPERIMENTAL ISOBARIC HEAT CAPACITY

products back into reactants. This shift was confirmed by a decrease in density, indicating a lower CO₂ loading in the solution, and by an increase in *p*H, which suggests a decrease in CO₂ loading according to equilibrium models. In **Table 8.11**, AMP solutions reached a maximum CO₂ loading of 0.2 mol-CO₂/mol-AMP due to bubble formation in the flow calorimeter at higher loadings.

An increase in CO₂ loading led to a decrease in isobaric heat capacity. For MEA solutions, the decrease was 13 % when α changed from (0 to 0.6) mol-CO₂/mol-MEA, for MDEA solutions 10 % when α changed from (0 to 0.6) mol-CO₂/mol-MDEA, and for AMP solutions 5 % when α changed from (0 to 0.2) mol-CO₂/mol-AMP, as can be seen in **Figures 8.16**, **8.19 and 8.22**. Regarding temperature, increases in c_p were observed in the studied range: from (4 to 5) % for MEA solutions (see **Figures 8.17**), from (6 to 7) % for MDEA solutions (see **Figure 8.20**), and 5 % for AMP solutions (see **Figure 8.23**). Pressure, unlike for binary amine-water solutions, had a slightly more pronounced effect under some experimental conditions. In **Figure 8.21**, a 2 % change in isobaric heat capacity was observed for MDEA solutions for α = 0.2 mol-CO₂/mol-MDEA at T = 293.15 K and for the same CO₂ loading at T = 353.15 K, as well as a 6 % change when α = 0.3 mol-CO₂/mol-MDEA at T = 333.15 K. For aqueous MEA solutions, changes in c_p with pressure were less than 2 % for all conditions, as can be seen in **Figure 8.18**. While for aqueous AMP solutions, changes less than 6 % were seen in **Figure 8.24**.

8.3.5. Experimental Isobaric Heat Capacity Data Fitting

The symbolic regression software TuringBot [201] was used to generate equations describing the behaviour of the isobaric heat capacity of the CO_2 -loaded aqueous amine solutions as a function of temperature T and CO_2 loading α . This robust and versatile tool has demonstrated its effectiveness in previous studies [204–206]. The motivation behind using this particular method is driven by the need to find the equation that best adapts to the behavior of c_p as a function of temperature and CO_2 loading. A single equation, suitable for binary systems, cannot adequately account for the specific characteristics of these reactive systems. The resultant equations for MEA solutions, MDEA solutions and AMP solutions are listed in **Equations 8.3, 8.4 and 8.5**, respectively.

$$c_p(T,\alpha) = b_1 + b_2 \cdot \frac{T}{b_3 + \alpha} \tag{8.3}$$

$$c_p(T,\alpha) = d_1 + d_2 \cdot T + \left(\frac{d_3 \cdot \alpha}{d_4 - d_5 \cdot \alpha + \alpha^2}\right)$$
(8.4)

$$c_p(T,\alpha) = e_1 + e_2 \cdot T - e_3 \cdot T \cdot \alpha^2 \tag{8.5}$$

where c_p is the isobaric heat capacity in kJ·kg⁻¹·K⁻¹; b_i , d_i and e_i are the fitted parameters for each system respectively; T is the temperature in Kelvin; and α is the CO₂ loading in mol-CO₂/mol-amine.

CHAPTER 8: EXPERIMENTAL ISOBARIC HEAT CAPACITY

The fitted coefficients and statistical parameters (AAD, MAD, and σ) are presented in **Tables 8.12, 8.13** and **8.14** for MEA + H₂O + CO₂, MDEA + H₂O + CO₂, and AMP + H₂O + CO₂, respectively. **Figure 8.25** shows that the model's predictions generally agree with the experimental data within the measurement uncertainty. Minor deviations (slightly above 1 %) were observed for one data point in the MEA solutions and two in the AMP solutions. No systematic deviations were observed in either isobaric heat capacity or CO₂ loading.

Table 8.12. Fitted parameters in **Equations 8.3** and statistical parameters AAD, MAD, and σ for MEA + H₂O + CO₂ mixture.

Parameters	$MEA + H_2O + CO_2$
b_1	2.6005
b_2	$3.699 \cdot 10^{-3}$
b_3	$9.0578 \cdot 10^{-1}$
AAD	0.6 %
MAD	1 %
$\sigma/(kJ\cdot kg^{-1}\cdot K^{-1})$	0.03

Table 8.13. Fitted parameters in **Equations 8.4** and statistical parameters AAD, MAD, and σ for MDEA + H₂O + CO₂ mixture.

Parameters	$MDEA + H_2O + CO_2$
d_1	2.592
d_2	$4.146 \cdot 10^{-3}$
d_3	$1.117 \cdot 10^{-1}$
d_4	-2.288·10 ⁻¹
d_5	$-7.170 \cdot 10^{-1}$
AAD	0.3 %
MAD	0.8 %
$\sigma/(kJ\cdot kg^{-1}\cdot K^{-1})$	0.02

Table 8.14. Fitted parameters in **Equations 8.5** and statistical parameters AAD, MAD, and σ for AMP + H₂O + CO₂ mixture.

Parameters	$AMP + H_2O + CO_2$
e_1	2.754
e_2	$4.062 \cdot 10^{-3}$
e_3	$2.173 \cdot 10^{-2}$

AAD	0.5 %
MAD	1 %
$\sigma/(kJ\cdot kg^{-1}\cdot K^{-1})$	0.03

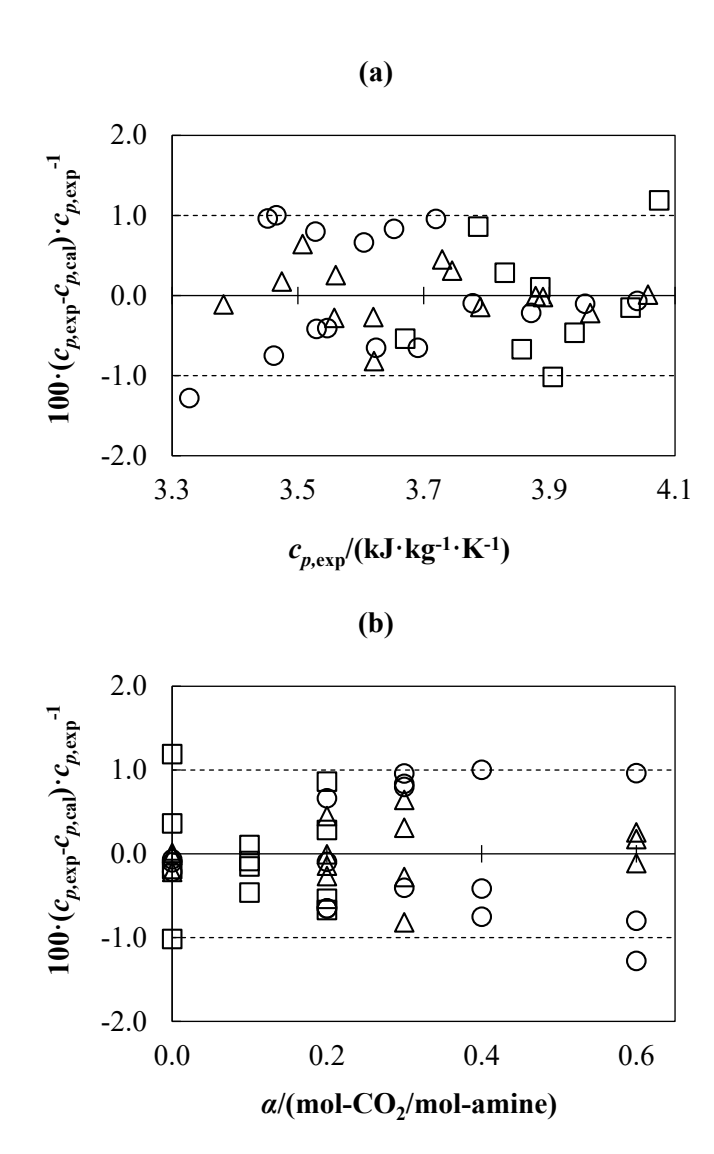


Figure 8.25. Relative deviations (%) between experimental isobaric heat capacity $c_{p,\text{exp}}$, and calculated isobaric heat capacity $c_{p,\text{cal}}$, using **Equation 8.3, 8.4 and 8.5** for (\bigcirc) MEA + H₂O + CO₂, (\triangle) MDEA + H₂O + CO₂, and (\square) AMP + H₂O + CO₂, respectively. (a) Relative deviations vs $c_{p,\text{exp}}$, and (b) Relative deviations vs CO₂ loading α . Dashed lines represent the relative expanded uncertainty of our measurements.

8.3.5.1. Comparison of Calculated Isobaric Heat Capacity with Experimental Literature Data

Weiland et al. [124] provided the only literature data for isobaric heat capacity of MEA + H_2O + CO_2 and MDEA + H_2O + CO_2 mixtures at 298.15 K, covering a wide range of CO_2 loadings. To allow this comparison, we calculated 5 points for MEA + H_2O + CO_2 (using **Equation 8.3**) and 10 points for

CHAPTER 8: EXPERIMENTAL ISOBARIC HEAT CAPACITY

MDEA + H₂O + CO₂ (using **Equation 8.4**). As shown in **Figure 8.26**, the resulting dataset showed an average absolute relative deviation between our calculated values and Weiland et al.'s data of 1 % (maximum 2 %) for MEA solutions and 2 % (maximum 3 %) for MDEA solutions.. These deviations arise from limitations in experimental uncertainties in the literature data (particularly CO₂ loading).

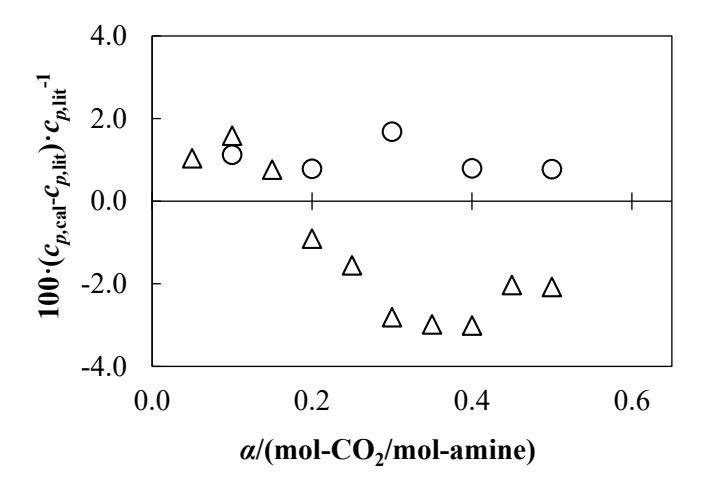
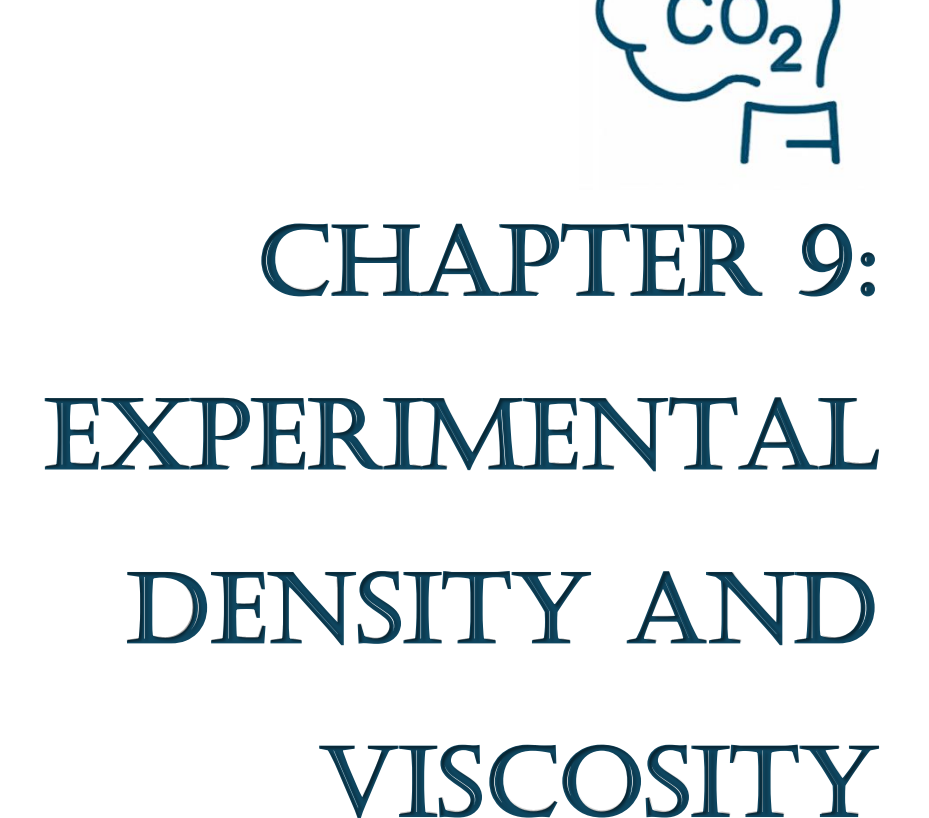


Figure 8.26. Relative deviations (%) vs CO₂ loading α of calculated isobaric heat capacity $c_{p,\text{cal}}$ using **Equation 8.3** for (\bigcirc) MEA + H₂O + CO₂ and **Equation 8.4** for (\triangle) MDEA + H₂O + CO₂, in comparison with the isobaric heat capacity literature values $c_{p,\text{lit}}$. Literature: Weiland et al. [124] (both mixtures).



9. Experimental Density and Viscosity

9.1. Introduction

Tertiary amines are known for their high CO₂ capture capacity and low enthalpy of absorption, as detailed in Chapter 1. However, their main drawback compared to primary or secondary amines is the slow reaction kinetics with CO₂. To address this, blended amines have gained attention due to their combination of high CO₂ absorption and fast reaction rates. Recently researchers have focused on using piperazine (PZ) and 2-amino-2-methyl-1-propanol (AMP) to promote the reaction between tertiary amines and CO₂. These studies have examined the kinetics of CO₂ absorption, CO₂ solubility, and the performance of these mixtures in pilot plants [40–48]. Despite this, there is still a lack of data on thermophysical properties such as density and viscosity, particularly at high CO₂ loading.

Dynamic viscosities measurements were achieved on:

- Two ternary systems: $MDEA + H_2O + CO_2$ and $AMP + H_2O + CO_2$.
- Two quaternary systems: $MDEA + PZ + H_2O + CO_2$ and $MDEA + AMP + H_2O + CO_2$.

Researchers such as [45,125,128,130,201] have studied the influence of CO_2 loading on the density and viscosity of MDEA + PZ + H_2O + CO_2 and MDEA + AMP + H_2O + CO_2 mixtures at various temperatures. However, only two references [100,129] provide experimental data across a wide range of amines mass fractions (CO_2 -free basis).

In this chapter, density measurements were carried out using an Anton Paar DMA 445 vibrating tube densimeter and viscosity was measured using a Ubbelohde capillary viscometer. These apparatus had been used in the Thermophysics Laboratory at the Imperial College London (UK) and they are described in detail in Chapter 6. The temperature ranged from 293.15 K to 353.15 K, and the pressure was maintained at atmospheric levels. For the systems MDEA + H₂O + CO₂ and AMP + H₂O + CO₂ the experimental density data are reported in Chapter 7, as they were measured using an Anton Paar DMA HPM vibrating tube densimeter. The experimental density measurements presented in this chapter were conducted to enable the calculation of dynamic viscosity in the quaternary systems, according to the Equation 6.2 detailed in Chapter 6. The dynamic viscosity data was correlated using modified Vogel-Fulcher-Tammann (VFT) equations, the specifics of which will be discussed later.

To enhance clarity for the variety of systems and compositions studied in this work, we have adopted a numbering scheme for the mixture components: MDEA(1), promoter: PZ or AMP (2), $H_2O(3)$ and $CO_2(4)$.

9.2. Ternary Mixtures

9.2.1. $MDEA + H_2O + CO_2$

9.2.1.1. Experimental Viscosity

The results of the viscosity measurements are presented in **Table 9.1** for MDEA + H_2O + CO_2 . To analyse the impact of CO_2 loading and temperature, the experimental dynamic viscosity data were plotted as a function of these variables, as shown in **Figure 9.1**. Density experimental data for the dynamic viscosity calculation of the CO_2 -unloaded solution were taken from Sobrino et al. [104]. For the CO_2 -loaded solution, density measurements are reported in Chapter 7 of this work.

Table 9.1. Experimental flow time t, kinematic viscosity v, and dynamic viscosity η , for the system MDEA(1) + H₂O(2) + CO₂(3) with amine mass fraction (CO₂-free basis) $w_1 = 0.2997$, at different conditions of temperature T, and CO₂ loading α in terms of mol-CO₂/mol-MDEA^a.

α	T/K	t/s	v/(mm ² ·s ⁻¹)	η/(mPa·s)
	292.96	730.28	3.64	3.73
0	313.08	388.45	1.93	1.97
U	333.12	242.11	1.21	1.21
	353.15	167.97	0.84	0.83
	292.95	727.27	3.62	3.75
0.099	313.07	393.14	1.96	2.01
0.099	333.10	247.07	1.23	1.25
	353.14	171.99	0.86	0.86
	292.95	728.74	3.63	3.79
0.209	313.08	398.60	1.99	2.05
0.209	333.11	251.00	1.25	1.28
	353.14	175.35	0.87	0.88
	292.96	721.94	3.60	3.82
0.424	313.08	407.22	2.03	2.13
	333.11	260.52	1.30	1.35
0.646	292.95	717.74	3.57	3.86
0.040	313.08	407.22	2.03	2.17
0.795	292.96	709.44	3.53	3.86
0.733	313.08	412.71	2.06	2.22

^aExpanded uncertainty (k = 2): U(T) = 0.02 K; $U_r(w) = 0.0003$; $U_r(\alpha) = 0.004$ and $U_r(\eta) = 0.01$.

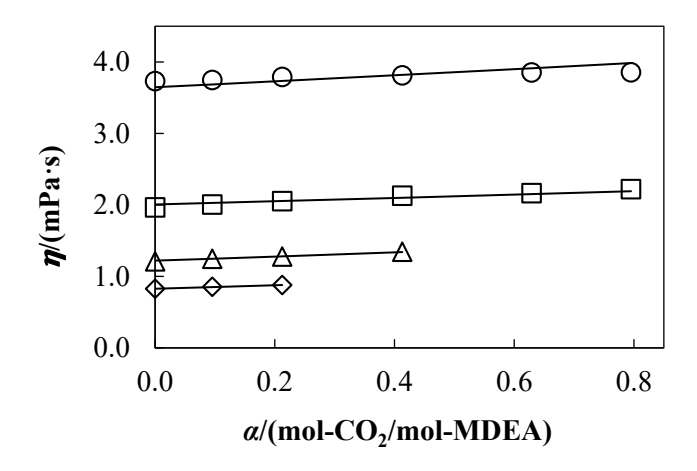


Figure 9.1. Experimental dynamic viscosity η , of the system MDEA + H₂O + CO₂ as a function of CO₂ loading α . Isotherms: (\bigcirc) T = 293 K, (\square) T = 313 K, (\triangle) T = 333 K, and (\diamondsuit) T = 353 K. Solid line: calculated viscosities using VFT modified correlation (**Equation 9.4**).

9.2.1.2. Comparison with Literature

The experimental conditions of the references used for the comparison of MDEA + H₂O (CO₂-free solution) are shown in **Table 9.2**. The relative deviations between the experimental dynamic viscosity data and the values reported in the literature are shown in **Figure 9.2**.

Table 9.2. Measurement conditions of literature data used to compare the experimental dynamic viscosity of MDEA(1) + $H_2O(2)$ mixture measured in this work at p = 0.1 MPa.

Reference	Viscometer	Conditions	Number of Points	$U_{ m r}^{ m a}$
Mandal et al. [92]	Ostwald Viscometer	$w_1 = 0.30$ T = (303.15 - 313.15) K	2	NA ^b
Sobrino et al.	Falling Body	$w_1 = 0.3000$	4	3 %
[104]	Viscometer	T = (293.15 - 313.15) K		5 70
Li et al. [89]	Cannon-Fenske	$w_1 = 0.30$	3	NA ^b
Li et al. [89]	Routine Viscometer	T = (303.15 - 333.15) K	3	1,17.1
Rinker et al. [106]	Two Cannon-Fenske- type viscometers (sizes 50 and 100) and one Ubbelohde-type viscometer (size 0)	$w_1 = 0.30$ $T = (333.15 - 353.15) \text{ K}$	2	NAb
Al-Ghawas et al. [105]	Cannon-Fenske Routine Viscometer	$w_1 = 0.$ T = (303.15 - 333.15) K	3	NA ^b

	Anton-Paar Physica			
Kummamuru	MCR	$w_1 = 0.30$		
et al. [129]	101 rheometer with a	T = (303.15 - 313.15) K	2	3 %
et al. [127]	double-gap	1 - (303.13 - 313.13) K		
	pressure cell XL			

^aRelative expanded uncertainty (k = 2), %.

^bNA: Not Available.

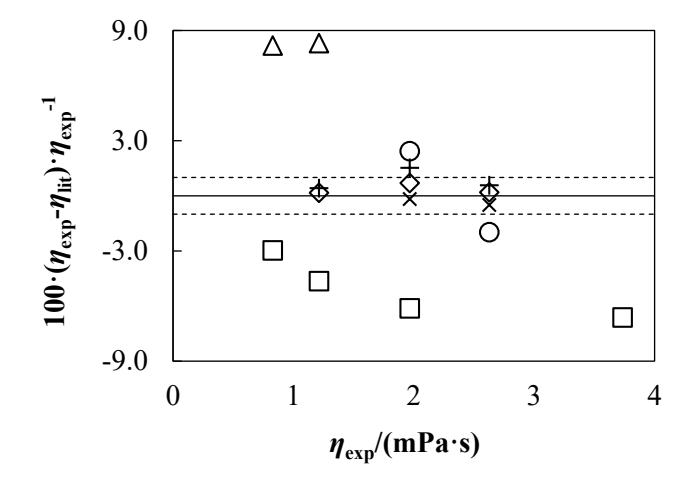


Figure 9.2. Relative deviations (%) of experimental dynamic viscosity measurements η_{exp} , in comparison with literature values η_{lit} . Literature for MDEA + H₂O: (\bigcirc) Mandal et al. [92], (\square) Sobrino et al. [104], (\diamondsuit) Li et al. [89], (\triangle) Rinker et al. [106], (+) Al-Ghawas et al. [105] and (*) Kummamuru et al. [129]. Dashed lines represent the relative expanded uncertainty of our density measurements.

9.2.2. $AMP + H_2O + CO_2$

9.2.2.1. Experimental Viscosity

The results of the viscosity measurements are presented in **Table 9.3** for AMP + $H_2O + CO_2$. To analyse the impact of CO_2 loading and temperature, the experimental dynamic viscosity data were plotted as a function of these variables, as shown in **Figure 9.3**. Density experimental data for the dynamic viscosity calculation of both CO_2 -unloaded solution and CO_2 -loaded solution are reported in Chapter 7 of this work.

Table 9.3. Experimental flow time t, kinematic viscosity v, and dynamic viscosity η , for the system AMP(1) + H₂O(2) + CO₂(3) with amine mass fraction (CO₂-free basis) $w_1 = 0.2997$, at different conditions of temperature T, and CO₂ loading α in terms of mol-CO₂/mol-AMP^a.

α	T/K	t/s	v/(mm ² ·s ⁻¹)	η/(mPa·s)
	292.96	915.85	4.56	4.56
	302.94	617.52	3.08	3.06
0	313.08	440.17	2.19	2.17
U	323.09	332.51	1.66	1.62
	333.11	260.32	1.30	1.26
	353.14	174.47	0.87	0.83
	292.96	166.92	5.10	5.19
	302.94	683.30	3.40	3.44
0.002	313.08	482.65	2.40	2.41
0.092	323.09	359.90	1.79	1.79
	333.11	279.53	1.39	1.38
	353.15	185.67	0.92	0.90
	292.96	184.91	5.65	5.84
	302.94	753.92	3.75	3.85
0.104	313.08	528.76	2.63	2.68
0.184	323.09	390.54	1.94	1.97
	333.10	300.95	1.50	1.51
	353.14	197.64	0.98	0.97
	292.96	228.13	6.97	7.41
	302.94	901.46	4.49	4.73
0.276	313.08	617.66	3.08	3.22
0.376	323.09	450.56	2.24	2.33
	333.11	343.26	1.71	1.76
	353.14	221.47	1.10	1.12
	292.96	245.75	7.51	8.07
	302.94	157.58	4.82	5.14
0.482	313.08	661.21	3.29	3.49
	323.09	480.08	2.39	2.51
	333.11	364.79	1.82	1.90
0.004	292.96	258.25	7.89	8.68
0.804	302.92	171.45	5.24	5.73
	l			

313.08 745.90 3.71 4.04

^aExpanded uncertainty (k = 2): U(T) = 0.02 K; $U_r(w) = 0.0003$; $U_r(\alpha) = 0.004$ and $U_r(\eta) = 0.01$.

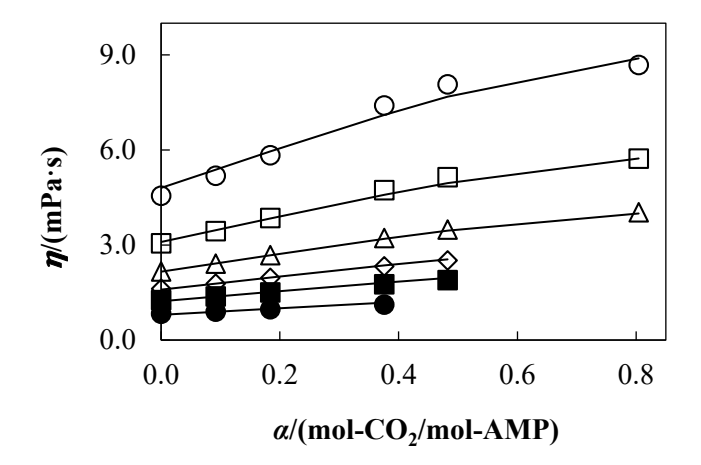


Figure 9.3. Experimental dynamic viscosity η , of the system AMP + H₂O + CO₂ as a function of CO₂ loading α . Isotherms: (\bigcirc) T = 293 K, (\square) T = 303 K, (\triangle) T = 313 K, (\diamondsuit) T = 323 K, (\blacksquare) T = 333 K, and (\bullet) T = 353 K. Solid line: calculated viscosities using VFT modified correlation (**Equation 9.5**).

9.2.2.2. Comparison with Literature

The experimental conditions of the references used for the comparison of AMP + H₂O (CO₂-free solution) are shown in **Table 9.4**. The relative deviations between the experimental dynamic viscosity data and the values reported in the literature are shown in **Figure 9.4**.

Table 9.4. Measurement conditions of literature data used to compare the experimental dynamic viscosity of AMP(1) + $H_2O(2)$ mixture measured in this work at p = 0.1 MPa.

Reference	Viscometer	Conditions	Number of Points	$U_{ m r}^{ m a}$
Mandal et al.	Ostwald Viscometer	$w_1 = 0.30$	4	NA ^b
[92]	Ostward Visconfeter	T = (293.15 - 323.15) K	7	INA
Li et al. [89]	Cannon-Fenske	$w_1 = 0.30$	5	3 %
Li et al. [69]	Routine Viscometer	T = (303.15 - 353.15) K	3	3 70
	Stabinger-type			
Rezaei et al.	kinematic viscometer	$w_1 = 0.30$	4	0.7 %
[93]	(SVM3000, Anton	T = (303.15 - 333.15) K	4	0.7 %
	Paar)			
Samanta et al.	Ostwald Viscometer	$w_1 = 0.30$	2	2 %
[82]	Ostward visconicter	T = (303.15 - 313.15) K	2	2 /0

Kummamuru	Anton-Paar Physica	$w_1 = 0.3$	5	2 %	
et al. [100]	MCR 101 rheometer	T = (303.15 - 353.15) K	3	2 %0	

^aRelative expanded uncertainty (k = 2), %.

^bNA: Not Available.

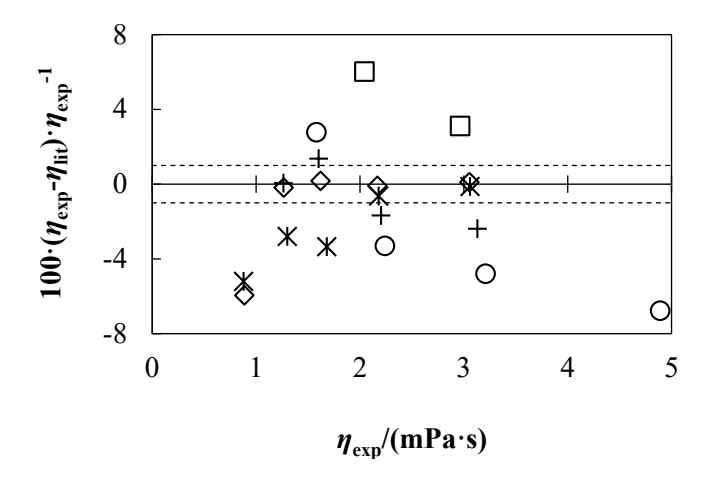


Figure 9.4. Relative deviations (%) of experimental dynamic viscosity measurements $\eta_{\rm exp}$, in comparison with literature values $\eta_{\rm lit}$. Literature for AMP + H₂O: (\bigcirc) Mandal et al. [92], (\diamondsuit) Li et al. [89], (\triangle) Rezaei et al. [93], (\square) Samanta et al. [82], and (*) Kummamuru et al. [100]. Dashed lines represent the relative expanded uncertainty of our density measurements.

9.2.3. Discussion

An increase in temperature leads to a decrease in dynamic viscosity across all studied systems. When temperature rises from (293 to 353) K, the dynamic viscosity of the MDEA + H₂O + CO₂ mixture decreases by up to 78 %, while for AMP + H₂O + CO₂ mixture, the reduction was less than 85 %.

Increasing the CO₂ loading leads to an increase in the dynamic viscosity across all studied mixtures. At T = 313 K, the dynamic viscosity of the MDEA + H₂O + CO₂ mixture rises by 13 % when CO₂ loading change from $\alpha = 0$ to $\alpha = 0.8$. For the AMP + H₂O + CO₂ mixture at the same temperature, the dynamic viscosity increases significantly by 86 % under the same change in CO₂ loading. As shown in **Figure 9.5**, AMP solutions are highly sensitive to change the dynamic viscosity when the CO₂ loading increases compared to other CO₂-loaded aqueous amine solutions reported in the literature by Zhang et al. [112] and in this work under the same conditions of temperature and amine mass fraction on a CO₂-free basis.

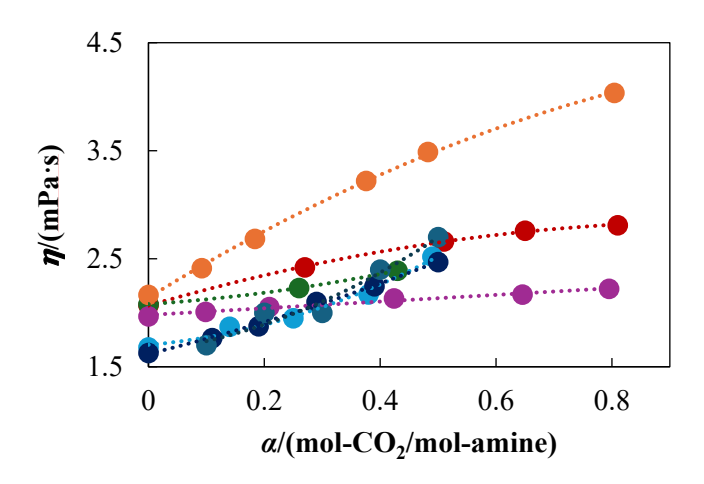


Figure 9.5. Experimental dynamic viscosity η , at amine mass fraction (CO₂-free basis) w = 0.3 and temperature T = 313 K. Mixtures: () AMP + H₂O + CO₂, () MDEA + H₂O + CO₂, () DEAE + H₂O + CO₂ [112], () DMAE + H₂O + CO₂ [112], () MEA + H₂O + CO₂ [112], () MEA + H₂O + CO₂ [110], and () MEA + H₂O + CO₂ [108]. Dashed lines are the quadratic fittings for each system.

A comparison of our dynamic viscosity data with experimental literature values was achievable for the binary systems MDEA + H_2O and $AMP + H_2O$, as can be observed in **Tables 9.2 and 9.4**. As illustrated in **Figures 9.2 and 9.4**, a certain degree of data dispersion can be observed, which is a consequence of the inherent challenges associated with viscosity measurements. Furthermore, the literature data often lacks information regarding the uncertainty associated with the reported dynamic viscosity values, further complicating the assessment of the accuracy of the experimental data. For the MDEA + H_2O mixture, 16 data points exhibit an average absolute relative deviation of 3 % with a maximum of 8 %. For the AMP + H_2O mixture, 20 data points showed an average absolute relative deviation of 3 % with a maximum of 6 %.

9.3. Quaternary Mixtures

9.3.1. MDEA + PZ +
$$H_2O$$
 + CO_2 (w_{amines} = 0.4000 CO_2 -free basis)

9.3.1.1. Experimental Density

Experimental density data, necessary for the dynamic viscosity calculation for MDEA + PZ + H₂O + CO_2 with MDEA mass fraction (CO_2 -free basis) $w_1 = 0.3500$ and PZ mass fraction (CO_2 -free basis) $w_2 = 0.0500$ are presented in **Table 9.5**. **Figure 9.6** illustrates the trends of density as a function of CO_2 loading at different temperatures.

Table 9.5. Experimental density ρ , for the system MDEA(1) + PZ(2) + H₂O(3) + CO₂(4) with MDEA mass fraction (CO₂-free basis) $w_1 = 0.3500$ and PZ mass fraction (CO₂-free basis) $w_2 = 0.0500$, at different conditions of temperature T, and CO₂ loading α in terms of mol-CO₂/mol-amines.

	$ ho/(\mathrm{kg}\cdot\mathrm{m}^{-3})$					
			T/K			
293.15	303.15	313.15	323.15	333.15	353.15	
		0	$\alpha = 0$			
1035.7	1030.1	1024.2	1017.7	1011.3	994.1	
		$\alpha =$	0.156			
1056.3	1050.8	1045.1	1038.7	1032.6	1018.5	
		$\alpha =$	0.189			
1062.3	1056.6	1050.2	1044.5	1037	1023.7	
		$\alpha =$	0.386			
1088.4	1082.9	1077	1070.9	1064		
		α =	0.682			
1124.9	1119.2	1113.4				

^aExpanded uncertainty (k = 2): U(T) = 0.02 K; $U_r(w) = 0.0003$; $U_r(\alpha) = 0.4$ % and $U_r(\rho) = 0.06$ %.

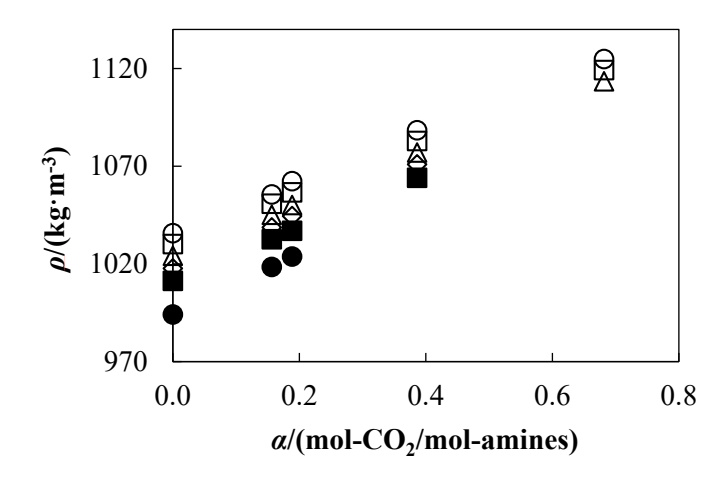


Figure 9.6. Experimental density ρ , of the system MDEA(1) + PZ(2) + H₂O(3) + CO₂(4) as a function of CO₂ loading α . Isotherms: (\bigcirc) T = 293.15 K, (\square) T = 303.15 K, (\triangle) T = 313.15 K, (\diamondsuit) T = 323.15 K, (\blacksquare) T = 333.15 K, and (\blacksquare) T = 353.15 K.

9.3.1.2. Experimental Viscosity

In **Table 9.6**, the experimental dynamic viscosity for MDEA + PZ + H_2O + CO_2 (w_{amines} = 0.4000 CO_2 -free basis) is presented. To analyse the impact of CO_2 loading and temperature, the experimental dynamic viscosity data were plotted as a function of these variables, as shown in **Figure 9.7**.

Table 9.6. Experimental flow time t, kinematic viscosity v, and dynamic viscosity η , using the Ubbelohde capillary viscometer for the system MDEA(1) + PZ(2) + H₂O(3) + CO₂(4) with MDEA mass fraction (CO₂-free basis) $w_1 = 0.3500$ and PZ mass fraction (CO₂-free basis) $w_2 = 0.0500$, at different conditions of temperature T, and CO₂ loading α in terms of mol-CO₂/mol-amines^a.

α	T/K	t/s	$v/(\mathbf{mm}^2 \cdot \mathbf{s}^{-1})$	η/(mPa·s)
	292.96	226.40	6.92	7.17
	302.94	151.85	4.64	4.78
0	313.08	658.63	3.28	3.36
U	323.09	488.37	2.43	2.48
	333.11	374.69	1.87	1.89
	353.14	241.32	1.20	1.19
	292.96	230.41	7.04	7.43
	302.93	157.15	4.80	5.05
0.156	313.08	692.69	3.45	3.61
0.156	323.09	519.13	2.59	2.69
	333.11	400.31	1.99	2.06
	353.14	260.57	1.30	1.32
	292.96	232.11	7.09	7.54
	302.94	158.78	4.85	5.13
0.100	313.08	702.59	3.50	3.67
0.189	323.09	525.87	2.62	2.74
	333.11	407.89	2.03	2.11
	353.15	265.14	1.32	1.35
	292.97	239.28	7.31	7.96
	302.94	165.88	5.07	5.49
0.386	313.08	739.95	3.68	3.97
	323.09	558.61	2.78	2.98
	333.11	438.30	2.18	2.32
	292.96	245.63	7.51	8.44
0.682	302.94	173.47	5.30	5.93
	313.08	784.06	3.90	4.35

^aExpanded uncertainty (k = 2): U(T) = 0.02 K; $U_r(w) = 0.0003$; $U_r(\alpha) = 0.004$ and $U_r(\eta) = 0.01$.

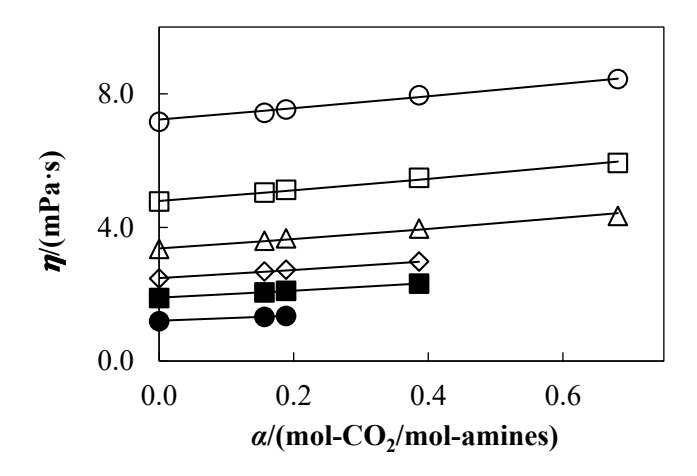


Figure 9.7. Experimental dynamic viscosity η , of the system MDEA + PZ + H₂O + CO₂ with total amine mass fraction (CO₂-free basis) w = 0.4000, as a function of CO₂ loading α . Isotherms: (\bigcirc) T = 293 K, (\bigcirc) T = 303 K, (\triangle) T = 313 K, (\bigcirc) T = 323 K, (\blacksquare) T = 333 K, and (\bullet) T = 353 K. Solid line: calculated viscosities using VFT modified correlation (**Equation 9.6**).

$$9.3.2.MDEA + AMP + H2O + CO2$$

9.3.2.1. Experimental Density

Density experimental data necessary for the dynamic viscosity calculation for MDEA + AMP + H_2O + CO_2 with MDEA mass fraction (CO_2 -free basis) $w_1 = 0.3500$ and AMP mass fraction (CO_2 -free basis) $w_2 = 0.0500$ are presented in **Table 9.7**. **Figure 9.8** illustrates the trends of density as a function of CO_2 loading at different temperatures.

Table 9.7. Experimental density ρ , for the system MDEA(1) + AMP(2) + H₂O(3) + CO₂(4) with MDEA mass fraction (CO₂-free basis) $w_1 = 0.3500$ and AMP mass fraction (CO₂-free basis) $w_2 = 0.0500$, at different conditions of temperature T, and CO₂ loading α in terms of mol-CO₂/mol-amines.

$ ho/(\mathrm{kg}\cdot\mathrm{m}^{-3})$							
	T/K						
293.15	303.15	313.15	323.15	333.15	353.15		
$\alpha = 0$							
1031.8	1026.3	1020.3	1013.3	1007	989.3		
		$\alpha = 0$.100				
1047.1	1041.5	1035.2	1025.6	1021.9	1007.4		
$\alpha = 0.200$							
1061.5	1055.5	1049.1	1042.5	1035.8	1019.3		
		$\alpha = 0$.400				

1087.2 1081.4 1075 1068.2 1057.8
$$\alpha = 0.707$$
 1124.2 1118.5 1112.2

^aExpanded uncertainty (k = 2): U(T) = 0.02 K; $U_r(w) = 0.0003$; $U_r(\alpha) = 0.4$ % and $U_r(\rho) = 0.06$ %.

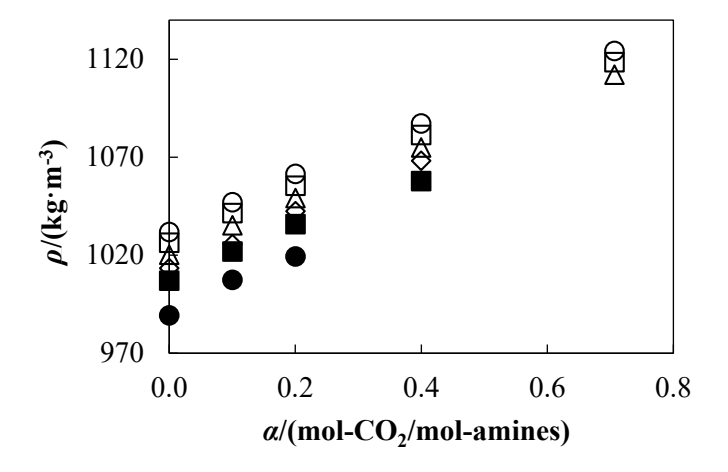


Figure 9.8. Experimental density ρ , of the system MDEA(1) + AMP(2) + H₂O(3) + CO₂(4) as a function of CO₂ loading α . Isotherms: (\bigcirc) T = 293.15 K, (\square) T = 303.15 K, (\triangle) T = 313.15 K, (\diamondsuit) T = 323.15 K, (\blacksquare) T = 333.15 K, and (\blacksquare) T = 353.15 K.

9.3.2.2. Experimental Viscosity

In **Table 9.8**, the experimental dynamic viscosity for MDEA + AMP + H_2O + CO_2 ($w_{amines} = 0.4000$ CO_2 -free basis) is presented. To analyse the impact of CO_2 loading and temperature, the experimental dynamic viscosity data were plotted as a function of these variables, as shown in **Figure 9.9**.

Table 9.8. Experimental flow time t, kinematic viscosity v, and dynamic viscosity η , for the system MDEA(1) + AMP(2) + H₂O(3) + CO₂(4) with MDEA mass fraction (CO₂-free basis) w_1 = 0.3500 and AMP mass fraction (CO₂-free basis) w_2 = 0.0500, at different conditions of temperature T, and CO₂ loading α in terms of mol-CO₂/mol-amines^a.

α	<i>T</i> /K	t/s	$v/(\text{mm}^2 \cdot \text{s}^{-1})$	$\eta/(mPa\cdot s)$
	292.96	214.20	6.55	6.75
	302.93	883.60	4.40	4.52
0	313.08	626.76	3.12	3.18
U	323.08	469.36	2.34	2.37
	333.11	358.28	1.78	1.80
	353.14	231.89	1.15	1.14
0.100	292.96	229.20	7.00	7.33

	302.93	154.21	4.71	4.91
	313.07	675.29	3.36	3.48
	323.09	502.96	2.50	2.57
	333.11	384.90	1.92	1.96
	353.14	249.10	1.24	1.25
	292.96	236.30	7.22	7.67
	302.94	159.50	4.87	5.14
0.200	313.08	694.26	3.46	3.63
0.200	323.09	519.34	2.59	2.70
	333.11	397.43	1.98	2.05
	353.14	257.88	1.28	1.31
-	292.96	244.71	7.48	8.13
	302.93	167.65	5.12	5.54
0.400	313.07	741.99	3.70	3.97
	323.08	554.08	2.76	2.95
	333.11	427.42	2.13	2.25
	292.96	252.15	7.71	8.66
0.707	302.93	176.28	5.39	6.03
	313.08	786.23	3.92	4.35
	2) II// 0 00 II	TT () 0.0000	TT() 0.004	1.77/)

^aExpanded uncertainty (k = 2): U(T) = 0.02 K; $U_r(w) = 0.0003$; $U_r(\alpha) = 0.004$ and $U_r(\eta) = 0.01$.

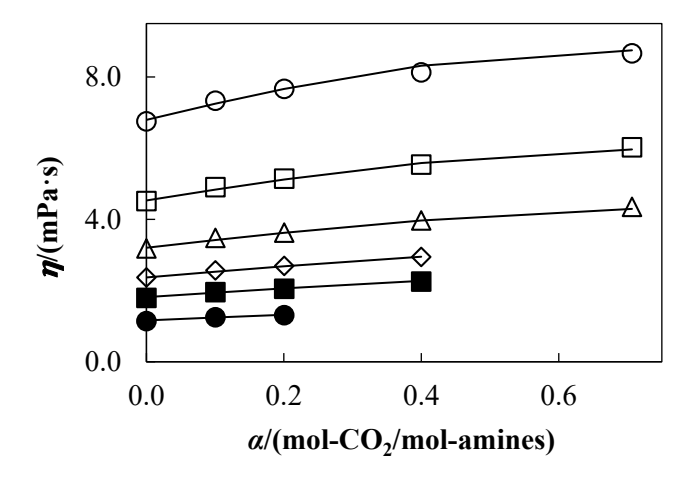


Figure 9.9. Experimental dynamic viscosity η , of the system MDEA + AMP + H₂O + CO₂ with total amine mass fraction (CO₂-free basis) w = 0.4000, as a function of CO₂ loading α . Isotherms: (\bigcirc) T = 293 K, (\bigcirc) T = 303 K, (\triangle) T = 313 K, (\bigcirc) T = 323 K, (\blacksquare) T = 333 K, and (\bullet) T = 353 K. Solid line: calculated viscosities using VFT modified correlation (**Equation 9.7**).

9.3.3.MDEA + PZ + $H_2O + CO_2$ ($w_{amines} = 0.3021 CO_2$ -free basis)

9.3.3.1. Experimental Density

Density experimental data necessary for the dynamic viscosity calculation for MDEA + PZ + H₂O + CO₂ with MDEA mass fraction (CO₂-free basis) $w_1 = 0.2024$ and PZ mass fraction (CO₂-free basis) $w_2 = 0.0997$ are presented in **Table 9.9**. **Figure 9.10** illustrates the trends of density as a function of CO₂ loading at different temperatures.

Table 9.9. Experimental density ρ , kinematic viscosity v, and dynamic viscosity η , for the system MDEA(1) + PZ(2) + H₂O(3) + CO₂(4) with MDEA mass fraction (CO₂-free basis) w_1 = 0.2024 and PZ mass fraction (CO₂-free basis) w_2 = 0.0997, at different conditions of temperature T, and CO₂ loading α in terms of mol-CO₂/mol-amines.

	$ ho/(\mathrm{kg}\cdot\mathrm{m}^{-3})$					
		T	/K			
293.15	303.15	313.15	323.15	333.15	353.15	
	$\alpha = 0$					
1024.5	1020.1	1014.7	1009.3	1003.4	986.6	
		$\alpha = 0$	0.300			
1058	1053.5	1048.5	1042.8	1037.1	1024.3	
		$\alpha = 0$	0.504			
1079.4	1074.8	1069.8	1064.2	1056.6		
	lpha = 0.774					
1107.4	1102.7	1097.7				

^aExpanded uncertainty (k = 2): U(T) = 0.02 K; $U_r(w) = 0.0003$; $U_r(\alpha) = 0.4$ % and $U_r(\rho) = 0.06$ %.

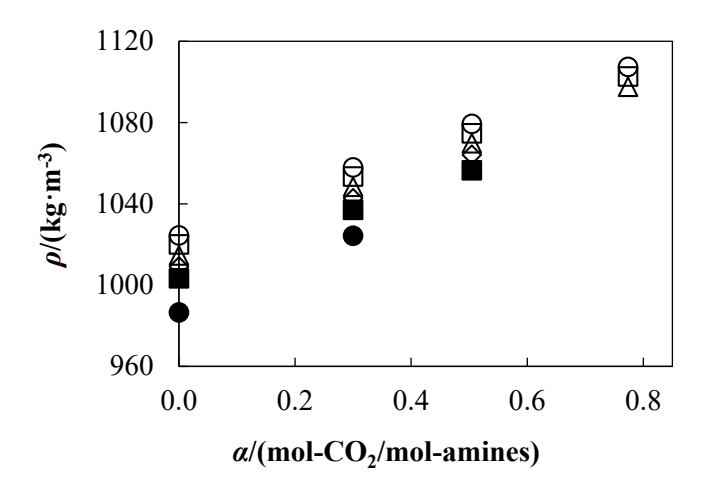


Figure 9.10. Experimental density ρ , of the system MDEA(1) + PZ(2) + H₂O(3) + CO₂(4) with total amine mass fraction (CO₂-free basis) w = 0.3021, as a function of CO₂ loading α . Isotherms: (\bigcirc) T = 293.15 K, (\square) T = 303.15 K, (\triangle) T = 313.15 K, (\diamondsuit) T = 323.15 K, (\blacksquare) T = 333.15 K, and (\bullet) T = 353.15 K.

9.3.3.2. Experimental Viscosity

In **Table 9.10**, the experimental dynamic viscosity for MDEA + PZ + $H_2O + CO_2$ ($w_{amines} = 0.3021 CO_2$ -free basis) is presented. To analyse the impact of CO_2 loading and temperature, the experimental dynamic viscosity data were plotted as a function of these variables, as shown in **Figure 9.11**.

Table 9.10. Experimental flow time t, kinematic viscosity v, and dynamic viscosity η , for the system MDEA(1) + PZ(2) + H₂O(3) + CO₂(4) with MDEA mass fraction (CO₂-free basis) w_1 = 0.2024 and PZ mass fraction (CO₂-free basis) w_2 = 0.0997, at different conditions of temperature T, and CO₂ loading α in terms of mol-CO₂/mol-amines.

a	T/K	t/s	v/(mm ² ·s ⁻¹)	η/(mPa·s)
	292.96	875.27	4.36	4.47
	302.94	614.73	3.06	3.12
0	313.08	450.77	2.24	2.28
U	323.09	343.63	1.71	1.73
	333.11	271.73	1.35	1.36
	353.14	183.35	0.91	0.90
	292.84	878.52	4.38	4.63
	302.93	629.16	3.13	3.30
0.300	313.07	469.99	2.34	2.45
	323.09	365.23	1.82	1.90
	333.10	292.75	1.46	1.51

	353.14	201.74	1.00	1.03
	292.96	883.36	4.40	4.75
	302.93	642.88	3.20	3.44
0.504	313.08	484.75	2.41	2.58
	323.09	379.88	1.89	2.01
	333.11	306.14	1.52	1.61
	292.96	888.31	4.42	4.90
0.774	302.93	652.54	3.25	3.58
	313.07	497.41	2.48	2.72

^aExpanded uncertainty (k = 2): U(T) = 0.02 K; $U_r(w) = 0.0003$; $U_r(\alpha) = 0.004$ and $U_r(\eta) = 0.01$.

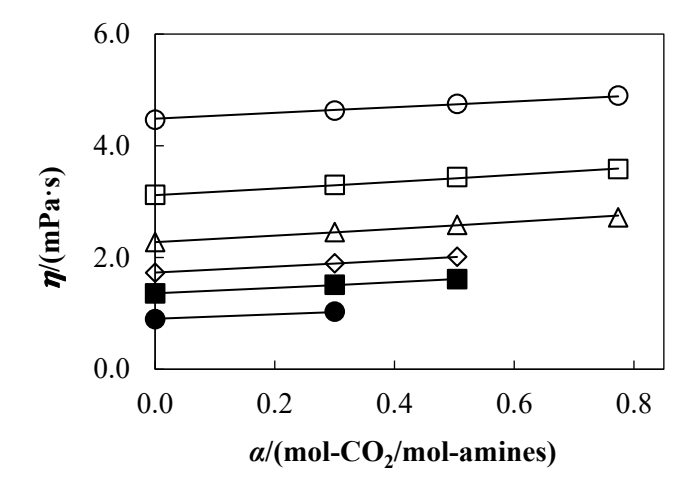


Figure 9.11. Experimental dynamic viscosity η , of the system MDEA + PZ + H₂O + CO₂ with total amine mass fraction (CO₂-free basis) w = 0.3021, as a function of CO₂ loading α . Isotherms: (\bigcirc) T = 293 K, (\bigcirc) T = 303 K, (\triangle) T = 313 K, (\bigcirc) T = 323 K, (\blacksquare) T = 333 K, and (\bullet) T = 353 K. Solid line: calculated viscosities using VFT modified correlation (**Equation 9.6**).

9.3.3.3. Experimental Viscosity Comparison with Literature

The relative deviations between the experimental dynamic viscosity data and the values reported in the only study found in the literature for the MDEA + PZ + H_2O with total amine mass fraction w = 0.3021 system at the specific amine mass fraction are illustrated in **Figure 9.12.**

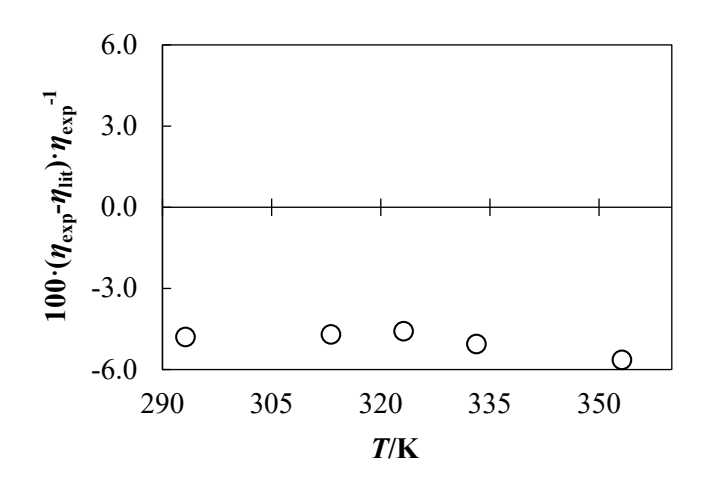


Figure 9.12. Relative deviations (%) of the experimental dynamic viscosity, of the system MDEA + PZ + H₂O with total amine mass fraction w = 0.3021, measured using the capillary viscometer η_{CV} , in comparison with the data reported by Kummamuru et al. [129].

9.3.4. Discussion

Regarding density, an increase in temperature from (293.15 to 353.15) K results in a 4 % decrease in density for all the studied quaternary systems. Conversely, when CO_2 loading increase from $\alpha = 0$ to $\alpha = 0.7$, the density increases by 9 % for both MDEA + PZ + H₂O + CO₂ ($w_{amines} = 0.4$) and MDEA + AMP + H₂O + CO₂ mixtures and by 8 % for MDEA + PZ + H₂O + CO₂ ($w_{amines} = 0.3$) system when CO_2 loading increase from $\alpha = 0$ to $\alpha = 0.8$. As shown in **Figure 9.13**, the densities of the MDEA + PZ + H₂O + CO₂ and MDEA + AMP + H₂O + CO₂ mixtures were higher than the densities reported by Patzschke et al. [202] for DEAE + PZ + H₂O + CO₂ and DMAE + PZ + H₂O + CO₂, at equivalent amine mass fraction and temperature. In addition, **Figure 9.13** shows a minimal difference (less than 1 %) between the densities of MDEA + PZ + H₂O + CO₂ and MDEA + AMP + H₂O + CO₂ mixtures.

At 313 K, when the CO₂ loading increase from $\alpha = 0$ to $\alpha = 0.7$ the dynamic viscosity increases by 29 % and 37 % in MDEA + PZ + H₂O + CO₂ ($w_{amines} = 0.4000$) and MDEA + AMP + H₂O + CO₂ systems, respectively. As observed in **Figure 9.14**, the contribution of CO₂ loading in the dynamic viscosity is lower in these systems compared to similar systems reported in the literature by Patzschke et al. [202] under the same temperature and amine mass fraction on a CO₂-free basis. For example, the viscosity of the DEAE + PZ + H₂O + CO₂ ($w_{amines} = 0.4$) mixture increases by 78 % when the CO₂ loading change from $\alpha = 0$ to $\alpha = 0.8$, as reported by Patzschke et al. [202]. Systems containing MDEA exhibit lower viscosity than those shown in **Figure 9.14**, which is advantageous for optimising CO₂ capture process unit sizing, enhancing mass transfer rates, and improving the operation of pumps, heat exchangers, and gas-liquid contactors. Additionally, **Figure 9.14** shows that the viscosity for the MDEA + PZ + H₂O + CO₂ ($w_{amines} = 0.4000$) and MDEA + AMP + H₂O + CO₂ systems differ by less than 6 %. A 19 % of

increment was observed in the dynamic viscosity of MDEA + PZ + H_2O + CO_2 ($w_{amines} = 0.3021$) when CO_2 loading increased from $\alpha = 0$ to $\alpha = 0.8$ at temperature of 313 K.

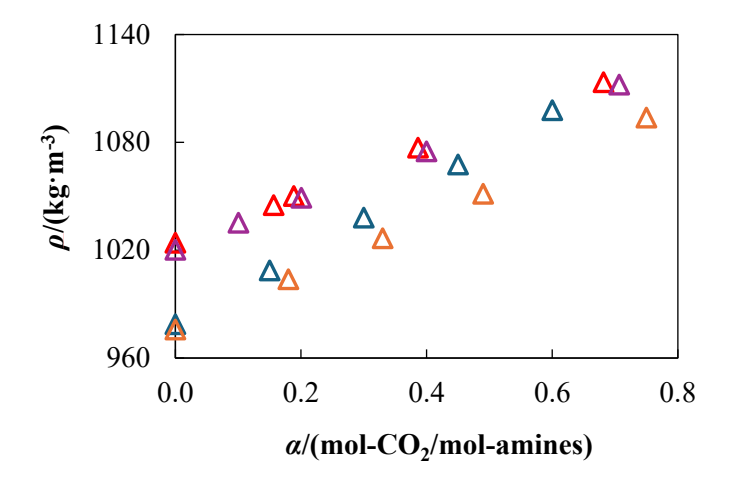


Figure 9.13. Experimental density ρ , at total amine mass fraction (CO₂-free basis) w = 0.4 and temperature T = 313 K. Mixtures: (\triangle) DEAE + PZ + H₂O + CO₂ [202], (\triangle) DMEA + PZ + H₂O + CO₂ [202], (\triangle) MDEA + PZ + H₂O + CO₂, and (\triangle) MDEA + AMP + H₂O + CO₂.

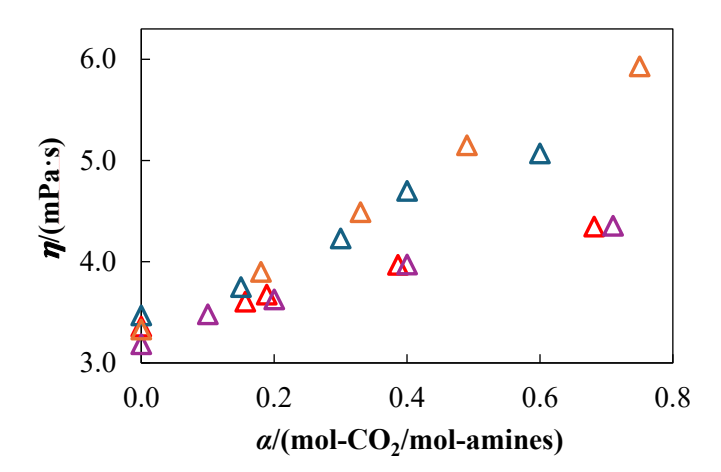


Figure 9.14. Experimental dynamic viscosity η , at total amine mass fraction (CO₂-free basis) w = 0.4 and temperature T = 313 K. Mixtures: (\triangle) DEAE + PZ + H₂O + CO₂ [202], (\triangle) DMEA + PZ + H₂O + CO₂ [202], (\triangle) MDEA + PZ + H₂O + CO₂, and (\triangle) MDEA + AMP + H₂O + CO₂.

A single literature reference [129] reports experimental dynamic viscosity data for the MDEA + PZ + $H_2O + CO_2$ system at a MDEA mass fraction (CO_2 -free basis) of $w_{MDEA} = 0.20$ and PZ mass fraction (CO_2 -free basis) $w_{PZ} = 0.10$. These measurements were conducted at a pressure of 0.4 MPa, which differs slightly from our experimental pressure of 0.1 MPa. While this pressure difference slightly affects the viscosity, the high combined uncertainty of 0.30 mPa at a 95.5 % confidence level reported by Kummamuru et al. [129] covers all five data points, as can be seen in **Figure 9.12**. To the best of our knowledge, no experimental dynamic viscosity data is available in the literature for the remaining

quaternary systems under the specific composition and temperature conditions investigated in this study.

9.4. Experimental Density Data Fitting

The experimental density of the CO₂-loaded solutions (quaternary mixtures) was studied in relation to temperature and CO₂ loading. A simplified version of the model proposed by Zhang et al. [112] and Patzschke et al. [202], which omits the amine mass fraction component, was employed. The density of the loaded mixtures (ρ_L) was found to be linearly proportional to the product of CO₂ loading (see **Equation 9.2**). This correlation method, originally developed by Liu et al. [203], was previously adapted by Zhang et al. [112] and Patzschke et al. [202], those who modified the denominator to include the density of water (ρ_w). This adjustment minimises the influence of temperature on the density of the CO₂-unloaded solution (ρ_0) (see **Equation 9.1**), as detailed in Zhang et al. [112] and Patzschke et al. [202]. The goodness-of-fit was assessed by calculating the statistical parameters AAD and MAD (see Equations 7.5 and 7.6 in Chapter 7).

$$\frac{\rho_0(T)}{\rho_w(T)} = a_1 + a_2 \cdot (T/T_0) \tag{9.1}$$

$$\rho_L(T,\alpha) = \rho_0 \cdot (1 + c \cdot \alpha) \tag{9.2}$$

where ρ_0 is the density of the CO₂-unloaded solution; ρ_w is the density of the water; a_1 and a_2 are two fitting's parameters; T is the experimental temperature; T_0 is the reference temperature (283.15 K); ρ_L is the density of the CO₂-loaded solution; α is the CO₂ loading, and c is a fitting's parameter.

All the fitted coefficients are shown in **Tables 9.11 and 9.12**, along with the statistical parameters AAD and MAD. As can be seen in **Table 9.12** and **Figure 9.15**, despite the fitting residuals being larger than the experimental density uncertainty, they show good agreement with the findings of Zhang et al. [112] and Patzschke et al. [202].

Table 9.11. Fitted coefficients a_1 , a_2 and c in Equations 9.1 and 9.2.

Parameters	$MDEA + PZ + H_2O +$	$MDEA + AMP + H_2O +$	$MDEA + PZ + H_2O +$
	CO_2 ($w_{amines} = 0.4000$)	$CO_2 (w_{\text{amines}} = 0.4000)$	CO_2 ($w_{amines} = 0.3021$)
a_1	1.1062	1.1079	1.0778
a_2	-0.06665	-0.0719	-0.0495
С	0.1304	0.1309	0.1067

Table 9.12. Statistical parameters AAD and MAD in density fitting.

System	CO ₂ -free solutions		CO ₂ -loaded solutions	
System	AAD	MAD	AAD	MAD
MDEA + PZ + H2O + CO2 $(wamines = 0.4000)$	0.04 %	0.06 %	0.1 %	0.5 %
$MDEA + AMP + H_2O + CO_2$ $(w_{amines} = 0.4000)$	0.03 %	0.08 %	0.1 %	0.5 %
MDEA + PZ + H2O + CO2 $(wamines = 0.3021)$	0.05 %	0.09 %	0.09 %	0.5 %

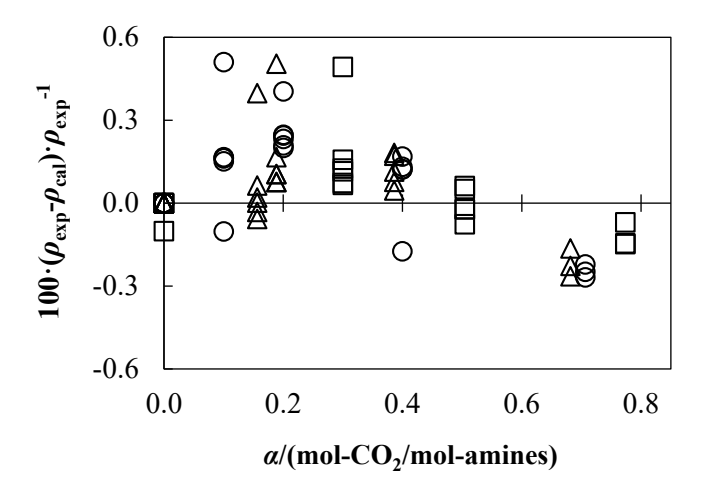


Figure 9.15. Relative deviations (%) between experimental density ρ_{exp} , and calculated density ρ_{cal} , using **Equations 9.1 and 9.2** vs CO₂ loading α . Mixtures: (\triangle) MDEA + PZ + H₂O + CO₂ (w_{amines} = 0.4000 CO₂-free basis), (\bigcirc) MDEA + AMP + H₂O + CO₂, and (\square) MDEA + PZ + H₂O + CO₂ (w_{amines} = 0.3021 CO₂-free basis).

9.5. Experimental Viscosity Data Fitting

The experimental viscosity data was correlated with temperature and CO₂ loading using models based on the Vogel-Fulcher-Tammann (VFT) model (see **Equation 9.3**). To optimise the models and reduce the number of parameters, symbolic regression (using TuringBot software [192]) was employed to identify the most effective mathematical form within the general structure of **Equation 9.3**. This same method was followed successfully by Zhang et al. [112] and Patzschke et al. [202] in their studies. The goodness-of-fit was assessed by calculating the statistical parameters AAD and MAD (see Equations 7.5 and 7.6 in Chapter 7).

$$ln\left[\frac{\eta(T,\alpha)}{\eta_w(T)}\right] = A(\alpha) + \frac{B(\alpha)}{T+C}$$
(9.3)

The resultant equations are: **Equation 9.4** for MDEA + $H_2O + CO_2$, **Equation 9.5** for AMP + $H_2O + CO_2$, **Equation 9.6** for MDEA + $PZ + H_2O + CO_2$, and **Equation 9.7** for MDEA + AMP + $H_2O + CO_2$.

$$\ln\left[\frac{\eta(T,\alpha)}{\eta_w(T)}\right] = a_1 \cdot \alpha + \frac{b_1 \cdot \alpha + b_2}{(T/T_0) - C} \tag{9.4}$$

$$\ln\left[\frac{\eta(T,\alpha)}{\eta_w(T)}\right] = a_1 \cdot \alpha + a_2 \cdot \alpha^2 \frac{b_1}{(T/T_0) - C} \tag{9.5}$$

$$\ln\left[\frac{\eta(T,\alpha)}{\eta_w(T)}\right] = a_1 \cdot \alpha + \frac{b_1 \cdot \alpha + b_2}{(T/T_0) - C} \tag{9.6}$$

$$\ln\left[\frac{\eta(T,\alpha)}{\eta_w(T)}\right] = a_1 \cdot \alpha + \frac{b_1 \cdot \alpha^2 + b_2}{(T/T_0) - C} \tag{9.7}$$

where η is the viscosity of the CO₂-loaded solution; η_w is the viscosity of the water; α is the CO₂ loading; T is the experimental temperature; T_0 is the reference temperature (283.15 K); and a_1 , a_2 , b_1 , b_2 and C are fitting's parameters.

All the fitted coefficients are shown in **Table 9.13**, along with the statistical parameters AAD and MAD. The average absolute deviation (AAD) for viscosity predictions was generally within the experimental uncertainty, apart from the AMP solution, as detailed in **Table 9.13**. However, the quaternary mixtures with higher total amine mass fractions exhibited deviations up to 2 % (see **Figures 9.18 and 9.19**). Despite extensive efforts with various models and modified Vogel-Fulcher-Tammann (VFT) equation structures, this represents the best fit achieved. While not ideal, these results demonstrate lower deviations compared to those reported in the literature, including studies by researchers like Zhang et al. [112] and Patzschke et al. [202], who employed modified VFT models and observed even larger deviations.

Table 9.13. Fitted coefficients in Equations 9.4 to 9.7 for each studied system.

Parameters	MDEA + H ₂ O	$AMP + H_2O +$	MDEA + PZ	MDEA +	MDEA + PZ
	+ CO ₂ (Eq.	CO ₂ (Eq. 9.5)	$+ H_2O + CO_2$	$AMP + H_2O +$	$+ H_2O + CO_2$
	9.4)		(w _{amines} =	CO ₂ (Eq. 9.7)	(w _{amines} =
			0.4000 CO ₂ -		0.3021 CO ₂ -
			free basis)		free basis)
			(Eq. 9.6)		(Eq. 9.6)
a_1	0.7257	1.149	1.232	0.6971	0.9187

a_2		-0.1220		•	
b_1	-0.2628	0.3529	-0.3475	-0.1667	-0.2861
b_2	0.5067	•	0.6851	0.6640	0.5307
C	0.6505	0.8134	0.6887	0.6885	0.6806
AAD	0.4 %	2.0 %	0.6 %	0.8 %	0.4 %
MAD	0.9 %	5 %	2 %	2 %	1 %

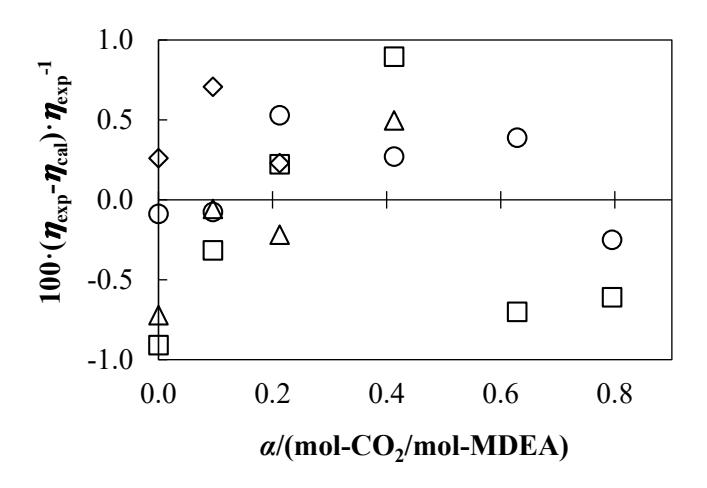


Figure 9.16. Relative deviations (%) between experimental dynamic viscosity $\eta_{\rm exp}$ and calculated dynamic viscosity $\eta_{\rm cal}$ using **Equation 9.4** vs CO₂ loading α . Isotherms: (\bigcirc) T = 293 K, (\square) T = 313 K, (\triangle) T = 333 K, and (\diamondsuit) T = 353 K. Mixture: MDEA + H₂O + CO₂.

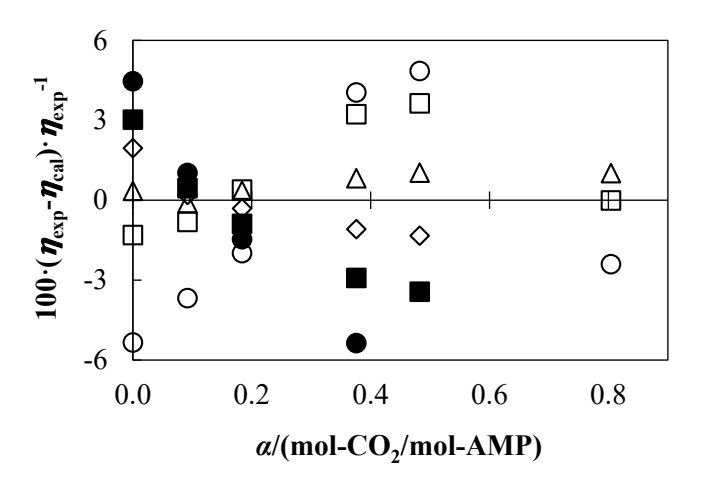


Figure 9.17. Relative deviations (%) between experimental dynamic viscosity $\eta_{\rm exp}$ and calculated dynamic viscosity $\eta_{\rm cal}$ using **Equation 9.5** vs CO₂ loading α . Isotherms: (\bigcirc) T = 293 K, (\bigcirc) T = 303 K, (\triangle) T = 313 K, (\diamondsuit) T = 323 K, (\blacksquare) T = 333 K, and (\bullet) T = 353 K. Mixture: AMP + H₂O + CO₂.

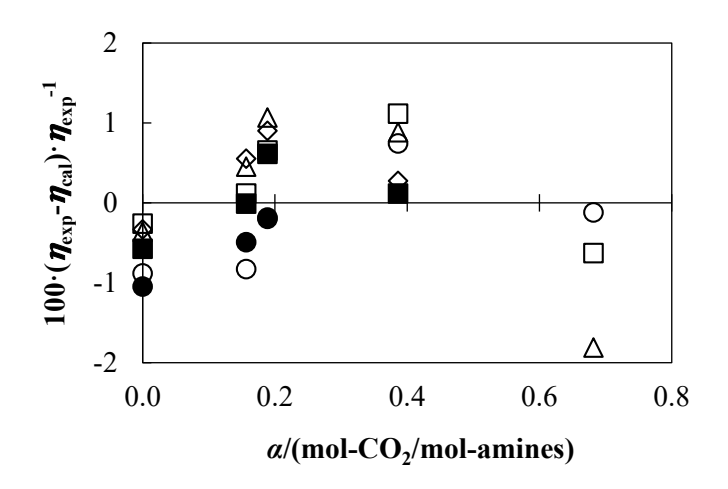


Figure 9.18. Relative deviations (%) between experimental dynamic viscosity $\eta_{\rm exp}$ and calculated dynamic viscosity $\eta_{\rm cal}$ using **Equation 9.6** vs CO₂ loading α . Isotherms: (\bigcirc) T = 293 K, (\square) T = 303 K, (\triangle) T = 313 K, (\diamondsuit) T = 323 K, (\blacksquare) T = 333 K, and (\bullet) T = 353 K. Mixture: MDEA + PZ + H₂O + CO₂ ($w_{\rm amines} = 0.4000$ CO₂-free basis).

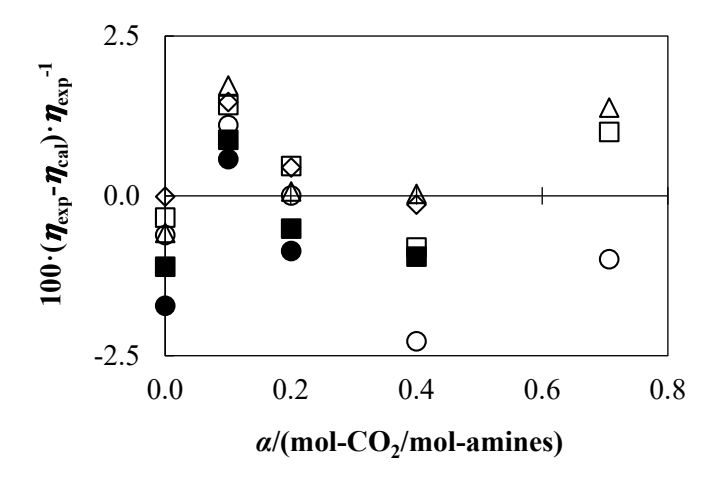


Figure 9.19. Relative deviations (%) between experimental dynamic viscosity $\eta_{\rm exp}$ and calculated dynamic viscosity $\eta_{\rm cal}$ using **Equation 9.7** vs CO₂ loading α . Isotherms: (\bigcirc) T = 293 K, (\square) T = 303 K, (\triangle) T = 313 K, (\diamondsuit) T = 323 K, (\blacksquare) T = 333 K, and (\bullet) T = 353 K. Mixture: MDEA + AMP + H₂O + CO₂.

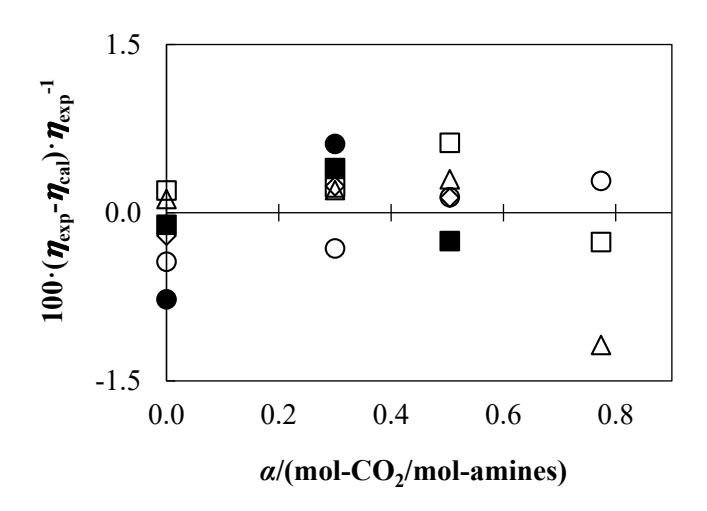


Figure 9.20. Relative deviations (%) between experimental dynamic viscosity $\eta_{\rm exp}$ and calculated dynamic viscosity $\eta_{\rm cal}$ using **Equation 9.6** vs CO₂ loading α . Isotherms: (\bigcirc) T = 293 K, (\square) T = 303 K, (\triangle) T = 313 K, (\diamondsuit) T = 323 K, (\blacksquare) T = 333 K, and (\bullet) T = 353 K. Mixture: MDEA + PZ + H₂O + CO₂ ($w_{\rm amines} = 0.3021$ CO₂-free basis).

9.5.1. Comparison of Calculated Dynamic Viscosity with Experimental Literature Data

Dynamic viscosity calculations, based on **Equation 9.6**, were carried out for the MDEA + PZ + H₂O + CO_2 with MDEA mass fraction (CO_2 -free basis) $w_1 = 0.2024$ and PZ mass fraction (CO_2 -free basis) $w_2 = 0.0997$. These calculations were compared to the only literature reference providing data for this specific amine composition: Kummamuru et al. [129]. As illustrated in **Figure 9.21** and **Table 9.14**, 31 comparison points across CO_2 loadings of 0, 0.6, and 0.68 were evaluated. All calculated values were found to be within the expanded uncertainty of 0.30 mPa·s reported by Kummamuru et al.

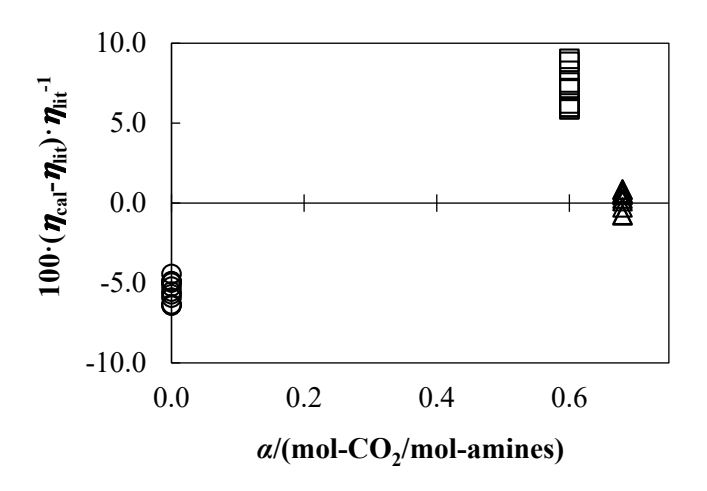


Figure 9.21. Relative deviations (%) vs CO₂ loading α of calculated dynamic viscosity η_{cal} using **Equation 9.6** for MDEA + PZ + H₂O + CO₂ ($w_{amines} = 0.3021$ CO₂-free basis), in comparison with the dynamic viscosity experimental literature values η_{lit} . Literature: Kummamuru et al. [129]. CO₂ loading:

CHAPTER 9: EXPERIMENTAL DENSITY AND VISCOSITY

(\bigcirc) α = 0 mol-CO₂/mol-amines, (\square) α = 0.6 mol-CO₂/mol-amines, and (\triangle) α = 0.68 mol-CO₂/mol-amines.

Table 9.14. Comparison between calculated dynamic viscosity η_{cal} using **Equation 9.6** for MDEA + PZ + H₂O + CO₂ (w_{amines} = 0.3021 CO₂-free basis) with the dynamic viscosity experimental literature values η_{lit} Kummamuru et al. [129]. CO₂ loading α in terms of mol-CO₂/mol-amines.

	α	= 0	α=	0.60	α=	0.68
T/K	$oldsymbol{\eta}_{ ext{lit}}$	$oldsymbol{\eta}_{ ext{cal}}$ - $oldsymbol{\eta}_{ ext{lit}}$	$oldsymbol{\eta}_{ ext{lit}}$	$oldsymbol{\eta_{\mathrm{cal}}} extsf{-}oldsymbol{\eta_{\mathrm{lit}}}$	$oldsymbol{\eta}_{ ext{lit}}$	η _{cal} -η _{lit}
303.15	3.28	-0.2				
308.15	2.81	-0.2	2.84	0.2	3.06	0.004
313.15	2.39	-0.1	2.45	0.2	2.67	0.02
318.15	2.09	-0.1	2.17	0.2	2.37	0.01
323.15	1.81	-0.08	1.9	0.2	2.1	0.02
328.15	1.62	-0.09	1.71	0.1	1.89	0.01
333.15	1.43	-0.07	1.53	0.1	1.7	0.01
338.15	1.3	-0.08	1.41	0.1	1.56	-0.004
343.15	1.17	-0.07	1.3	0.08	1.43	-0.01
348.15	1.06	-0.07	1.19	0.07	1.31	-0.01
353.15	0.95	-0.05	1.09	0.07	1.19	0.01



CONCLUSIONS AND FUTURE WORK

CONCLUSIONS

This research investigates the thermodynamic properties of amine-based CO₂ absorbents, focusing on binary, ternary, and quaternary mixtures.

- 1. A comprehensive literature review revealed significant gaps in existing data, particularly for measurements at elevated temperatures and pressures, as well as for CO₂-loaded aqueous amine solutions.
- 2. Experimental procedures involved handling hazardous substances and operating under high-pressure and high-temperature conditions. Safety enhancements were implemented, including the installation of safety valves and rupture discs. Strict personal protective equipment protocols were enforced to minimise risks associated with handling amines.
- 3. Equilibrium cells was used for precise CO₂ loading into aqueous amine solutions with a relative expanded uncertainty lower than 0.4 % (95.5 % confidence level).
- 4. Experimental data for density, viscosity, and isobaric heat capacity were obtained over a wide range of temperatures, pressures, and concentrations. These data are crucial for optimising CO₂ capture processes, particularly in areas like fluid dynamics modelling, mass transfer calculations, equipment selection (pumps, packing), and energy efficiency assessments.
- 5. Density measurements were conducted using a vibrating tube densimeter (Anton Paar DMA HPM) with a maximum relative expanded uncertainty of 0.2 % (95.5 % confidence level).
 - Measurements were conducted at temperatures from 293.15 K to 393.15 K and pressure up to 100 MPa.
 - Density increased with pressure and CO₂ loading.
 - Density decreased with increasing temperature and amine mass fraction.
 - Good agreement with literature data within reported uncertainties.
 - A modified Tammann-Tait equation effectively correlated density data with respect to pressure, temperature, and molality, achieving adequate agreement with experimental values.
- 6. Isobaric heat capacity measurements were performed using a flow calorimeter with a relative expanded uncertainty of 1% (95.5 % confidence level).

CONCLUSIONS AND FUTURE WORK

- Measurements were conducted at temperatures from 293.15 K to 353.15 K and pressure up to (20 or 25) MPa.
- Isobaric heat capacity showed minimal dependence on temperature and pressure.
- Isobaric heat capacity decreased with increasing amine mass fraction and CO₂ loading.
- Good agreement with limited available literature data.
- Empirical correlations accurately model the isobaric heat capacity as a function of temperature and concentration for CO₂-unloaded and CO₂-loaded solutions.
- 7. Viscosity measurements were conducted using an Ubbelohde capillary viscometer with a relative expanded uncertainty of 1 % (95.5 % confidence).
 - Measurements were conducted at temperatures up to 353.15 K and atmospheric pressure.
 - Viscosity decreased significantly with increasing temperature.
 - Viscosity decreased with increasing CO₂ loading.
 - Experimental results were in good agreement with available literature data, considering the inherent challenges and uncertainties associated with viscosity measurements.
 - The modified VFT model was adequate to correlate viscosity with temperature and CO₂ loading.

CONCLUSIONS AND FUTURE WORK

FUTURE WORK

While this thesis has made significant progress in measuring the thermophysical properties of CO₂-loaded aqueous amine solutions, significant research challenges remain. Future investigations should prioritise the following:

- 1. Study the effect of amine mass fraction on the thermodynamic properties of CO₂-loaded aqueous amine solutions.
- 2. Investigate the pressure dependence of viscosity in CO₂-unloaded and CO₂-loaded aqueous amine solutions.
- 3. Develop correlation models for the thermodynamic properties of CO₂-loaded aqueous amine solutions as a function of temperature, pressure, CO₂ loading, and amine mass fraction.
- 4. Develop predictive models for the thermodynamic properties of CO₂-loaded aqueous amine solutions.
- 5. Estimate and compare the reaction kinetics of CO₂ absorption in different loaded aqueous amine solutions.
- 6. Compare the measured thermophysical properties of CO₂-loaded aqueous amine solutions with literature data for amino acid-based CO₂ absorbents.



- [1] IPCC, Climate Change: The Physical Science Basis, Cambridge University Press, Cambridge, United Kingdom and New York, NY, USA (2021). https://www.ipcc.ch/report/sixth-assessment-report-working-group-i/ (accessed February 18, 2025).
- [2] IPCC, Climate Change 2023. Synthesis Report, Cambridge University Press, Cambridge, UK and New York, NY, USA (2023). https://www.ipcc.ch/report/sixth-assessment-report-cycle/(accessed February 19, 2024).
- [3] X. Lan, P. Tans, K.W. Thoning, Trends in globally-averaged CO2 determined from NOAA Global Monitoring Laboratory measurements. Version Monday, 06-Jan-2025 10:06:16 MST, (2024). https://doi.org/https://doi.org/10.15138/9N0H-ZH07.
- [4] X. Lan, K.W. Thoning, E.J. Dlugokencky, Trends in globally-averaged CH4, N2O, and SF6 determined from NOAA Global Monitoring Laboratory measurements. Version 2024-05, (2024). https://doi.org/https://doi.org/10.15138/P8XG-AA10.
- [5] United Nations Framework Convention on Climate Change (UNFCCC), The Paris Agreement, (2015). https://unfccc.int/process-and-meetings/the-paris-agreement (accessed January 8, 2025).
- [6] European Commission, A European Green Deal, (2021). https://commission.europa.eu/strategy-and-policy/priorities-2019-2024/european-green-deal en.
- [7] IPCC, Special Report on Carbon Dioxide Capture and Storage, Cambridge University Press, UK (2005) 431. https://www.ipcc.ch/report/carbon-dioxide-capture-and-storage/ (accessed February 18, 2025).
- [8] J.C.M. Pires, Negative emissions technologies: A complementary solution for climate change mitigation, Science of the Total Environment 672 (2019) 502–514. https://doi.org/10.1016/j.scitotenv.2019.04.004.
- [9] M.E. Boot-Handford, J.C. Abanades, E.J. Anthony, M.J. Blunt, S. Brandani, N. Mac Dowell, J.R. Fernández, M.C. Ferrari, R. Gross, J.P. Hallett, R.S. Haszeldine, P. Heptonstall, A. Lyngfelt, Z. Makuch, E. Mangano, R.T.J. Porter, M. Pourkashanian, G.T. Rochelle, N. Shah, J.G. Yao, P.S. Fennell, Carbon capture and storage update, Energy Environ Sci 7 (2014) 130–189. https://doi.org/10.1039/c3ee42350f.
- [10] M. Erans, E.S. Sanz-Pérez, D.P. Hanak, Z. Clulow, D.M. Reiner, G.A. Mutch, Direct air capture: process technology, techno-economic and socio-political challenges, Energy Environ Sci 15 (2022) 1360–1405. https://doi.org/10.1039/d1ee03523a.
- [11] Carbon Brief, Explainer: 10 ways 'negative emissions' could slow climate change, (2016). https://www.carbonbrief.org/explainer-10-ways-negative-emissions-could-slow-climate-change/ (accessed May 22, 2024).

- [12] A. Kumar, A.K. Tiwari, D. Milani, Decarbonizing hard-to-abate heavy industries: Current status and pathways towards net-zero future, Process Safety and Environmental Protection 187 (2024) 408–430. https://doi.org/https://doi.org/10.1016/j.psep.2024.04.107.
- [13] M. Bui, C.S. Adjiman, A. Bardow, E.J. Anthony, A. Boston, S. Brown, P.S. Fennell, S. Fuss, A. Galindo, L.A. Hackett, J.P. Hallett, H.J. Herzog, G. Jackson, J. Kemper, S. Krevor, G.C. Maitland, M. Matuszewski, I.S. Metcalfe, C. Petit, G. Puxty, J. Reimer, D.M. Reiner, E.S. Rubin, S.A. Scott, N. Shah, B. Smit, J.P.M. Trusler, P. Webley, J. Wilcox, N. Mac Dowell, Carbon capture and storage (CCS): The way forward, Energy Environ Sci 11 (2018) 1062–1176. https://doi.org/10.1039/c7ee02342a.
- [14] Department for Energy Security & Net Zero UK, Carbon Capture, Usage and Storage: a vision to establish a competitive market, (2023). https://www.gov.uk/government/publications/carbon-capture-usage-and-storage-a-vision-to-establish-a-competitive-market/carbon-capture-usage-and-storage-a-vision-to-establish-a-competitive-market (accessed May 22, 2024).
- [15] B.S. Zainal, P.J. Ker, H. Mohamed, H.C. Ong, I.M.R. Fattah, S.M.A. Rahman, L.D. Nghiem, T.M.I. Mahlia, Recent advancement and assessment of green hydrogen production technologies, Renewable and Sustainable Energy Reviews 189 (2024) 113941. https://doi.org/https://doi.org/10.1016/j.rser.2023.113941.
- [16] B.S. Zainal, K.P. Jern, H. Mohamed, H.C. Ong, I.M.R. Fattah, S.M.A. Rahman, L.D. Nghiem, T.M.I. Mahlia, Corrigendum to Recent advancement and assessment of green hydrogen production technologies [Renew. Sustain. Energy Rev. 189 (2024) 5–5/113941], Renewable and Sustainable Energy Reviews 202 (2024) 114734. https://doi.org/https://doi.org/10.1016/j.rser.2024.114734.
- [17] N. MacDowell, N. Florin, A. Buchard, J. Hallett, A. Galindo, G. Jackson, C.S. Adjiman, C.K. Williams, N. Shah, P. Fennell, An overview of CO2 capture technologies, Energy Environ Sci 3 (2010) 1645–1669. https://doi.org/10.1039/c004106h.
- [18] G. Puxty, M. Maeder, The fundamentals of post-combustion capture, in: P.H.M. Feron (Ed.), Absorption-Based Post-Combustion Capture of Carbon Dioxide, Elsevier Ltd., 2016: pp. 13– 33.
- [19] Scottish Carbon Capture & Storage, Global CCS Map, (2024). https://www.sccs.org.uk/resources/global-ccs-map (accessed May 23, 2024).
- [20] Global CCS Institute, Global Status of CCS 2024. Collaborating for a Net-Zero Future, (2024). https://www.globalccsinstitute.com/resources/global-status-report/ (accessed January 27, 2025).
- [21] R.R. Bottoms, Process for Separating Acid Gases, 1930.
- [22] A.L. Kohl, R.B. Nielsen, Gas Purification, 5th ed., Gulf Publishing Co., Houston, TX, 1997.
- [23] D. Aaron, C. Tsouris, Separation of CO2 from flue gas: A review, Sep Sci Technol 40 (2005) 321–348. https://doi.org/10.1081/SS-200042244.

- [24] R.K. Abdulrahman, I.M. Sebastine, Natural gas sweetening process simulation and optimization: A case study of Khurmala field in Iraqi Kurdistan region, J Nat Gas Sci Eng 14 (2013) 116–120. https://doi.org/10.1016/j.jngse.2013.06.005.
- [25] R.L. Casselman, Sour-Gas Sweetening During Offshore Drillstem Tests-A Case History, SPE Production Engineering (1990) 103–106.
- [26] F. Meng, Y. Meng, T. Ju, S. Han, L. Lin, J. Jiang, Research progress of aqueous amine solution for CO2 capture: A review, Renewable and Sustainable Energy Reviews 168 (2022) 112902. https://doi.org/10.1016/J.RSER.2022.112902.
- [27] G.T. Rochelle, Conventional amine scrubbing for CO2 capture, in: P.H.M. Feron (Ed.), Absorption-Based Post-Combustion Capture of Carbon Dioxide, Elsevier Ltd., 2016: pp. 35–67. https://doi.org/10.1016/B978-0-08-100514-9.00003-2.
- [28] L.G. Wade, J.W. Simek, Amines, in: Organic Chemistry, 10th Global Edition, Pearson Education Limited, 2023: pp. 998–1058.
- [29] S.C. Tiwari, A. Bhardwaj, K.D.P. Nigam, K.K. Pant, S. Upadhyayula, A strategy of development and selection of absorbent for efficient CO2 capture: An overview of properties and performance, Process Safety and Environmental Protection 163 (2022) 244–273. https://doi.org/10.1016/J.PSEP.2022.05.025.
- [30] Chowdhury, H. Yamada, T. Higashii, K. Goto, M. Onoda, CO2 Capture by Tertiary Amine Absorbents: A Performance Comparison Study, Ind Eng Chem Res 52 (2013) 8323–8331. https://doi.org/10.1021/ie400825u.
- [31] N. El Hadri, D.V. Quang, E.L.V. Goetheer, M.R.M. Abu Zahra, Aqueous amine solution characterization for post-combustion CO2 capture process, Appl Energy 185 (2017) 1433–1449. https://doi.org/10.1016/j.apenergy.2016.03.043.
- [32] D. Tong, J.P.M. Trusler, G.C. Maitland, J. Gibbins, P.S. Fennell, Solubility of carbon dioxide in aqueous solution of monoethanolamine or 2-amino-2-methyl-1-propanol: Experimental measurements and modelling, International Journal of Greenhouse Gas Control 6 (2012) 37–47. https://doi.org/10.1016/j.ijggc.2011.11.005.
- [33] F. Bougie, M.C. Iliuta, Sterically hindered amine-based absorbents for the removal of CO2 from gas streams, J Chem Eng Data 57 (2012) 635–669. https://doi.org/10.1021/JE200731V.
- [34] G.T. Rochelle, Thermal degradation of amines for CO2 capture, Curr Opin Chem Eng 1 (2012) 183–190. https://doi.org/10.1016/j.coche.2012.02.004.
- [35] H. Li, Y. Le Moullec, J. Lu, J. Chen, J.C. Valle Marcos, G. Chen, F. Chopin, CO2 solubility measurement and thermodynamic modeling for 1-methylpiperazine/water/CO2, Fluid Phase Equilib 394 (2015) 118–128. https://doi.org/10.1016/j.fluid.2015.03.021.
- [36] A. V. Rayer, Y. Armugam, A. Henni, P. Tontiwachwuthikul, High-pressure solubility of carbon dioxide (CO2) in aqueous 1-methyl piperazine solution, J Chem Eng Data 59 (2014) 3610–3623. https://doi.org/10.1021/je500526m.

- [37] Z. Liu, A. Esmaeili, H. Zhang, H. Xiao, J. Yun, L. Shao, Carbon dioxide absorption with aqueous amine solutions promoted by piperazine and 1-methylpiperazine in a rotating zigzag bed, Fuel 302 (2021). https://doi.org/10.1016/j.fuel.2021.121165.
- [38] V. Vamja, C. Shukla, R. Bandyopadhyay, S.K. Dash, Density, Viscosity, and Surface Tension of Aqueous 1-Methylpiperazine and Its Carbonated Solvents for the CO2 Capture Process, J Chem Eng Data 69 (2024) 904–914. https://doi.org/10.1021/acs.jced.3c00651.
- [39] T. Zarogiannis, A.I. Papadopoulos, P. Seferlis, Systematic selection of amine mixtures as post-combustion CO2 capture solvent candidates, J Clean Prod 136 (2016) 159–175. https://doi.org/10.1016/j.jclepro.2016.04.110.
- [40] Y.M. Huang, A.N. Soriano, A.R. Caparanga, M.H. Li, Kinetics of absorption of carbon dioxide in 2-amino-2-methyl-l-propanol+N-methyldiethanolamine+water, J Taiwan Inst Chem Eng 42 (2011) 76–85. https://doi.org/10.1016/j.jtice.2010.04.007.
- [41] H. Suleman, A.S. Maulud, Z. Man, Experimental measurements and modelling of carbon dioxide solubility in aqueous AMP/MDEA and Piperazine/MDEA blends, Fluid Phase Equilib 463 (2018) 142–148. https://doi.org/10.1016/j.fluid.2018.02.016.
- [42] C. Costa, R. Di Felice, P. Moretti, M. Oliva, R. Ramezani, Piperazine and methyldiethanolamine interrelationships in CO2 absorption by aqueous amine mixtures. Part II-Saturation rates of mixed reagent solutions, Canadian Journal of Chemical Engineering 98 (2020) 2516–2529. https://doi.org/10.1002/cjce.23820.
- [43] A. Ahmed, A. Henni, A. Guibadj, A. Hadjadj, Enhancement of kinetic rates of CO2 in aqueous solutions of piperazine and methyldiethanolamine with addition of sulfolane, Canadian Journal of Chemical Engineering 100 (2022) 103–124. https://doi.org/10.1002/cjce.24222.
- [44] C. Nwaoha, P. Tontiwachwuthikul, A. Benamor, CO2 capture from water-gas shift process plant: Comparative bench-scale pilot plant investigation of MDEA-PZ blend vs novel MDEA activated by 1,5-diamino-2-methylpentane, International Journal of Greenhouse Gas Control 82 (2019) 218–228. https://doi.org/10.1016/j.ijggc.2019.01.009.
- [45] A.A. Khan, G.N. Halder, A.K. Saha, Experimental investigation on efficient carbon dioxide capture using piperazine (PZ) activated aqueous methyldiethanolamine (MDEA) solution in a packed column, International Journal of Greenhouse Gas Control 64 (2017) 163–173. https://doi.org/10.1016/j.ijggc.2017.07.016.
- [46] M. Jin, L.Y. Zhou, P. Lu, G.X. Yu, Absorption of CO2 from flue gas using mixed amine solution, in: Adv Mat Res, 2013: pp. 2201–2204. https://doi.org/10.4028/AMR.781-784.2201.
- [47] J. Ying, S. Raets, D. Eimer, The Activator Mechanism of Piperazine in Aqueous Methyldiethanolamine Solutions, in: Energy Procedia, Elsevier Ltd, 2017: pp. 2078–2087. https://doi.org/10.1016/j.egypro.2017.03.1342.
- [48] F. Closmann, T. Nguyen, G.T. Rochelle, MDEA/Piperazine as a solvent for CO2 capture, in: Energy Procedia, 2009: pp. 1351–1357. https://doi.org/10.1016/j.egypro.2009.01.177.

- [49] X. Wang, C. Song, Capture of CO2 from Concentrated Sources and the Atmosphere, in: M. Aresta, I. Karimi, S. Kawi (Eds.), An Economy Based on Carbon Dioxide and Water: Potential of Large Scale Carbon Dioxide Utilization, Springer International Publishing, Cham, Switzerland, 2019: pp. 35–72. https://doi.org/10.1007/978-3-030-15868-2 2.
- [50] M.T. Mota-Martinez, J.P. Hallett, N. Mac Dowell, Solvent selection and design for CO2 capture-how we might have been missing the point, Sustain Energy Fuels 1 (2017) 2078–2090. https://doi.org/10.1039/c7se00404d.
- [51] J.-C. De Hemptinne, G.M. Kontogeorgis, R. Dohrn, I.G. Economou, A. Ten Kate, S. Kuitunen, L. Fele, Z. Ilnik, M.G. De Angelis, V. Vesovic, A View on the Future of Applied Thermodynamics, Ind. Eng. Chem. Res 61 (2022) 14664–14680. https://doi.org/10.1021/acs.iecr.2c01906.
- [52] H. Li, B. Dong, Z. Yu, J. Yan, K. Zhu, Thermo-physical properties of CO2 mixtures and their impacts on CO2 capture, transport and storage: Progress since 2011, Appl Energy 255 (2019). https://doi.org/10.1016/j.apenergy.2019.113789.
- [53] P. Brúder, F. Owrang, H.F. Svendsen, Pilot study-CO2 capture into aqueous solutions of 3-methylaminopropylamine (MAPA) activated dimethyl-monoethanolamine (DMMEA), International Journal of Greenhouse Gas Control 11 (2012) 98–109. https://doi.org/10.1016/j.ijggc.2012.07.004.
- [54] P. Brúder, K.G. Lauritsen, T. Mejdell, H.F. Svendsen, CO2 capture into aqueous solutions of 3-methylaminopropylamine activated dimethyl-monoethanolamine, Chem Eng Sci 75 (2012) 28–37. https://doi.org/10.1016/j.ces.2012.03.005.
- [55] A.T. Zoghi, A. Rahimi, F. Feyzi, A.H. Jalili, Measuring and modeling equilibrium solubility of carbon dioxide in aqueous solution of dimethylaminoethanol and 3-methylaminopropylamine, Thermochim Acta 686 (2020). https://doi.org/10.1016/j.tca.2020.178565.
- [56] A. Rahimi, A.T. Zoghi, F. Feyzi, A.H. Jalili, Experimental Study of Density, Viscosity and Equilibrium Carbon Dioxide Solubility in Some Aqueous Alkanolamine Solutions, J Solution Chem 48 (2019) 489–501. https://doi.org/10.1007/s10953-019-00872-4.
- [57] National Institute of Health (NIH) USA, PubChem database, (2004). https://pubchem.ncbi.nlm.nih.gov/ (accessed January 28, 2025).
- [58] S. Kim, J. Chen, T. Cheng, A. Gindulyte, J. He, S. He, Q. Li, B.A. Shoemaker, P.A. Thiessen,
 B. Yu, L. Zaslavsky, J. Zhang, E.E. Bolton, PubChem 2025 update, Nucleic Acids Res 53 (2025)
 D1516–D1525. https://doi.org/10.1093/nar/gkae1059.
- [59] Z. Xu, S. Wang, C. Chen, Solubility of N2O in and Density and Viscosity of Aqueous Solutions of 1,4-Butanediamine, 2-(Diethylamino)-ethanol, and Their Mixtures from (298.15 to 333.15)
 K, J. Chem. Eng. Data 58 (2013) 39. https://doi.org/10.1021/je301371p.

- [60] L. Lebrette, Y. Maham, T.T. Teng, L.G. Hepler, A.E. Mather, Volumetric properties of aqueous solutions of mono, and diethylethanolamines at temperatures from 5 to 80 °C II, Thermochim Acta 386 (2002) 119–126. https://doi.org/10.1016/S0040-6031(01)00813-9.
- [61] K. Maneeintr, N. Phumkokrux, P. Boonpipattanapong, S. Assabumrungrat, T. Charinpanitkul, Measurement of Solubility and Physical Properties of Aqueous Solution of 2-(Diethylamino)ethanol for CO2 Capture, Energy Procedia 142 (2017) 3625–3630. https://doi.org/10.1016/j.egypro.2017.12.254.
- [62] S.S. Karunarathne, D.A. Eimer, L.E. Øi, Density, Viscosity, and Excess Properties of MDEA + H2O, DMEA + H2O, and DEEA + H2O Mixtures, Appl. Sci 10 (2020) 3196. https://doi.org/10.3390/app10093196.
- [63] D.D.D. Pinto, J.G.M.S. Monteiro, B. Johnsen, H.F. Svendsen, H. Knuutila, Density measurements and modelling of loaded and unloaded aqueous solutions of MDEA (N-methyldiethanolamine), DMEA (N,N-dimethylethanolamine), DEEA (diethylethanolamine) and MAPA (N-methyl-1,3-diaminopropane), International Journal of Greenhouse Gas Control 25 (2014) 173–185. https://doi.org/10.1016/j.ijggc.2014.04.017.
- [64] B. Hawrylak, S.E. Burke, R. Palepu, Partial Molar and Excess Volumes and Adiabatic Compressibilities of Binary Mixtures of Ethanolamines with Water, J Solution Chem 29 (2000).
- [65] F.-Q. Zhang, H.-P. Li, M. Dai, J.-P. Zhao, J.P. Chao, Volumetric properties of binary mixtures of water with ethanolamine alkyl derivatives, Thermochimica Acta 254 (1995) 347–357.
- [66] A. Awasthi, Ultrasonic Speeds, Molar Isentropic Compressions and FTIR analysis of aqueous solutions of 2-dialkylaminoethanols from 293.15 to 313.15 K, Phys Chem Liquids 60 (2022) 33–46. https://doi.org/10.1080/00319104.2021.1907844.
- [67] Y. Maham, L. Lebrette, A.E. Mather, Viscosities and Excess Properties of Aqueous Solutions of Mono and Diethylethanolamines at Temperatures between 298.15 and 353.15 K, J. Chem. Eng. Data 47 (2002) 550–553. https://doi.org/10.1021/je015528d.
- [68] S.S. Karunarathne, D.A. Eimer, K.J. Jens, L.E. Øi, Density, viscosity, and excess properties of ternary aqueous mixtures of MDEA + MEA, DMEA + MEA, and DEEA + MEA, Fluids 5 (2020). https://doi.org/10.3390/fluids5010027.
- [69] S. Cabani, S.T. Lobo, E. Matteo Ii, Apparent Molal Heat Capacities of Organic Solutes in Water. V. Aminoalcohols, Arninoethers, Diamines, and Polyethers, J Solution Chem 8 (1979) 5–10.
- [70] C. Zhu, X. Liu, T. Fu, X. Gao, Y. Ma, Density, viscosity and excess properties of N, N-dimethylethanolamine +2-(ethylamino) ethanol +H2O at T = (293.15 to 333.15) K, J Mol Liq 319 (2020) 114095. https://doi.org/10.1016/J.MOLLIQ.2020.114095.
- [71] Chowdhury, S. Akhtar, M.A. Saleh, M.U. Khandaker, Y.M. Amin, A.K. Arof, Volumetric and viscometric properties of aqueous solutions of some monoalkanolamines, J Mol Liq 223 (2016) 299–314. https://doi.org/10.1016/J.MOLLIQ.2016.08.033.

- [72] K. Viet, B. Tran, M. Sato, K. Yanase, T. Yamaguchi, H. Machida, K. Norinaga, Density and Viscosity Calculation of a Quaternary System of Amine Absorbents before and after Carbon Dioxide Absorption, J. Chem. Eng. Data 66 (2021) 3057–3071. https://doi.org/10.1021/acs.jced.1c00195.
- [73] D. Pandey, M.K. Mondal, Viscosity, density, and derived thermodynamic properties of aqueous 2-(ethylamino)ethanol (EAE), aqueous aminoethylethanolamine (AEEA), and its mixture for post-combustion CO2 capture, J Mol Liq 332 (2021) 115873. https://doi.org/10.1016/J.MOLLIQ.2021.115873.
- [74] E. Álvarez, D. Gómez-Díaz, M.D. La Rubia, J.M. Navaza, Densities and viscosities of aqueous ternary mixtures of 2-(methylamino)ethanol and 2-(ethylamino)ethanol with diethanolamine, triethanolamine, N-methyldiethanolamine, or 2-amino-1-methyl-1-propanol from 298.15 to 323.15 K, J Chem Eng Data 51 (2006) 955–962. https://doi.org/10.1021/je050463q.
- [75] H. Gao, G. Gao, H. Liu, X. Luo, Z. Liang, R.O. Idem, Density, Viscosity, and Refractive Index of Aqueous CO2-Loaded and -Unloaded Ethylaminoethanol (EAE) Solutions from 293.15 to 323.15 K for Post Combustion CO2 Capture, J Chem Eng Data 62 (2017) 4205–4214. https://doi.org/10.1021/acs.jced.7b00586.
- [76] J.G.M.S. Monteiro, S. Hussain, H. Majeed, E.O. Mba, A. Hartono, H. Knuutila, H.F. Svendsen, Kinetics of CO2 absorption by aqueous 3-(methylamino)propylamine solutions: Experimental results and modeling, AIChE Journal 60 (2014) 3792–3803. https://doi.org/10.1002/aic.14546.
- [77] X. Wang, K. Kang, W. Wang, Y. Tian, Volumetric properties of binary mixtures of 3-(methylamino)propylamine with water, N-methyldiethanolamine, N, N-dimethylethanolamine, and N, N-diethylethanolamine from (283.15 to 363.15) K, J Chem Eng Data 58 (2013) 3430–3439. https://doi.org/10.1021/je400679k.
- [78] A. V. Rayer, K.Z. Sumon, A. Henni, P. Tontiwachwuthikul, Physicochemical properties of {1-methyl piperazine (1) + water (2)} system at T = (298.15 to 343.15) K and atmospheric pressure, Journal of Chemical Thermodynamics 43 (2011) 1897–1905. https://doi.org/10.1016/J.JCT.2011.06.020.
- [79] S. Poozesh, A. V. Rayer, A. Henni, Molar Heat Capacity (Cp) of Aqueous Cyclic Amine Solutions from (298.15 to 353.15) K, J Chem Eng Data 58 (2013) 1989–2000. https://doi.org/10.1021/je400178k.
- [80] E. Álvarez, D. Gómez-Díaz, M.D. La Rubia, J.M. Navaza, Densities and viscosities of aqueous ternary mixtures of 2-(methylamino)ethanol and 2-(ethylamino)ethanol with diethanolamine, triethanolamine, N-methyldiethanolamine, or 2-amino-1-methyl-1-propanol from 298.15 to 323.15 K, J Chem Eng Data 51 (2006) 955–962. https://doi.org/10.1021/je050463q.
- [81] A. Shojaeian, A. Haghtalab, Solubility and density of carbon dioxide in different aqueous alkanolamine solutions blended with 1-butyl-3-methylimidazolium acetate ionic liquid at high pressure, J Mol Liq 187 (2013) 218–225. https://doi.org/10.1016/j.molliq.2013.07.016.

- [82] A. Samanta, S.S. Bandyopadhyay, Density and viscosity of aqueous solutions of piperazine and (2-Amino-2-methyl-1-propanol + piperazine) from 298 to 333 K, J Chem Eng Data 51 (2006) 467–470. https://doi.org/10.1021/je050378i.
- [83] M. Stec, T. Spietz, L. Więcław-Solny, A. Tatarczuk, A. Wilk, A. Sobolewski, Density of unloaded and CO2-loaded aqueous solutions of piperazine and 2-amino-2-methyl-1-propanol and their mixtures from 293.15 to 333.15 K, Phys Chem Liquids 54 (2016) 475–486. https://doi.org/10.1080/00319104.2015.1115328.
- [84] J. Na, B.M. Min, Y.C. Park, J.H. Moon, D.H. Chun, J.S. Lee, H.Y. Shin, Measurement and correlation of densities and excess volumes for water +N-Methyldiethanolamine (MDEA), Water + 2-Amino-2-Methyl-1-Propanol (AMP), MDEA + AMP and Water + MDEA +AMP systems, Korean Chemical Engineering Research 56 (2018) 204–211. https://doi.org/10.9713/kcer.2018.56.2.204.
- [85] A. Henni, J.J. Hromek, P. Tontiwachwuthikul, A. Chakma, Volumetric properties and viscosities for aqueous AMP solutions from 25°C to 70°C, J Chem Eng Data 48 (2003) 551–556. https://doi.org/10.1021/je0201119.
- [86] C. Chan, Y. Maham, A.E. Mather, C. Mathonat, Densities and volumetric properties of the aqueous solutions of 2-amino-2-methyl-1-propanol, n-butyldiethanolamine and n-propylethanolamine at temperatures from 298.15 to 353.15 K, Fluid Phase Equilib 198 (2002) 239–250.
- [87] S. Xu, F.D. Otto, A.E. Mather, Physical Properties of Aqueous AMP Solutions, J Chem Eng Data 36 (1991) 71–75. https://doi.org/10.1021/je00001a021.
- [88] G. Murshid, A.M. Shariff, L.K. Keong, M.A. Bustam, Physical properties of aqueous solutions of piperazine and (2-amino-2-methyl-1-propanol + piperazine) from (298.15 to 333.15) K, J Chem Eng Data 56 (2011) 2660–2663. https://doi.org/10.1021/je1012586.
- [89] M.-H. Li, Y.-C. Lie, Densities and Viscosities of Solutions of Monoethanolamine + N-Methyldiethanolamine + Water and Monoethanolamine + 2-Amino-2-methyl-l-propanol + Water, J. Chem. Eng. Data 39 (1994) 444–447.
- [90] B. Das, B. Deogam, B. Mandal, Experimental and theoretical studies on efficient carbon dioxide capture using novel bis(3-aminopropyl)amine (APA)-activated aqueous 2-amino-2-methyl-1-propanol (AMP) solutions, RSC Adv 7 (2017) 21518–21530. https://doi.org/10.1039/c7ra01286a.
- [91] J. Aguila-Hernández, R. Gómez-Quintana, F. Murrieta-Guevara, A. Romero-Martínez, A. Trejo, Liquid density of aqueous blended alkanolamines and N-methylpyrrolidone as a function of concentration and temperature, J Chem Eng Data 46 (2001) 861–867. https://doi.org/10.1021/je0002944.
- [92] B.P. Mandal, M. Kundu, S.S. Bandyopadhyay, Density and viscosity of aqueous solutions of (N-methyldiethanolamine + monoethanolamine), (N-methyldiethanolamine + diethanolamine),

- (2-amino-2-methyl-1-propanol + monoethanolamine), and (2-amino-2-methyl-1-propanol + diethanolamine), J Chem Eng Data 48 (2003) 703–707. https://doi.org/10.1021/je020206a.
- [93] A. Rezaei, P. Pakzad, M. Mofarahi, A.A. Izadpanah, M. Afkhamipour, C.H. Lee, Densities and Viscosities of Binary and Ternary Solutions of Triethylenetetramine, 2-Amino-2-methyl-1-propanol, and Water for Carbon Dioxide Capture, J Chem Eng Data 66 (2021) 2942–2958. https://doi.org/10.1021/acs.jced.0c01052.
- [94] A. Zúñiga-Moreno, L.A. Galicia-Luna, J.M. Bernal-García, G.A. Iglesias-Silva, Densities and Derived Thermodynamic Properties of 2-Amino-2-methyl-1-propanol + Water Mixtures at Temperatures from (313 to 363) K and Pressures up to 24 MPa, J Chem Eng Data 53 (2008) 1047. https://doi.org/10.1021/JE800129G.
- [95] X. Liu, C. Zhu, T. Fu, Y. Ma, Volumetric and viscometric properties of ternary solution of (piperazine +2-Amino-2-methyl-1-propanol + H2O) at T = (303.15–343.15) K, J Mol Liq 310 (2020). https://doi.org/10.1016/j.molliq.2020.113187.
- [96] L.M. Welsh, R.A. Davis, Density and Viscosity of Aqueous Blends of N-Methyldiethanolamine and 2-Amino-2-methyl-1-propanol, J. Chem. Eng. Data 40 (1995) 257–259. https://doi.org/10.1021/je00017a055.
- [97] F. Chenlo, R. Moreira, G. Pereira, M.J. Vázquez, E. Santiago, Viscosities of single-solute and binary-solute aqueous systems of monoethanolamine, diethanolamine, and 2-amino-2-methyl-1-propanol, J Chem Eng Data 46 (2001) 276–280. https://doi.org/10.1021/je000241m.
- [98] F. Chenlo, R. Moreira, G. Pereira, M.J. Vázquez, Viscosities of binary and ternary aqueous solutions of 2-amino-2-methylpropan-1-ol, 2-amino-2-methylpropane-1,3-diol, and 2-amino-2-methylpropan-1-ol hydrochloride, Collect Czechoslov Chem Commun 67 (2002) 293–301. https://doi.org/10.1135/cccc20020293.
- [99] H. Bosch, G.F. Versteeg, W.P.M. Van Swaaij, Kinetics of the reaction of CO with the sterically hindered amine 2-amino-2-methylpropanol at 298 K, Chem Eng Sci 45 (1990) 1167–1173.
- [100] N.B. Kummamuru, N.B. Kummamuru, D.A. Eimer, Z. Idris, Viscosity Measurement and Correlation of Unloaded and CO2-Loaded Aqueous Solutions of N-Methyldiethanolamine + 2-Amino-2-methyl-1-propanol, J Chem Eng Data 65 (2020) 3072–3078. https://doi.org/10.1021/acs.jced.0c00088.
- [101] K. Zhang, B. Hawrylak, R. Palepu, P.R. Tremaine, Thermodynamics of aqueous amines: Excess molar heat capacities, volumes, and expansibilities of {water + methyldiethanolamine (MDEA)} and {water + 2-amino-2-methyl-1-propanol (AMP)}, Journal of Chemical Thermodynamics 34 (2002) 679–710. https://doi.org/10.1006/jcht.2002.0937.
- [102] Y.J. Chen, M.H. Li, Heat capacity of aqueous mixtures of monoethanolamine with 2-amino-2-methyl-l-propanol, J Chem Eng Data 46 (2001) 102–106. https://doi.org/10.1021/je000146d.
- [103] L.F. Chiu, M.H. Li, Heat capacity of alkanolamine aqueous solutions, J Chem Eng Data 44 (1999) 1396–1401. https://doi.org/10.1021/je990131j.

- [104] M. Sobrino, E.I. Concepción, Á. Gómez-Hernández, M.C. Martín, J.J. Segovia, Viscosity and density measurements of aqueous amines at high pressures: MDEA-water and MEA-water mixtures for CO2 capture, J Chem Thermodyn 98 (2016) 231–241. https://doi.org/10.1016/J.JCT.2016.03.021.
- [105] H.A. Al-Ghawas, D.P. Hagewlesche, G. Rulz-Ibanez, O.C. Sandall, Physicochemical Properties Important for Carbon Dioxide Absorption in Aqueous Methyldiethanolamine, J. Chem. Eng. Data 34 (1989) 385–391. https://doi.org/10.1021/je00058a004.
- [106] E.B. Rinker, D.W. Oelschlager, A. Tomas Colussi, K.R. Henry, O.C. Sandall, Viscosity, Density, and Surface Tension of Binary Mixtures of Water Tertiary Mixtures of These Amines with Water over the Temperature Range 20-100 °C, J. Chem. Eng. Data 39 (1994) 392–395.
- [107] R.H. Weiland, J.C. Dingman, D.B. Cronin, G.J. Browning, Density and Viscosity of Some Partially Carbonated Aqueous Alkanolamine Solutions and Their Blends, J. Chem. Eng. Data 43 (1998) 378–382.
- [108] T.G. Amundsen, L.E. Øi, D.A. Eimer, Density and viscosity of monoethanolamine + water + carbon dioxide from (25 to 80) °C, J Chem Eng Data 54 (2009) 3096–3100. https://doi.org/10.1021/je900188m.
- [109] J. Han, J. Jin, D.A. Eimer, M.C. Melaaen, Density of water (1) + monoethanolamine (2) + CO2
 (3) from (298.15 to 413.15) K and surface tension of water (1) + monoethanolamine (2) from (303.15 to 333.15) K, J Chem Eng Data 57 (2012) 1095–1103. https://doi.org/10.1021/JE2010038.
- [110] A. Hartono, E.O. Mba, H.F. Svendsen, Physical properties of partially CO2 loaded aqueous monoethanolamine (MEA), J Chem Eng Data 59 (2014) 1808–1816. https://doi.org/10.1021/je401081e.
- [111] H. Ju, W. Elmoudir, A. Aboudheir, N. Mahinpey, Density, Viscosity, Refractive Index, and Electrical Conductivity of Degraded Monoethanolamine Solutions at Standard Temperatures, J. Chem. Eng. Data 63 (2018) 1969–1976. https://doi.org/10.1021/acs.jced.7b01101.
- [112] J. Zhang, P.S. Fennell, J.P.M. Trusler, Density and Viscosity of Partially Carbonated Aqueous Tertiary Alkanolamine Solutions at Temperatures between (298.15 and 353.15) K, J. Chem. Eng. Data 60 (2015) 2392–2399. https://doi.org/10.1021/acs.jced.5b00282.
- [113] S.A. Jayarathna, A. Weerasooriya, S. Dayarathna, D.A. Eimer, M.C. Melaaen, Densities and surface tensions of CO2 loaded aqueous monoethanolamine solutions with r = (0.2 to 0.7) at T = (303.15 to 333.15) K, J Chem Eng Data 58 (2013) 986–992. https://doi.org/10.1021/je301279x.
- [114] S.A. Jayarathna, C.K. Jayarathna, D.A. Kottage, S. Dayarathna, D.A. Eimer, M.C. Melaaen, Density and surface tension measurements of partially carbonated aqueous monoethanolamine solutions, J Chem Eng Data 58 (2013) 343–348. https://doi.org/10.1021/je300920t.

- [115] S.S. Karunarathne, D.A. Eimer, L.E. Øi, Density, viscosity and free energy of activation for viscous flow of CO2 loaded 2-amino-2-methyl-1-propanol (AMP), monoethanol amine (MEA) and H2O mixtures, J Mol Liq 311 (2020). https://doi.org/10.1016/j.molliq.2020.113286.
- [116] R. Ramezani, I.M. Bernhardsen, R. Di Felice, H.K. Knuutila, Physical properties and reaction kinetics of CO2 absorption into unloaded and CO2 loaded viscous monoethanolamine (MEA) solution, J Mol Liq 329 (2021). https://doi.org/10.1016/J.MOLLIQ.2021.115569.
- [117] T. Spietz, M. Stec, A. Wilk, A. Krótki, A. Tatarczuk, L. Więcław-Solny, Density correlation of carbonated amine solvents for CO2 loading determination, Asia-Pacific Journal of Chemical Engineering 13 (2018). https://doi.org/10.1002/apj.2248.
- [118] M.S. Ojala, N. Ferrer Serrano, P. Uusi-Kyyny, V. Alopaeus, Comparative study: Absorption enthalpy of carbon dioxide into aqueous diisopropanolamine and monoethanolamine solutions and densities of the carbonated amine solutions, Fluid Phase Equilib 376 (2014) 85–95. https://doi.org/10.1016/J.FLUID.2014.05.038.
- [119] J. Zhang, P.S. Fennell, J.P.M. Trusler, Density and Viscosity of Partially Carbonated Aqueous Tertiary Alkanolamine Solutions at Temperatures between (298.15 and 353.15) K, J Chem Eng Data 60 (2015) 2392–2399. https://doi.org/10.1021/acs.jced.5b00282.
- [120] Z. Idris, N.B. Kummamuru, D.A. Eimer, Viscosity measurement of unloaded and CO2-loaded aqueous monoethanolamine at higher concentrations, J Mol Liq 243 (2017) 638–645. https://doi.org/10.1016/J.MOLLIQ.2017.08.089.
- [121] U. Arachchige, B. Singh, K. Prajapati, M.C. Melaaen, Dynamic Viscosity of Partially Carbonated Aqueous Monoethanolamine (MEA) from (20 to 150) °C, Applied Chemical Engineering 2 (2019). https://doi.org/10.24294/ace.v1i2.660.
- [122] D. Fu, L.H. Chen, L.G. Qin, Experiment and model for the viscosity of carbonated MDEA-MEA aqueous solutions, Fluid Phase Equilib 319 (2012) 42–47. https://doi.org/10.1016/j.fluid.2012.01.029.
- [123] N.S. Matin, J.E. Remias, K. Liu, Application of electrolyte-NRTL model for prediction of the viscosity of carbon dioxide loaded aqueous amine solutions, Ind Eng Chem Res 52 (2013) 16979–16984. https://doi.org/10.1021/ie4026874.
- [124] R.H. Weiland, J.C. Dingman, D.B. Cronin, Heat Capacity of Aqueous Monoethanolamine, Diethanolamine, N-Methyldiethanolamine, and N-Methyldiethanolamine-Based Blends with Carbon Dioxide, 1997.
- [125] M. Shokouhi, A.H. Jalili, F. Samani, M. Hosseini-Jenab, Experimental investigation of the density and viscosity of CO2-loaded aqueous alkanolamine solutions, Fluid Phase Equilib 404 (2015) 96–108. https://doi.org/10.1016/j.fluid.2015.06.034.
- [126] J. Han, J. Jin, D.A. Eimer, M.C. Melaaen, Density of water (1) + diethanolamine (2) + CO2 (3) and water (1) + N-methyldiethanolamine (2) + CO2 (3) from (298.15 to 423.15) K, J Chem Eng Data 57 (2012) 1843–1850. https://doi.org/10.1021/je300345m.

- [127] S.A. Jayarathna, D.A. Kottage, D.A. Eimer, M.C. Melaaen, Densities of partially carbonated aqueous diethanolamine and methyldiethanolamine solutions, J Chem Eng Data 57 (2012) 2975–2984. https://doi.org/10.1021/je300530z.
- [128] A.H. Jalili, A.T. Zoghi, M. Shokouhi, A. Mehdizadeh, Vapor-Liquid Equilibria and Density of CO2-Loaded Aqueous Methyldiethanolamine + Piperazine + Sulfolane Solutions, J Chem Eng Data 69 (2024) 1842–1861. https://doi.org/10.1021/acs.jced.4c00017.
- [129] N.B. Kummamuru, Z. Idris, D.A. Eimer, Viscosity Measurement and Correlation of Unloaded and CO2-Loaded Aqueous Solutions of N-Methyldiethanolamine-Piperazine, J Chem Eng Data 64 (2019) 4692–4700. https://doi.org/10.1021/acs.jced.9b00021.
- [130] D. Fu, L. Qin, H. Hao, Experiment and model for the viscosity of carbonated piperazine-N-methyldiethanolamine aqueous solutions, J Mol Liq 186 (2013) 81–84. https://doi.org/10.1016/j.molliq.2013.05.027.
- [131] D. Vega-Maza, Caracterización termodinámica de combustibles líquidos de nueva generación con componentes renovables mediante un nuevo calorímetro isobárico de alta presión y medidas densitométricas. PhD Thesis, University of Valladolid, 2009.
- [132] J.M. Smith, H.C. Van Ness, M.M. Abbott, M.T. Swihart, Introduction to Chemical Engineering Thermodynamics, 8th ed., McGraw-Hill Education, New York, 2018.
- [133] L. Lugo, M.J.P. Comuñas, E.R. López, J. Fernández, (p, Vm, T, x) measurements of dimethyl carbonate + octane binary mixtures I. Experimental results, isothermal compressibilities, isobaric expansivities and internal pressures, Fluid Phase Equilib 186 (2001) 235–255.
- [134] W. Wagner, R. Kleinrahm, H.W. Losch, J.T.R. Watson, V. Majer, A.A.H. Pádua, L.A. Woolf, J.C. Holste, A.M. De Figueiredo Palavra, K. Fujii, J.W. Stansfeld, Density, in: A.R.H. Goodwin, K.N. Marsh, W.A. Wakeham (Eds.), Measurement of the Thermodynamic Properties of Single Phases. Experimental Thermodynamics, Elsevier, 2003. https://doi.org/10.1016/s1874-5644(03)80016-4.
- [135] R.F. Chang, M.R. Moldover, High-temperature high-pressure oscillating tube densimeter, Review of Scientific Instruments 67 (1996) 251–256. https://doi.org/10.1063/1.1146580.
- [136] E.F. May, W.J. Tay, M. Nania, A. Aleji, S. Al-Ghafri, J.P. Martin Trusler, Physical apparatus parameters and model for vibrating tube densimeters at pressures to 140 MPa and temperatures to 473 K, Review of Scientific Instruments 85 (2014). https://doi.org/10.1063/1.4894469.
- [137] J.S. Rowlinson, F.L. Swinton, Liquids and Liquids Mixtures, 3rd ed., Butterworths, 3rd ed. London: , 1982.
- [138] J.M. Smith, H.C. Van Ness, M.M. Abbott, Introduction to Chemical Engineering Thermodynamics., 7th ed., McGraw-Hill Chemical Engineering Series. McGraw-Hill, Boston, 2005.
- [139] B.E. Poling, J. O'Connell, J.M. Prausnitz, The properties of gases and liquids, Fifth Edition, McGraw-Hill, 2001.

- [140] K.N. Marsh, J.B. Ott, C.J. Wormald, H. Yao, I. Hatta, P.M. Claudy, S. Van Herwaarden, Calorimetry, in: A.R.H. Goodwin, K.N. Marsh, W.A. Wakeham (Eds.), Measurement of the Thermodynamic Properties of Single Phases. Experimental Thermodynamics., Elservier, 2003.
- [141] T.G. Zijlema, G.-J. Witkamp, G.M. Van Rosmalen, Specific Heats and Enthalpies of Mixing of Amine-H2O and Amine-H2O-NaCl Mixtures, J. Chem. Eng. Data 44 (1999) 1335–1337. https://doi.org/10.1021/je9900878.
- [142] S.M. Sarge, G.W.H. Hohne, W. Hemminger, Calorimetry: Fundamentals, Instrumentation and Applications, Wiley-VCH, 2014.
- [143] E. Calvet, H. Prat, Recent Progress in Microcalorimetry, Pergamon Press, 1963.
- [144] SETARAM, Calvet Calorimeters, (2024). https://setaramsolutions.com/standard-solutions/calvet-calorimeters (accessed June 11, 2024).
- [145] M. Mundhwa, A. Henni, Molar heat capacity of various aqueous alkanolamine solutions from 303.15 K to 353.15 K, J Chem Eng Data 52 (2007) 491–498. https://doi.org/10.1021/je0604232.
- [146] A.V. Rayer, A. Henni, P. Tontiwachwuthikul, Molar heat capacities of solvents used in CO2 capture: A group additivity and molecular connectivity analysis, Can J Chem Eng 90 (2012) 367–376. https://doi.org/10.1002/CJCE.20646.
- [147] R.W. Olivia, R.B. Leron, M.H. Li, Molar heat capacities of aqueous 2-amino-2-ethyl-1,3-propanediol solutions and their ternary mixtures containing piperazine or lithium salts, Fluid Phase Equilib 365 (2014) 74–79. https://doi.org/10.1016/J.FLUID.2013.12.017.
- [148] S.Y. Lin, R.B. Leron, M.H. Li, Molar heat capacities of aqueous binary and ternary mixtures (with piperazine) of two diamines: N,N,N',N'-Tetramethylethylenediamine and N,N,N',N'-tetramethyl-1,3-propanediamine, J Taiwan Inst Chem Eng 45 (2014) 1291–1297. https://doi.org/10.1016/j.jtice.2013.12.019.
- [149] Y.R. Chen, A.R. Caparanga, A.N. Soriano, M.H. Li, Liquid heat capacity of the solvent system (piperazine + n-methyldiethanolamine + water), Journal of Chemical Thermodynamics 42 (2010) 54–59. https://doi.org/10.1016/j.jct.2009.07.005.
- [150] S.V. Gupta, Viscometry for Liquids. Calibration of Viscometers, Springer, 2014.
- [151] M. Richter, J.P.M. Trusler, Vibrating-Wire Viscometry, Int J Thermophys 45 (2024). https://doi.org/10.1007/s10765-024-03413-4.
- [152] M.J. Assael, W.A. Wakehamb, Vibrating-wire viscometry on liquids at high pressure, Fluid Phase Equilib 75 (1992) 269–285.
- [153] M.J. Assael, M. Papadaki, M. Oix, S.M. Richardson, W.A. Wakeham, An Absolute Vibrating-Wire Viscometer for Liquids at High Pressures, Int J Thermophys 12 (1991).
- [154] K.R. Harris, A Falling Body High-Pressure Viscometer, Int J Thermophys 44 (2023). https://doi.org/10.1007/s10765-023-03285-0.
- [155] A.J. Rowane, R.R. Mallepally, B.A. Bamgbade, M.S. Newkirk, H.O. Baled, W.A. Burgess, I.K. Gamwo, D. Tapriyal, R.M. Enick, M.A. McHugh, High-temperature, high-pressure viscosities

- and densities of toluene, Journal of Chemical Thermodynamics 115 (2017) 34–46. https://doi.org/10.1016/j.jct.2017.07.015.
- [156] Health and Safety Executive, COSHH Essentials: Easy Steps to Control Chemicals, 1999. https://books.google.es/books/about/COSHH_Essentials.html?id=VYhIAAAACAAJ&redir_es c=y (accessed January 13, 2025).
- [157] Health and Safety Executive, Control of substances hazardous to health. The Control of Substances Hazardous to Health Regulations 2002 (as amended). Approved Code of Practice and guidance, Sixth edition, 2013. https://www.hse.gov.uk/pubns/books/l5.htm (accessed January 13, 2025).
- [158] The European Parliament and of the Council of the European Union, Regulation (EC) No. 1907/2006: Registration, Evaluation, Authorisation and Restriction of Chemicals (REACH), establishing a European Chemicals Agency, amending Directive 1999/45/EC and repealing Council Regulation (EEC) No 793/93 and Commission Regulation (EC) No 1488/94 as well as Council Directive 76/769/EEC and Commission Directives 91/155/EEC, 93/67/EEC, 93/105/EC and 2000/21/EC, (2006). https://eur-lex.europa.eu/legal-content/EN/TXT/PDF/?uri=CELEX:32006R1907 (accessed January 13, 2025).
- [159] U. Health and Safety Executive, Control of Substances Hazardous to Health (COSHH): Controlling exposure to chemicals a simple control banding approach, (2017) 1–23. www.hse.gov.uk/pubns/guidance/coshh-technical-basis.pdf (accessed May 22, 2024).
- [160] B.K. Choi, S.M. Kim, J.S. Lee, Y.C. Park, D.H. Chun, H.Y. Shin, H.J. Sung, B.M. Min, J.H. Moon, Effect of Blending Ratio and Temperature on CO2 Solubility in Blended Aqueous Solution of Monoethanolamine and 2-Amino-2-methyl-propanol: Experimental and Modeling Study Using the Electrolyte Nonrandom Two-Liquid Model, ACS Omega 5 (2020) 28738–28748. https://doi.org/10.1021/acsomega.0c04046.
- [161] M. Xiao, W. Zheng, H. Liu, X. Luo, H. Gao, Z. Liang, Thermodynamic analysis of carbamate formation and carbon dioxide absorption in N-methylaminoethanol solution, Appl Energy 281 (2021). https://doi.org/10.1016/j.apenergy.2020.116021.
- [162] C. Gouedard, D. Picq, F. Launay, P.L. Carrette, Amine degradation in CO2 capture. I. A review, International Journal of Greenhouse Gas Control 10 (2012) 244–270. https://doi.org/10.1016/J.IJGGC.2012.06.015.
- [163] S.B. Fredriksen, K.J. Jens, Oxidative degradation of aqueous amine solutions of MEA, AMP, MDEA, Pz: A review, Energy Procedia 37 (2013) 1770–1777. https://doi.org/10.1016/J.EGYPRO.2013.06.053.
- [164] B. Lagourette, C. Boned, H. Saint-Guirons, P. Xans, H. Zhout, Densimeter calibration method versus temperature and pressure, Meas. Sci. Technol 3 (1992) 699–703.

- [165] A.T. Sousa, P. Sousa Fialho, C.A. Nieto De Castro, R. Tufeu, B. Le Neindre, Density of HCFC 142b and its mixture with HCFC 22, Fluid Phase Equilib 80 (1992) 213–225. https://doi.org/10.1016/0378-3812(92)87069-Y.
- [166] J.J. Segovia, O. Fandiño, E.R. López, L. Lugo, M. Carmen Martín, J. Fernández, Automated densimetric system: Measurements and uncertainties for compressed fluids, J Chem Thermodyn 41 (2009) 632–638. https://doi.org/10.1016/J.JCT.2008.12.020.
- [167] R. García-Morales, F.J. Verónico-Sánchez, J. Domenzaín-González, A. Zúñiga-Moreno, C. Bouchot, O. Elizalde-Solis, Liquid to solid phase transition detection by using a vibrating tube densimeter along with densities up to 137 MPa of beef tallow fatty acid alkyl esters, Journal of Chemical Thermodynamics 192 (2024). https://doi.org/10.1016/j.jct.2024.107259.
- [168] E.C. Ihmels, J. Gmehling, Densities of toluene, carbon dioxide, carbonyl sulfide, and hydrogen sulfide over a wide temperature and pressure range in the sub- and supercritical state, Ind Eng Chem Res 40 (2001) 4470–4477. https://doi.org/10.1021/ie001135g.
- [169] H. Stabinger, H. Leopold, O. Kratky, Eine neue Methode zur Präzisionsmessung der Dichte von Flüssigkeiten - Kurze Mitteilung, Monatsh Chem 98 (1967) 436–438. https://doi.org/10.1007/BF00899963.
- [170] O. Kratky, H. Leopold, H. Stabinger, Z. Angew, Physik 27 (1969) 273–281.
- [171] Anton Paar, Intrumentos Analíticos Premiun, (2024). https://www.anton-paar.com/es-es/(accessed May 6, 2024).
- [172] P. Baybutt, The ALARP principle in process safety, Process Safety Progress 33 (2014) 36–40. https://doi.org/10.1002/prs.11599.
- [173] U. Health and Safety Executive, Managing risks and risk assessment at work, (2024). https://www.hse.gov.uk/simple-health-safety/risk/index.htm (accessed May 22, 2024).
- [174] L. Lugo, M.J.P. Comuñas, E.R. López, J. Fernández, (p, Vm, T, x) measurements of dimethyl carbonate+octane binary mixtures: I. Experimental results, isothermal compressibilities, isobaric expansivities and internal pressures, Fluid Phase Equilib 186 (2001) 235–255. https://doi.org/https://doi.org/10.1016/S0378-3812(01)00518-0.
- [175] M.J.P. Comuñas, J.P. Bazile, A. Baylaucq, C. Boned, Density of diethyl adipate using a new vibrating tube densimeter from (293.15 to 403.15) K and up to 140 MPa calibration and measurements, J Chem Eng Data 53 (2008) 986–994. https://doi.org/10.1021/JE700737C.
- [176] W. Wagner, A. Pruß, The IAPWS Formulation 1995 for the Thermodynamic Properties of Ordinary Water Substance for General and Scientific Use, J. Phys. Chem. Ref. Data 31 (2002) 387–535. https://doi.org/10.1063/1.1461829.
- [177] Joint Committee for Guides in Metrology (JCGM) 100:2008, Evaluation of measurement data. Guide to the expression of uncertainty in measurement, (2008).
- [178] E.W. Lemmon, R. Span, Short fundamental equations of state for 20 industrial fluids, J Chem Eng Data 51 (2006) 785–850. https://doi.org/10.1021/je050186n.

- [179] J.H. Dymond, R. Malhotra, J.D. Isdale, N.F. Glen, (p, Q, T) of n-heptane, toluene, and oct-1-ene in the range 298 to 373 K and 0.1 to 400 MPa and representation by the Tait equation, J. Chem. Thermodynamics 20 (1988) 603–614. https://doi.org/10.1016/0021-9614(88)90090-0.
- [180] E.W. Lemmon, I.H. Bell, M.L. Huber, M.O. McLinden, NIST Standard Reference Database 23: Reference Fluid Thermodynamic and Transport Properties-REFPROP, Version 10.0, National Institute of Standards and Technology, Standard Reference Data Program, Gaithersburg, (2018). https://doi.org/https://doi.org/10.18434/T4/1502528.
- [181] J.J. Segovia, D. Vega-Maza, C.R. Chamorro, M.C. Martín, High-pressure isobaric heat capacities using a new flow calorimeter, Journal of Supercritical Fluids 46 (2008) 258–264. https://doi.org/10.1016/J.SUPFLU.2008.01.011.
- [182] Inc. Agilent Technologies, Agilent 1100 Series Isocratic Pump Reference Manual, (2002) 1–264. https://www.agilent.com/en-us/library/usermanuals?N=135 (accessed May 16, 2024).
- [183] E.I. Concepción, A. Moreau, D. Vega-Maza, X. Paredes, M.C. Martín, Heat capacities of different amine aqueous solutions at pressures up to 25 MPa for CO2 capture, J Mol Liq 377 (2023) 121575. https://doi.org/10.1016/j.molliq.2023.121575.
- [184] SI Analytics, ViscoClock plus, (2024). https://www.xylemanalytics.com/en/general-product/id-372/viscoclock-plus (accessed October 21, 2024).
- [185] Anton Paar, Automatic Kinematic Viscometer SVM 3001, (2024). https://www.anton-paar.com/us-en/products/details/svm-series/?sku=105001 (accessed November 8, 2024).
- [186] S. Al Ghafri, G.C. Maitland, J.P.M. Trusler, Densities of aqueous MgCl2(aq), CaCl2(aq), KI(aq), NaCl(aq), KCl(aq), AlCl3(aq), and (0.964 NaCl + 0.136 KCl)(aq) at temperatures between (283 and 472) K, pressures up to 68.5 MPa, and molalities up to 6 mol·kg-1, J Chem Eng Data 57 (2012) 1288–1304. https://doi.org/10.1021/je2013704.
- [187] S. Al Ghafri, G.C. Maitland, J.P.M. Trusler, Correction to "Densities of aqueous MgCl2(aq), CaCl2(aq), KI(aq), NaCl(aq), KCl(aq), AlCl3(aq), and (0.964 NaCl + 0.136 KCl)(aq) at temperatures between (283 and 472) K, pressures up to 68.5 MPa, and molalities up to 6 mol·kg-1," J Chem Eng Data 64 (2019) 2912–2912. https://doi.org/10.1021/acs.jced.9b00316.
- [188] E.I. Concepción, Á. Gómez-Hernández, M.C. Martín, J.J. Segovia, Density and viscosity measurements of aqueous amines at high pressures: DEA-water, DMAE-water and TEA-water mixtures, J Chem Thermodyn 112 (2017) 227–239. https://doi.org/10.1016/J.JCT.2017.05.001.
- [189] J.H. Dymond, R. Malhotra, The Tait Equation: 100 Years On, Int J Thermophys 9 (1988).
- [190] The MathWorks Inc., MATLAB (R2023b), (2023). https://matlab.mathworks.com/ (accessed February 5, 2024).
- [191] P.R. Bevington, D.K. Robinson, Data Reduction and Error Analysis for the Physical Sciences., McGraw-Hill, London, 1992.

- [192] TURINGBOT SOFTWARE CONSULTORIA EM TECNOLOGIA DA INFORMAÇÃO LTDA, TuringBot Software, (2024). https://turingbotsoftware.com/ (accessed February 3, 2025).
- [193] S. Cabani, G. Conti, E. Matteoli, A. Tani, Apparent Molal Heat Capacities of Organic Compounds in Aqueous Solution, Journal of the Chemical Society, Faraday Transactions 1: Physical Chemistry in Condensed Phases 73 (1977) 476–486. https://doi.org/10.1039/F19777300476.
- [194] I.M.S. Lampreia, A.F.S. Santos, Ultrasound Speeds and Molar Isentropic Compressions of Aqueous 2-(Ethylamino)ethanol Mixtures from 283.15 to 303.15 K, J Solution Chem 39 (2010) 808–819. https://doi.org/10.1007/s10953-010-9546-5.
- [195] B.P. Soares, V. Štejfa, O. Ferreira, S.P. Pinho, K. Růžička, M. Fulem, Vapor pressures and thermophysical properties of selected ethanolamines, Fluid Phase Equilib 473 (2018) 245–254. https://doi.org/10.1016/J.FLUID.2018.05.032.
- [196] H.J. Song, M.G. Lee, H. Kim, A. Gaur, J.W. Park, Density, viscosity, heat capacity, surface tension, and solubility of CO2 in aqueous solutions of potassium serinate, J Chem Eng Data 56 (2011) 1371–1377. https://doi.org/10.1021/je101144k.
- [197] K. Kim, H. Lim, J. Kim, J.H. Kang, H.S. Park, J. Park, H. Song, Density, Dynamic Viscosity, Surface Tension, Vapor Pressure, Heat Capacity, and Thermal Conductivity of Aqueous 2-(Isopropylamino)ethanol Solutions at Temperatures from (298.15 to 353.15) K, J Chem Eng Data 68 (2023) 1872–1880. https://doi.org/10.1021/acs.jced.3c00137.
- [198] S. Seyam, I. Dincer, M. Agelin-Chaab, Optimization and comparative evaluation of novel marine engines integrated with fuel cells using sustainable fuel choices, Energy 301 (2024). https://doi.org/10.1016/j.energy.2024.131629.
- [199] D.A. Howard, B.N. Jørgensen, Z. Ma, Multi-Method Simulation and Multi-Objective Optimization for Energy-Flexibility-Potential Assessment of Food-Production Process Cooling, Energies (Basel) 16 (2023). https://doi.org/10.3390/en16031514.
- [200] S.A. Shaikh, M.F.N. Taufique, K. Balusu, S.S. Kulkarni, F. Hale, J. Oleson, R. Devanathan, A. Soulami, Finite Element Analysis and Machine Learning Guided Design of Carbon Fiber Organosheet-Based Battery Enclosures for Crashworthiness, Applied Composite Materials (2024). https://doi.org/10.1007/s10443-024-10218-z.
- [201] P. Haratipour, A. Baghban, A.H. Mohammadi, S.H.H. Nazhad, A. Bahadori, On the estimation of viscosities and densities of CO2-loaded MDEA, MDEA + AMP, MDEA + DIPA, MDEA + MEA, and MDEA + DEA aqueous solutions, J Mol Liq 242 (2017) 146–159. https://doi.org/10.1016/j.molliq.2017.06.123.
- [202] C.F. Patzschke, J. Zhang, P.S. Fennell, J.P.M. Trusler, Density and Viscosity of Partially Carbonated Aqueous Solutions Containing a Tertiary Alkanolamine and Piperazine at

- Temperatures between 298.15 and 353.15 K, J Chem Eng Data 62 (2017) 2075–2083. https://doi.org/10.1021/acs.jced.7b00144.
- [203] J. Liu, S. Wang, A. Hartono, H.F. Svendsen, C. Chen, Solubility of N2O in and density and viscosity of aqueous solutions of piperazine, ammonia, and their mixtures from (283.15 to 323.15) K, J Chem Eng Data 57 (2012) 2387–2393. https://doi.org/10.1021/je300102d.

ABOUT THE AUTHOR

Yisel Pérez Milian earned her Bachelor of Chemical Engineering from the Central University of Las Villas in Cuba between 2013 and 2018. Following graduation, she remained at the university, where she taught General Chemistry and conducted research on bioethanol production from sugarcane honey through fermentation.

In 2020, she was awarded a Santander-UA scholarship, enabling her to pursue a Master's degree in Environmental and Sustainable Chemistry at the University of Alicante. Her master's thesis investigated air quality within the port environment of Alicante. During her studies, she also completed a curricular internship at the university, calculating the university's carbon footprint and compiling a comprehensive technical report.

In 2021, she obtained a pre-doctoral contract co-funded by the University of Valladolid and Banco Santander. This allowed her to start doctoral research within the TermoCal group at the University of Valladolid. The following section provides a summary of her research activities undertaken during this period.

Table 1. Publications

Number	Reference	Authors
	"Densities and isobaric heat capacities at high pressures of aqueous	Y. Pérez-Milian, A.
	solutions of 2-diethylaminoethanol (DEAE) or 2-	Moreau, J.D.
1	ethylaminoethanol (EAE) for CO ₂ capture". Journal of Molecular	Arroyave, F.
	Liquids 404 (2024) 124851.	Vélez, X. Paredes,
	https://doi.org/10.1016/j.molliq.2024.124851	D. Vega-Maza.
	"Measurement of high-pressure properties for aqueous solutions of	Y. Pérez-Milian, D.
	amines: Densities and isobaric heat capacities of 3-	Vega-Maza, J.D.
2	(methylamino)propylamine and 1-methylpiperazine binary	Arroyave, F.
	mixtures". Journal of Molecular Liquids 430 (2025) 127685.	Vélez, X. Paredes,
	https://doi.org/10.1016/j.molliq.2025.127685	A. Moreau.

Table 2. Book Chapter

Number	Reference	Authors
1	"A comparative study of thermophysical properties of aqueous amine solutions for CO ₂ mitigation", 2023, International Conference on Efficiency, Cost, Optimization, Simulation and Environmental Impact of Energy Systems. ISBN: 978-171387492-8.	E.I. Concepción, A. Moreau, J.J. Segovia, Y. Pérez- Milian, J.D. Arroyave, M.C. Martín.

Table 3. International and National Conferences.

Number	Conference / Place / Date	Contribution type
	Y. Pérez-Milian, A. Moreau, D. Vega-Maza	
	"Diseño del sistema de seguridad de un densímetro de tubo	
1	vibrante para la medida de la densidad de mezclas CO2 y	Oral presentation
1	aminas".	Oral presentation
	VIII Jornadas de Investigadoras de Castilla y León: La Aventura	
	de la Ciencia y la Tecnología, León (Spain), 2022.	
	A. Moreau, Y. Pérez-Milian, J.J. Segovia, M.C. Martín, X.	
	Paredes, M.A. Villamañán, D. Vega-Maza.	
2	"Speed of sound measurements of propane with hydrogen".	Co-author
	32 nd European Symposium on Applied Thermodynamics (ESAT),	
	Graz (Austria), 2022.	
	Y. Pérez-Milian, A. Moreau, D. Vega-Maza	
	"Caracterización termofísica de mezclas de CO2 con	
3	soluciones acuosas de aminas para la captura de CO2".	Oral presentation
	11th International Seminar on Thermodynamic Engineering of	
	Fluids (11ISTEF), Tarragona (Spain), 2022.	
	J.J. Segovia, A. Moreau, Y. Pérez-Milian, X. Paredes, M.C.	
4	Martín, C.R. Chamorro, M.A. Villamañán, <u>D. Vega-Maza.</u>	Co-author
4	"Metrología para la descarbonización de la red de gas".	Co-author
	7º Congreso Español de Metrología, Ávila (Spain), 2022.	
	Y. Pérez-Milian, A. Moreau, D. Vega-Maza.	
5	"Densidad y capacidad calorífica isobárica a alta presión de	Oral presentation
	soluciones acuosas de amina para la captura de CO2".	

	IX Jornadas de Investigadoras de Castilla y León: La Aventura de	
	la Ciencia y la Tecnología, Salamanca (Spain), 2023.	
	Y. Pérez-Milian, A. Moreau, D. Vega-Maza.	
	"Densidad a alta presión de mezclas acuosas de aminas para	
6	la captura de CO2".	Poster presentation
	XV Reunión de Jóvenes Investigadores Iberoamericanos,	
	Tordesillas (Spain), 2023	
	E.I. Concepción, A. Moreau, J.J. Segovia, Y. Pérez-Milian, J.D.	
	Arroyave, M.C. Martín.	
	"A comparative study of thermophysical properties of	
7	aqueous amine solutions for CO2 mitigation".	Co-author
	36 th International Conference on Efficiency, Cost, Optimization,	
	Simulation and Environmental Impact of Energy, Las Palmas de	
	Gran Canaria (Spain), 2023.	
	Y. Pérez-Milian, J.D. Arroyave, A. Moreau, D. Vega-Maza.	
	"High-pressure density measurement of an aqueous solution	
8	of MEA with CO ₂ for carbon capture process".	Oral presentation
	12 th International Seminar on Thermodynamic Engineering of	
	Fluids, Tarragona (Spain) 2023.	
	D. Vega-Maza, Y. Pérez-Milian, A. Moreau, X. Paredes, M.C.	
	Martín, J.J. Segovia.	
9	"Densities of aqueous solutions of 2-diethylaminoethanol and	Co-author
	2-ethylaminoethanol".	Co-author
	26 th IUPAC International Conference of Chemical	
	Thermodynamics, Osaka (Japan), 2023.	
	J.D. Arroyave, Y. Pérez-Milian, D. Vega-Maza, A. Moreau, X.	
	Paredes, J.J. Segovia, M.C. Martín.	
10	"Modelling and experimental measurements of CO ₂ in	Co-author
10	aqueous amines".	Co dadioi
	8 th International Solvothermal and Hydrothermal Association	
	Conference, Valladolid (Spain), 2023.	
	Y. Pérez-Milian, A. Moreau, D. Vega-Maza, X. Paredes, J.J.	
	Segovia, M.C. Martín.	
11	"Densities of aqueous solutions of amines up to 100 MPa".	Poster presentation
	22 nd European Conference on Thermophysical Properties, Venice	
	(Italy), 2023.	

	Y. Pérez-Milian, J.D. Arroyave, A. Moreau, D. Vega-Maza, X.	
	Paredes, J.J. Segovia.	
12	"Isobaric heat capacities at high pressures of DEAE-water	Onel managetation
12	and EAE-water mixtures for CO2 capture".	Oral presentation
	22 nd European Conference on Thermophysical Properties, Venice	
	(Italy), 2023.	
	Y. Pérez-Milian, J.D. Arroyave, A. Moreau, D. Vega-Maza, J.J.	
	Segovia.	
13	"Captura de CO2: densidad de soluciones acuosas de aminas	Poster presentation
13	cargadas con CO ₂ ".	Poster presentation
	X Jornadas de Investigadoras de Castilla y León: La Aventura de	
	la Ciencia y la Tecnología, Valladolid (Spain), 2024.	
	J.D. Arroyave, Y. Pérez-Milian, D. Vega-Maza, <u>A. Moreau</u> , M.C.	
	Martín.	
	"Solubility of carbon dioxide in aqueous solution of	
14	Monoethanolamine and N-Methyldiethanolamine:	Co-author
	experimental measurements and modelling".	
	22 nd Symposium on Thermophysical Properties, Boulder, CO	
	(USA), 2024.	
	Y. Pérez-Milian, J.D. Arroyave, <u>A. Moreau</u> , D. Vega-Maza, X.	
15	Paredes, J.J. Segovia.	
	"Density and Isobaric Heat Capacity of CO2-Loaded Amines	Co-author
13	for Carbon Capture".	Co-autifoi
	22 nd Symposium on Thermophysical Properties, Boulder, CO	
	(USA), 2024.	

Table 4. Courses and Workshops.

Number	Courses/Workshops	Place
1	Recursos de información para doctorandos (segunda edición), 2022.	Escuela de Doctorado de la Universidad de Valladolid (EsDuUVa).
2	CCSx: Climate Change: Carbon Capture and Storage (online), 2022.	University of Edinburgh (Scotland).

3	Iniciación a la escritura y publicación de artículos científicos (Ingenierías y Arquitectura), 2022.	Escuela de Doctorado de la Universidad de Valladolid (EsDuUVa).
4	Carrera Científica Investigadora, 2023.	PressTech Group, BioEcoUVa Institute.
	Cómo escribir Abstracts y artículos científicos en	Escuela de Doctorado de la
5	inglés (Ciencias, Ciencias de la Salud, Ingeniería y	Universidad de Valladolid
	Arquitectura), 2023.	(EsDuUVa).
		Escuela de Ingenierías
6	Curso de Cromatografía HPLC, 2023.	Industriales, Universidad de
		Valladolid.
	Realización de figuras de calidad para artículos científicos (segunda edición), 2023.	Escuela de Ingenierías
7		Informáticas, Universidad de
	cientificos (segunda edicion), 2023.	Valladolid.
8	Inglés B2.2, 2023	Centro de Idiomas, Universidad
8	Higies B2.2, 2023	de Valladolid.
	Iniciación a la escritura de propuestas de proyectos	Escuela de Doctorado de la
9	de investigación, 2024.	Universidad de Valladolid
	de investigación, 2024.	(EsDuUVa).
10	Basic and intermediate openLCA Training, 2024.	BioEcoUVa Institute.
11	Carreras investigadoras emergentes: trayectorias	Universitat Ramon Llull -
11	profesionales fuera de la universidad, 2024.	FPCEE Blanquerna.
12	IA para la salud docente, 2025.	Universidad de Valladolid
13	Realizando la tesis doctoral: mapa de ruta, 2025.	Universidad de Valladolid
14	Gestión Integral de Proyectos de Innovación, 2025.	Universidad de Valladolid

International Research Visit

Research Visit (3 months): "Viscosity measurement for CO_2 -loaded aqueous amines solutions". Thermophysics Laboratory, Department of Chemical Engineering, Imperial College London, UK. Dates: 02/09/2024 to 02/12/2024.